Universidad Francisco de Vitoria | Escuela Internacional de Doctorado

Escuela Internacional de Doctorado
Universidad Francisco de Vitoria

TESIS DOCTORAL

DESARROLLO Y CARACTERIZACIÓN DE ANTICUERPOS TERAPÉUTICOS MULTIESPECÍFICOS

LAURA RUBIO PÉREZ

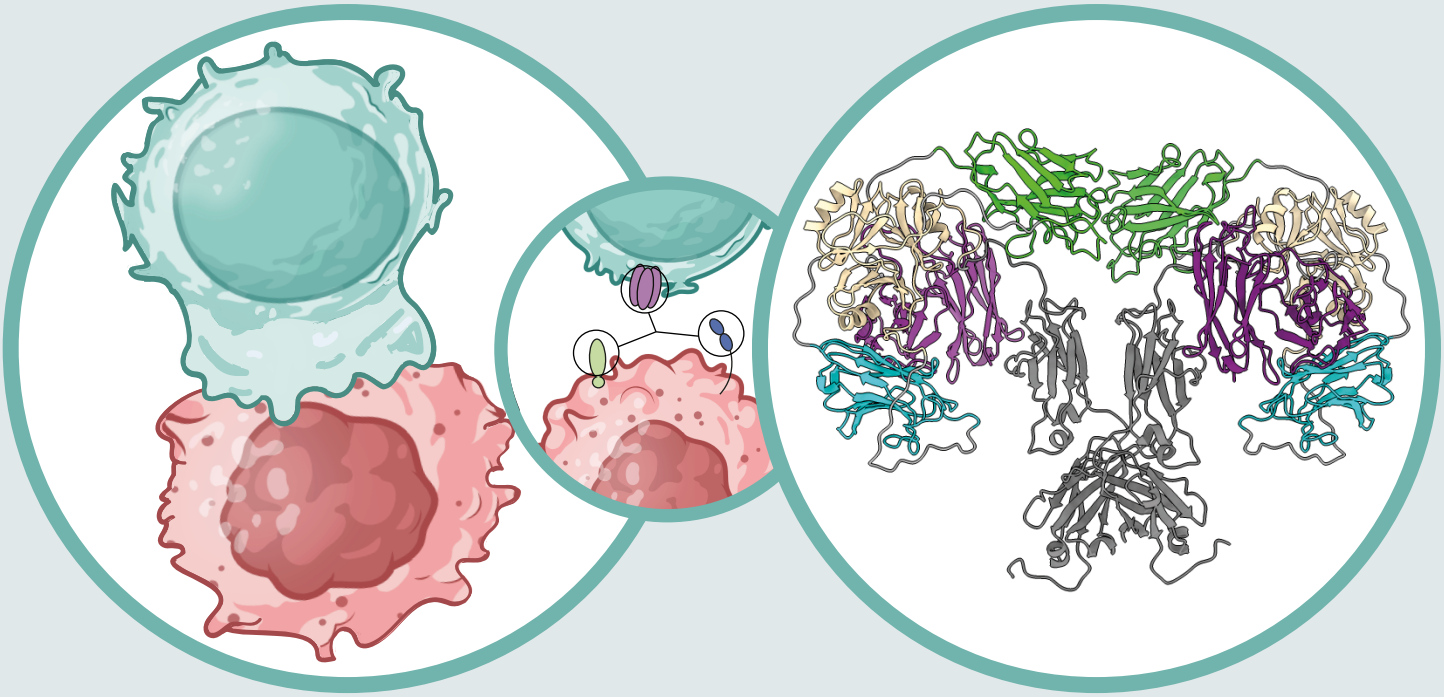

Directores
Luis Álvarez-Vallina
Cruz Santos Tejedor

Madrid, 2024

UNIVERSIDAD FRANCISCO DE VITORIA

ESCUELA INTERNACIONAL DE DOCTORADO

Programa de Doctorado en Biotecnología, Medicina y Ciencias Biosanitarias

TESIS DOCTORAL

DESARROLLO Y CARACTERIZACIÓN DE ANTICUERPOS TERAPÉUTICOS MULTIESPECÍFICOS

MEMORIA PARA OPTAR AL GRADO DE DOCTOR PRESENTADA POR

Laura Rubio Pérez

DIRECTORES

Dr. Luis Álvarez-Vallina

Dr. Cruz Santos Tejedor

Pozuelo de Alarcón (Madrid), 2024

Esta Tesis Doctoral, realizada en la Unidad de Inmunoterapia del Cáncer (UNICA)/Grupo de Inmuno-oncología e Inmunoterapia, del Servicio de Inmunología del Hospital Universitario 12 de Octubre de Madrid, ha sido financiada por la Cátedra de Inmunología UFV-Merck, la Fundación CRIS contra el Cáncer (FCRIS-2021-0090), la Asociación Española contra el Cáncer (PROYE19084ALVA), el Ministerio de Ciencia e Innovación (PDC2021-121711-100), la Comunidad de Madrid (P2022/BMD-7225) y el Instituto de Salud Carlos III (DTS/00089 y PI/2001030) con el apoyo del Consejo Regional Europeo Fondos FEDER para el desarrollo.

A mis padres

AGRADECIMIENTOS

Tras estos años de esfuerzo y dedicación, muchas personas han sido clave para que esta tesis doctoral sea una realidad. Quiero dedicar este espacio para reconocer y agradecer a todos aquellos que me han apoyado y guiado a lo largo de este camino.

En primer lugar, quisiera expresar mi agradecimiento a mi director de tesis y jefe durante estos 4 años, Luis Álvarez Vallina, por su supervisión, su profundo conocimiento en el campo y su búsqueda de la excelencia durante el proceso de realización de esta tesis doctoral. También quiero expresar mi gratitud por el tiempo y el esfuerzo que ha dedicado a revisar los borradores, discutir ideas y proporcionar comentarios detallados. Extiendo mi agradecimiento al co-director y tutor de tesis, Cruz Santos, por haber formado parte de este trabajo en cada etapa de este proyecto y por toda la ayuda que ha proporcionado.

También, me gustaría agradecer a Belén Blanco, quien me dio la oportunidad de empezar en este grupo de investigación, me enseñó las primeras técnicas y me animó a tomar la decisión de seguir en el mundo de la investigación realizando la tesis doctoral. Y, por supuesto, a Leadartis, especialmente a Marta Compte, ya que su experiencia, comprensión, paciencia y ayudas en los momentos de pánico contribuyeron a mi aprendizaje y experiencia en este mundo. Sigo manteniendo que habría que erigir una estatua en su honor. Asimismo, quiero agradecer a Rocío, por enseñarme un trato tan amable y cariñoso con los ratones, así como por compartir el truco de su prodigioso dedo meñique para una mejor sujeción.

A todos mis compañeros, antiguos y nuevos, del grupo del laboratorio UNICA-CIT, por su apoyo y colaboración a lo largo del doctorado. A Elena, por integrarse rápidamente en los entresijos de este laboratorio con tanta motivación. A Sara, que siempre ha formado parte de este laboratorio como una uniqueña más. A Miriam, por sus maneras de contar los dramas, las caras y su mítico levantamiento de ceja.

Además, quería expresar un especial agradecimiento a los compañeros que han estado en los momentos de mayor estrés y alegría a lo largo de este largo camino. Su apoyo, confianza y cariño han sido necesarios para poder conseguir esta meta: A Anaïs, por haber sido mi hermana mayor durante un tiempo, gracias por dejarme conocerte en las largas tardes a deshoras que compartíamos a finales de 2020, eres una persona maravillosa que tiene mucho que enseñar, tanto en lo laboral como en lo personal. A Ainhoa, por enseñarme a llevar la frustración con humor y, sobretodo, lo más importante y básico de mis años aquí: purificar. A Antonio y sus patatas, fuiste uno de los grandes descubrimientos, caracterizándote por ser una persona increíble, súper divertida y cariñosa, y con un amplio conocimiento de todo, aunque no lo reconozcas. Tienes mucho que enseñarnos.

A Carmen, por ser única, siempre fiel a ti misma, gracias por haberme dado la oportunidad de conocerte tanto, haberme enseñado tantas cosas y ser tan buena amiga. A Marina, por haber estado aguantando sola mi último tramo en esta aventura, siempre con una sonrisa, animando y apoyando. Has sido mi persona ansiolítica este último año, y mi compañera de dramas de dianas. A Laura, porque eres una persona increíble, siempre has ayudado a todo el mundo sin esperar nada a cambio y por todos los momentos que nos has regalado con tus historias inventadas. A Oana, eres una de las mejores personas que he podido conocer en mi vida y la primera en enseñarme más a fondo la mayoría de técnicas básicas del laboratorio. Fuiste la primera predoc del laboratorio a la que vi y recuerdo que estabas comiendo un bocadillo a las cinco de la tarde en un cuartucho mal acondicionado para tal fin. No sé por qué decidí quedarme al ser testigo de eso, pero no me arrepiento ni un momento. Gracias a ello, he podido conocer a gente tan maravillosa que ahora puedo llamar amigas. Habéis sido un apoyo importantísimo en estos años, tanto dentro como fuera del laboratorio, adictas de los escapes.

A Raquel, por haber sido la primera persona a la que conocí al llegar a Madrid y seguir estando ahí, compartiendo nuestros problemas y alegrías durante todos estos años, escuchándonos quejarnos de lo mismo una y otra vez en bucle.

A mis amigas de la uni, ocho personas increíbles que compartimos unos años inolvidables y complicados, donde aprendimos entre todas a ser adultas responsables: Miranda, Oumaima, Sandra, Sara, Sheila, Zaira y, en especial, a Xiomara y Laura Marsal. Esas amigas que, aunque nos veamos una vez al año por la distancia, parece que no haya pasado el tiempo y sigamos recordando cada una de las anécdotas surrealistas que compartimos.

Por último, y más importante, a mi familia. A mi hermano Carlos, por ese amor incondicional y porque siempre hemos estado y estaremos el uno para el otro. Y, en especial, a mis padres, por haberme apoyado siempre, haber creído en mí y haber fomentado que cumpliese mis sueños. A ti, mamá, por haber sido la figura de mujer inspiradora a la que quiero llegar a ser: independiente, inteligente, con una fortaleza imparable, y un amor insuperable. A ti, papá, que me has enseñado esa inquietud por aprender, el afán por el conocimiento, la persona que me introdujo y fomentó ese pensamiento científico. Esta tesis es un logro que hubiera querido compartir contigo más que con nadie. Sé que hubieras estado orgulloso y hubieras querido estar presente el día de la defensa de la tesis. Tu amor y todos los consejos que me has dado, hasta el último día, me han acompañado en todo este camino y me acompañarán siempre. Juntos me habéis enseñado a aprender a adaptarme a cada situación y a estar siempre orgullosa de mis acciones. Os admiro a los dos, habéis sido mis dos pilares más fuertes.

ÍNDICE

ABREVIATURAS

AAT	Antígeno asociado a tumor
ACE2	*Angiotensin Converting Enzyme 2,* Enzima convertidora de angiotensina 2
ACT	*Adoptive Cell Therapy*, terapia celular adoptiva
ADCC	*Antibody-Dependent Cellular Cytotoxicity*, Citotoxicidad celular dependiente de anticuerpo
ADCP	*Antibody-Dependent Cellular Phagocytosis*, Fagocitosis celular dependiente de anticuerpo
APC	*Antigen Presenting Cell*, Célula presentadora de antígeno
ATTACK	*Asymmetric Tandem Trimerbody for T cell Activation and Cancer Killing*
B-ALL	*B cell Acute Lymphoid Leukemia*, Leucemia linfoide aguda de células B
BCMA	*B Cell Maturation Antigen*, Antígeno de maduración de célula B
BiKE	*Bispecific NK cell Engager*
BiTE	*Bispecific T cell Engager*
CAR	*Chimeric Antigen Receptor*, Receptor de antígenos quimérico
cCD1	Célula dendrítica convencional de tipo 1
CCR	Cáncer colorrectal
CD	Célula dendrítica
CDC	*Complement-Dependent Cytotoxicity*, Citotoxicidad dependiente de complemento
CDR	*Complementary Determining Regions*, Región determinante de complementariedad
CEA	*Carcinoembryonic Antigen*; Antígeno carcinoembrionario
C_H	Dominio constante de la cadena pesada *(Heavy)*
CHIKV	Virus chikungunya
CRD	*Cysteine-Rich pseudo repeats Domain*
CTA	*Cancer/Testis Antigen*
CTLA-4	*Cytotoxic T Lymphocyte Antigen 4*, *antígeno 4 asociado al linfocito T citotóxico*
DART	*Dual-Affinity Retargeting*
dsDb	*disulfide stabilized Diabody*
EE.UU.	Estados Unidos de América
EGF	*Epidermal Growth Factor*, Factor de crecimiento epidérmico
EGFR	*Epidermal Growth Factor Receptor*, Receptor del factor de crecimiento epidérmico

EMA	*European Medicines Agency*, Agencia Europea del Medicamento
EpCAM	*Epithelial Cell Adhesion Molecule*, Molécula de adhesión celular epitelial
Fab	*Fragment antigen-binding*, Fragmento de unión al antígeno
FAP	*Fibroblast Activation Protein*, Proteína de activación de fibroblastos
Fc	Fragmento cristalizable
FcR	*Fc Receptor*, Receptor para la región Fc de la inmunoglobulina G
FcRn	*Fc Receptor neonatal*, Receptor Fc neonatal
FDA	*Food and Drug Administration*, Administración de Alimentos y Medicamentos de los EE.UU.
Fv	Fragmento variable
GPCR5D	*G protein-coupled receptor class C group 5 member D,* Miembro D del grupo 5 de la familia de receptores acoplados a proteína G
HAMA	*Human Anti-Mouse Antibodies*, Anticuerpos humanos anti-ratón
HER2	*Human Epidermal Growth Factor Receptor 2*, Receptor 2 del factor de crecimiento epidérmico humano
HLA	*Human Leukocyte Antigen*, Antígeno leucocitario humano
HSA	*Human Serum Albumin*, Seroalbúmina humana
ICI	*Immune Checkpoint Inhibitor*, Inhibidor de puntos de control inmunes
IFN-γ	Interferón-γ
Ig	Inmunoglobulina
IL-2	Interleucina-2
kDa	Kilodalton
KiH	*Knobs-into-Hole*s
LAG3	*Lymphocyte-Activation Gene 3*, Gen de activación linfocitaria 3
LiTE	*Light T-cell Engager*
LNH	Linfoma no Hodgkin
mAb	*monoclonal Antibody*, Anticuerpo monoclonal
NF-kB	Factor nuclear kappa B
NK	*Natural Killer*, Célula asesina natural
NSCLC	*Non-small cell lung cáncer*, Cáncer de pulmón de células no pequeñas
PD-1	*Programmed Death 1*, Proteína de muerte programada 1
PD-L1	*Programmed Death Ligand 1*, Ligando 1 de muerte programada
RBD	*Receptor Binding Domain*, Dominio de unión al receptor

S	Proteína *Spike* del SARS-CoV-2
SARS-CoV-2	*Acute Respiratory Syndrome Coronavirus 2*, Coronavirus del síndrome respiratorio agudo grave de tipo 2
scDb	*single-chain Diabody*
scFv	*single-chain Fragment variable*, Fragmento variable de cadena única
sdAb	*single-domain antibody*, Anticuerpo monodominio
STAb	*Secretion of T cell redirecting bispecific Antibodies*, Secreción de anticuerpos de tipo TCE
TCE	*T Cell Engager*, Anticuerpo biespecífico para redirección de células T
TCR	*T Cell Receptor*, Receptor de antígeno de la célula T
TCR-T	TCRs transgénicos
TIE	Dominios de trimerización derivados del colágeno
TIGIT	*T cell immunoreceptor with Ig and ITIM domains*, Inmunoglobulina de células T y dominio ITIM
TIL	*Tumor-Infiltrating Lymphocyte*s, Linfocitos infiltrantes del tumor
TIM3	*T cell Immunoglobulin and Mucin-domain containing* 3*,* Inmunoglobulina de células T que contiene un dominio de mucina 3
TN	*Tandem nanobody*
TNFRSF	*Tumor Necrosis Factor superfamily,* Superfamilia de receptores del factor de necrosis tumoral
TNF-α	*Tumor Necrosis Factor* α, Factor de necrosis tumoral α
TT	*Tandem Trimerbody*
UE	Unión Europea
VEGF-A	*Vascular Endothelial* G*rowth Factor A*, Factor A de crecimiento del endotelio vascular
V_H	Dominio variable de la cadena pesada (*heavy*)
V_{HH}	*Variable domain of a Heavy-chain-only antibodies*, Dominio variable de anticuerpos formados solo por cadena pesada
VIH	Virus de la inmunodeficiencia humana
V_L	Región variable de cadena ligera (*light*)

RESUMEN

La tecnología de anticuerpos recombinantes ha experimentado un considerable avance en los últimos años, con un número creciente de moléculas en desarrollo clínico, debido a la necesidad de desarrollar tratamientos más efectivos y específicos para diferentes patologías, como el cáncer y las infecciones virales. Aunque existen varias plataformas tecnológicas para la generación de anticuerpos multiespecíficos, aún persisten limitaciones relacionadas con la estabilidad, inmunogenicidad y farmacocinética de las moléculas generadas.

En este trabajo hemos desarrollado un anticuerpo biespecífico PD-L1/EGFR mediante la fusión de un *tandem trimerbody* con las regiones bisagra y Fc de la IgG_1 humana. Este anticuerpo, denominado IgTT-1E, se caracterizó estructural y funcionalmente, demostrando capacidad de reconocer simultáneamente los antígenos EGFR y PD-L1, inhibir la proliferación mediada por EGF, bloquear la interacción PD-1/ PD-L1 e inducir actividad de citotoxicidad celular dependiente de anticuerpos específica de antígeno y desgranulación de las células NK. También demostró una potente actividad anti-tumoral en modelos de ratón humanizados portadores de xenoinjertos de cáncer de mama triple negativo y de cáncer de pulmón, en los que el control del crecimiento tumoral se asoció con un aumento significativo del número de células T $CD8^+$. Estos resultados apoyan el desarrollo clínico del anticuerpo IgTT-1E para el tratamiento de tumores $EGFR^+$.

Con la finalidad de mejorar las tasas de respuesta global de las terapias basadas en el bloqueo de los puntos de control inmune, se han desarrollado estrategias combinadas con anticuerpos agonistas anti-4-1BB para estimular las células T infiltrantes de tumor. Sin embargo, el desarrollo clínico de estos anticuerpos se ha visto obstaculizado debido a la aparición de toxicidades significativas. En este trabajo hemos generado un anticuerpo triespecífico anti-4-1BB/EGFR/PD-L1 basado en la plataforma IgTT, empleando una región Fc silenciada mediante la introducción de mutaciones específicas. Este anticuerpo, denominado IgTT-4E1-S, demostró capacidad de unión simultánea a EGFR, PD-L1 y 4-1BB en solución, bloqueo eficaz de la interacción PD-L1/PD1 y potente coestimulación mediada por 4-1BB, pero sólo en presencia de células que expresan EGFR. Además, también demostró la activación de las funciones efectoras de células T primarias humanas en co-cultivos con células tumorales que expresaban tanto EGFR como PD-L1. Estos resultados demuestran la viabilidad de la IgTT-4E1-S para bloquear específicamente el eje PD-L1/PD-1 e inducir una actividad agonista 4-1BB condicional asociada a la expresión de EGFR.

Los anticuerpos neutralizantes de las infecciones víricas han demostrado potencial para proporcionar protección inmediata contra el SARS-CoV-2. Estas respuestas pueden mejorarse mediante la combinación de neutralización viral y estimulación de la respuesta inmune adaptativa. En este trabajo se ha desarrollado un anticuerpo neutralizante de “amplio espectro”,

denominado TN^T, basado en la plataforma *trimerbody* y en un anticuerpo monodominio biparatópico anti-RBD en tándem, que puede unirse simultáneamente a los seis epítopos de RBD. Posteriormente, se generó un anticuerpo biespecífico, denominado TN^TDNGR-1, con capacidad de dirigir los viriones neutralizados a las células dendríticas convencionales de tipo 1, mediante la fusión de un scFv anti-DNGR-1 en el extremo C-terminal del TN^T. La administración del TN^TDNGR-1, pero no del TN^T, protegió a ratones transgénicos K18-hACE2 de una infección letal por SARS-CoV-2, potenciando respuestas humorales específicas y respuestas de células T $CD8^+$.

SUMMARY

Recombinant antibody technology has made significant progress in recent years, with an increasing number of molecules in clinical development, driven by the need to develop more effective and specific treatments for a range of diseases such as cancer and viral infections. Although there are several technological platforms for the generation of multispecific antibodies, there are still limitations in terms of stability, immunogenicity and pharmacokinetics of the generated candidates.

In this work, we have developed a PD-L1/EGFR bispecific antibody by fusing a tandem trimerbody with the hinge and Fc regions of human IgG1. This antibody, termed IgTT-1E, was structurally and functionally characterized and demonstrated the ability to simultaneously recognize EGFR and PD-L1 antigens, inhibit EGF-mediated proliferation, block PD-1/PD-L1 interaction and induce antigen-specific antibody-dependent cellular cytotoxicity activity and NK cell degranulation. It also demonstrated potent anti-tumor activity in humanized xenograft mouse models of triple negative breast cancer and lung cancer, where tumor growth control was associated with a significant increase in $CD8^+$ T cell numbers. These results support the clinical development of the IgTT-1E antibody for the treatment of $EGFR^+$ cancers.

To improve the overall response rates of checkpoint blockade-based therapies, combination strategies with anti-4-1BB agonist antibodies have been developed to stimulate tumor-infiltrating T cells. However, the clinical development of these antibodies has been hampered by the occurrence of significant toxicities. In this work, we have generated a tri-specific anti-4-1BB/EGFR/PD-L1 antibody based on the IgTT platform using a silenced Fc region by introducing specific mutations. This antibody, designated IgTT-4E1-S, demonstrated simultaneous binding capacity to EGFR, PD-L1 and 4-1BB in solution, effective blockade of PD-L1/PD1 interaction and potent 4-1BB-mediated co-stimulation, but only in the presence of $EGFR^+$ cells. In addition, activation of effector functions of human primary T cells in co-cultures with tumor cells expressing both EGFR and PD-L1 was also shown. These results demonstrate the ability of IgTT-4E1-S to specifically block the PD-L1/PD-1 axis and induce conditional 4-1BB agonist activity associated with EGFR expression.

Neutralizing antibodies have shown the potential to provide immediate protection against SARS-CoV-2 infection. The response can be enhanced by combining viral neutralization and immune stimulation to induce adaptive immune responses. In this work, a broad neutralizing antibody, termed TN^T, was developed based on the trimerbody platform and a tandem biparatopic anti-RBD nanobody capable of binding to all six RBD epitopes simultaneously. Subsequently, a bispecific antibody, termed TN^TDNGR-1, with the ability to target neutralized virions to conventional type 1 dendritic cells was generated by fusing an anti-DNGR-1 scFv to the C-

terminus of TN^T. Administration of TN^TDNGR-1, but not TN^T, protected K18-hACE2 transgenic mice from lethal SARS-CoV-2 infection by enhancing specific humoral responses and $CD8^+$ T cell responses.

INTRODUCCIÓN

1. Anticuerpos

1.1 Estructura general

Los anticuerpos o inmunoglobulinas (Ig) son moléculas que "conectan" el reconocimiento de epítopos específicos con mecanismos efectores, tales como la citotoxicidad celular dependiente de anticuerpos (ADCC; del inglés, *Antibody-Dependent Cellular Cytotoxicity*), la citotoxicidad dependiente de complemento (CDC; del inglés, *Complement-Dependent Cytotoxicity*) y la fagocitosis celular dependiente de anticuerpos (ADCP; del inglés, *Antibody-Dependent Cellular Phagocytosis*).

Estas moléculas son glicoproteínas globulares (150 kDa) y cada anticuerpo se compone de una unidad básica (monómero), que incluye dos cadenas ligeras idénticas (L; del inglés, *Light*) y dos cadenas pesadas idénticas (H; del inglés, *Heavy*). Las cuatro cadenas se unen entre sí mediante enlaces no covalentes y covalentes (disulfuro), dando lugar a una estructura en forma de Y con los fragmentos de unión al antígeno (Fab; del inglés, *Fragment antigen-binding*) en el extremo de los dos brazos de la Y. El Fab contiene las regiones variables (V), las cuales constan de tres regiones determinantes de complementariedad hipervariables (CDR; del inglés, *Complementary Determining Regions*) que forman el sitio de unión al antígeno y confieren la especificidad antigénica. Por tanto, cada inmunoglobulina G (IgG) es bivalente, uniéndose a dos sitios antigénicos idénticos, aumentando así su afinidad y prolongando su retención en el organismo. La función efectora es mediada por el dominio Fc (fragmento cristalizable). El segmento formado por el dominio constante de la cadena pesada 2 (C_{H2}) y la región bisagra interacciona con receptores para el fragmento Fc (FcR; del inglés, Fc Receptor) de las células efectoras y promueve la activación de la cascada del complemento (Figura 1a, b, c).

Los anticuerpos se clasifican en cinco clases según la secuencia de sus regiones constantes de cadena pesada: IgM, IgD, IgG, IgE e IgA (Figura 1e). De estas cinco clases, la IgG es la más ampliamente utilizada en estrategias de inmunoterapia. Además, debido a que su peso molecular excede el límite de aclaramiento renal (70 kDa) y a la interacción a través del segmento formado entre los dominios C_{H2} y C_{H3} con el receptor Fc neonatal (FcRn; del inglés, *Fc Receptor neonatal*), que la protege de la degradación catabólica intracelular (Figura 1d), la IgG tiene una vida media sérica larga[1–3].

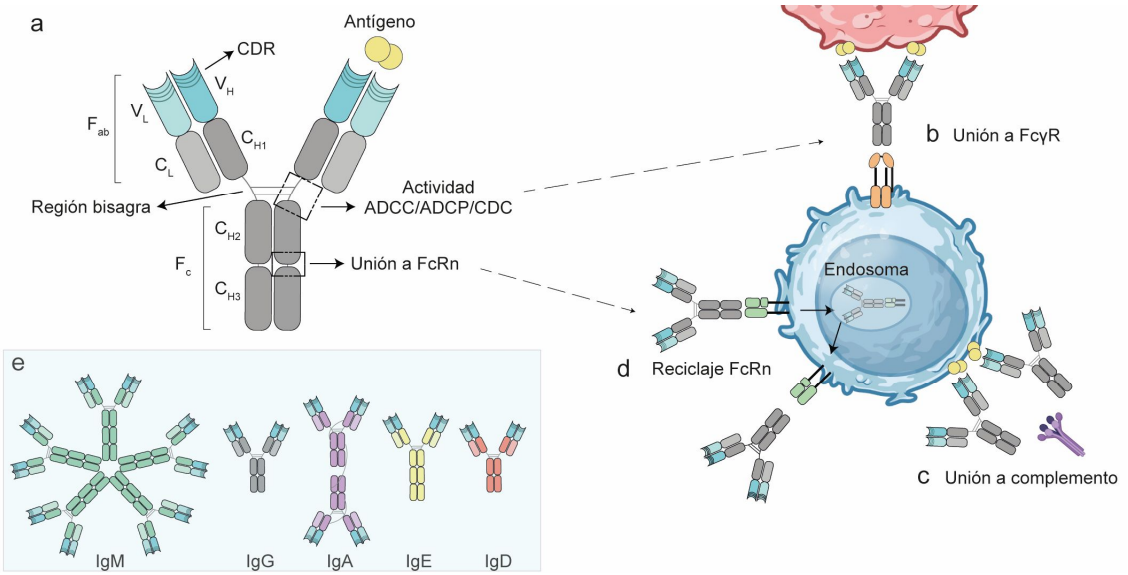

Figura 1. Estructura de la IgG. **a)** La IgG se compone de dos cadenas pesadas (C) y dos cadenas ligeras (L). Las regiones Fab contiene la zona de unión al antígeno, que se establece a través de los CDR. **b)** La región formada por el C_{H2} y la zona bisagra del dominio Fc permite la unión a los FcR de las células inmunes efectoras y **c)** la activación de la cascada del complemento; **d)** mientras que las regiones C_{H2} y C_{H3} interaccionan con el FcRn, promoviendo el reciclaje del anticuerpo. **e)** Estructura de las 5 clases de inmunoglobulinas según la región constante de la cadena pesada.

1.2 Anticuerpos monoclonales

Hace más de un siglo, Paul Ehrlich acuñó el término "bala mágica" para referirse a un agente terapéutico ideal que podría actuar selectivamente sobre patógenos o tumores sin dañar las células normales. No obstante, no fue hasta el año 1975 cuando se desarrolló la tecnología de los **hibridomas**, lo que permitió la generación de anticuerpos monoclonales (mAb; del inglés, *monoclonal Antibody*)[4]. Esta técnica se basa en la fusión de un linfocito B procedente del bazo de un ratón inmunizado, cuya función es producir el anticuerpo, con una célula de mieloma, que aporta la capacidad de proliferación ilimitada. El resultado es la obtención de anticuerpos producidos por un solo clon de células, los cuales reconocen un único epítopo de interés.

Inicialmente, estos mAbs tenían un origen murino, lo que originaba inmunogenicidad en humanos y tenían una capacidad limitada para inducir respuestas efectoras. Sin embargo, los avances en la ingeniería de anticuerpos permitieron el desarrollo de plataformas flexibles para la creación de mAbs **quiméricos** (≈ 25 % murinos, los cuales poseen regiones variables murinas y regiones constantes humanas), **humanizados** (≈ 5-10 % murinos, que poseen los CDR de origen murino, mientras que el resto del anticuerpo es humano) y totalmente **humanos** (Figura 2), que

han permitido resolver muchas de las limitaciones previas[1,5]. El desarrollo de las tecnologías para humanizar los mAbs fue posible gracias Gregory Winter y William J. Harris, quienes plantearon la posibilidad de insertar los CDR de un mAb murino en un dominio variable humano[6], basándose en técnicas de ingeniería genética y ADN recombinante. Sin embargo, los anticuerpos quiméricos y humanizados pueden presentar una afinidad baja e inmunogenicidad, debido a que, en algunos pacientes, se producen respuestas de anticuerpos humanos anti-ratón (HAMA; del inglés, *Human Anti-Mouse Antibodies*)[7]. Actualmente, en la clínica se usan principalmente anticuerpos humanizados o completamente humanos, los cuales se desarrollan empleando tecnologías como las genotecas de anticuerpos en bacteriófagos (*phage display*) o la inmunización de animales transgénicos con genes Ig humanos[3,8,9].

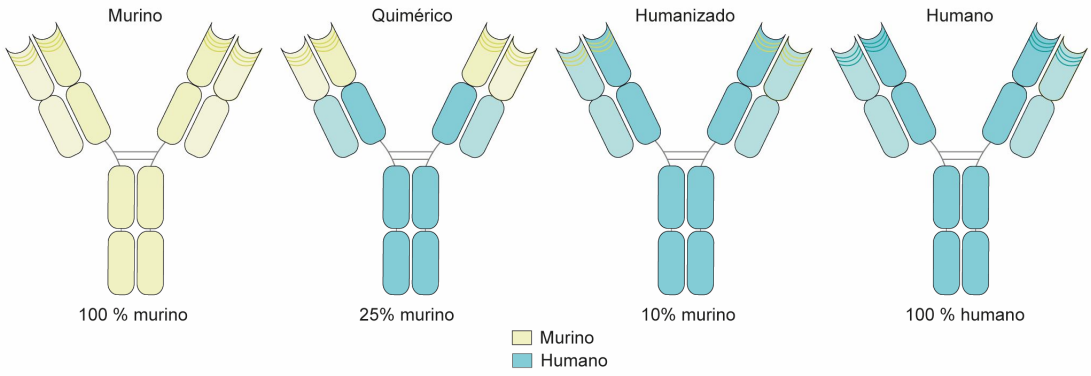

Figura 2. Esquema de la evolución de la humanización de anticuerpos, que incluye mAbs murinos, quiméricos, humanizados y completamente humanos. Las regiones de origen murino se muestran en amarillo; mientras que las regiones de origen humano, en azul.

1.3 Anticuerpos de nueva generación

Se han desarrollado diversos formatos de anticuerpos recombinantes con el objetivo de mejorar su farmacocinética, función efectora, tamaño e inmunogenicidad mediante técnicas de ingeniería de anticuerpos, que implican modificaciones en sus propiedades bioquímicas y biofísicas[2,10]. Las técnicas de ingeniería de anticuerpos se vieron impulsadas a partir del año 1989, cuando se consiguió desarrollar los procedimientos para la clonación y expresión de genes de anticuerpos[11]. Estas técnicas permiten producir anticuerpos con alta especificidad y afinidad, al mismo tiempo que reducen la inmunogenicidad y los efectos adversos[3,12], entre las que destacan:

a) Generación de fragmentos de anticuerpos:

En el proceso fisiológico de generación de anticuerpos se pueden diferenciar dos etapas fundamentales. En primer lugar, se produce el reordenamiento del repertorio genético natural de Igs. Posteriormente, los linfocitos B que expresan estos anticuerpos experimentan hipermutaciones somáticas cuando entran en contacto con el antígeno, las cuales se concentran especialmente en las CDR, con el objetivo de generar variantes moleculares con mayor afinidad, que se caracteriza por una cinética de disociación del antígeno más lenta. Este proceso natural que ocurre en la generación de anticuerpos se puede replicar artificialmente mediante la generación de genotecas de anticuerpos, los cuales son sometidos a un proceso de cribado para evaluar la capacidad de unión al antígeno diana[3,13,14]. Para esto, se han desarrollado diversas tecnologías de exhibición (*display*) de fragmentos de anticuerpos *in vitro*, que incluyen genotecas en bacteriófagos filamentosos (*phage display*), bacterias (*bacterial display*), levaduras (*yeast display*), o incluso ribosomas (*ribosome display*), cuya finalidad es generar anticuerpos recombinantes de forma rápida y efectiva[14]. Sin embargo, es necesario desarrollar métodos de selección (*screening*) específicos y evitar las uniones no específicas.

La clonación constituye un paso esencial en la generación de fragmentos recombinantes de anticuerpos, los cuales ofrecen algunas ventajas sobre los anticuerpos completos. El **fragmento Fab** (50 kDa) incorpora la cadena ligera completa (dominios V_L y C_L) y los dominios V_H y C_{H1} de la cadena pesada de una Ig convencional, conectados por un enlace disulfuro intercatenario. El **fragmento variable (Fv)** (25-30 kDa) está formado únicamente por las regiones V_L y V_H de un anticuerpo. Por otro lado, el **Fv de cadena única** o **scFv** (del inglés, *single-chain Fragment variable*) es un Fv con los dominios V_H y V_L conectados por un polipéptido flexible, generalmente tres repeticiones de cuatro glicinas y una serina $(G_4S)_3$ (Figura 3). El **anticuerpo de dominio único** (**sdAb**; del inglés, *single-domain antibody*), también denominado *nanobody* (12-15 kDa), deriva de las regiones variables de anticuerpos compuestos únicamente por cadenas pesadas, identificados en camélidos (V_{HH}; del inglés, *Variable domain of Heavy-chain only antibodies*) y peces cartilaginosos[3,15]. Por último, los formatos de anticuerpos biespecíficos se basan en la combinación de dos dominios de reconocimiento de antígenos diferentes en múltiples configuraciones[16].

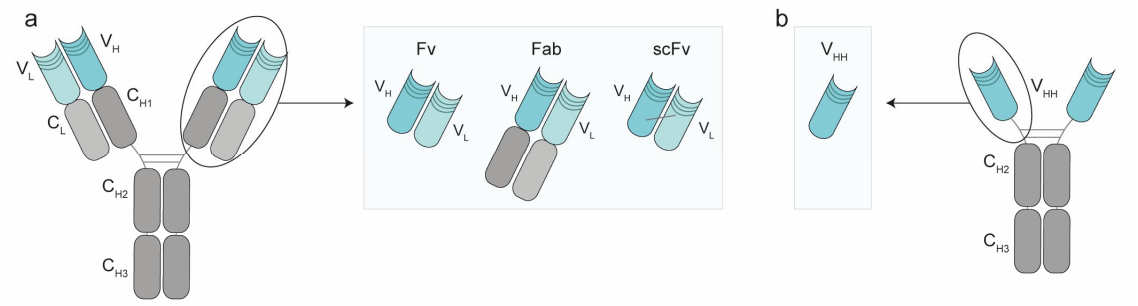

Figura 3. Representación de los fragmentos de anticuerpos. a) Representación esquemática de la estructura de la IgG y de los fragmentos derivados Fv, Fab y scFv. **b)** Representación esquemática de la estructura de un anticuerpo que solo consta de cadenas pesadas y de un dominio V_{HH} derivado de él mismo.

b) Anticuerpos no basados en Ig:

Los anticuerpos multiespecíficos con formatos no similares a la Ig (sin región Fc) están compuestos por fragmentos derivados de anticuerpos fusionados mediante enlaces flexibles y/o dominios de multimerización. Los fragmentos de unión pueden ser Fab, scFv o V_{HH}[17]. La multimerización de estos fragmentos permite ajustar el tamaño, la forma, la valencia y la especificidad del anticuerpo para optimizar su función, vida media y capacidad de penetración tumoral[18].

El formato más utilizado es el ***tandem* scFv**, que consiste en la fusión de dos scFv a través de un conector peptídico flexible (*linker*) corto, generalmente un módulo G_4S. Un tipo de *tandem* scFv es el **BiTE®** (del inglés, *Bispecific T cell Engager*), basado en la fusión de un scFv anti-CD3 y un scFv anti-antígeno asociado a tumor (AAT). Otras variantes de este formato sería el denominado **LiTE** (del inglés, *Light T-cell Engager*) y **BiKE** (del inglés, *Bispecific NK-cell Engager*), en los que el scFv anti-AAT es sustituido por un V_{HH} anti-AAT o el scFv anti-CD3 es sustituido por un scFv anti-CD16, respectivamente. Otra variante de este formato es el **triplebody**, basado en la fusión en *tandem* de tres scFv[16] (Figura 4).

Otro formato ampliamente utilizado es el **diabody**, el cual está formado por dos cadenas independientes, donde una contiene los dominios V_HA-V_LB y la otra cadena contiene los dominios V_HB-V_LA, siendo A y B dos anticuerpos de distintas especificidades. En este caso, se favorece la heterodimerización de los dominios V_H y V_L de la misma especificidad, pero de cadenas distintas. Sin embargo, pueden producirse homodimerizaciones no funcionales, por lo que se han desarrollado diferentes modificaciones para favorecer la heterodimerización, como podría ser puentes disulfuros en el caso del **dsDb** (del inglés, *disulfide stabilized Diabody*)[19] y del

DART® (del inglés, *Dual-Affinity Retargeting*)[20,21]; o la fusión de las dos cadenas por un *linker* adicional, como en el caso del **scDb** (del inglés, *single-chain Diabody*)[22] (Figura 4). Además de estos anticuerpos, se ha generado una gran diversidad de formatos, algunos de los cuales se recogen en la Figura 4.

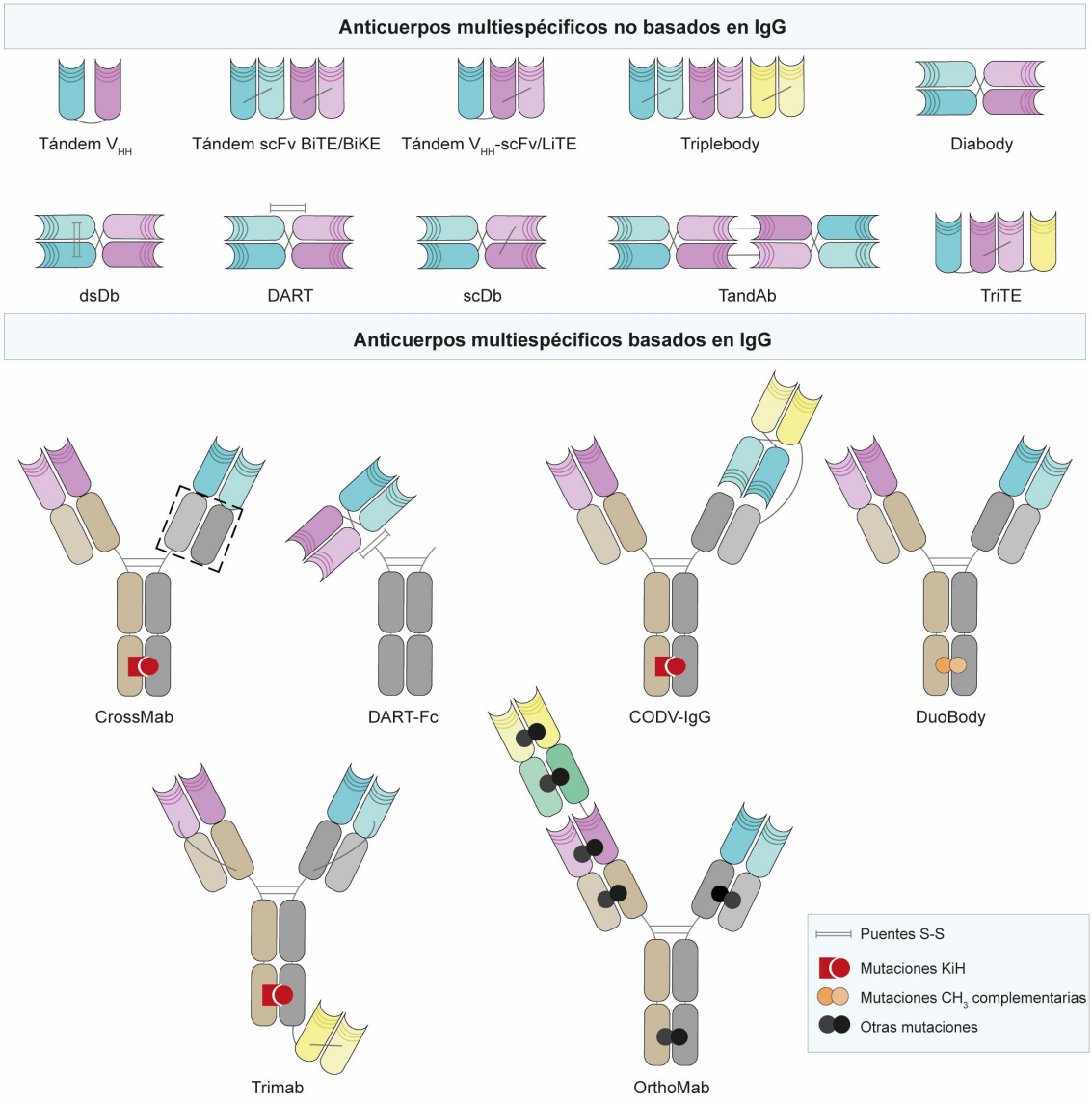

Figura 4. Plataformas tecnológicas para generar anticuerpos multiespecíficos. Representaciones esquemáticas de algunos formatos de anticuerpos multiespecíficos no basados en la estructura de la IgG (no contienen Fc; arriba), y de formatos basados en la IgG (contienen Fc; abajo).

c) Anticuerpos basados en Ig:

Los formatos similares a la Ig son moléculas que imitan parcial o totalmente a los anticuerpos naturales, incluyendo una región Fc, ya sea funcional o no. La región Fc de la IgG es un componente clave de los anticuerpos terapéuticos debido a su capacidad para generar una

homodimerización eficaz, aumentar la vida media sérica a través de la interacción con el FcRn, y mejorar la afinidad funcional y los tiempos de retención tumoral gracias a su bivalencia[23,24]. Además, la región Fc de la IgG induce funciones efectoras, ADCC y la activación del complemento, específicamente hacia las células reconocidas por el anticuerpo[24]. No obstante, el alto peso molecular de algunos formatos de anticuerpos multiespecíficos con Fc dificulta la penetración tisular, a pesar de garantizar una vida media sérica prolongada[16].

La ingeniería de la región Fc ofrece diversas posibilidades. Se puede modificar la actividad efectora, dado que esta región activa la cascada del complemento e interacciona con los FcγR de las células NK (del inglés, *Natural Killer*) y de los macrófagos, activándolas. Para aumentar o disminuir la afinidad de unión a los FcγR, se pueden introducir mutaciones específicas en la región Fc y modificaciones en los oligosacáridos o en el nivel de glicosilación[3]. En determinadas aplicaciones es necesario que los anticuerpos no muestren ninguna actividad en la región Fc. Por ejemplo, los anticuerpos biespecíficos basados en Ig que activan células T, se diseñan con una región Fc no funcional (silenciada), para evitar la activación inespecífica de los linfocitos T[3,25,26]. Además, las funciones efectoras ADCC y CDC también pueden modificarse mediante cambio de isotipo, ya que estas varían entre las diferentes subclases de IgG. También se pueden alterar las propiedades farmacocinéticas y la vida media del anticuerpo, modificando la interacción entre el dominio Fc y los receptores FcRn, mediante la introducción de mutaciones. Las interacciones fuertes proporcionan a los anticuerpos una mayor estabilidad en la circulación sanguínea, mientras que las interacciones débiles aceleran su eliminación[27].

Los primeros anticuerpos multiespecíficos se producían mediante la co-transfección de ADN o el método del cuadroma (hibridoma híbrido), el cual da lugar a una línea celular que produce dos cadenas pesadas diferentes y dos cadenas ligeras diferentes, generando así moléculas IgG biespecíficas. Sin embargo, esta aproximación genera también múltiples subproductos no funcionales[28]; por tanto, dado que el rendimiento de purificación obtenido es bajo debido a su heterogeneidad, este proceso no es adecuado para la producción a gran escala[29]. Para superar estas limitaciones se han generado nuevas técnicas.

El método **"Knobs-into-Holes"** (KiH), desarrollado por Carter et al[30], resuelve la formación no deseada de homodímeros de cadenas pesadas al incluir una mutación "knob" en un dominio Fc y una mutación "hole" en otro dominio Fc, promoviendo la heterodimerización de la Fc[24,29]. Además, para abordar el emparejamiento incorrecto de las cadenas ligeras y pesadas de dos anticuerpos diferentes y, con la finalidad de producir una población homogénea de IgG bispecíficas, la metodología KiH puede combinarse con la **tecnología CrossMab**[31,32]. Con esta

tecnología, dos dominios de uno de los Fab del anticuerpo son intercambiados entre sí (V_H-V_L o C_{H1}-C_L), forzando así el acoplamiento entre la cadena ligera y pesada correspondientes (Figura 4). Sin embargo, la incorporación de múltiples mutaciones en cadenas pesadas incrementa el riesgo de inmunogenicidad y reduce la estabilidad de las regiones Fc.

Para superar este inconveniente, se han generado diferentes estrategias con el objetivo de producir anticuerpos multipespecíficos portadores de regiones Fc, como la fusión directa de un scFv a un anticuerpo completo o a un dominio Fc completo incluyendo la región bisagra[24]. Un ejemplo de la primera estrategia es el trabajo de Li et al.[33], donde se generó un anticuerpo biespecífico con una IgG completa y un scFv fusionado en el extremo N-terminal. Por otro lado, un ejemplo de la segunda aproximación es el estudio de Koopmans et al.[34], donde un *tandem* scFv biespecífico está fusionado a un dominio Fc. Otro ejemplo sería el **DART-Fc**, formado por la fusión de un DART® al extremo N-terminal de una región Fc (Figura 4). Otra plataforma para superar la desventaja mencionada anteriormente es **CODV-Ig**[35], donde las cadenas pesadas y ligeras de una IgG se extienden mediante la adición N-terminal de los dominios variables derivados de una segunda IgG (Figura 4).

Una estrategia que persigue el correcto ensamblaje es la tecnología **DuoBody®**, que permite generar anticuerpos biespecíficos mediante la producción de dos anticuerpos parentales de manera independiente y su posterior ensamblaje por medio de un proceso denominado "intercambio controlado de brazo Fab". Este proceso se basa en el uso de condiciones reductoras y mutaciones puntuales en los dominios C_{H3}[36] (Figura 4). Otra estrategia para generar anticuerpos multiespecíficos es el formato **TriMAb**, que promueve la heterodimerización de dos cadenas pesadas distintas usando la tecnología KiH y el acoplamiento correcto de las cadenas ligeras de cada Fab mediante *linkers* adicionales (V_L-C_L-$(G_4S)_6$-V_H-C_{H1}). También se puede incorporar a esta estructura uno o dos scFv fusionados al Fc para generar variantes tri o tetraespecíficas[16,37] (Figura 4).

Otra estrategia para el desarrollo de este tipo de anticuerpos sería el formato **OrthoMab**. Esta se basa en la creación de una interfaz Fab ortogonal cadena pesada/cadena ligera que utiliza cambios entre los dominios C_{H1}-C_L y V_H-V_L para favorecer el correcto ensamblaje de las cadenas pesada y ligera que provienen del mismo anticuerpo parental, junto al uso de mutaciones en los dominios CH_3 para promover el apareamiento entre cadenas pesadas de diferentes especificidades[38]. Además, este formato puede utilizarse para añadir fragmentos Fab adicionales a través del uso de *linkers* para generar más multiespecificidades (Figura 4).

d) Tecnología *Trimerbody*:

Aún con todas las estrategias descritas anteriormente, el desarrollo de anticuerpos multipecíficos plantea importantes retos, ya que la estabilidad de algunas construcciones puede estar comprometida. Asimismo, la producción de anticuerpos multiespecíficos puede verse obstaculizada por subproductos no deseados debidos a un ensamblaje incorrecto[16], además de la inmunogenicidad potencialmente asociada con las mutaciones introducidas, las cuales son necesarias para un ensamblaje correcto.

Los *trimerbodies* son anticuerpos multiméricos que pueden solventar alguno de estos inconvenientes, ya que se basan en las propiedades funcionales y estructurales de los dominios de multimerización del colágeno XVIII o XV[39]. Estos dominios de trimerización (TIE) son de tamaño pequeño (menor de 60 aminoácidos) y no son inmunogénicos. La plataforma *trimerbody* permite el desarrollo de anticuerpos multivalentes (tri-, tetra- o hexavalentes) y mono- o multiespecíficos (bi- o tri-específicos).

La primera generación de *trimerbodies* se basó en la fusión de scFvs en el extremo N-terminal o C-terminal de los dominios TIE del colágeno XV[40] o del colágeno XVIII[41,42], obteniendo anticuerpos monoespecíficos y trivalentes de 110 kDa (Figura 5). Posteriormente, se generaron anticuerpos hexavalentes, fusionando scFvs con la misma o diferente especificidad en ambos extremos N- y C-terminal del dominio TIE, obteniendo anticuerpos de un peso molecular de 190 kDa. Además, también se generaron anticuerpos con V_{HH} fusionados, o con una combinación de V_{HH} y scFv en ambos extremos del TIE (denominados *trimerbodies* asimétricos)[43,44](Figura 5). También se han generado *trimerbodies* asimétricos con scFvs frente a un AAT en el extremo N-terminal y ribotoxina fúngica en el extremo C-terminal del TIE, que se han denominado trimertoxinas[45].

La tecnología *trimerbody* también permite la generación de moléculas multiespecíficas con una estequiometría definida y una orientación controlada en una sola cadena polipeptídica. El formato ***tandem trimerbody*** (TT) es una fusión de tres V_{HH} y tres dominios TIE^{XVIII} con *linkers* de glicina y serina intercalados, obteniendo una molécula que es capaz de reconocer sus antígenos con alta especificidad y afinidad[46]. La evolución más destacable del formato TT es el denominado **ATTACK** (del inglés, *Asymmetric Tandem Trimerbody for T cell Activation and Cancer Killing*), generado mediante la fusión de tres V_{HH} dirigidos a un AAT en el extremo N-terminal, y un scFv individual anti-CD3 fusionado al extremos C-terminal del TIE, obteniendo un TT asimétrico con capacidad de activar células T en presencia del antígeno tumoral especifico[47,48] (Figura 5).

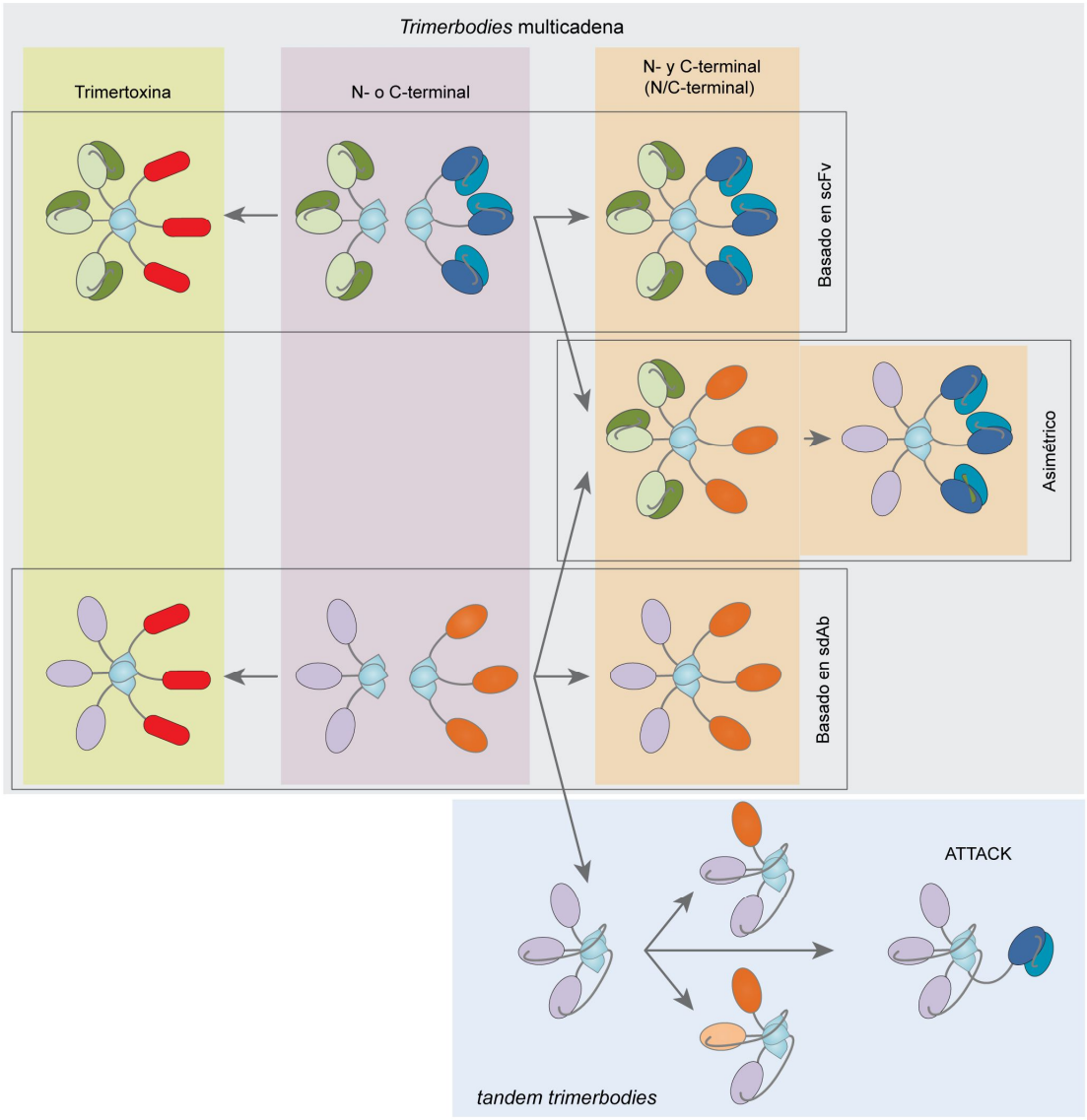

Figura 5. Diagramas esquemáticos que muestran la estructura de diferentes *trimerbodies* multicadena y *tandem trimerbodies*. Los *trimerbodies* multicadena (recuadro gris) son moléculas generadas mediante la fusión de scFv y/o V_{HH} (simétricos o asimétricos) con los extremos N- y/o C-terminal del dominio TIE. Las trimertoxinas son *trimerbodies* asimétricos con una especificidad tumoral en el extremo N-terminal y una toxina en el extremo C-terminal. Los *tandem trimerbodies* (recuadro azul) se generan fusionando al extremo N-terminal tres V_{HH} conectados mediante *linkers* peptídicos con tres dominios TIE, en una sola cadena polipeptídica. Por último, la molécula ATTACK se genera mediante la fusión de un scFv anti-CD3 en el extremo C-terminal de un *tandem trimerbody* con especificidad anti-tumoral. Figura adaptada de Compte et al[48].

2. Aplicaciones de los anticuerpos en oncología.

El cáncer es un reto considerable para la medicina moderna, ya que exige enfoques terapéuticos innovadores capaces de actuar eficazmente sobre las células tumorales y aprovechar, al mismo tiempo, las competencias del sistema inmunitario. Inducir respuestas inmunes anti-tumorales específicas y duraderas ha sido una tarea compleja debido a que, durante muchas décadas, se ha debatido sobre el papel del sistema inmune en la biología del cáncer. Algunos tumores pueden inhibir las respuestas inmunes mediante la generación de entornos inmunosupresores, o mediante el desarrollo de mecanismos de escape activo a la acción de las células del sistema inmunitario[49,50]. Por tanto, para desarrollar inmunoterapias anti-tumorales efectivas y seguras hay que superar numerosos obstáculos, como la selección de los antígenos diana, que pueden expresarse en tejidos normales y generar fenómenos de toxicidad; la inactivación o agotamiento de las células T; y el desarrollo de un microambiente tumoral inmunosupresor[50,51].

La inmunoterapia del cáncer utiliza diversos enfoques para modular el sistema inmune, entre los que se incluyen la estimulación de los mecanismos efectores y la inhibición de los mecanismos supresores. Existen diferentes estrategias de estimulación, como la vacunación con antígenos tumorales, el incremento de la presentación antigénica y los virus oncolíticos. Además, también se utilizan anticuerpos agonistas frente a miembros de la superfamilia de receptores del factor de necrosis tumoral (TNFRSF; del inglés, *Tumor Necrosis Factor superfamily*), los cuales proporcionan señales coestimuladoras a los linfocitos T. Para contrarrestar los mecanismos inmunosupresores, se han empleado anticuerpos para reducir la actividad o el número de células T reguladoras, o bloquear receptores inhibidores (puntos de control inmune), entre otras. El objetivo es interrumpir las señales que inhiben las respuestas inmunes, permitiendo así que las células T ataquen las células tumorales de manera más eficaz [52,53].

La identificación de antígenos apropiados ha sido uno de los principales desafíos en el desarrollo de terapias basadas en anticuerpos. Estas terapias pueden tener mecanismos de acción diversos, como modular la función de un antígeno o receptor (actuando como agonistas o antagonistas), o del sistema inmune (mediante modificaciones en la actividad efectora de la Fc y la activación de células T); o la administración de un fármaco conjugado con un anticuerpo dirigido a un AAT específico. Las terapias con mAbs focalizadas en un antígeno único tiene limitaciones, como son la aparición de resistencias debido a la pérdida de expresión del antígeno diana[54]. Para incrementar la eficacia terapéutica es necesario actuar sobre varios AAT

simultáneamente[55]. Por este motivo, en los últimos años, los anticuerpos biespecíficos han surgido como una alternativa a la terapia combinada. La finalidad de esta estrategia es actuar sobre múltiples moléculas implicadas en el proceso patogénico con un único fármaco. Desde una perspectiva tecnológica y regulatoria, esto simplifica el desarrollo al reducir las etapas de fabricación y limitar las pruebas preclínicas y clínicas a una entidad molecular única.

Según la *Antibody Society*[56], hasta marzo de 2024 hay 206 anticuerpos terapéuticos aprobados en la Unión Europea (UE) y en Estados Unidos (EE.UU.) por la Agencia Europea del Medicamento (EMA; del inglés, *European Medicines Agency*) y por la Administración de Alimentos y Medicamentos (FDA; del inglés, *Food and Drug Administration*), respectivamente. De estos, 96 presentan indicaciones oncológicas (Tabla 1 y Anexo). Además, casi otra veintena de anticuerpos están en el proceso final de revisión y otros muchos se encuentran en distintas fases de ensayos clínicos.

Tabla 1. Anticuerpos aprobados en la UE o EE.UU. para uso terapéutico en oncología (marzo de 2024).

Nombre genérico	Diana	Fuente/Modificaciones Fc	Primeras indicaciones	Año
Edrecolomab	EpCAM	Mur/No	CCR	1995
Rituximab	CD20	Quim/No	LNH	1997
Trastuzumab	HER2	Huz/No	Cáncer de mama	1998
Gemtuzumab ozogamicin	CD33	Huz/S228P	LMA	2000
Alemtuzumab	CD52	Huz/No	Esclerosis múltiple; LMC	2001
Ibritumomab tiuxetan	CD20	Mur/No	LNH	2002
Cetuximab	EGFR	Quim/No	CCR	2003
Tositumomab-I131	CD20	Mur/No	LNH	2003
Bevacizumab	VEGF-A	Huz/No	CCR	2004
Panitumumab	EGFR	Hum/No	CCR	2006
Catumaxomab	EPCAM, CD3	Híbrido rata-ratón/No	Ascitis maligna	2009
Ofatumumab	CD20	Hum/No	LLC-B	2009
Brentuximab vedotin	CD30	Quim/No	LH, LACG	2011
Ipilimumab	CTLA-4	Hum/No	Melanoma metastásico	2011
Pertuzumab	HER2	Huz/No	Cáncer de mama	2012
Ado-trastuzumab emtansine	HER2	Huz/No	Cáncer de mama	2013
Obinutuzumab	CD20	Huz/Bajo en fucosa	LLC-B	2013
Blinatumomab	CD19, CD3ε (tan-scFv)	Mur/No aplicable	LLA-B	2014
Nivolumab	PD-1	Hum/S228P	Melanoma, NSCLC	2014
Pembrolizumab	PD-1	Huz/S228P	Melanoma	2014
Ramucirumab	VEGFR2	Hum/No	Cáncer gástrico	2014
Daratumumab	CD38	Hum/No	MM	2015
Dinutuximab	GD2	Quim/No	Neuroblastoma	2015

Elotuzumab	SLAMF7	Huz/No	MM	2015
Necitumumab	EGFR	Hum/No	NSCLC	2015
Atezolizumab	PD-L1	Huz/Aglycosylado (N297A)	Cáncer de vejiga	2016
Olaratumab	PDGFRα	Hum/No	Sarcoma tejido blando	2016
Avelumab	PD-L1	Hum/No	CCM	2017
Durvalumab	PD-L1	Hum/L234F;L235E;P331S	Cáncer de vejiga	2017
Inotuzumab ozogamicin	CD22	Huz/S228P	LLA-B	2017
Cemiplimab	PD-1	Hum/S228P	CCE	2018
Emapalumab	IFNg	Hum/No	LHH primaria	2018
Mogamulizumab	CCR4	Huz/Afucosilado	Síndrome de Sézary	2018
Moxetumomab pasudotox	CD22 (inmunotoxina dsFv)	Mur/No aplicable	Leucemia de células pilosas	2018
[fam-]trastuzumab deruxtecan	HER2	Huz/No	Cáncer de mama metastásico HER2+	2019
Enfortumab vedotin	Nectin-4	Hum/No	Cáncer urotelial	2019
Polatuzumab vedotin	CD79b	Hum/No	LCBGD	2019
Belantamab mafodotin	BCMA	Hum/Afucosilado	MM	2020
Isatuximab	CD38	Quim/No	MM	2020
Margetuximab-cmkb	HER2	Quim/F243L; R292P; Y300L; V305I; P396L	HER2+ cáncer de mama metastásico	2020
Naxitamab-gqgk	GD2	Huz/No	Neuroblastoma	2020
Sacituzumab govitecan	TROP-2	Huz/No	Cáncer de mama triple negativo	2020
Tafasitamab	CD19	Huz/S239D; I332E	LCBGD	2020
Amivantamab	EGFR, cMET	Hum/Bajo en fucosa; K409R; F405L	NSCLC con mutaciones en el exon 20 de EGFR	2021
Dostarlimab	PD-1	Huz/S228P	Cáncer endometrial	2021
Loncastuximab tesirine	CD19	Huz/No	LCBGD	2021
Tisotumab vedotin	Tissue factor	Hum/No	Cáncer cervical	2021
Mirvetuximab soravtansine	FRα	Huz/No	Cáncer de ovario	2022
Mosunetuzumab	CD20, CD3ε	Huz/*a)	Linfoma folicular	2022
Relatlimab	LAG-3	Hum/S228P	Melanoma	2022
Tebentafusp	gp100, CD3ε (scFv-TCR)	Huz/No	Melanoma uveal metastásico	2022
Teclistamab	BCMA, CD3ε	Huz/*b)	MM	2022
Tremelimumab	CTLA-4	Hum/No	Cáncer hepático	2022
Elranatamab	BCMA, CD3ε	Huz/IgG1RRR o IgG2deltaA-RRRR; IgG1EEE o IgG2deltaA-EEEE	MM	2023
Epcoritamab	CD20, CD3ε	Huz/*c)	LCBGD	2023
Glofitamab	CD20, CD3ε (Fab-Fc x Fab-Fab-Fc)	Huz/*d)	LCBGD	2023
Retifanlimab	PD-1	Huz/S228P	CCM	2023
Talquetamab	GPCR5D, CD3ε	Huz/*d)	MM	2023
Tislelizumab	PD-1	Huz/S228P; E233P, F234V, L235A, D265A	Carcinoma esofágico de células escamosas	2023
Toripalimab	PD-1	Huz/S228P	Carcinoma nasofaríngeo	2023

Mur: murino; **Quim**: quimérico; **Huz**: humanizado; **Hum**: Humano; **CCR**: Cáncer colorrectal; **LNH**: linfoma no Hodgkin; **LMA**: leucemia mieloide aguda; **LMC**: leucemia mieloide crónica; **LLC-B**: leucemia linfoblástica

crónica de células B; **LH**: linfoma Hodgkin; **LACG**: linfoma anaplásico de células grandes; **LLA-B**: leucemia linfoblástica aguda de células B; **NSCLC**: Cáncer de pulmón de células no pequeñas, (del inglés, *Non-small cell lung cáncer*); **MM**: mieloma múltiple; **CCM**: carcinoma de células de Merkel; **CCE:** cáncer de células escamosas; **LHH**: linfohistiocitosis hemofagocítica; **LCBGD:** linfoma de células B grandes difuso; ***a)** Hetero HH: T366W x T366S-L368A-Y407V (KiH); N297G (Fc-aglicosilado); ***b)** Hetero HH: F405L-R409K x WT (R409); ambas cadenas: S228P y F234A, L235A; ***c)** Hetero HH, HL intercambiado: L234F x K409R (ensamblaje biespecífico); ambas cadenas: L234F, L235E, D265A (Fc silenciado); ***d)** Hetero HH: S354C-T366W x Y349C-T366S-L368A-Y407V (KiH y extra cisteínas); acoplamiento HL: CrossMab; ambas cadenas: L234A, L235A, P329G (Fc-silenciado).

2.1 Anticuerpos dirigidos frente a antígenos asociados al tumor

Para el desarrollo de tratamientos oncológicos basados en mAbs, se ha empleado una amplia variedad de AATs expresados en neoplasias hematológicas [CD19, CD20, CD22, CD30, CD33, CD38, CD52, CD79b, antígeno de maduración de célula B (BCMA; del inglés, *B Cell Maturation Antigen*), SLAMF7, miembro D del grupo 5 de la familia de receptores acoplados a proteína G (GPCR5D; del inglés, *G protein-coupled receptor, class C group 5 member D*)], y en tumores sólidos [receptor del factor de crecimiento epidérmico (EGFR; del inglés, *Epidermal Growth Factor Receptor*), receptor del factor de crecimiento epidérmico humano 2 (HER2/ErbB2/neu), molécula de adhesión de células epiteliales (EpCAM; del inglés, *Epithelial Cell Adhesion Molecule*), antígeno carcinoembrionario (CEA; del inglés, *Carcinoembryonic Antigen*), factor de crecimiento del endotelio vascular (VEGF-A; del inglés, *Vascular Endothelial Growth Factor A*), Nectina-4, GD2 y DLL3][18,56] (Figura 6). Para estos AATs se han desarrollado diferentes tipos de anticuerpos, aprobados o en revisión, los cuales se recogen en la Tabla 1 y Anexo.

El cáncer colorrectal, de pulmón y de cabeza y cuello, presentan una incidencia alta y muestran, con frecuencia, una expresión elevada de factores de crecimiento y sus receptores, como la familia del factor de crecimiento epidérmico (EGF; del inglés, *Epidermal Growth Factor*). La sobreexpresión de dos de estos receptores, EGFR y HER2, se ha vinculado o relacionado con un comportamiento clínico más agresivo. Estos receptores se componen de un dominio de unión extracelular, un segmento transmembrana y un dominio intracelular proteína tirosina quinasa, que incluye un segmento regulador carboxilo terminal[57]. La activación de los receptores se produce mediante la homodimerización o formación de dímeros entre dos receptores idénticos; o mediante la heterodimerización de receptores diferentes de la misma familia. La formación de estos dímeros está promovida por la unión del ligando o por la sobreexpresión de receptores en la membrana celular[57,58]. Tras la dimerización del receptor, se activa la proteína tirosina quinasa

y se produce la autofosforilación en residuos de tirosina. Esto desencadena la señalización mitogénica y otras actividades celulares[59,60].

Por este motivo se han desarrollado anticuerpos dirigidos a bloquear el receptor EGFR. Por ejemplo, el mAb cetuximab, que bloquea la interacción entre el ligando EGF y el receptor EGFR e inhibe la activación RAS-ERK, es efectivo en el cáncer colorrectal (CCR) metastásico[61]. También han sido aprobados los anticuerpos anti-EGFR panitumumab y necitumumab, así como el anticuerpo biespecífico EGFR x c-MET amivantamab. En otras regiones geográficas distintas a EE.UU. y Europa, existen otros mAbs en el mercado como son nimotuzumab y cetuximab conjugado al fotosensibilizador IR700[56].

También se han desarrollado V_{HH} inhibidores de EGFR, los cuales presentan ventajas frente a los mAbs, como la posibilidad de interaccionar con epítopos no accesibles para los anticuerpos convencionales, los cuales suelen presentar paratopos planos. Estos V_{HH} pueden inhibir la activación del EGFR inducida por el ligando, empleando varios mecanismos: bloqueando la unión del ligando al EGFR de manera estérica, similar al cetuximab, como el V_{HH} 7D12; o interaccionando con un epítopo próximo a la unión de los dominios II/III del EGFR, impidiendo así los cambios conformacionales necesarios en el receptor para la unión de alta afinidad con el ligando y la dimerización, como en el caso de los V_{HH} EgA1 y 9G8[62,63].

2.2 Terapia con inhibidores de puntos de control inmune

Los inhibidores de los puntos de control inmune (ICI; del inglés, *Immune Checkpoint Inhibitors*) representan una de las estrategias de inmunoterapia anti-tumoral más prometedora. Durante la última década, la FDA ha aprobado múltiples mAbs de este tipo para el tratamiento de diferentes tipos de cáncer; y las dianas más destacadas son: PD-1 (del inglés, *Programmed Death 1*), PD-L1 (del inglés, *Programmed Death Ligand* 1), CTLA-4 (del inglés, *Cytotoxic T Lymphocyte 4*), LAG3 (del inglés, *Lymphocyte-Activation Gene 3*), TIM3 (del inglés, *T cell Immunoglobulin and Mucin-domain containing 3*) y TIGIT (del inglés, *T cell immunoreceptor with Ig and ITIM domains*)[53,56,64–66] (Tabla 1 y Anexo) (Figura 6). Este tipo de inmunoterapia ha demostrado un éxito clínico notable en pacientes que no respondían a terapias convencionales. Además, las respuestas duraderas observadas en algunos pacientes sugieren la posibilidad de inducir memoria inmune efectiva.

Los tratamientos con mAbs anti-PD-1 y anti-PD-L1 han demostrado notable actividad clínica en múltiples tipos de cáncer. El mAb atezolizumab se convirtió en el primer anti-PD-L1 aprobado,

en el año 2017, para el tratamiento del carcinoma urotelial. Por otro lado, tanto el avelumab como el durvalumab han sido aprobados para el tratamiento de varios tipos de tumores sólidos[67–71]. Hasta marzo de 2024, en EE.UU. y Europa han sido aprobados para uso clínico, o están en revisión para ello, siete bloqueadores PD-L1 y ocho PD-1, los cuales previenen la interacción PD1/PD-L1[56]. Además, la expresión de PD-L1 en el tumor se ha utilizado como biomarcador para identificar a los pacientes que podrían beneficiarse del tratamiento con ICIs. Sin embargo, existe un porcentaje significativo de pacientes que no responden a estos tratamientos y, además, es necesario abordar los efectos adversos asociados a estas terapias[72].

La proteína PD-1 contiene 288 aminoácidos y se expresa principalmente en los linfocitos T, aunque también se encuentra en linfocitos B, células NK y monocitos. Su función principal es autolimitar las respuestas inmunes para minimizar el daño de los tejidos sanos circundantes[73]. La proteína consta de un dominio intracelular, un dominio transmembrana, y un dominio inmunoglobulina extracelular. El dominio intracelular incluye una secuencia que forma un motivo de inhibición inmune basado en tirosina. El receptor PD-1 tiene dos ligandos principales, PD-L1 y PD-L2, formados por un dominio N-terminal que interacciona con PD-1, y un dominio C-terminal, cuya función es desconocida[74].

La proteína PD-L1 se expresa a niveles bajos en tejidos humanos normales, con la excepción de la amígdala, la placenta y una pequeña población de células con características similares a macrófagos en el pulmón e hígado[75,76]. Además, la expresión de PD-L1 puede ser inducida por el interferón gamma (IFN-γ) en prácticamente cualquier célula nucleada, por lo que se incrementa en contextos inflamatorios[75]. La función fisiológica de la regulación positiva de PD-L1 es limitar la inflamación y reducir el daño tisular, inhibiendo tanto la proliferación como la producción de citocinas por parte de las células T activadas[75]. Sin embargo, en el entorno tumoral, la inducción de PD-L1 actúa como un mecanismo de retroalimentación negativa para suprimir respuestas inmunes anti-tumorales[77]. Además, las células cancerosas pueden expresar PD-L1 de forma intrínseca, independientemente de la presencia de IFN-γ. De hecho, la pérdida del gen PTEN, la señalización constitutiva de la quinasa del linfoma anaplásico (ALK) y las mutaciones del EGFR pueden aumentar directamente la expresión de PD-L1 en las células tumorales[78–80].

El objetivo de la “terapia anti-PD”, la cual engloba mAbs dirigidos tanto a PD-1 como a PD-L1, son las células del microambiente tumoral que expresan PD-L1, responsables de la inhibición de las células T efectoras PD-1^+ [75–77]. Sin embargo, la importancia clínica de la expresión de PD-L1 varía según la histología tumoral. En algunos tipos de cáncer, una alta expresión de PD-L1 se correlaciona con mejores resultados; mientras que, en otros tumores, no se asocia con mayor

supervivencia[81,82]. Otro pilar de la terapia anti-PD radica en su capacidad para reactivar respuestas inmunes preexistentes. Aunque es poco probable que los tumores con una baja infiltración de células inmunes se beneficien de la terapia anti-PD, esta situación podría mejorar al combinarla con tratamientos que promuevan la atracción de células inflamatorias hacia el tumor[83].

2.3 Anticuerpos coestimuladores

Los mAbs dirigidos contra PD-1 o PD-L1 han demostrado respuestas clínicas efectivas en algunos pacientes, los cuales pueden experimentar un control duradero de la progresión tumoral; sin embargo, en la mayoría de los casos el beneficio es mínimo. Con el objetivo de aumentar la proporción de pacientes respondedores a la inmunoterapia, se ha explorado el uso de mAbs agonistas frente a diferentes receptores inmunomoduladores como OX40, CD27, CD40, GITR y 4-1BB, los cuales se encuentran en desarrollo clínico[84,85] (Figura 6).

El receptor 4-1BB, también conocido como CD137, fue descubierto en el año 1989 y se caracterizó inicialmente como un gen inducible presente en linfocitos T activados. La interacción entre el 4-1BB y su ligando 4-1BBL, ejerce un efecto regulador positivo en la respuesta celular T[86]. Tras la activación de los linfocitos T a través de su receptor específico para el antígeno (TCR; del inglés, *T Cell Receptor*), el 4-1BB se expresa transitoriamente y, cuando interacciona con su ligando natural o un ligando sintético, se induce una coestimulación independiente de CD28. Esto origina la proliferación y producción de citocinas por parte de las células T a través de la señalización del factor de transcripción nuclear kappa B (NF-kB), además de proteger de la muerte celular programada y prolongar la supervivencia de las células T $CD8^+$ activadas y de memoria[43,85,87–90]. El 4-1BBL se expresa en células presentadoras de antígeno (APC; del inglés, *Antigen Presenting Cell*) activadas, como las células dendríticas (CD), monocitos, células NK, neutrófilos, eosinófilos y macrófagos, así como linfocitos B[91].

Tras la interacción con mAbs agonistas, el 4-1BB se internaliza hacia un compartimento endosomal, desde donde continúa señalizando. Esta señalización induce la liberación de interleucina-2 (IL-2) e IFN-γ, además de aumentar la expresión de genes antiapoptóticos de la familia Bcl-2[92]. De esta manera, los mAbs agonistas anti-4-1BB inducen y potencian la inmunidad anti-tumoral[93–95], ya que estimulan y activan linfocitos T efectores $CD8^+$ para que produzcan INF-γ, linfocitos NKT y células presentadoras de antígeno[96]. Esto origina un aumento en el número y la actividad de los linfocitos T de memoria específicos para antígenos tumorales, lo que resulta en respuestas inmunes duraderas[97].

Los mAbs urelumab (BMS-663513) y utomilumab (PF-05082566) han sido evaluados en ensayos clínicos[98]. Ambos son mAbs totalmente humanos, de tipo IgG_4 (urelumab) o IgG_2 (utomilumab). Urelumab mostró gran potencial en estudios preclínicos[99]. Sin embargo, se asoció con toxicidad hepática severa, lo que llevó a la suspensión de los ensayos clínicos[100,101]. En comparación con urelumab, utomilumab mostró un perfil de seguridad más favorable, ya que no se observaron toxicidades limitantes de dosis ni aumentos en los niveles de enzimas hepáticas en un grupo de 27 pacientes[102]. La diferencia en la toxicidad de urelumab o utomilumab puede deberse a las diferentes propiedades de unión a 4-1BB[103], ya que ambos mAbs reconocen epítopos diferentes, siendo utomilumab un agonista de 4-1BB menos potente que urelumab[85,102]. Sin embargo, ningún anticuerpo anti-4-1BB de tipo IgG ha sido aprobado para uso clínico en EE.UU. o EU debido a las toxicidades asociadas con las interacciones Fc-FcγR.

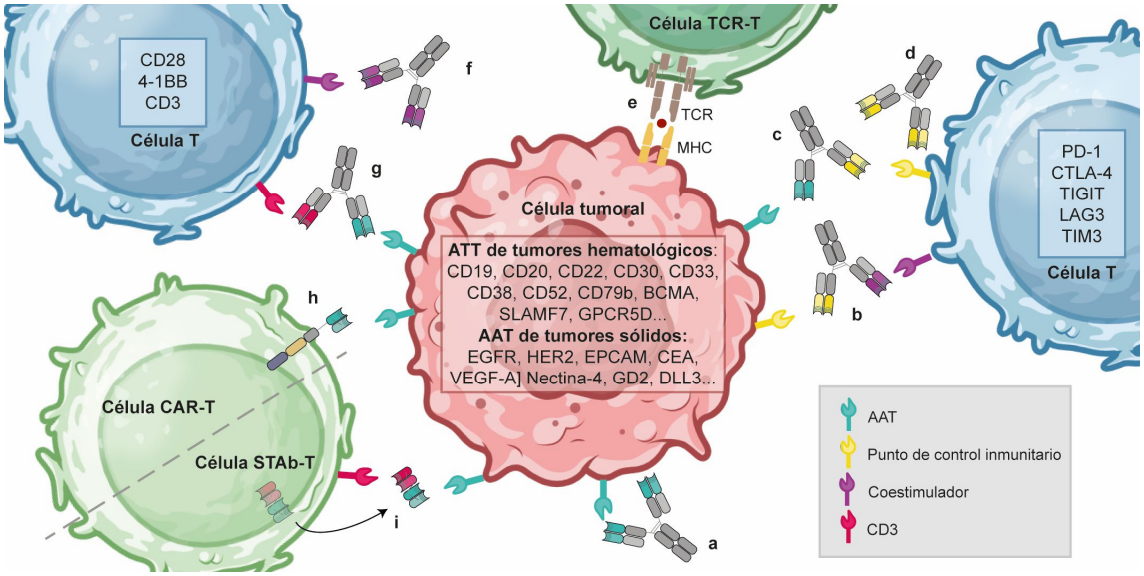

Figura 6. Aplicaciones terapéuticas de los anticuerpos en oncología. **a)** Inhibición de la señalización mediante la unión de un mAb a un AAT. **b)** Coestimulación de células inmunes mediada por un anticuerpo biespecífico a través de la unión a simultánea a PD-L1 y 4-1BB. **c)** Bloqueo del punto de control inmune por un anticuerpo biespecífico mediante la unión simultánea a un AAT en las células tumorales. **d)** Bloqueo de los puntos de control inmune mediante un mAb con actividad ICI. **e)** Célula T modificada con un TCR transgénico (TCR-T), que reconoce el antígeno intratumoral expresado en el contexto de MHC. **f)** Coestimulación de células inmunes mediada por la interacción con un mAb agonista. **g)** Redirección de las células T mediante un anticuerpo que reconoce un AAT en la célula tumoral y CD3 de la célula T. **h)** Célula T modificada con un CAR (CAR-T) específico frente a un AAT que reconoce de forma MHC-independiente. **i)** Célula T modificada para la secreción de anticuerpos biespecíficos con actividad TCE (STAb-T). Ilustración generada con *Biorender*.

2.4 Anticuerpos T *cell engagers* (TCE)

Los anticuerpos biespecíficos para la redirección de células T (TCE; del inglés, *T Cell Engager*) han experimentado un gran desarrollo en los últimos 20 años, encontrándose actualmente más de 100 anticuerpos de este tipo en evaluación clínica. Los TCE se unen simultáneamente a un AAT expresado en la superficie tumoral y a la cadena CD3ε del complejo TCR/CD3, redirigiendo la función efectora de las células T hacia el tumor (Figura 6). La mayoría de este tipo de anticuerpos poseen un único sitio de unión a CD3, para evitar la activación sistémica de las células T independiente de antígeno (*off-target*), debido al agrupamiento (*clustering*) de complejos TCR/CD3[104,105].

El primer TCE aprobado fue el catumaxomab (2009), un anticuerpo biespecífico EpCAM x CD3ε híbrido ratón/rata[106] (Tabla 1), para el tratamiento de la ascitis maligna en pacientes con carcinomas $EpCAM^+$ por vía exclusivamente intraperitoneal. Sin embargo, el catumaxomab inducía reacciones infusionales graves y era altamente inmunogénico, debido a su origen murino. Posteriormente, se diseñaron TCE de nueva generación que carecían de la región Fc. El blinatumomab es un anticuerpo biespecífico CD19 x CD3ε en formato *tandem*-scFv para el tratamiento de leucemia linfoide aguda de células B (B-ALL; del inglés, *B cell Acute Lymphoid Leukemia*) que se aprobó en el año 2014[104] (Tabla 1). Sin embargo, al no disponer de dominio Fc su vida media sérica es muy corta debido a la ausencia de reciclaje mediado por el FcRn, lo que origina la necesidad de infusión continuada para obtener niveles terapéuticos. Por este motivo la mayoría de los TCE en desarrollo se basan en IgG que incorporan dominios Fc inertes o silenciados, o en fragmentos de anticuerpos que incorporan estrategias de extensión de vida media mediadas por la albúmina humana (HSA; del inglés, *Human Serum Albumin*). Los anticuerpos biespecíficos mosunetuzumab (CD20 × CD3ε)[107] y teclistamab (BCMA × CD3ε)[108] fueron los primeros anticuerpos TCE heterodiméricos 1+1 basados en IgG y aprobados en 2022 para el tratamiento del linfoma no Hodgkin (LNH) folicular en recaída/refractario o el mieloma múltiple, respectivamente (Tabla 1).

2.5 Anticuerpos en terapias celulares

La terapia celular adoptiva (ACT; del inglés, *Adoptive Cell Therapy*) es una estrategia de inmunoterapia emergente que se basa en la capacidad efectora de los linfocitos para destruir células tumorales primarias y metastásicas. El proceso se inicia con el aislamiento de linfocitos de sangre periférica, de los ganglios linfáticos peritumorales o directamente del tejido tumoral; su expansión *ex vivo* y posterior reinfusión en el paciente. Se han desarrollado diferentes ACTs

basadas en la infusión de TIL, células T modificadas genéticamente con TCR con especificidad anti-tumoral y células T modificadas con receptores de antígenos quiméricos (CAR; del inglés, *Chimeric Antigen Receptor*)[66,109]. Una estrategia adicional que se ha desarrollado en los últimos años se basa en la modificación de células T para que secreten TCE (STAb; del inglés, *Secretion of T cell-engaging Antibodies*) (Figura 6).

La terapia con células T que expresan TCRs transgénicos (TCR-T) implica la expresión de las cadenas α y β del TCR y confieren a la célula T modificada la especificidad antigénica del TCR transferido. Esta terapia es potencialmente accesible a cualquier paciente cuyo tumor exprese el alelo HLA (del inglés, *Human Leukocyte Antigen*) reconocido por el TCR-T y el antígeno diana, que debe ser procesado y presentado en el contexto HLA. La estrategia ha demostrado potencial terapéutico en ensayos clínicos con TCR-T específicos para el CTA (del inglés, *Cancer/Testis Antigen*) NY-ESO-1, en pacientes con diferentes tipos de cáncer, como el mieloma múltiple, el melanoma y el sarcoma sinovial[110]. Sin embargo, el uso clínico de TCR-T frente a CTA se ha asociado a fenómenos de citotoxicidad debido a la destrucción de los tejidos sanos que expresan el antígeno diana y, además, se trata de una estrategia altamente personalizada[53,66].

Los CAR están formados por un dominio extracelular de reconocimiento antigénico, normalmente un scFv, un dominio transmembrana y una región de señalización intracelular, compuesta por uno o dos dominios de coestímulo (normalmente CD28 y/o 4-1BB) y un dominio de señalización derivado de la cadena ζ del TCR[111]. Las células CAR-T obtienen las propiedades de reconocimiento antigénico del anticuerpo y pueden reconocer AATs expresados en la superficie de la célula tumoral[53,112]. Este tipo de terapia ha mostrado una gran eficacia clínica en pacientes con linfomas y leucemias de células B $CD19^{+}$, y en pacientes con mieloma múltiple, que expresa el antígeno BCMA. Sin embargo, la principal desventaja es una tasa de recaídas alta, que se ha relacionado con una expansión y persistencia *in vivo* subóptima, que podría depender de la viabilidad, eficacia de transducción y del fenotipo de las células CAR-T. Además, la eficacia de las células CAR-T es muy limitada en tumores sólidos, debido a la alta heterogeneidad clonal y a la existencia de un microambiente inmunosupresor, que dificulta el tráfico y la funcionalidad de las células T en el tumor[66,113,114].

En la actualidad están en desarrollo otras estrategias basadas en la infusión de células T modificadas para la secreción de TCE, denominadas células STAb-T. Las terapias STAb-T se basan en la modificación genética de distintos tipos celulares con ácidos nucleicos o vectores virales que codifican TCEs específicos frente a diferentes AATs. Las células más utilizadas son las células T, ya que pueden actuar simultáneamente como factorías del TCE y como efectores. Las ventajas

potenciales de la terapia STAb-T frente a la terapia CAR-T son: que el reclutamiento de las células T no se restringe a las células modificadas, como en el caso de las células CAR-T, sino que es extensible a las células T no modificadas presentes en proximidad, generando respuestas anti-tumorales más intensas; además, la topología de la sinapsis inmune inducida por los TCE es muy similar a la fisiológica mediada por el TCR[18,115]. La actividad anti-tumoral de las células STAb-T ha sido demostrada a nivel preclínico en diferentes modelos de neoplasias hematológicas[116–118].

2.6 Combinación de anticuerpos para el tratamiento del cáncer

La proliferación celular inducida por estímulos oncogénicos constituye el origen del desarrollo del cáncer. La supresión del crecimiento descontrolado mediante la inhibición de EGFR con el anticuerpo cetuximab tiene efectos muy significativos en algunos pacientes con CCR y cáncer de cabeza y cuello[119]. El efecto del cetuximab puede incrementarse con la administración combinada con un mAb agonista anti-4-1BB[120]. En las células NK activadas mediante cetuximab, aumenta la expresión de 4-1BB, lo que induce la activación de las células NK y de las células T de memoria. A su vez, el anticuerpo anti-4-1BB mejora la desgranulación y la citotoxicidad de las células NK, fortaleciendo así las respuestas inmunes[102,121]. Por otro lado, el bloqueo de la señalización de PD-1 resulta en la activación de los linfocitos T y potenciación de la inmunidad anti-tumoral en tratamientos combinados con mAbs bloqueantes PD-1/PD-L1 y mAbs agonistas anti-4-1BB[16,102,122–127]. También se han desarrollado estrategias basadas en anticuerpos biespecíficos 4-1BB x AAT, con el objetivo de confinar la coestimulación mediada por 4-1BB en el microambiente tumoral. Los AAT frente a los que se han desarrollado este tipo de anticuerpos biespecíficos han sido: EGFR, proteína de activación de fibroblastos (FAP), CD19, B7-H3 (CD276) y HER2[43,44,121,128–133].

3. Aplicaciones de los anticuerpos en infecciones virales.

La primera descripción de los anticuerpos, aún no denominados así, puede documentarse en los trabajo de Emil von Behring y Shibasaburo Kitasato, quienes describieron en 1890 la presencia en la sangre de sustancias (“antitoxinas”) que neutralizaban la acción de las toxinas diftérica y tetánica[134]. A fecha de hoy, según la *Antibody Society*[56], 17 anticuerpos han sido aprobados por la EMA y la FDA para el tratamiento de enfermedades infecciosas (Tabla 2). Es importante destacar que la generación de anticuerpos multiespecíficos no está limitada al campo de la inmunoterapia del cáncer, sino que son ampliamente utilizados para el tratamiento de infecciones virales. Trabajos recientes describen fusiones en tándem de tres o cuatro V_{HH}

acoplados a una región Fc y dirigidos frente a la hemaglutinina del influenzavirus[135] o frente a la espícula del SARS-Cov-2[136].

Tabla 2. Anticuerpos aprobados en la UE o EE.UU. para uso terapéutico en enfermedades infecciosas (marzo de 2024).

Nombre genérico	Diana	Fuente/Modificaciones Fc	Primeras indicaciones	Año
Nebacumab	Endotoxina	Hum/No	SGN	1991
Palivizumab	VRS	Huz/No	Prevención VRS	1998
Raxibacumab	B. anthrasis	Hum/No	Infección ántrax	2012
Bezlotoxumab	CDEB	Hum/No	Prevención RCD	2016
Obiltoxaximab	B. anthrasis	Quim/No	Prevención ántrax	2016
Ibalizumab (ibalizumab-uiyk)	CD4	Huz/No	Infección HIV	2018
Ansuvimab-zykl	Virus ébola GP	Hum/No	Infección Ébola	2020
Atoltivimab, maftivimab, and odesivimab-ebgn	Virus ébola	Hum/No	Infección Ébola	2020
Casirivimab + imdevimab	SARS-CoV-2	Hum/No	COVID-19	2021
Regdanvimab	SARS-CoV-2	Hum/No	COVID-19	2021
Sotrovimab	SARS-CoV-2	Hum/M428L, N434S	COVID-19	2021
Nirsevimab	RSV	Hum/M252Y, S254T, T256E	Prevención VRS	2022
Tixagevimab, cilgavimab	SARS-CoV-2	Hum/L234F, L235E, M252Y, S254T, T256E, P331S	COVID-19	2022
Amubarvimab + Romlusevimab	SARS-CoV-2	Hum/M252Y, S254T, T256E	SARS-CoV-2	rev
No INN; RabiShield	Virus rabia GP G	Hum	Exposición rabia	rev
Ormutivimab	Virus rabia sGP 4	Hum/No	Profilaxis post-exposición rabia	rev
Docaravimab and Miromavimab	Virus rabia	Mur/No	Exposición rabia	rev

Mur: murino; **Quim**: quimérico; **Huz**: humanizado; **Hum**: Humano; **SGN**: sepsis Gramnegativa; **VRS**: virus respiratorio sincitial; **RCD**: recurrencia de *Clostridium difficile*; **CDEB**: Enterotoxina B de *Clostridium difficile*; **GP**: glicoproteína; **sGP**: glicoproteína de superficie; **rev**: en revisión.

En función de su mecanismo de acción, los anticuerpos antivirales pueden clasificarse en neutralizantes y no neutralizantes. Los anticuerpos no neutralizantes se unen a una zona de la superficie del virus sin impedir la infección ni eliminar la carga viral, pero que permite el reclutamiento de funciones efectoras, como son la ADCC o la fagocitosis mediada por anticuerpos[137]. Por otro lado, los anticuerpos neutralizantes interaccionan con un epítopo específico de la envoltura vírica y bloquean las interacciones con el receptor de la célula del huésped o inhiben la liberación del genoma vírico. Los anticuerpos neutralizantes pueden inhibir múltiples cepas de un mismo virus y pueden ofrecer una gran protección contra las infecciones agudas; sin embargo, en las infecciones crónicas su utilidad es limitada[138].

3.1 Anticuerpos neutralizantes.

Los virus con envoltura se internalizan mediante la adhesión a un receptor de superficie celular; mientras que los virus sin envoltura lo hacen a través de la lisis de la membrana de la célula huésped o creando estructuras similares a poros. Los anticuerpos pueden neutralizar los virus en el punto de entrada o en la fase posterior a la unión[137,139]:

a) Inhibición en el punto de entrada

Puede ocurrir mediante la unión del anticuerpo a epítopos en la envoltura viral (Figura 7a) necesarios para la internalización del virus en la célula del huésped; o bien mediante la interacción con receptores o correceptores en la membrana de la célula huésped (Figura 7b); impidiendo, en ambos casos, la unión ligando-receptor necesaria para la internalización viral.

b) Inhibición posterior a la unión del complejo anticuerpo-virus

Este proceso puede producirse por tres mecanismos diferentes:

- La unión del anticuerpo a la envoltura del virus inhibe los cambios conformacionales necesarios para la fusión con la membrana celular (Figura 7c). En algunos virus, la unión a un receptor, correceptor o a ambos desencadena el cambio conformacional necesario para la fusión de la membrana. Un ejemplo es el virus de la inmunodeficiencia humana (VIH), donde la interacción de la gp120 del virus con el CD4 de la célula del huésped da lugar a cambios conformacionales en la envoltura viral, lo que resulta en la exposición de un sitio de unión transitoria para el correceptor CCR5. Esto promueve otros cambios conformacionales en gp41 que le permite insertar su péptido de fusión en la membrana de la célula huésped para iniciar la fusión de membranas e internalización viral. De esta manera, los anticuerpos neutralizantes dirigidos a gp41 puede evitar los cambios conformacionales necesarios para la fusión de membranas[139].
- En los virus que requieren un pH endosomal reducido para conseguir la fusión de la membrana viral, los anticuerpos neutralizantes unidos al virus en el interior del endosoma inhiben el cambio de pH, impidiendo así la liberación del virión (Figura 7d).
- Por último, los anticuerpos neutralizantes pueden detectar el virión, evitando que su material genético se inserte en el genoma de la célula del huésped.

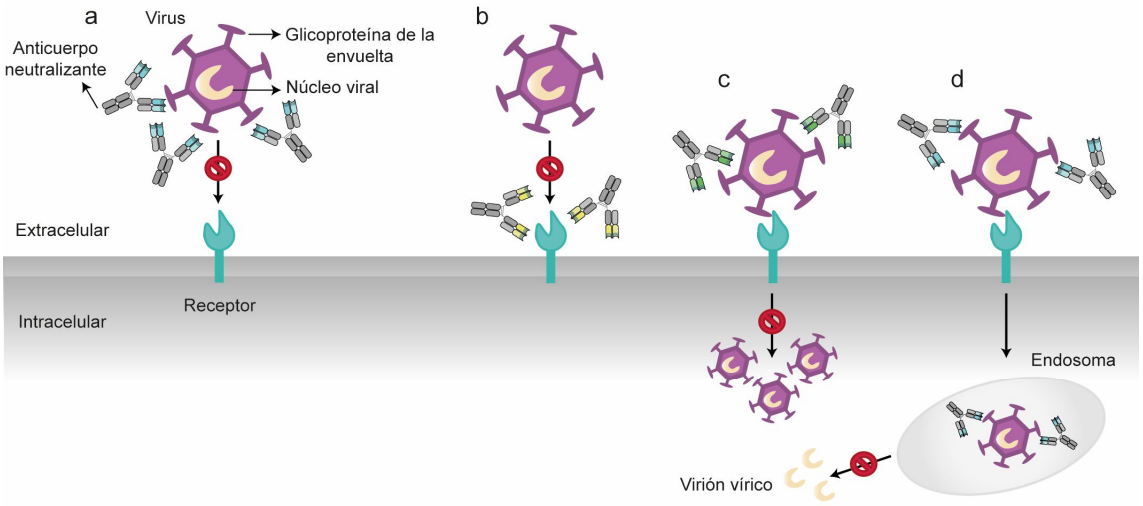

Figura 7. Mecanismos de acción de los anticuerpos neutralizantes. a) Interacción con un epítopo en la envoltura de la glicoproteína viral. **b)** Interacción con receptores de la célula del huésped. **c)** Interacción con el virus e inhibición del cambio conformacional que permite la fusión de la membrana. **d)** Inhibición del cambio de pH en el endosoma necesario para la fusión de la membrana, impidiendo así la liberación del virión.

3.2 Aplicaciones clínicas de los anticuerpos neutralizantes

Los anticuerpos neutralizantes son efectivos frente a infecciones virales agudas como el virus chikungunya, el virus del sarampión y el poliovirus; sin embargo, en infecciones crónicas como influenza, Ébola, VIH y virus Lassa, estos anticuerpos no ofrecen respuestas satisfactorias debido a la alta tasa de mutaciones en algunas cepas virales.

En el contexto de la infección por el VIH, fue en el año 1989 cuando se desarrolló la primera molécula anti-viral formada por una fusión del fragmento extracelular del receptor CD4 con una región Fc. Los anticuerpos neutralizantes de "amplio espectro", obtenidos en ciertos grupos de pacientes infectados por el VIH-1, producen buenos resultados terapéuticos y de prevención de la infección al administrarse a otros huéspedes. Actualmente conocemos que la neutralización se produce a través de la unión entre el dominio Fc y los FcγR de la célula del huésped, bloqueando así la internalización viral. Se están desarrollando ensayos clínicos donde se combinan anticuerpos que poseen una potente actividad neutralizadora del VIH con agentes de reversión de la latencia, reduciendo el conjunto de células que expresan el virus[137,140].

Por otro lado, el virus chikungunya (CHIKV) posee glicoproteínas de envoltura genéticamente conservadas, y es en los endosomas acidificados donde se permite que estas glicoproteínas se

fusionen con la membrana celular[141]. Por este motivo, los anticuerpos neutralizantes que se unen a los FcγR o a epítopos de las glicoproteínas bloquean eficientemente la internalización de este virus en la célula del huésped.

Por último, el coronavirus del síndrome respiratorio agudo grave de tipo 2 (SARS-CoV-2, del inglés: S*evere Acute Respiratory Syndrome Coronavirus 2*), un patógeno zoonótico que ha causado la reciente enfermedad COVID-19 en el año 2019, ha originado el desarrollo de un gran número de mAbs neutralizantes, de los cuales, algunos han recibido la autorización de uso de emergencia en EE.UU.[142]. La glicoproteína *Spike* (S), que es la principal diana para la neutralización por anticuerpos, posee dos subunidades: dominio N-terminal y dominio C-terminal. Para que el virus se internalice en la célula huésped, es necesario que esta glicoproteína se acople al receptor de la superficie celular de la enzima convertidora de angiotensina 2 (ACE2; del inglés, *Angiotensin Converting Enzyme 2*)[143]. Los anticuerpos neutralizantes contra el dominio de unión al receptor (RBD; del inglés*, Receptor Binding Domain*) en la proteína S o contra el receptor ACE2 han obtenido buenos resultados[144]. Sin embargo, la aparición de numerosas cepas con mutaciones en el dominio RBD evita la neutralización por este tipo de anticuerpos[145]. Por este motivo, se han desarrollado numerosas estrategias de multimerización basadas en el uso de V_{HH}, para generar anticuerpos biespecíficos, anticuerpos biparatópicos, construcciones fusionadas a regiones Fc y *trimerbodies*[146,147], consiguiendo no solo neutralizar el proceso de infección viral, sino suprimir la aparición de mutaciones de escape. Por último, se han descrito diferentes estrategias con anticuerpos con unión optimizada a receptores Fc*γ*IIa y Fc*γ*IIIa, que han mostrado mejores resultados para prevenir o tratar el COVID-19[148].

OBJETIVOS

El objetivo general de este trabajo ha sido la generación y caracterización de anticuerpos multiespecíficos terapéuticos mediante la plataforma *trimerbody* para su uso en cáncer y enfermedades infecciosas. Para ello, se plantearon los siguientes objetivos específicos:

1. Diseño de anticuerpos hexavalentes monoespecíficos anti-EGFR; biespecíficos anti-PD-L1 y anti-EGFR; y triespecíficos anti-4-1BB, anti-EGFR y anti-PD-L1. Este formato, denominado IgTT, se basa en la fusión de un *tandem trimerbody* (TT) con las regiones bisagra y Fc de la IgG_1 humana.

2. Estudios *in vitro* para determinar la capacidad de los anticuerpos IgTT para inducir proliferación, secreción de citoquinas y ADCC en las células T y NK humanas primarias en co-cultivo con diferentes líneas celulares con diferentes perfiles antigénicos.

3. Estudios *in vivo* para determinar el efecto anti-tumoral del anticuerpo IgTT biespecífico en modelos murinos inmunodeficientes humanizados.

4. Generación y caracterización de anticuerpos biespecíficos en formato *trimerbody* multicadena para neutralizar el virus SARS-CoV2 y redirigirlo hacia células dendríticas. Estudios *in vitro* e *in vivo* para determinar su potencial terapéutico.

PUBLICACIONES

ARTÍCULO I: ***A PD-L1/EGFR bispecific antibody combines immune checkpoint blockade and direct anti-cancer action for an enhanced anti-tumor response*****.**

Laura Rubio-Pérez, Rodrigo Lázaro-Gorines, Seandean L. Harwood, Marta Compte, Rocío Navarro, Antonio Tapia-Galisteo, Jaume Bonet, Belén Blanco, Simon Lykkemark, Ángel Ramírez-Fernández, Mariola Ferreras-Gutiérrez, Carmen Domínguez-Alonso, Laura Díez-Alonso, Alejandro Segura-Tudela, Oana Hangiu, Ainhoa Erce-Llamazares, Francisco J. Blanco, Cruz Santos, José L. Rodríguez-Peralto, Laura Sanz and Luis Álvarez-Vallina.

Oncoimmunology, 2023, VOL. 12, NO. 1, 2205336

DOI: 10.1080/2162402X.2023.2205336

Introducción:

Los anticuerpos ICI han demostrado respuestas clínicas duraderas en varios tipos de cáncer; sin embargo, la tasa de respuesta global sigue siendo limitada. Los nuevos formatos de anticuerpos biespecíficos que combinan el efecto ICI y una acción directa sobre las células tumorales a través de un AAT podrían mejorar la eficacia de las inmunoterapias actuales. El EGFR es un AAT con un papel relevante en cáncer, ya que su desregulación favorece la proliferación, la inhibición de la apoptosis y la invasión de las células tumorales. Por lo tanto, los anticuerpos anti-EGFR marcan las células tumorales para su destrucción por efectores del sistema inmune, a la vez que inhiben la fosforilación de residuos de tirosina intracelulares clave, impidiendo así la señalización mitogénica mediada por ligando. En este trabajo se describe y caracteriza un nuevo formato anticuerpo biespecífico anti-PD-L1/EGFR simétrico, denominado IgTT, mediante la fusión de un *tandem trimerbody* con las regiones bisagra y Fc de la IgG_1 humana.

Objetivos:

1. Diseño y generación de vectores de expresión que codifican para el anticuerpo monoespecífico anti-EGFR IgTT-E y el anticuerpo biespecífico anti-PD-L1/EGFR IgTT-1E.
2. Expresión en células de mamífero y purificación mediante cromatografía de afinidad.
3. Caracterización estructural y funcional de los anticuerpos purificados.
4. Evaluación *in vitro* de la inhibición de la proliferación y viabilidad celular, capacidad de bloqueo de la interacción PD-1/PD-L1 e inducción de citotoxicidad por células T y células NK en co-cultivos con diferentes líneas celulares $EGFR^+/PD\text{-}L1^+$.
5. Evaluación *in vivo* de la eficacia terapéutica del IgTT-1E en modelos de ratón humanizados.

Conclusiones:

1. Los anticuerpos recombinantes IgTT-E e IgTT-1E se secretaron eficientemente por células humanas y se purificaron mediante cromatografía de afinidad Strep-Tactin, eluyendo como un único pico. Las fracciones presentaban un alto grado de pureza y el tamaño esperado mediante electroforesis en geles SDS-PAGE en condiciones reductoras.
2. Ambos anticuerpos purificados demostraron ser funcionales, interaccionando específicamente con sus antígenos diana en solución de manera simultánea y en un contexto celular.

3. Ambos anticuerpos inhiben la fosforilación de EGFR y la proliferación de células tumorales mediada por EGF *in vitro*.
4. El anticuerpo IgTT-1E bloqueó eficazmente la interacción PD-1/PD-L1 e indujo actividad citotóxica dependiente de anticuerpos específica de antígeno, así como la desgranulación de las células NK *in vitro*.
5. El anticuerpo IgTT-1E mostró potente eficacia terapéutica en dos modelos de ratón humanizados portadores de xenoinjertos de cáncer de mama triple negativo y de cáncer de pulmón, donde el control del crecimiento tumoral se asoció a un incremento significativo de la proporción de células T $CD8^+$.

Publicación:

ONCOIMMUNOLOGY
2023, VOL. 12, NO. 1, 2205336
https://doi.org/10.1080/2162402X.2023.2205336

Taylor & Francis
Taylor & Francis Group

ORIGINAL RESEARCH

OPEN ACCESS Check for updates

A PD-L1/EGFR bispecific antibody combines immune checkpoint blockade and direct anti-cancer action for an enhanced anti-tumor response

Laura Rubio-Pérez[a,b,c,d], Rodrigo Lázaro-Gorines[a,b,c], Seandean L. Harwood[e], Marta Compte[f], Rocío Navarro[f], Antonio Tapia-Galisteo[a,b,c], Jaume Bonet[g], Belén Blanco[a,b,c], Simon Lykkemark[h], Ángel Ramírez-Fernández[a,b,c], Mariola Ferreras-Gutiérrez[i], Carmen Domínguez-Alonso[a,b,c], Laura Díez-Alonso[a,b,c], Alejandro Segura-Tudela[a,b,c], Oana Hangiu[a,b,f], Ainhoa Erce-Llamazares[a,b,f], Francisco J. Blanco[i], Cruz Santos[j], José L. Rodríguez-Peralto[k,l,m,n], Laura Sanz[n,o], and Luis Álvarez-Vallina[a,b,c,d]

[a]Cancer Immunotherapy Unit (UNICA), Department of Immunology, Hospital Universitario 12 de Octubre, Madrid, Spain; [b]Immuno-Oncology and Immunotherapy Group, Instituto de Investigación Sanitaria 12 de Octubre (imas12), Madrid, Spain; [c]H12O-CNIO Cancer Immunotherapy Clinical Research Unit, Spanish National Cancer Research Centre (CNIO), Madrid, Spain; [d]Chair for Immunology UFV/Merck, Universidad Francisco de Vitoria (UFV), Madrid, Spain; [e]Department of Molecular Biology and Genetics, Aarhus University, Aarhus C, Denmark; [f]Department of Antibody Engineering, Leadartis SL, QUBE Technology Park, Madrid, Spain; [g]Institute of Bioengineering, École Polytechnique Fédérale de Lausanne, Lausanne, Switzerland; [h]Immunotherapy and Cell Engineering Laboratory, Department of Engineering, Aarhus University, Aarhus C, Denmark; [i]Centro de Investigaciones Biológicas Margarita Salas (CIB), CSIC, Madrid, Spain; [j]Faculty of Experimental Sciences, Universidad Francisco de Vitoria (UFV), Madrid, Spain; [k]Department of Pathology, Hospital Universitario 12 de Octubre, Madrid, Spain; [l]Department of Pathology, Universidad Complutense, Madrid, Spain; [m]Cutaneous Oncology Group, Instituto de Investigación Sanitaria 12 de Octubre (imas12), Madrid, Spain; [n]Centro de Investigación Biomédica en Red en Oncología (CIBERONC), Madrid, Spain; [o]Molecular Immunology Unit, Hospital Universitario Puerta de Hierro Majadahonda, Madrid, Spain

ABSTRACT

Immune checkpoint blockade (ICB) with antibodies has shown durable clinical responses in a wide range of cancer types, but the overall response rate is still limited. Other effective therapeutic modalities to increase the ICB response rates are urgently needed. New bispecific antibody (bsAb) formats combining the ICB effect and a direct action on cancer cells could improve the efficacy of current immunotherapies. Here, we report the development of a PD-L1/EGFR symmetric bsAb by fusing a dual-targeting tandem trimmer body with the human IgG1 hinge and Fc regions. The bsAb was characterized in vitro and the antitumor efficacy was evaluated in humanized mice bearing xenografts of aggressive triple-negative breast cancer and lung cancer. The IgG-like hexavalent bsAb, designated IgTT-1E, was able to simultaneously bind both EGFR and PD-L1 antigens, inhibit EGF-mediated proliferation, effectively block PD-1/PD-L1 interaction, and induce strong antigen-specific antibody-dependent cellular cytotoxicity activity in vitro. Potent therapeutic efficacies of IgTT-1E in two different humanized mouse models were observed, where tumor growth control was associated with a significantly increased proportion of $CD8^+$ T cells. These results support the development of IgTT-1E for the treatment of $EGFR^+$ cancers.

ARTICLE HISTORY
Received 2 January 2023
Revised 16 April 2023
Accepted 17 April 2023

KEYWORDS
Cancer immunotherapy, bispecific antibody; dual action; epithelial growth factor receptor; immune checkpoint blockade

Introduction

Modulating immune responses using monoclonal antibodies (mAbs) is one of the most promising approaches for cancer immunotherapy[1]]. Immune checkpoints are coinhibitory and costimulatory receptors that are crucial for maintaining self-tolerance and modulating immune responses[2]. However, inhibitory checkpoints can be "hijacked" by tumors to evade immune responses[3]. MAb-based blockade of coinhibitory immune receptors, such as cytotoxic T lymphocyte antigen 4 (CTLA-4), programmed cell death-1 (PD-1) receptor, or PD-1 ligand (PD-L1) has shown durable tumor clinical responses in a wide range of cancer types, but their efficacy is limited to 10% to 30% of patients[4]. Different factors, such as the tumor mutational burden and immunogenicity of cancer cells, the composition of the tumor microenvironment (TME) and the degree of immune cell infiltration, influence the response to immune checkpoint blockade (ICB)[5]. Increasing the response rates to ICB is likely to require the design of therapeutic combinations that are tailored to the aforementioned factors[6]. On the other hand, EGFR is a receptor tyrosine kinase well-known as a tumor-associated antigen (TAA) with an important functional role, since EGFR deregulation promotes proliferation, apoptosis inhibition and invasion of cancer cells[7]. Therefore, mAb targeting EGFR not only mark tumor cells for immune killing but also may inhibit phosphorylation of key intracellular tyrosine residues, thus preventing ligand-mediated mitogenic signaling[8].

As of January 2023, seven immune checkpoint blockers (ICB) preventing PD1/PD-L1 interaction had been approved for clinical use by the Food and Drug Administration (FDA) and the European Medicines Agency (EMA), and six others are in regulatory review, being *atezolizumab* the first anti-PD-L1

CONTACT Luis Álvarez-Vallina lav.imas12@h12o.es Cancer Immunotherapy Unit (UNICA), Department of Immunology, Hospital Universitario 12 de Octubre, Avda. Cordoba s/n, Madrid 28041, Spain
Supplemental data for this article can be accessed online at https://doi.org/10.1080/2162402X.2023.2205336

mAb in the market (2017). With respect to EGFR, three conventional mAbs [*cetuximab*, *panitumumab* –both approved for colorectal cancer (CRC)- and *necitumumab* -for non-small cell lung cancer (NSCLC)- and the bispecific antibody (bsAb) *amivantamab* (EGFR x c-MET, for NSCLC with EGFR exon 20 insertion mutations) are currently in the market. Antibody therapeutics that are approved for marketing in regions other than the US or EU include two anti-EGFR (*nimotuzumab* and *cetuximab* conjugated to the photosensitizer IR700) and seven anti-PD1[9].

Designing agents that combine the immunomodulatory effect of an ICB and a direct action on cancer cells could open new perspectives in cancer immunotherapy. Here, we generated a novel PD-L1/EGFR bispecific antibody (bsAb) by fusing a dual-targeting tandem trimerbody (TT)[10] with the human IgG1 hinge and Fc regions. The TT format has been previously described and is a single-chain fusion of three single-domain V_{HH} antibodies with three collagen XVIII trimerization domains (TIE)[8–10], with intercalating glycine-serine-based linkers. Each V_{HH} is encoded separately, allowing mono-, bi-, and tri-specific molecules to be produced[7]. Here, the first V_{HH} was replaced by a PD-L1-specific scFv, and an EGFR-specific V_{HH} was used in the second and third V_{HH} positions. The resulting IgG-like hexavalent bsAb, designated IgTT-1E, simultaneously bound both targeted antigens, inhibited EGF-mediated proliferation, effectively blocked PD-1/PD-L1 interaction and induced potent antigen-specific antibody-dependent cellular cytotoxicity (ADCC) activity *in vitro*. A potent therapeutic effect of IgTT-1E was observed in humanized mice bearing aggressive $EGFR^{+}PD\text{-}L1^{+}$ human triple-negative breast cancer (TNBC) and lung cancer cell-line – derived xenografts (CDX). These data provide a promising basis for the further clinical development of IgTT-1E and similarly designed symmetric antibodies against different targets.

Materials and methods

Cell lines and culture conditions

HEK-293 (CRL-1573), A431 (CRL-1555), NIH/3T3 (CRL-1658), MDA-MB-231 (HTB-26) and CHO-K1 (CCL-61) cells were cultured in Dulbecco's modified Eagle's medium (DMEM) (Life Technologies, cat# 10313021) supplemented with 2 mmol/l L-glutamine, 10% (v/v) heat-inactivated fetal bovine serum (FBS) (Merck Life Science, cat# F7524-500 ML), and antibiotics (100 units/mL penicillin, 100 mg/mL streptomycin; both from Life Technologies) at 37 °C in 5% CO_2 humidity. A549 (CCL-185) cells were cultured in RPMI-1640 (Lonza, cat# 12-702Q) supplemented with 2 mmol/l L-glutamine, 10% (v/v) heat-inactivated FBS, and antibiotics. All these cell lines were obtained from the American Type Culture Collection. NIH/3T3 cells expressing human EGFR ($3T3^{EGFR}$) were kindly provided by Dr. A. Villalobo [Instituto de Investigaciones Biomédicas "Alberto Sols". IIBm (CSIC-UAM), Madrid, Spain]. Jurkat T cells stably expressing human PD-1 and NFAT-induced luciferase ($Jurkat^{NFAT\text{-}RE\text{–}luc/PD\text{-}1}$) and CHO-K1 cells stably expressing human PD-L1 (PD-L1 aAPC/CHO-K1), were obtained from Promega (cat# J1250). CHO-K1 cells stably expressing human PD-L1 ($CHO^{PD\text{-}L1}$) were obtained from Genlantis (xCELLerate™ PD-L1 Stable Cell Line, XCL-PDL1) and CHO-K1 cells stably expressing human EGFR (CHO^{EGFR}), or both ($CHO^{EGFR\text{-}PD\text{–}L1}$) were generated using human EGFR encoding commercial lentiviral particles (G&P Biosciences, cat# LTV0169). All cell lines were routinely screened for mycoplasma contamination by PCR using the Mycoplasma Plus TM Primer Set (Biotools B&M Labs, cat# 90022).

Construction of expression vectors

The plasmid pCR3.1-FLAG/Strep-αEGFR$_3$-TIE-αCD3 was generated by cloning the insert OncoM-FLAG/Strep-αEGFR flanked by *Hind*III-*Not*I (GeneArt AG, Thermo Fischer) into the plasmid pCR3.1-αEGFR$_3$-TIE-αCD3 encoding the bispecific EGFR x anti-CD3 ATTACK[11]. Then, the FLAG/Strep-αEGFR V_{HH}-based tandem trimerbody (TT) was subcloned as *Hind*III/*Bam*HI into pCR3.1-hFc-His vector containing a human IgG_1 hinge and Fc region, resulting in pCR3.1-FLAG/Strep-αEGFR$_3$-hFc-His (IgTT-E). To generate the PD-L1/EGFR bispecific IgTT (IgTT-1E) expressing vector, the OncoM-FLAG/Strep-αPD-L1 fragment flanked by *Hind*III-*Not*I (GeneArt AG) was cloned into the plasmid pCR3.1-FLAG/Strep-αEGFR$_3$-hFc-His. All the sequences were verified using primers FwCMV and RvBGH oligonucleotides (Table S1).

Expression and purification of recombinant antibodies

HEK-293 cells were transfected with the appropriated vectors by Lipofectamine 3,000 transfection kit (Fisher Scientific, cat# 15292465) and selected in complete DMEM supplemented with 500 µg/ml of G418 to generate stable cell lines. Conditioned media were collected and processed using Strep-Tactin purification system (IBA Lifesciences) in an ÄKTA Prime plus system (Life Technologies). The purified antibodies were dialyzed overnight at 4 °C against PBS pH 7.4 supplemented with 150 mM NaCl and analyzed by sodium dodecyl sulfate (SDS)-polyacrylamide gel electrophoresis (PAGE) under reducing conditions.

Western blotting

Protein samples were analyzed by mean of 10–20% Tris-glycine SDS-PAGE under reducing conditions, transferred onto nitrocellulose membranes (Thermo Fisher Scientific, cat# IB23002) and probed with mouse anti-FLAG IgG_1 (clone M2, Sigma-Aldrich, cat# F3165) (1 µg/ml), followed by incubation with HRP-conjugated goat anti-mouse IgG (GAM-HRP) (1:10,000 dilution) (Sigma, cat# A2554). Visualization of protein bands was performed with Pierce ECL Plus Western Blotting Substrate (Thermo Scientific, cat# 32132), using ChemiDoc MP Imaging System and Image Lab software (both from BioRad).

Enzyme-linked immunosorbent assay

The human EGFR-Fc (EGFR-Fc, R&D Systems, cat# 344-ER) or human PD-L1-Fc (PD-L1-Fc, Peprotech, cat# 310–35)

chimeras were immobilized (2.5 µg/ml in PBS) on Maxisorp 96-well plates (NUNC Brand Products, cat# 44240) overnight at 4°C. After washing and blocking, conditioned media or purified protein solution (1 µg/ml) was added and incubated for 1 hour at room temperature. The wells were washed and HRP-conjugated anti-poly Histidine (Sigma-Aldrich, cat# A7058), HRP-conjugated anti-FLAG (M2 clone, Sigma-Aldrich, cat# A8592), mouse anti-Myc (clone 9E10, Millipore, cat# 05–419) or HRP-conjugated goat anti-human IgG (GAH) (Sigma-Aldrich, cat# A0170) were added (1 µg/ml). After washing, in the case of mouse anti-Myc, GAM-HRP (1:2,000 dilution) (Jackson ImmunoResearch, cat# 115-085-166) was added for 1 hour at room temperature. Finally, after washing, the plate was developed using 100 µl 3,3′,5,5′-tetramethylbenzidine (TMB) (Sigma-Aldrich, cat# T0440) and stopped by 100 µl of 1 N H_2SO_4. Absorbance was read at 450–620 nm using Multiskan FC photometer (Thermo Scientific).

Size exclusion chromatography-multiangle light scattering

The experiments were performed on a Superdex 200 Increase 10/300 GL column (Cytiva) attached in-line to a DAWN EOS light scattering photometer (Wyatt Technology) and an ultraviolet light absorbance detector (ThermoFinnigan SpectraSYSTEM UV2000). The chromatography was run at room temperature and the scattering detector was thermostatized at 23 °C. The column was equilibrated with running buffer (PBS pH 7.4 plus 150 mM NaCl, 0.1 µm filtered) and the size exclusion chromatography-multiangle light scattering (SEC-MALS) system was calibrated with a sample of BSA (Albumin, Monomer bovine, Sigma-Aldrich, cat#A1900) at 2 mg/ml in the same buffer. 230 µl of the antibody solutions at 0.3 or 0.4 mg/ml were injected into the column at a flow rate of 0.5 ml/min. The column has an exclusion volume of 8.6 ml, and no absorbance (no aggregated proteins) was observed in the chromatograms at this volume. Data acquisition and analysis were performed using ASTRA software (Wyatt Technology). The reported molar masses correspond to the center of the chromatography peaks. Based on numerous measurements on BSA samples under similar conditions the estimation of the experimental error in the molar mass is around 5%.

Molecular Modeling

The IgTT-E three-dimensional representation was built by homology modeling using MODELLER[12]. Two templates were combined to generate the model, the V_{HH}-based monospecific TT was built using as template the anti-CEA TT constructed in a previous work[13], while the Fc domain was based on the human IgG1 B12 structure (pdb:1HZH.H)[14], obtained from the Protein Data Bank[15]. The Fc template was obtained with BLAST[16]; with an e-value of 1e-169 and a 99% of sequence identity for the domain. The structure of 1HZH was also used to guide dimerization. The IgTT-1E model was built by combining the IgTT-E model and the interleukin 18 receptor antagonist scFv (pdb:6NK9.D)[17] for the anti-PD-L1 scFv domain. The template was obtained through BLAST with and e-value of 2e-138 and 83% of sequence identity for the domain.

Biolayer interferometry

The binding of the IgTT-E to immobilized EGFR-Fc, and of the IgTT-1E to immobilized EGFR-Fc and PD-L1-Fc was measured using biolayer interferometry (BLI) on an Octet RED96 system (Fortebio). The binding to EGFR was compared to that of *cetuximab* (ctx) (Merck KGaA, Darmstadt, Germany), and the binding to PD-L1 was compared with *atezolizumab* (atz) (Fritz Hoffmann-La Roche, Basel, Switzerland). Both antigens were immobilized onto AR2G biosensors (Fortebio) at pH 5.0 using amine reactive coupling. Antibodies in HEPES-buffered saline (HBS; 20 mM HEPES, 150 mM NaCl, pH 7.4) at 10 nM were associated with either immobilized antigen for 30 minutes, after which the dissociation of antibody from the biosensor was measured for 30 minutes in HBS buffer only. After the IgTT-1E and ctx had bound to immobilized EGFR, bispecific binding to PD-L1-Fc in solution was then investigated by the subsequent treatment of the biosensors with 20 nM of PD-L1-Fc in HBS for 30 minutes. To determine binding kinetics to immobilized EGFR and PD-L1, the Octet Data Analysis (Fortebio) software was used to fit the experiment data to a 1:1 binding model with an asymptotic association phase and an exponential decay dissociation phase and regression to the chi^2 value.

Serum stability

Purified IgTT-1E was incubated in 60% (v/v) human serum (Sigma-Aldrich, cat# H4522) at 37°C for 96 hours. The binding activity of the sample at 0 time point was set as 100% to calculate the corresponding decay in PD-L1 and EGFR binding by enzyme-linked immunosorbent assay (ELISA). Samples were analyzed with Multiskan FC Photometer and GraphPad Prism software. Results correspond to one experiment performed in triplicate.

Flow cytometry

CHO^{EGFR} or $CHO^{PD\text{-}L1}$ cells (1×10^5 cells/well) were incubated for 1 hour on ice with purified antibodies (6.67 nM), washed and incubated for 30 minutes with a PE-conjugated $F(ab')_2$ GAH IgG antibody (Jackson ImmunoResearch, cat# 109-116-170). *Trastuzumab* (tra) (Fritz Hoffmann-La Roche), atz and ctx (6.67 nM) were used as controls. After washing, DAPI (Sigma Aldrich, cat# D9542) was added and samples were analyzed with FACSCAnto II Flow Cytometer (Becton Dickinson).

Inhibition of EGFR-mediated cell proliferation and signaling

A431 cells were seeded in complete DMEM in 96-well plates. After 24 hours, the medium was replaced by DMEM 1% FBS containing equimolar concentrations (0.19–50 nM) of ctx, atz, IgTT-E or IgTT-1E and incubated for 72 hours. Viability was

assessed using the CellTiter-Glo luminescent assay (Promega, cat# G7570). For EGFR signaling studies, A431 cells were starved overnight in DMEM 1% FBS and then incubated for 4 hours in serum-free DMEM in the presence of 0.1 μM ctx, atz, IgTT-E or IgTT-1E, followed by 5 min incubation with 25 ng/ml of human EGF (MiltenyiBiotec, cat# 130-093-825). After stimulation, cells were lysed in Laemmli lysis buffer, separated under reducing conditions on 4–12% Tris-glycine gels, transferred to nitrocellulose membrane and incubated with the rabbit anti-human phosphor-EGFR (Tyr1068) mAb (clone D7A5; Cell Signaling Technology, cat# 3777) followed by incubation with an IRDye800CW-conjugated donkey anti-rabbit antibody (LI-COR Biosciences, cat# 925–32213). Simultaneously, anti-β-actin mouse mAb (Abcam, cat# ab8226) was added as a loading control, followed by IRDye680RD-conjugated donkey anti-mouse (LI-COR Biosciences, cat# 925–68072). Visualization and quantitative analysis of protein bands were carried out with the Odyssey system (LI-COR Biosciences).

PD-1/PD-L1 Blockade Bioassay

The PD-1/PD-L1 Bioassay (Promega, cat# J1250) was used following manufacturer´s instructions. Briefly, 2.5×10^4 PD-L1 aAPC/CHO-K1 cells/well were seeded in 96-well white plates in DMEM 10% FBS and incubated overnight at 37 ºC. Then, medium was removed and different final concentrations (400; 66.7; 6.67; 0.667 and 0.0667 nM) of atz, ctx, IgTT-E or IgTT-1E were added in 40 μl RPMI 1% FBS/well. Then, 1.25×10^5 Jurkat PD-1 cells/well were added in 40 μl RPMI 1% FBS/well and incubated 6 hours at 37 ºC. Then, 80 μl of BioGlo Reagent (Promega, cat# G7941) were added and bioluminescence, as an indicator of activation, was measured in a Tecan Infinite F200 Fluorescence Microplate Reader (Life Sciences, Tecan).

ADCC reporter bioassay

The ADCC reporter Bioassay (Promega, cat# G7010) was used following manufacturer´s instructions. Briefly, 1.2×10^4 CHO and CHO^{EGFR} cells/well were seeded in 96-well white plates in DMEM 10% FBS and incubated overnight at 37 ºC. Then, medium was removed and different final concentrations (400, 66.7; 6.67; 0.667; 0.0667 nM) of atz, ctx or IgTT-1E were added in 25 μl RPMI 1% FBS/well. Then, 7.5×10^4 ADCC $Jurkat^{CD16}$ effector cells/well were added in 25 μl RPMI 1% FBS and incubated 6 hours at 37 ºC. Finally, 75 μl/well of BioGlo Reagent (Promega) were added and bioluminescence, as an indicator of ADCC activity, was measured in a Tecan Infinite F200 Fluorescence Microplate Reader.

Cytotoxicity assay

Peripheral blood mononuclear cells (PBMC) were isolated from peripheral blood of volunteer healthy donors by density gradient centrifugation using lymphoprep (Axis – Shield, cat# AXS-1114544). All donors provided written informed consent in accordance with the Declaration of Helsinki. For cytotoxicity assay, $EGFR^+$ and PD-$L1^+$ $MDA\text{-}MB231^{Luc}$ and A549 cells were co-cultured with freshly isolated PBMC at two different effector-to-target (E:T) ratios (5:1 and 10:1) in presence of atz, ctx, IgTT-1E or polyclonal control human IgG (6.67 nM). After 48 hours, cells were stained for 30 minutes at 4 ºC with V450-conjugated anti-CD45 mAb (Becton Dickinson, cat# 560367) and 7-AAD (BD Biosciences, cat# 559925) in 50 μl of PBS 2% FBS using TruCount Absolute Counting Tubes (BD Biosciences, cat# 663028). Finally, the samples were diluted by adding 450 μl of PBS before proceeding to flow cytometry analysis. Cytotoxicity was determined by recording the residual live target cells ($7AAD^-$ and $CD45^-$).

NK cells degranulation assay

Degranulation of NK cells following *in vitro* stimulation was assessed by a flow cytometry-based assay. CHO, $CHO^{PD\text{-}L1}$ and CHO^{EGFR} cells were seeded in 96-well U-bottom plates at 5×10^5 cells/well and co-cultured with 2.5×10^6 PBMC/well (5:1 E:T ratio) in the presence of monensin and PE-labeled anti-CD107a mAb (clone H4A3, BD Biosciences, cat# 555801). Then, IgTT-1E, ctx and atz were added to final concentrations of 6.67; 0.667 and 0.0667 nM. As basal degranulation control, PBMC were plated without target cells. A staining control well received neither degranulation stimuli nor the anti-CD107a mAb. After incubating for 4 hours, plates were centrifuged and cells were resuspended in PBS 0.5% FBS and stained with FITC-labeled anti-human CD3 (clone SK7, BD Biosciences, cat# 345763) and APC-labeled anti-human CD56 (clone B159, BD Pharmingen, cat# 555518) mAbs, and analyzed by a FACSCAnto II Flow Cytometer (BD Biosciences). NK cells were identified as $CD3^-CD56^+$ events with light scatter characteristics of lymphocytes.

Mice

$NOD.Cg\text{-}Prkdc^{SCID}IL2rg^{tm1Wjl}/SzJ$ (NSG, The Jackson Laboratory) female mice were housed under pathogen-free conditions with daily cycles of 12 hours light/12 hours darkness, and sterilized water and food were available *ad libitum*. All animal procedures conformed to European Union Directive 86/609/EEC and Recommendation 2007/526/EC, enforced in Spanish law under RD 1201/2005. Animal protocols were approved by the respective Ethics Committee of Animal Experimentation of the participant institutions (imas12 and Instituto Investigación Sanitaria Puerta de Hierro-Segovia de Arana); they were performed in strict adherence to the guidelines stated in the International Guiding Principles for Biomedical Research Involving Animals, established by the Council for International Organizations of Medical Sciences. The experimental study protocols were additionally approved by local government (PROEX 166/19). Mice were kept under anesthesia during all manipulations and all efforts were made to minimize suffering.

Therapeutic studies

$MDA\text{-}MB\text{-}231^{luc}$ cells were resuspended in 30% (v/v) matrigel (Corning, cat#356231) in PBS. Cells were injected directly into the second left mammary fat pad of NSG female mice (2×10^6/

mouse), followed by an intraperitoneal (i.p.) injection of freshly isolated human PBMC (1×10^7/mouse). Tumor growth was evaluated weekly by bioluminescence imaging. Mice were treated every three days with five intraperitoneal injections of PBS, atz, ctx or IgTT-1E (4 mg/kg), or atz/ctx (2 mg/kg) in combination. Mice weights were measured twice a week to monitor toxicity and animals were euthanized at any sign of distress and/or due to 20% of weight loss. For *in vivo* bioluminescence imaging, mice were anesthetized using inhaled isoflurane, injected intraperitoneally with 125 mg/kg D-luciferin (Promega, cat# E1605) dissolved in 200 µl of sterile PBS. Animals were imaged 10 minutes after D-luciferin injection using the Bruker In-Vivo Xtreme (Bruker). The photon flux emitted by the luciferase-expressing cells was measured as an average radiance (photons/sec/cm^2/sr). Imaging analysis was performed using Bruker Molecular Imaging Software (Bruker). At the end of the experiment anesthetized animals were sacrificed and the different organs (liver, spleen, and tumor) were rapidly harvested and processed. A549 cells (2×10^6/mouse) resuspended in 30% (v/v) matrigel in PBS were implanted subcutaneously (s.c.) into the dorsal space of NSG mice, followed by an intraperitoneal injection of freshly isolated human PBMC (1×10^7 cells/mouse). Tumor growth was monitored by caliper measurements twice a week. Mice were treated every three days with five intraperitoneal injections of PBS, IgTT-1E (4 mg/kg) or atz/ctx (2 mg/kg) in combination. Mice weights were measured as described above. Mice were euthanized when the weight loss was≥15% compared to baseline, when tumor size reached a diameter of 1.0 cm in any dimension, when tumors ulcerated, or at any sign of distress.

Immunohistochemistry

Tumors from different treatment groups were collected at different times after implantation, fixed in 10% neutral buffered formalin (Sigma-Aldrich, cat#HT501128) for 48 hours and after extensive washing in PBS, tissues were embedded in paraffin. Four-µm-thick sections were incubated with mouse mAbs listed in Table S2 on a Bond^{TM} Automated System (Leica Microsystems) according to the manufacturer's instructions. Nuclei were counter stained with Harris' hematoxylin. Whole digital slides were acquired with a slide scanner (AxioScan Z1, Zeiss), and total versus positive cells were automatically quantified (AxioVision 4.6 software package, Zeiss).

Statistical analysis

All plots were created using GraphPad Prism 9.0, which was also used to perform statistical analysis. In general, the *in vitro* experiments were done in triplicates and values are presented as mean ± SD. Significant differences (*P* value) were identified using a two-tailed, unpaired Student's t test assuming a normal distribution, or a one-way analysis of variance (ANOVA), adjusted by Dunnett's test for multiple comparisons, as indicated. *P* values are shown in the corresponding figures. Two-way ANOVA was used to analyze experiments that evaluated the interaction of two variables, such as cell type and therapy, following multiple comparison testing using either Dunnett or Tukey, as appropriate. Mean tumor volumes are presented for each group using a scatter plot as mean ± SD. To assess the differences between treatment groups, *P* values were determined by one-way ANOVA adjusted by the Bonferroni correction for multiple comparison tests. Survival curves were estimated for each group using the Kaplan-Meier method and individual curves were analyzed by Log-rank (Mantel-Cox) test. Significant differences were calculated by comparing each group to the others.

Results

Generation and characterization of monospecific and bispecific IgTTs

In this study, we generated an EGFR-specific IgTT (Figure 1a) by fusing a V_{HH}-based monospecific TT (Figure 1b), consisting of three identical EGFR-specific V_{HH} (clone EGa1)[13]-TIE modules connected by two glycine-serine-based linkers on a single-chain molecule[7], to the human IgG1 hinge-Fc regions (IgTT-E, Figure 1c). This antibody was further modified (Figure 1d) by replacing the N-terminal V_{HH} with an anti-PD-L1 scFv derived from *atezolizumab* (atz) (Figure 1e) to generate a PD-L1/EGFR bispecific IgTT (IgTT-1E, Figure 1f). The models presented in Figure 1 are snapshots of dynamic conformations in which the flexible connectors confer the V_{HH} and scFv binding domains variable distances and areas of influence around the Fc region. IgTT antibodies were purified from conditioned medium from stably transfected HEK-293 cells by Strep-Tactin affinity chromatography, and both molecules eluted as single peaks (Fig. a, b). Protein yields for IgTT-E and IgTT1E were 5.7 and 3.4 mg/L, respectively (Fig. S1a). SEC-MALS measurements for IgTT-E and IgTT-1E resulted in major symmetric peaks with molar masses of 227 and 240 kDa, respectively (Fig. S1a, b), close to the calculated values for each dimeric species in solution (202 and 223 kDa, respectively). In reducing SDS-PAGE, two main bands corresponding to the IgTT-E and IgTT-1E monomers can be identified (Fig. S1c). The smaller minority bands are most likely result of linker cleavage that does not disturb the structural organization of the molecule, as is evident from the observation of single peaks in SEC (Fig. S1a).

The binding of both IgTT antibodies to their cognate antigens was investigated using biolayer interferometry (BLI). Monospecific IgTT-E and bispecific IgTT-1E were found to bind immobilized human EGFR-Fc (EGFR) similarly to *cetuximab* (ctx) (Figure 2a,b), and IgTT-1E bound to human PD-L1-Fc (PD-L1) comparably to atz (Figure 2c). In all four interactions, less than 5% dissociation was measured during a period of 30 minutes, which was not sufficient to accurately determine the dissociation rate constant (KD). The upper bound for their dissociation rate constant is 3×10^{-5}/s and the lower bound for the half-life of their interactions is 7 hours. Therefore, these kinetic experiments demonstrate picomolar affinity or stronger for all the measured interactions, as is expected for bivalent and trivalent antibodies in an experiment which permits multivalent antigen binding, but do not determine precise KD values (Table S3). Additionally, after the binding of IgTT-1E and ctx to immobilized EGFR, the ability of the antibodies to simultaneously bind PD-L1 was investigated by additionally

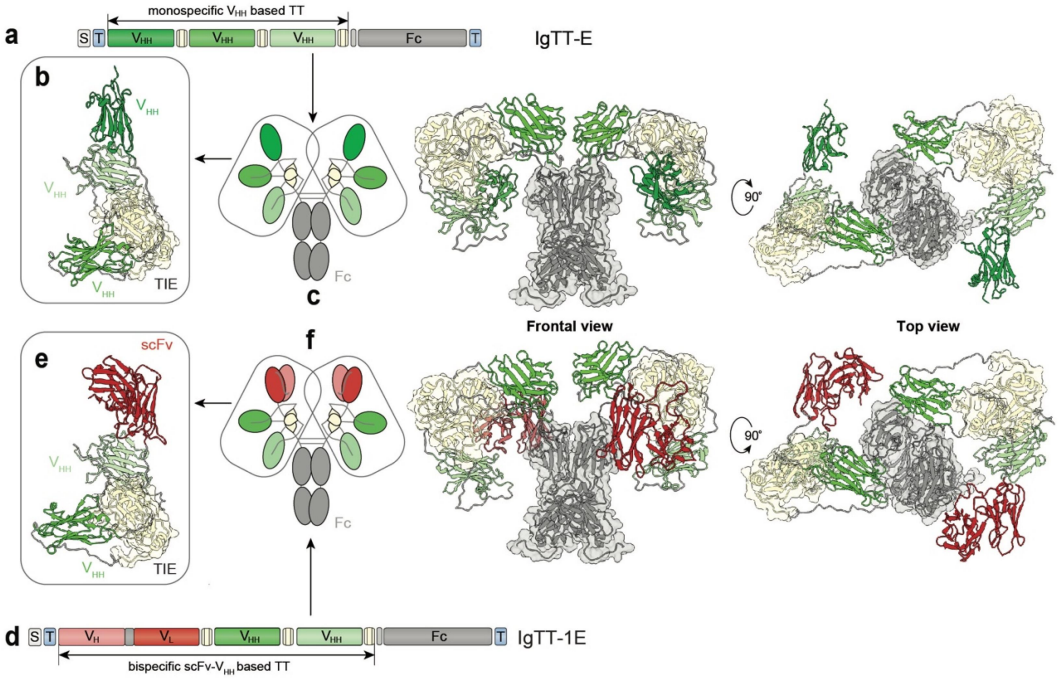

Figure 1. Molecular diagrams and models of the IgTT-E and IgTT-1E antibodies. Gene layout of the monospecific IgTT-E (a), bearing a signal peptide from oncostatin M (white box), three anti-EGFR V_{HH} (green boxes), three collagen-derived trimerization (TIE) domains (yellow boxes) flanked by peptide linkers and the Fc encoding element (gray boxes). N-terminal FLAG-Strep and C-terminal Myc-His tags (blue boxes) were appended for purification and immunodetection purposes. Schematic diagram showing the three-dimensional model of the TT (b), the molecular diagram and the three-dimensional modelizations of the IgTT-E, in front and top views (c). Gene layout of the bispecific IgTT-1E (d), bearing a signal peptide from oncostatin M (white box), one anti-PD-L1 scFv (red box) and two anti-EGFR V_{HH} genes (green boxes), three TIE domains (yellow boxes) flanked by peptide linkers and the Fc encoding element (gray boxes). N-terminal FLAG-Strep and C-terminal Myc-His tags (blue boxes). Schematic diagram showing the three-dimensional model of the TT (e), the molecular diagram and the three-dimensional modelizations of the IgTT-1E in front and top views (f).

associating the antibody-loaded biosensors with PD-L1 in solution. IgTT-1E, but not ctx, showed a clear simultaneous binding to PD-L1 while maintaining its interaction with EGFR (Figure 2d), further demonstrating its bispecificity and a lack of steric hindrance between its two cognate interactions. The ability of both antibodies to specifically detect human EGFR and PD-L1 in a cellular context was analyzed by flow cytometry, using ctx and atz as binding controls, and *trastuzumab* (tra) as negative control (Figure 2e). Furthermore, IgTT-1E demonstrated high stability in physiological-like conditions with no significant loss of binding activity after incubation at 37 ºC for 96 hours in human serum (Figure S1d).

Effect of IgTT-1E on EGFR-mediated signaling and PD-1/PD-L1 blockade

We next studied the capacity of IgTT-1E to inhibit proliferation and EGFR phosphorylation using the ligand-competitive inhibitor ctx as a positive control and the anti-PD-L1 atz as a negative control. The epidermoid carcinoma A431 cell line is EGFR gene-amplified (1.2×10^6 sites/cell) and mostly depend on the EGFR/MAPK pathway for continuous proliferation[18,19]. The anti-EGFR EgA1 V_{HH} binds an epitope close to junction of EGFR domains II/III, hindering the conformational changes in EGFR necessary for high-affinity ligand binding and receptor dimerization[20]. As shown in Figure 3a, IgTT-E, IgTT-1E and ctx, but not atz, inhibited A431 cell proliferation in a dose-dependent manner ($P = <0.0001$, 0.0049 and<0.0001; respectively, for the highest doses of both IgTTs, vs. equimolar doses of control antibody). The phosphorylation status of tyrosine 1068 (Tyr1068) was determined, as this tyrosine is the docking site for Grb2 and its phosphorylation allows the initiation of EGFR mitogenic cascade. Correspondingly, the inhibitory effect on cell proliferation correlated mechanistically with a reduction of EGFR phosphorylation (Figure 3b). The IgTT-1E efficiently blocked PD-1/PD-L1 interaction, as shown by the significant induction of luciferase activity on APC/CHO-K1 cells ($P < 0.0001$), similar to observed with the PD-L1 blocking antibody atz ($P < 0.0001$). In contrast, no PD-1/PD-L1 blocking activity was observed in the presence of ctx or IgTT-E (Figure 3c).

Determination of Fc-mediated effector functions

For measuring ADCC activity, Jurkat cells constitutively expressing human FcγRIIIa (CD16) on the cell surface and a luciferase reporter driven by a NFAT response element (Jurkat^{CD16}) were co-cultured with CHO cells stably expressing human EGFR (CHO^{EGFR}) or nontransfected CHO cells as negative control. As shown in Figure 3d, the activation of Jurkat^{CD16} cells by ctx and IgTT-1E in co-cultures with CHO^{EGFR} cells led to a significant increase in luciferase activity ($P < 0.0001$ and $P = 0.0074$, respectively). In the absence of EGFR-mediated interactions (co-cultures with nontransfected CHO cells), ctx and IgTT-1E showed no induction over untreated Jurkat^{CD16} cells (Figure 3d). Similarly, atz showed no activation in co-cultures with CHO^{EGFR} or CHO cells (Figure 3d). The atz Fc region has

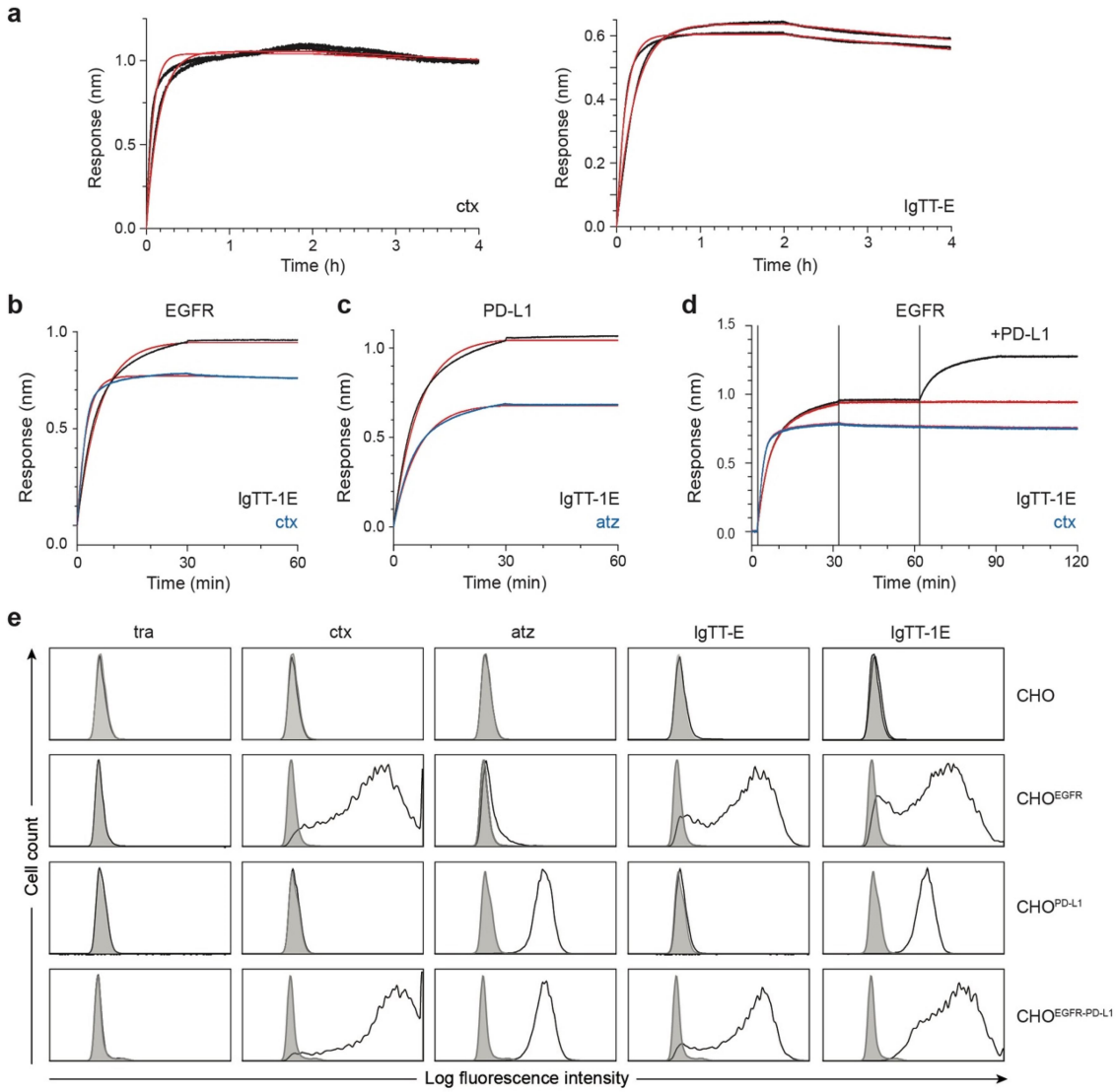

Figure 2. Binding characteristics of mono- and bispecific IgTT antibodies to EGFR, PD-L1, and both antigens simultaneously. (a) BLI-derived sensorgrams (in black) for the interaction between cetuximab (ctx) or IgTT-E and immobilized human EGFR-Fc. (b) Human EGFR-Fc was immobilized onto biosensors and 10 nM of either the IgTT-1E (black trace) or ctx (blue trace) was associated for 30 minutes, followed by 30 minutes of dissociation in buffer only. (c) as in the previous panel, binding to immobilized human PD-L1-Fc was investigated using atezolizumab (atz, blue trace) as a comparison antibody. The results of fitting to a 1:1 binding model are shown as red traces. Kinetic rate parameters from fitting are given in Table S3. A single experimental sensorgram of each antibody is shown; duplicate biosensors were included in the experiment and showed negligible variation. (d) Simultaneous binding to both immobilized human EGFR-Fc and human PD-L1-Fc in solution was demonstrated for IgTT-1E (black trace) but not ctx (blue trace). Human EGFR-Fc-coated biosensors were loaded with either IgTT-1E or ctx (as in the panel b), after which biosensors were immersed in 20 nM of human PD-L1-Fc or kept in buffer (red trace). (e) the binding to human EGFR and PD-L1 on the cell surface of CHO, CHO^{EGFR}, $CHO^{PD\text{-}L1}$ and $CHO^{EGFR\text{-}PD\text{-}L1}$ cells by trastuzumab (tra), ctx, atz, IgTT-E and IgTT-1E at 6.67 nM was measured by FACS. Cells incubated with PE-conjugated isotype control mAb are shown as gray-filled histogram. The y-axis shows the relative cell number, and the x-axis represents the intensity of fluorescence expressed on a logarithmic scale.

been engineered to reduce binding to Fcγ receptors and minimize ADCC[21,22]. $EGFR^{+}PD\text{-}L1^{+}$ cancer cells (MDA-MB231 or A549) were co-cultured with human PBMC at two different E:T ratios (5:1 and 10:1) in the presence of atz, ctx, IgTT-1E or control human IgG (6.67 nM). A significant decrease in the residual live target cells was observed with IgTT-1E and ctx compared to atz and control IgG at both E:T ratios. IgTT-1E eliminated nearly 55% of the A549 cells and 70% of the MDA-$MD23^{Luc}$ cells at the highest E:T ratio (Figure 3e). Furthermore, the IgTT-1E-mediated degranulation by NK cells was studied after co-culturing CHO and CHO^{EGFR} cells with PBMC at a 5:1 E:T ratio in the presence of different antibody concentrations. Both ctx and IgTT-1E increased CD107a cell surface expression compared to PBMC co-cultured CHO^{EGFR} cells in the presence of atz. No changes in CD107a cell expression were detected when PBMC were co-cultured with CHO cells (Figure 3f, Figure. S2 and Table S4).

Therapeutic effect of IgTT-1E in vivo

The therapeutic potential of IgTT-1E was first investigated in PBMC-driven humanized NSG mice bearing human MDA-MB-231 TNBC CDXs. MDA-$MB\text{-}231^{Luc}$ cells were injected into the second right mammary fat pad (MFP) and human PBMC intraperitoneally (i.p.). Mice were treated every three days for five i.p. injections in total, atz, ctx, IgTT-1E or the atz/ctx combination (combo) (Figure 4a). IgTT-1E monotherapy reduced tumor

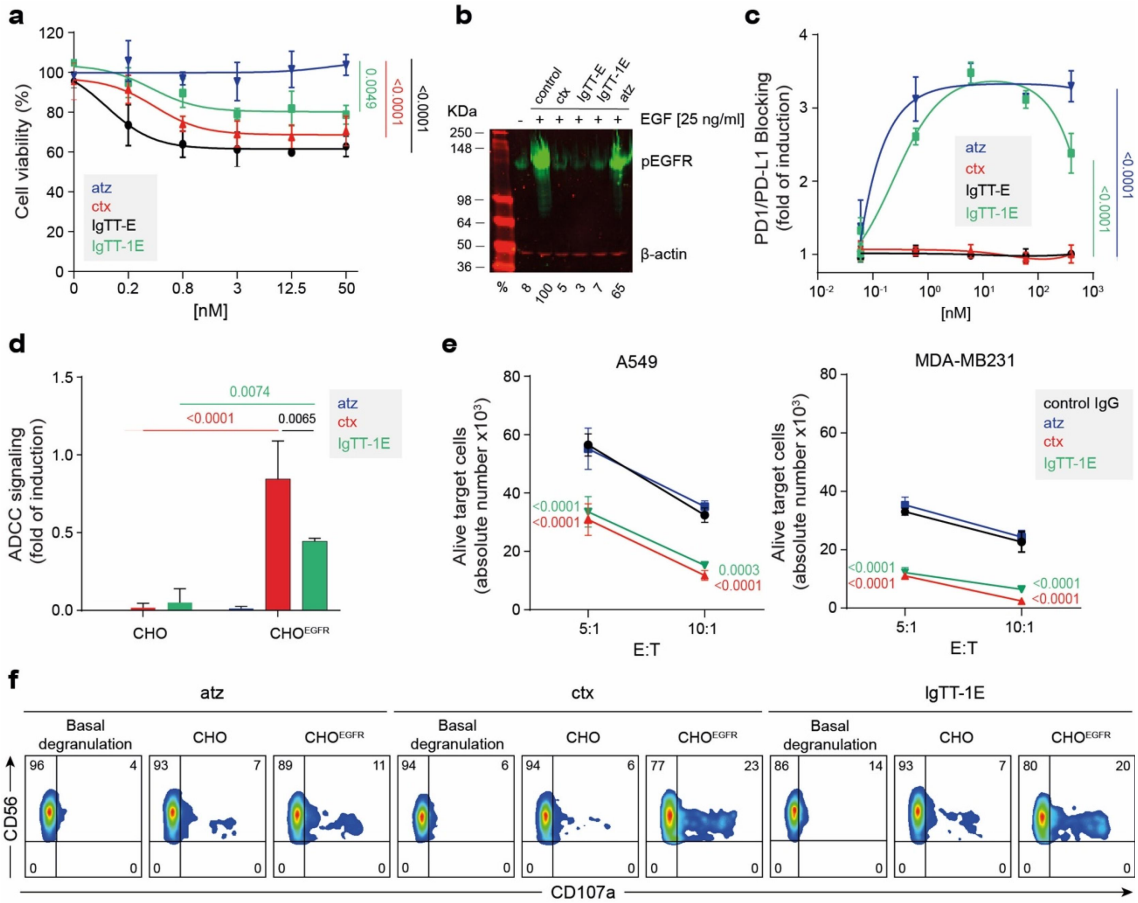

Figure 3. IgTT-1E reduces cell proliferation and induces cytotoxicity. (a) Inhibition of A431 cell proliferation through blocking of EGF/EGFR signaling. The cells were treated with the indicated doses of IgTT-E, IgTT-1E, ctx (positive control) or atz (negative control). Viable cells after 72 hours of treatment were plotted relative to untreated controls. Results are expressed as a mean ± SD ($n = 3$). Significance was measured by one-way ANOVA with Dunnett's multiple comparisons test. (b) Inhibition of EGFR phosphorylation was assessed by western blotting. After pre-incubation with 50 nM of each antibody for 4 hours, cells were stimulated for 5 minutes with EGF or vehicle. Using the β-actin as load and signal control, the percentages of each phosphorylation band with respect to the positive control were calculated. (c) PD-1/PD-L1 blockade bioassay assesses the inhibitory activities of PD-L1 blocking antibody IgTT-1E. Y-axis represents reporter gene fold induction. Ctx was used as negative control and atz as positive control. Results are expressed as mean ± SD ($n = 3$). Significance was measured by one-way ANOVA with Dunnett's multiple comparisons test. (d) ADCC reporter bioassay response to ctx, atz and IgTT-1E, using ADCC bioassay effector Jurkat^{CD16} cells against CHO and CHO^{EGFR} target cells. Target cells were incubated with ctx (positive control), atz (negative control) and IgTT-1E followed by addition of ADCC bioassay effector cells at a 6:1 E:T ratio. After 6 hours of coincubation at 37°C Bio-Glo™ Luciferase Assay Reagent was added for luminescence determination. Data shown represent the mean ± standard deviation of triplicates. Data are presented as the mean ± SD ($n = 3$). Quantification shown as mean ± SD, ($n = 3$). Significance was determined by two-way ANOVA with Tukey's multiple comparisons test. (e) the number of alive (7AAD$^-$) target A549 and MDA-MB231 cells determined after 48 hour co-culture with PBMC cells at 5:1 and 10:1 E:T ratios in presence of control human IgG, atz, ctx and IgTT-1E. Results are shown as mean ± SD ($n = 3$). Significance was determined by two-way ANOVA with Dunnett's multiple comparisons test. (f) Human PBMC were incubated with ctx, atz and IgTT-1E (0.667 nM) for 4 hours prior to flow cytometry evaluation of CD107a cell surface expression on NK cells, gated as CD3$^-$CD56$^+$ cells.

bioluminescence in 4 out of 5 treated mice, similar to what was found in the groups receiving atz or combination therapy (Figure 4b,c). Consistent with these antitumor results, a significant overall survival benefit was observed for the mice that had been treated with atz ($P = 0.0122$) or IgTT-1E ($P = 0.0054$) compared to ctx (Figure 4d). To further validate the antitumor activity of IgTT-1E, we performed a second study with PBMC-driven humanized NSG mice bearing human A549 lung cancer CDXs. When tumors reached approximately 0.2 cm in diameter, mice were randomized into groups with similar mean tumor sizes and SDs and treated every three days for five i.p. injections in total of IgTT-1E or the atz/ctx combination (Figure 4e). IgTT-1E monotherapy was able to reduce tumor growth by approximately 85% ($P = 0.0001$), while the combination therapy showed an approximately 90% tumor growth reduction ($P = 0.0001$) (Figure 4f). There were no significant body weight decreases in any group (Figure 4g). In both treatment groups, inhibition of tumor growth was associated with significantly increased numbers of intratumoral CD8$^+$ T cells (Figure 4h, i and Figure S3), while no CD56$^+$ NK cells were detected on tumor tissues (Fig. S4).

Discussion

In recent years, new cancer immunotherapy strategies have been developed based on the generation of bsAb with improved properties over conventional mAbs[8,12,14,23]. Currently, there are five FDA-approved bsAbs for cancer

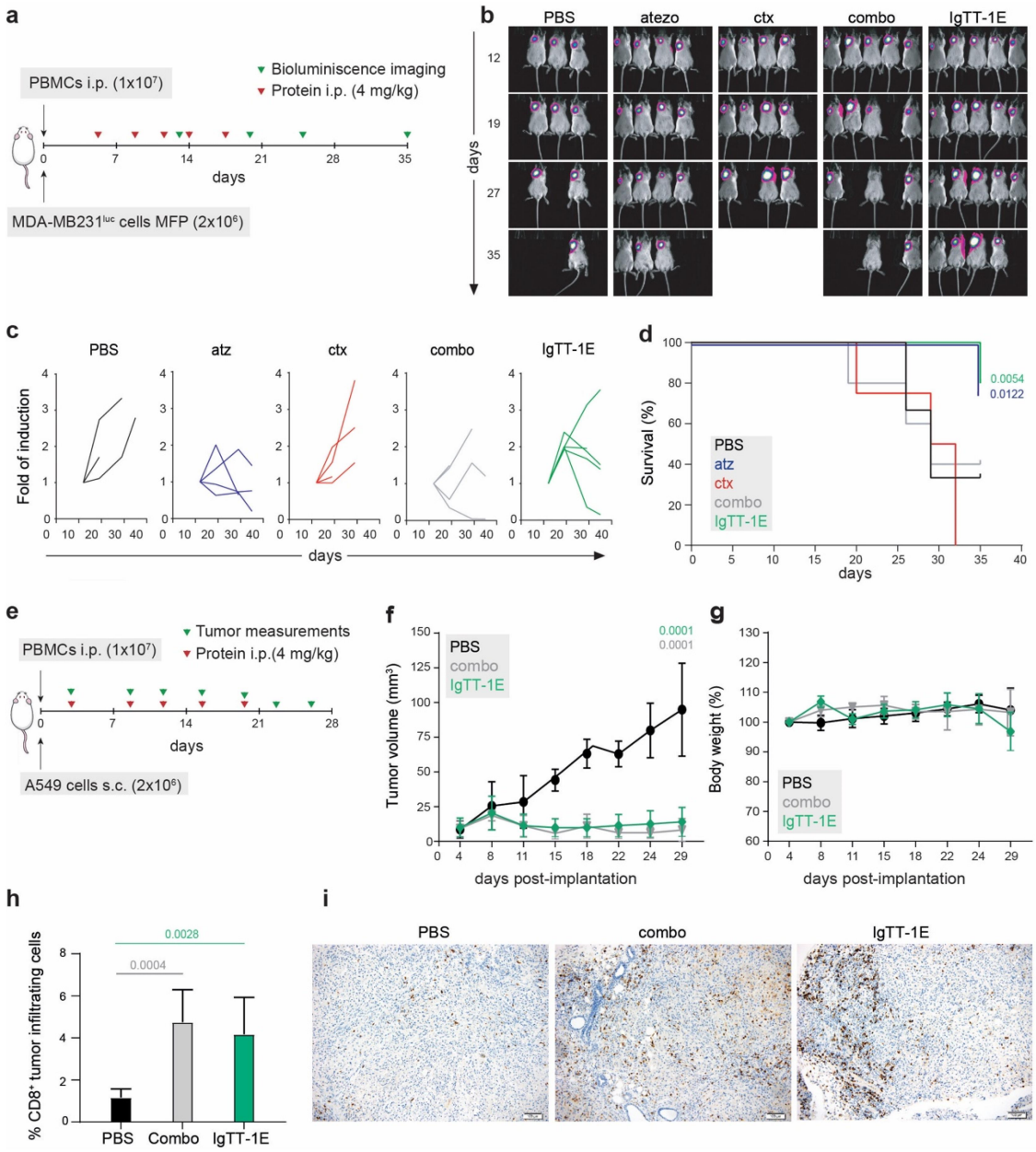

Figure 4. IgTT-1E treatment promoted significant tumor growth inhibition in NSG mouse models. (a) Timeline of experimental design. MDA-MB-231^{Luc} cells were implanted into the right mammary fat pad (MFP) of NSG mice, and human PBMC were injected intraperitoneally (i.P.). Mice were treated with five i.P. injections of PBS, atz, ctx, atz + ctx (combo) or IgTT-1E. (b) Weekly bioluminescence imaging showing tumor progression. (c) Quantification of tumor burden (as bioluminescence fold induction from each mouse) at the indicated time points. (d) Kaplan-Meier plot of survival data. (e) Timeline of experimental design. NSG mice were subcutaneously (s.C.) inoculated with A549 tumor cells and i.P. with human PBMC, follow by five i.P. injections of PBS, atz + ctx combo or IgTT-1E. Tumor progression was monitored weekly by diameter measuring. (f) Average tumor volume growth in each mice group. Data are presented as the mean ± SD. Significance was determined by one-way ANOVA adjusted by the Bonferroni correction for multiple comparison test. (g) Change in mouse body weight over time for each group. (h) Quantitative analysis of intratumoral CD8$^+$ T cells in paraffin-embedded mouse tumor tissue (PBS $n = 4$, combo $n = 6$, IgTT-1E $n = 6$) by immunohistochemistry. Data were calculated as percentage of CD8$^+$ versus total cell number and presented as mean ± SD. Significance was measured by one-way ANOVA with Dunnett's multiple comparisons test. (i) Immunohistochemical staining for CD8 of representative tissue slides from the tumor of mice treated with PBS, atz + ctx combo or IgTT-1E. Scale bars (100 µm) are shown.

treatment, *blinatumomab* for acute B cell lymphoblastic leukemia, *amivantamab-vmjw* for NSCLC, *tebentafusp-tebn* for uveal melanoma, *mosunetuzumab-axgb* for follicular lymphoma, and *teclistamab-cqyv* for multiple myeloma[12,15], and more than 120 candidates are in clinical development[16]. Despite advances in antibody engineering, the generation of IgG-like bsAb remains challenging when the antigen-binding sites are Fab-like with the variable regions of both the heavy chain (V_H) and light chain (VL), as this makes it difficult to obtain functional bsAb from the random assembly of ten possible H_2L_2 combinations (this is commonly referred to as the chain-association issue)[17–20]. Therefore, to overcome this and other limitations a wide variety of antibody engineering strategies have been developed in recent years[9,23]. Symmetric bsAbs are generated by the assembly of antibodies with unmodified heavy chain (HC) constant (C_H) regions[21,23]. Most

symmetric bsAbs in clinical development are bulky molecules with tetravalent (2 + 2) designs in which extra antibody fragments are fused to homodimeric antibody molecules[22,23]. Otherwise, the generation of asymmetric IgG-like bsAbs continues to be challenging because two critical issues need to be simultaneously addressed: the heterodimerization of two different HC chains and the discrimination between the two L/H chain interactions[21,23,24]. Correct HC heterodimerization is facilitated using engineering strategies such as knobs-into-holes and crossMAb technologies[23,25–28]. However, most of these strategies employ multiple mutations within the C_H domains, which can negatively affect the favorable properties associated with native Fc regions, such as high stability and solubility, as well as increasing their immunogenicity[29].

Here, we generated a novel PD-L1/EGFR IgG-like bsAb by novel antibody engineering that solves some of the problems associated with bispecific heterodimeric IgG antibody generation, such as the chain-association issue[17–20]. The IgTT format is based on the fusion of a mono or multispecific TT[7] with the human IgG1 hinge and Fc region, generating a hexavalent IgG-like antibody capable of bivalently recognizing up to three different antigens. We initially generated a monospecific IgTT molecule targeting EGFR, a well-characterized TAA that is the one of the most commonly overexpressed membranous oncogenic protein in epithelial cancers[30]. In addition, we have demonstrated the suitability of the IgTT format for dual-targeting strategies combining TAA-recognition with an ICB, in a single molecule. Both IgTT molecules specifically bind to their targeted antigens, and the IgTT-1E displayed simultaneous binding to both antigens. As previously described, the interaction of EGa1 V_{HH} with EGFR inhibited EGFR phosphorylation and cell proliferation[7,11,31]. Furthermore, the bispecific IgTT-1E efficiently blocked PD-1/PD-L1 interaction and promoted efficient EGFR-mediated ADCC.

The combined PD-L1 and EGFR targeting by bsAbs has been shown to enhance PD-L1 blockade selectively in the TME, due to EGFR overexpression in cancer cells, and to reduce potential off-tumor binding to PD-L1-expressing normal cells[32]. Because of its distinctive properties including tetravalent binding to EGFR, bivalent binding to PD-L1, and a molecular mass similar to IgG, the IgTT-1E is expected to demonstrate improved tumor localization compared to previously generated bsAbs. Furthermore, EGFR overexpression and activation promotes PD-L1 expression by cancer cells[33]. Therefore, EGFR is a particularly suitable TAA for the development of next-generation bispecific ICB. Compared to other IgG-like bsAbs simultaneously targeting EGFR and PD-L1[34,35], the IgTT-1E is based on an IgG1 wild-type homodimeric Fc region retaining ADCC activity as in Li et al.[35]. Indeed, IgTT-1E might induce ADCC activity in the intratumoral space reducing the tumor burden and priming immune responses, as has been shown with *cetuximab*[36]. The concomitant presence of PD-L1 blocking domains in the same spatial location would be essential to overcome immunosuppressive counter-mechanisms in the TME and fully mobilize the adaptive and innate immunity against tumor cells. In addition, the presence of a functional Fc region in the molecule, as in the case of *cetuximab*, has been shown to induce NK cell-dendritic cell (DC) crosstalk, promoting DC maturation and leading to $CD8^+$ T cell priming[37–47]. Therefore, IgTT-1E may provide sustained $CD8^+$ T activity by inducing NK-DC crosstalk and blocking PD-1/PD-L1 interaction, leading to a more prolonged function of tumor-infiltrating lymphocytes.

Acknowledgments

We thank Carlos Alfonso for help with SEC-MALS experiments.

Disclosure statement

M.C., R.N., and O.H. are all employees of Leadartis. L.A.-V. and L.S. are co-founders of Leadartis. The remaining authors declare no competing interests.

Funding

L.A-V. was supported by grants from the MCIN/AEI/10.13039/501100011033 (PID2020-117323RB-100 and PDC2021-121711-100), the Instituto de Salud Carlos III (DTS20/00089), the CRIS Cancer Foundation (FCRIS-2021-0090), the Spanish Association Against Cancer (PROYE19084ALVA), the Fundación "La Caixa" (HR21-00761 project IL7R_LungCan) and the Fundación de Investigación Biomédica 12 de Octubre Programa Investiga (2022-0082). B.B and L.S. were supported by grants PI20/01030 and PI19/00132 from the Instituto de Salud Carlos III (PI20/01030). FJB and MF-G were supported by grants PID2020-113225GB-I00 and PRE2018-085788 funded by MCIN/AEI/10.13039/501100011033. L.R-P. was supported by a predoctoral fellowship from the Immunology Chair, Universidad Francisco de Vitoria/Merck. C. D-A. was supported by a predoctoral fellowship from the MCIN/AEI/10.13039/501100011033 (PRE2018-083445). L.D-A. was supported by a Rio Hortega fellowship from the Instituto de Salud Carlos III (CM20/00004). O.H. was supported by an industrial PhD fellowship from the Comunidad de Madrid (IND2020/BMD-17668). AE-L was supported industrial PhD fellowship from the Instituto de Salud Carlos III (IFI18/00045).

ORCID

Laura Rubio-Pérez http://orcid.org/0000-0002-2877-6092
Rodrigo Lázaro-Gorines http://orcid.org/0000-0002-6885-3486
Seandean L. Harwood http://orcid.org/0000-0003-4654-8832
Marta Compte http://orcid.org/0000-0002-7138-9266
Rocío Navarro http://orcid.org/0000-0002-0083-7711
Antonio Tapia-Galisteo http://orcid.org/0000-0002-0507-8435
Jaume Bonet http://orcid.org/0000-0001-5210-4387
Belén Blanco http://orcid.org/0000-0001-5085-7756
Simon Lykkemark http://orcid.org/0000-0001-8920-6926
Ángel Ramírez-Fernández http://orcid.org/0000-0002-3265-6878
Mariola Ferreras-Gutiérrez http://orcid.org/0000-0003-4421-3158
Carmen Domínguez-Alonso http://orcid.org/0000-0002-0446-9629
Laura Díez-Alonso http://orcid.org/0000-0002-9545-6910
Alejandro Segura-Tudela http://orcid.org/0000-0002-5506-0153
Francisco J. Blanco http://orcid.org/0000-0003-2545-4319
Cruz Santos http://orcid.org/0000-0001-5164-5050
José L. Rodríguez-Peralto http://orcid.org/0000-0002-6578-7153
Laura Sanz http://orcid.org/0000-0002-3119-3218
Luis Álvarez-Vallina http://orcid.org/0000-0003-3053-6757

Ethics approval

All procedures involving animals were in accordance with the ethical standards of the corresponding institutional and regional/national committees.

Data availability statement

The datasets used and/or analyzed during the current study are available from the corresponding author [LA-V] on reasonable request.

Consent to participate

Informed consent was obtained from all participants included in the study.

References

1. Mahoney KM, Rennert PD, Freeman GJ. Combination cancer immunotherapy and new immunomodulatory targets. Nat Rev Drug Discov. 2015;14:561–584. doi:10.1038/nrd4591.
2. Sharpe AH, Pauken KE. The diverse functions of the PD1 inhibitory pathway. Nat Rev Immunol. 2018;18:153–167. doi:10.1038/nri.2017.108.
3. Freeman GJ, Long AJ, Iwai Y, Bourque K, Chernova T, Nishimura H, Fitz LJ, Malenkovich N, Okazaki T, Byrne MC, et al. Engagement of the PD-1 immunoinhibitory receptor by a novel B7 family member leads to negative regulation of lymphocyte activation. J Exp Med. 2000;192:1027–1034. doi:10.1084/jem.192.7.1027.
4. Wei SC, Duffy CR, Allison JP. Fundamental mechanisms of immune checkpoint blockade therapy. Cancer Discov. 2018;8:1069–1086. doi:10.1158/2159-8290.CD-18-0367.
5. Morad G, Helmink BA, Sharma P, Wargo JA. Hallmarks of response, resistance, and toxicity to immune checkpoint blockade. Cell. 2021;184:5309–5337. doi:10.1016/j.cell.2021.09.020.
6. Kubli SP, Berger T, Araujo DV, Siu LL, Mak TW. Beyond immune checkpoint blockade: emerging immunological strategies. Nat Rev Drug Discov. 2021;20:899–919. doi:10.1038/s41573-021-00155-y.
7. Roskoski R. The ErbB/HER family of protein-tyrosine kinases and cancer. Pharmacol Res. 2014;79:34–74. doi:10.1016/j.phrs.2013.11.002.
8. Levantini E, Maroni G, Del Re M, Tenen DG. EGFR signaling pathway as therapeutic target in human cancers. Semin Cancer Biol. 2022;85:253–275. doi:10.1016/j.semcancer.2022.04.002.
9. Antibody therapeutics approved or in regulatory review in the EU or US [Internet]. The Antibody Society. [accessed 2023 March 1]. https://www.antibodysociety.org/resources/approved-antibodies/
10. Cuesta AM, Sainz-Pastor N, Bonet J, Oliva B, Alvarez-Vallina L. Multivalent antibodies: when design surpasses evolution. Trends Biotechnol. 2010;28:355–362. doi:10.1016/j.tibtech.2010.03.007.
11. Cuesta AM, Sánchez-Martín D, Blanco-Toribio A, Villate M, Enciso-Álvarez K, Álvarez-Cienfuegos A, Sainz-Pastor N, Sanz L, Blanco FJ, Álvarez-Vallina L. Improved stability of multivalent antibodies containing the human collagen XV trimerization domain. MAbs. 2012;4:226–232. doi:10.4161/mabs.4.2.19140.
12. Lazarovici P, Lelkes PI. Pardaxin induces exocytosis in bovine adrenal medullary chromaffin cells independent of calcium. J Pharmacol Exp Ther. 1992;263:1317–1326.
13. Alvarez-Cienfuegos A, Nuñez-Prado N, Compte M, Cuesta AM, Blanco-Toribio A, Harwood SL, Villate M, Merino N, Bonet J, Navarro R, et al. Intramolecular trimerization, a novel strategy for making multispecific antibodies with controlled orientation of the antigen binding domains. Sci Rep. 2016;6:28643. doi:10.1038/srep28643.
14. Saphire EO, Parren PW, Pantophlet R, Zwick MB, Morris GM, Rudd PM, Dwek RA, Stanfield RL, Burton DR, Wilson IA. Crystal structure of a neutralizing human IGG against HIV-1: a template for vaccine design. Science. 2001;293:1155–1159. doi:10.1126/science.1061692.
15. Berman HM, Westbrook J, Feng Z, Gilliland G, Bhat TN, Weissig H, Shindyalov IN, Bourne PE. The Protein Data Bank. Nucleic Acids Res. 2000;28:235–242. doi:10.1093/nar/28.1.235.
16. Altschul SF, Gish W, Miller W, Myers EW, Lipman DJ. Basic local alignment search tool. J Mol Biol. 1990;215:403–410. doi:10.1016/S0022-2836(05)80360-2.
17. Liu S, Miersch S, Li P, Bai B, Liu C, Qin W, Su J, Huang H, Pan J, Sidhu SS, et al. A synthetic human antibody antagonizes IL-18Rβ signaling through an allosteric mechanism. J Mol Biol. 2020;432:1169–1182. doi:10.1016/j.jmb.2020.01.012.
18. Janmaat ML, Kruyt FAE, Rodriguez JA, Giaccone G. Response to epidermal growth factor receptor inhibitors in non-small cell lung cancer cells: limited antiproliferative effects and absence of apoptosis associated with persistent activity of extracellular signal-regulated kinase or Akt kinase pathways. Clin Cancer Res. 2003;9:2316–2326.
19. Meira DD, Nóbrega I, de Almeida VH, Mororó JS, Cardoso AM, Silva RLA, Albano RM, Ferreira CG. Different antiproliferative effects of matuzumab and cetuximab in A431 cells are associated with persistent activity of the MAPK pathway. Eur J Cancer. 2009;45:1265–1273. doi:10.1016/j.ejca.2008.12.012.
20. Schmitz KR, Bagchi A, Roovers RC, van Bergen En Henegouwen PMP, Ferguson KM. Structural evaluation of EGFR inhibition mechanisms for nanobodies/VHH domains. Structure. 2013;21:1214–1224. doi:10.1016/j.str.2013.05.008.
21. Deng R, Bumbaca D, Pastuskovas CV, Boswell CA, West D, Cowan KJ, Chiu H, McBride J, Johnson C, Xin Y, et al. Preclinical pharmacokinetics, pharmacodynamics, tissue distribution, and tumor penetration of anti-PD-L1 monoclonal antibody, an immune checkpoint inhibitor. MAbs. 2016;8:593–603. doi:10.1080/19420862.2015.1136043.
22. Shah NJ, Kelly WJ, Liu SV, Choquette K, Spira A. Product review on the Anti-PD-L1 antibody atezolizumab. Human Vacc Immunother. 2018;14:269–276. doi:10.1080/21645515.2017.1403694.
23. Harwood SL, Alvarez-Cienfuegos A, Nuñez-Prado N, Compte M, Hernández-Pérez S, Merino N, Bonet J, Navarro R, Van Bergen En Henegouwen PMP, Lykkemark S, et al. ATTACK, a novel bispecific T cell-recruiting antibody with trivalent EGFR binding and monovalent CD3 binding for cancer immunotherapy. Oncoimmunology. 2017;7:e1377874. doi:10.1080/2162402X.2017.1377874.
24. Surowka M, Schaefer W, Klein C. Ten Years in the making: application of CrossMab technology for the development of therapeutic bispecific antibodies and antibody fusion proteins. MAbs. 2021;13:1967714. doi:10.1080/19420862.2021.1967714.
25. Blanco B, Domínguez-Alonso C, Alvarez-Vallina L. Bispecific immunomodulatory antibodies for cancer immunotherapy. Clin Cancer Res. 2021;27:5457–5464. doi:10.1158/1078-0432.CCR-20-3770.
26. Esfandiari A, Cassidy S, Webster RM. Bispecific antibodies in oncology. Nat Rev Drug Discov. 2022;21:411–412. doi:10.1038/d41573-022-00040-2.
27. Henricks LM, Schellens JHM, Huitema ADR, Beijnen JH. The use of combinations of monoclonal antibodies in clinical oncology. Cancer Treat Rev. 2015;41:859–867. doi:10.1016/j.ctrv.2015.10.008.
28. Progress in overcoming the chain association issue in bispecific heterodimeric IgG antibodies - PubMed [Internet]. [accessed 2022 December 19]. https://pubmed.ncbi.nlm.nih.gov/22925968/
29. Rath T, Baker K, Dumont JA, Peters RT, Jiang H, Qiao S-W, Lencer WI, Pierce GF, Blumberg RS. Fc-fusion proteins and FcRn: structural insights for longer-lasting and more effective therapeutics. Crit Rev Biotechnol. 2015;35:235–254. doi:10.3109/07388551.2013.834293.
30. Clarke SC, Ma B, Trinklein ND, Schellenberger U, Osborn MJ, Ouisse L-H, Boudreau A, Davison LM, Harris KE, Ugamraj HS, et al. Multispecific antibody development platform based on

human heavy chain antibodies. Front Immunol. 2019;9:3037. doi:10.3389/fimmu.2018.03037.
31. Labrijn AF, Meesters JI, de Goeij BECG, van den Bremer ETJ, Neijssen J, van Kampen MD, Strumane K, Verploegen S, Kundu A, Gramer MJ, et al. Efficient generation of stable bispecific IgG1 by controlled Fab-arm exchange. Proc Natl Acad Sci U S A. 2013;110:5145–5150. doi:10.1073/pnas.1220145110.
32. Wu Y, Yi M, Zhu S, Wang H, Wu K. Recent advances and challenges of bispecific antibodies in solid tumors. Exp Hematol Oncol. 2021;10:56. doi:10.1186/s40164-021-00250-1.
33. Brinkmann U, Kontermann RE. The making of bispecific antibodies. MAbs. 2017;9:182–212. doi:10.1080/19420862.2016.1268307.
34. Marvin JS, Zhu Z. Recombinant approaches to IgG-like bispecific antibodies. Acta Pharmacol Sin. 2005;26:649–658. doi:10.1111/j.1745-7254.2005.00119.x.
35. Merchant AM, Zhu Z, Yuan JQ, Goddard A, Adams CW, Presta LG, Carter P. An efficient route to human bispecific IgG. Nat Biotechnol. 1998;16:677–681. doi:10.1038/nbt0798-677.
36. Labrijn AF, Janmaat ML, Reichert JM, Parren PWHI. Bispecific antibodies: a mechanistic review of the pipeline. Nat Rev Drug Discov. 2019;18:585–608. doi:10.1038/s41573-019-0028-1.
37. Spiess C, Zhai Q, Carter PJ. Alternative molecular formats and therapeutic applications for bispecific antibodies. Mol Immunol. 2015;67:95–106. doi:10.1016/j.molimm.2015.01.003.
38. J-H H, Kim J-E, Kim Y-S. Immunoglobulin Fc heterodimer platform technology: from design to applications in therapeutic antibodies and proteins. Front Immunol. 2016;7:394. doi:10.3389/fimmu.2016.00394.
39. Ridgway JB, Presta LG, Carter P. 'Knobs-into-holes' engineering of antibody CH3 domains for heavy chain heterodimerization. Protein Eng. 1996;9:617–621. doi:10.1093/protein/9.7.617.
40. Nuñez-Prado N, Compte M, Harwood S, Álvarez-Méndez A, Lykkemark S, Sanz L, Álvarez-Vallina L. The coming of age of engineered multivalent antibodies. Drug Discov Today. 2015;20:588–594. doi:10.1016/j.drudis.2015.02.013.
41. Thomas R, Weihua Z. Rethink of EGFR in cancer with its kinase independent function on board. Front Oncol. 2019;9:800. doi:10.3389/fonc.2019.00800.
42. Akbay EA, Koyama S, Carretero J, Altabef A, Tchaicha JH, Christensen CL, Mikse OR, Cherniack AD, Beauchamp EM, Pugh TJ, et al. Activation of the PD-1 pathway contributes to immune escape in EGFR-driven lung tumors. Cancer Discov. 2013;3:1355–1363. doi:10.1158/2159-8290.CD-13-0310.
43. Chen N, Fang W, Zhan J, Hong S, Tang Y, Kang S, Zhang Y, He X, Zhou T, Qin T, et al. Upregulation of PD-L1 by EGFR activation mediates the immune escape in EGFR-Driven NSCLC: implication for optional immune targeted therapy for NSCLC patients with EGFR mutation. J Thorac Oncol. 2015;10:910–923. doi:10.1097/JTO.0000000000000500.
44. Koopmans I, Hendriks D, Samplonius DF, Ginkel RJ, Heskamp S, Wierstra PJ, Bremer E, Helfrich W. A novel bispecific antibody for EGFR-directed blockade of the PD-1/PD-L1 immune checkpoint. Oncoimmunology. 2018;7:e1466016. doi:10.1080/2162402X.2018.1466016.
45. Li L, Deng L, Meng X, Gu C, Meng L, Li K, Zhang X, Meng Y, Xu W, Zhao L, et al. Tumor-targeting anti-EGFR x anti-PD1 bispecific antibody inhibits EGFR-overexpressing tumor growth by combining EGFR blockade and immune activation with direct tumor cell killing. Transl Oncol. 2021;14:100916. doi:10.1016/j.tranon.2020.100916.
46. Ferris RL, Lenz H-J, Trotta AM, García-Foncillas J, Schulten J, Audhuy F, Merlano M, Milano G. Rationale for combination of therapeutic antibodies targeting tumor cells and immune checkpoint receptors: harnessing innate and adaptive immunity through IgG1 isotype immune effector stimulation. Cancer Treat Rev. 2018;63:48–60. doi:10.1016/j.ctrv.2017.11.008.
47. Srivastava RM, Lee SC, Andrade Filho PA, Lord CA, Jie H-B, Davidson HC, López-Albaitero A, Gibson SP, Gooding WE, Ferrone S, et al. Cetuximab-activated natural killer and dendritic cells collaborate to trigger tumor antigen–specific T-cell immunity in head and neck cancer patients. Clin Cancer Res. 2013;19:1858–1872. doi:10.1158/1078-0432.CCR-12-2426.

Supplementary Files

A PD-L1/EGFR bispecific antibody combines immune checkpoint blockade and direct anti-cancer action for an enhanced anti-tumor response

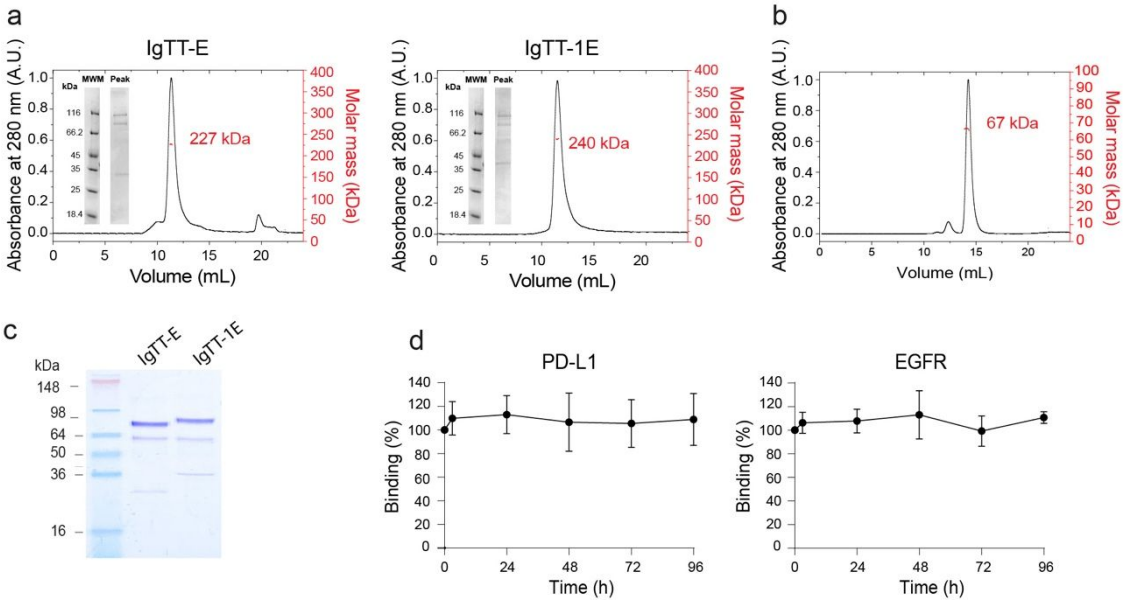

Figure S1. Purified IgTT-E and IgTT-1E elute in a single peak. (a) SEC-MALS analysis of IgTT-E and IgTT-1E molecules. The black line corresponds to the UV absorbance at 280nm (left axis) and the red line to the measured molar mass (right axis). Experiments were performed once after checking the performance of the apparatus on a BSA sample at 2 g/L under the same conditions **(b)**. The absolute molar masses of the eluted antibodies (indicated in the graphs) were calculated from the intensity of the scattered light at 18 angles, which is independent on the elution volume, the shape of the antibody, or the potential interaction of the protein with the matrix of the column. The theoretical masses calculated from the amino acid sequences (assuming the formation of dimers) were 202 and 223 kDa. The theoretical mass of the BSA monomer is 66 kDa. The inset in **(a)** shows the reducing SDS-PAGE analysis of the central fraction of the major peak from a chromatogram done before the SEC-MALS experiment, using the same column and the same buffer. **(a)** SDS-PAGE analysis of purified IgTT-E and IgTT-1E in reducing conditions. **(d)** Serum stability of purified IgTT-1E was analyzed by relative binding to immobilized PD-L1 or EGFR after sample incubation in human serum at 37 °C for different time periods. Experiments were performed in triplicates.

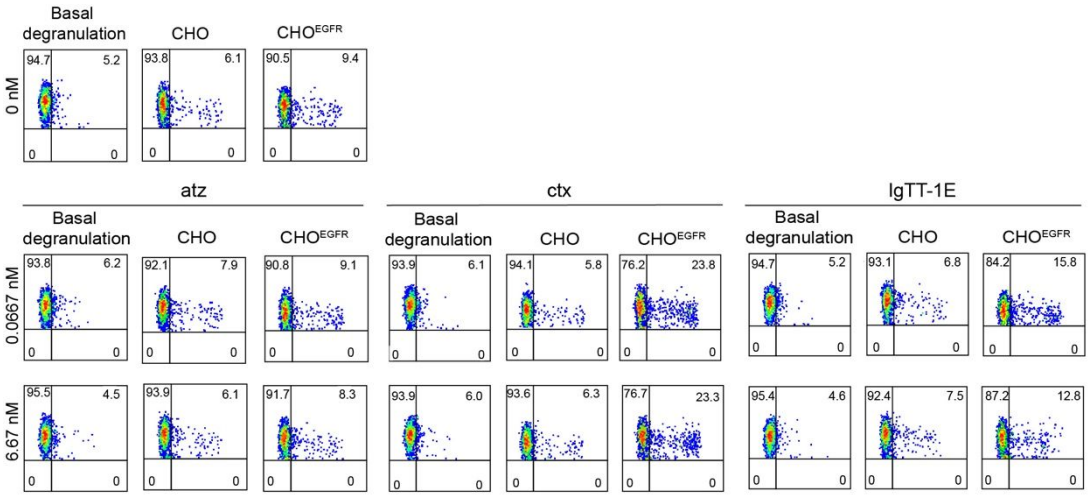

Figure S2. Antibody-mediated NK cells degranulation assay. Fresh isolated PBMC from healthy donor were cocultured with different concentrations of atz, ctx, or IgTT-1E for 4 hours in presence of CHO or CHO^{EGFR} cells. CD107a surface expression on NK cells ($CD3^-$ and $CD56^+$) was evaluated by flow cytometry.

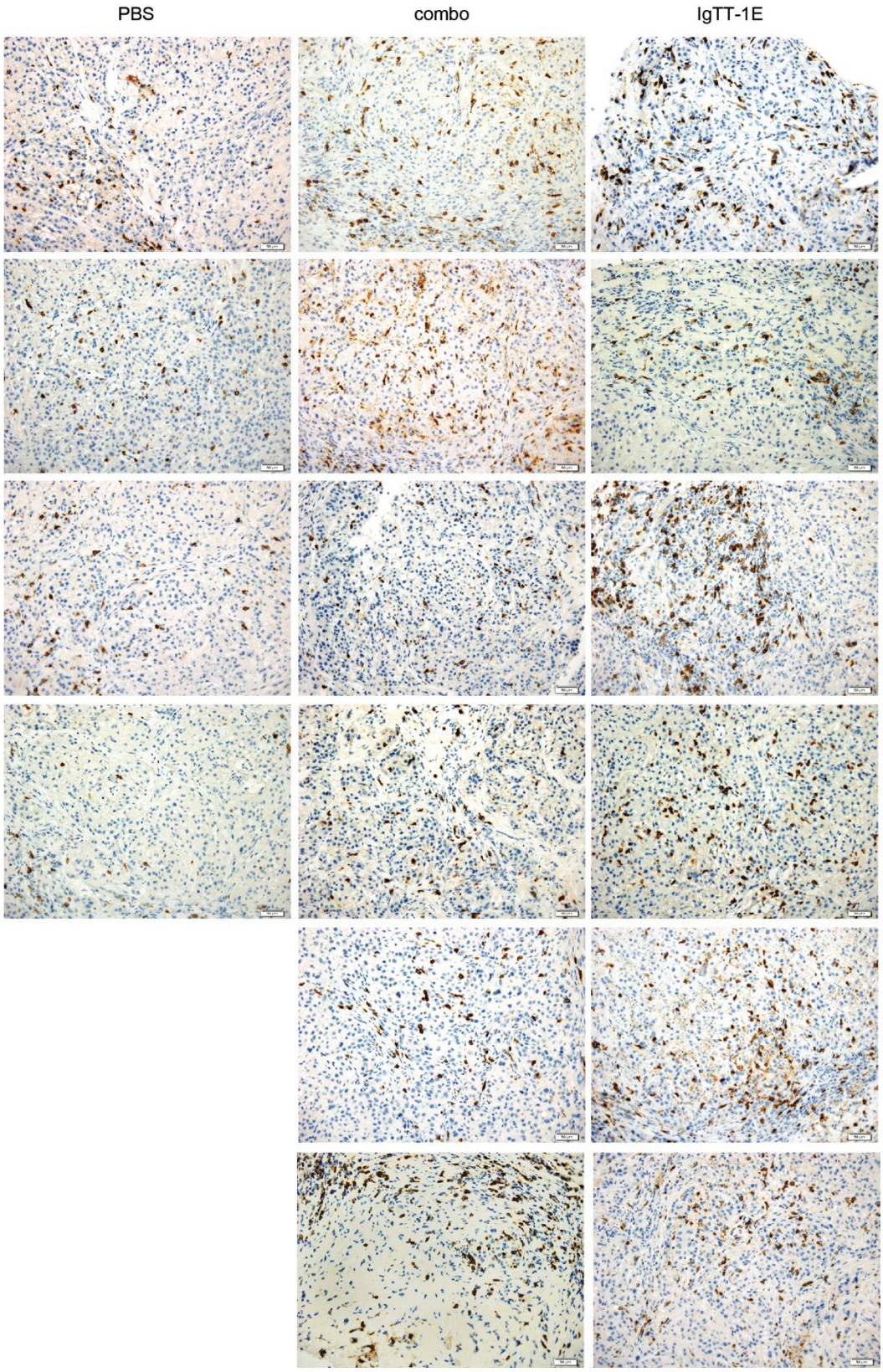

Figure S3. Immunohistochemical staining for CD8 of tumor tissue slides of mice treated with PBS, atz/ctx combination therapy (combo) or IgTT-1E. Scale bars (50 μm) are shown.

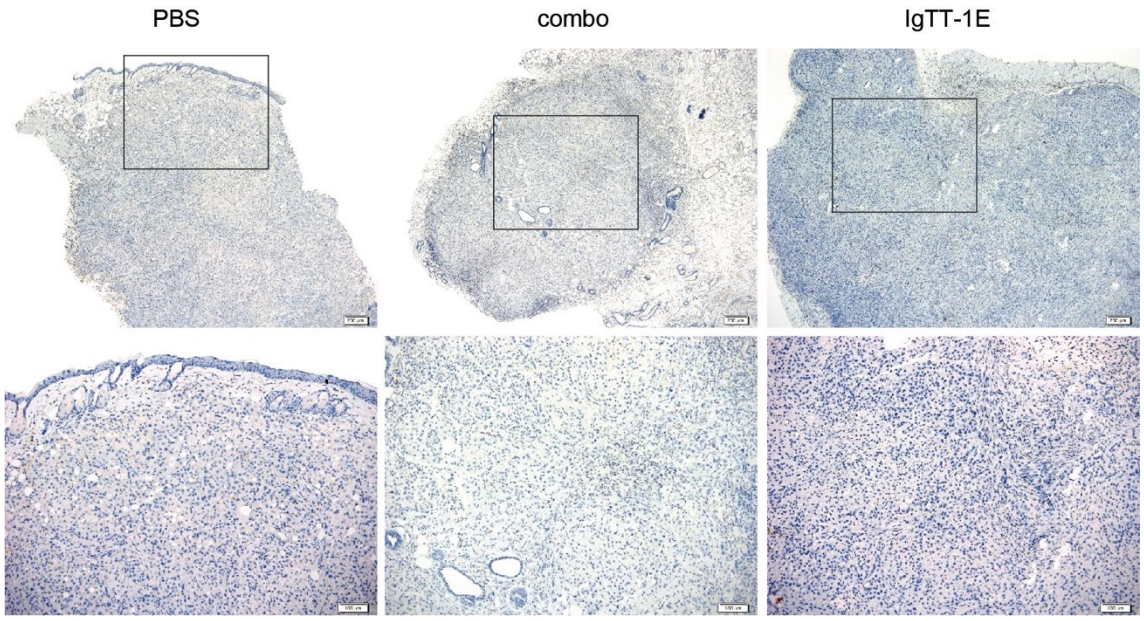

Figure S4. Immunohistochemical staining for CD56 of tumor tissue slides of mice treated with PBS, atz/ctx combination therapy (combo) or IgTT-1E. Scale bars are shown.

Table S1. **Oligonucleotides used in this study**

Name	**Sequence (5´-3´)**
FwCMV	CGCAAATGGGCGGTAGGCGTG
RvBGH	TAGAAGGCACAGTCGAGG

Oligonucleotides were synthesized by Thermo Scientific.

Table S2. Antibodies used for immunohistochemistry

Antibody	Clone	Species	Clonality	Reference number	Supplier	Dilution
anti-huCD45	X16/99	mouse	monoclonal	LCA-L-CE	Leica	1:40
anti-huCD3	LN10	mouse	monoclonal	CD3-565-L-CE	Leica	1:25
anti-huCD8	4B11	mouse	monoclonal	CD8-4b11-l-ce-h	Leica	1:50
anti-huCD56	504	mouse	monoclonal	CD56-504-L-CE	Leica	1:80

Table S3. Equilibrium and kinetics constants determined from biolayer interferometry.

Antigen	Antibody	K_D (M)	k_a ($M^{-1}s^{-1}$)	k_d (s^{-1})
EGFR	IgTT-1E	<1.0E-12	2.77E+05	<1.0E-07
	ctx (IgG)	1.16E-11	6.80E+05	7.90E-06
PD-L1	IgTT-1E	<1.0E-12	2.46E+05	<1.0E-07
	atz (IgG)	<1.0E-12	2.57E+05	<1.0E-07

Table S4. Number of $CD107a^+$ cells in NK degranulation assay.

Conditions	Antibodies	Total No. cells	$CD3^-CD56^+$ No. cells	$CD107a^+$ No. cells
Basal degranulation	atz	20,000	1,957	200
	ctx	20,000	2,073	152
	IgTT-1E	20,000	2,195	143
CHO	atz	20,000	1,805	158
	ctx	20,000	1,728	133
	IgTT-1E	20,000	1,907	191
CHO-EGFR	atz	20,000	1,911	175
	ctx	20,000	1,317	364
	IgTT-1E	20,000	1,524	363

ARTÍCULO II: ***Characterization of a trispecific PD-L1 blocking antibody that exhibits EGFR-conditional 4-1BB agonist activity*****.**

Laura Rubio-Pérez, Susana Frago, Marta Compte, Rocío Navarro, Seandean L. Harwood, Rodrigo Lázaro-Gorines, Marina Gómez-Rosel, Oana Hangiu, Noelia Silva-Pilipich, Lucía Vanrell, Cristian Smerdou, Luis Álvarez-Vallina

Antibodies, 2024, 13(2), 34

DOI:10.3390/antib13020034

Introducción:

Los ICIs son efectivos en muchos tipos de cáncer, pero la tasa general de repuesta es baja (20-30%). La combinación de ICIs con anticuerpos inmunoestimuladores de células T es una estrategia que ha demostrado una mejora en la actividad antitumoral en numerosos estudios. Sin embargo, el desarrollo clínico de los anticuerpos anti-4-1BB inmunoestimuladores se ha visto obstaculizado por el desarrollo de toxicidades significativas, mediadas por la interacción entre la región Fc y los receptores FcγR. En este trabajo hemos generado un anticuerpo triespecífico anti-4-1BB/EGFR/PD-L1 para combinar el bloqueo del eje PD-L1/PD-1 con la coestimulación 4-1BB confinada específicamente al microambiente tumoral, basado en la plataforma IgTT y con una región Fc silenciada.

Objetivos:

1. Diseño y generación de vectores de expresión que codifican para los anticuerpos triespecíficos IgTT-4E1 e IgTT-4E1-S.
2. Expresión de los anticuerpos recombinantes en células de mamífero y purificación mediante cromatografía de afinidad.
3. Caracterización estructural y funcional de los anticuerpos purificados.
4. Evaluación *in vitro* de la capacidad de bloqueo de la interacción PD-1/PD-L1, de inducir co-estimulación a través de la unión a 4-1BB y de generar actividad citotóxica mediada por la Fc silenciada.
5. Estudio de la secreción de IFNγ en un contexto de co-cultivo con células T primarias y líneas celulares tumorales $EGFR^+$/$PD\text{-}L1^+$.

Conclusiones:

1. Los anticuerpos recombinantes IgTT-4E1 e IgTT-4E1-S (con la región Fc silenciada) se secretaron eficientemente por células humanas y se purificaron mediante cromatografía de afinidad Strep-Tactin, eluyendo como un único pico. Las fracciones presentaban un alto grado de pureza y el tamaño esperado mediante electroforesis en geles SDS-PAGE en condiciones reductoras.
2. Ambos anticuerpos purificados reconocieron específicamente los antígenos diana en solución de manera simultánea y en un contexto celular.
3. El anticuerpo IgTT-4E1-S mostró una actividad ADCC significativamente más baja en comparación con el anticuerpo IgTT-4E1.

4. El anticuerpo IgTT-4E1-S bloqueó eficazmente la interacción PD-1/PD-L1 e indujo una potente coestimulación mediada por 4-1BB sólo en co-cultivos con células que expresaban EGFR, pero no en co-cultivos con células que expresaban PD-L1.
5. La IgTT-4E1-S potencia la activación y funciones efectoras de células T primarias humanas co-cultivadas con células tumorales doble positivas para EGFR y PD-L1.

Graphical abstract:

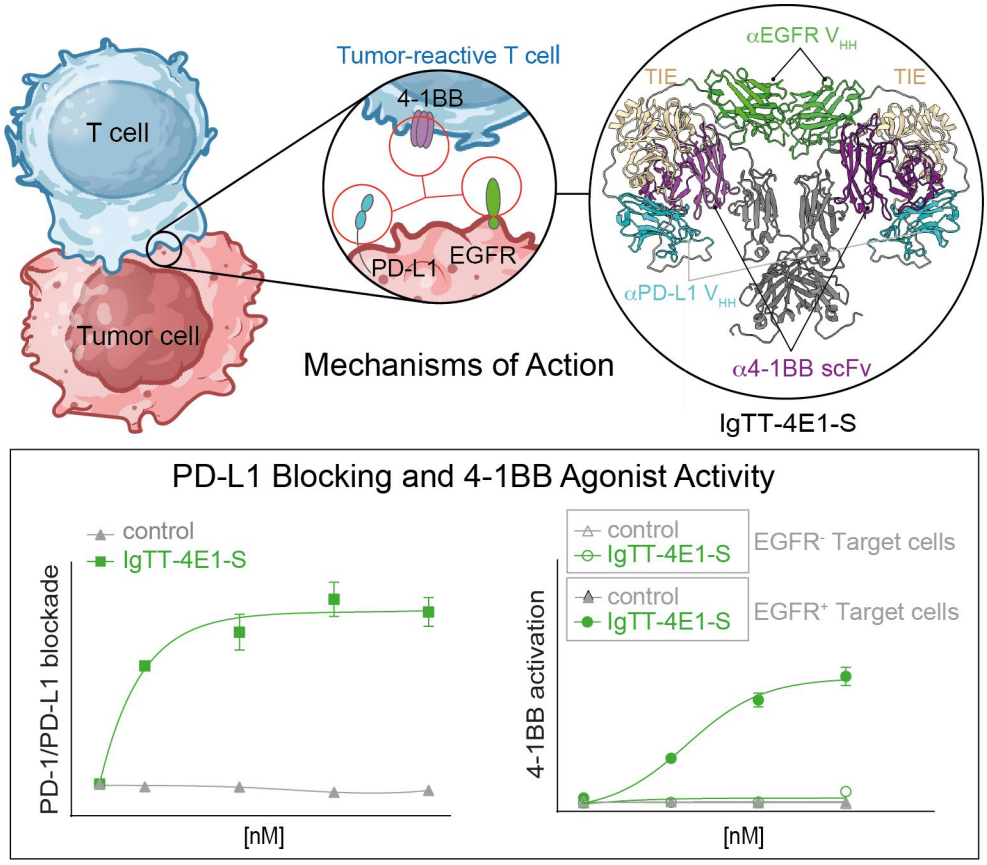

Publicación:

antibodies

IMPACT FACTOR 4.7

Indexed in: PubMed

CITESCORE 9.6

Brief Report

Characterization of a Trispecific PD-L1 Blocking Antibody That Exhibits EGFR-Conditional 4-1BB Agonist Activity

Laura Rubio-Pérez, Susana Frago, Marta Compte, Rocío Navarro, Seandean L. Harwood, Rodrigo Lázaro-Gorines, Marina Gómez-Rosel, Oana Hangiu, Noelia Silva-Pilipich, Lucía Vanrell et al.

Special Issue

Emerging Antibody Engineering Strategies and Applications for Immunotherapy of Cancer

Edited by

Dr. Christian Klein, Prof. Dr. Sophia Karagiannis and Dr. Ann White

MDPI

https://doi.org/10.3390/antib13020034

antibodies

MDPI

Brief Report

Characterization of a Trispecific PD-L1 Blocking Antibody That Exhibits EGFR-Conditional 4-1BB Agonist Activity

Laura Rubio-Pérez [1,2,3,4], Susana Frago [5], Marta Compte [5], Rocío Navarro [5], Seandean L. Harwood [6], Rodrigo Lázaro-Gorines [1,2,3], Marina Gómez-Rosel [1,2,3], Oana Hangiu [1,2,5], Noelia Silva-Pilipich [7,8], Lucía Vanrell [9,10], Cristian Smerdou [7,8] and Luis Álvarez-Vallina [1,2,3,4,*]

1 Cancer Immunotherapy Unit (UNICA), Department of Immunology, Hospital Universitario12 de Octubre (H12O), 28041 Madrid, Spain; laura.rubio.imas12@h12o.es (L.R.-P.); rlazaro@cnio.es (R.L.-G.); marinagomezrosel.imas12@h12o.es (M.G.-R.); oana.hangiu@leadartis.com (O.H.)
2 Immuno-Oncology and Immunotherapy Group, Instituto de Investigación Sanitaria 12 de Octubre (imas12), 28041 Madrid, Spain
3 H12O-CNIO Cancer Immunotherapy Clinical Research Unit, Spanish National Cancer Research Centre (CNIO), 28029 Madrid, Spain
4 Chair for Immunology UFV/Merck, Universidad Francisco de Vitoria (UFV), Pozuelo de Alarcón, 28223 Madrid, Spain
5 Department of Antibody Engineering, Leadartis SL, QUBE Technology Park, Tres Cantos, 28760 Madrid, Spain; susana.frago@leadartis.com (S.F.); marta.compte@leadartis.com (M.C.); rocio.navarro@leadartis.com (R.N.)
6 Department of Molecular Biology and Genetics, Aarhus University, 8000 Aarhus C, Denmark; sdlh@mbg.au.dk
7 Division of DNA and RNA Medicine, Cima Universidad de Navarra, 31008 Pamplona, Spain; nsilva.1@alumni.unav.es (N.S.-P.); csmerdou@unav.es (C.S.)
8 Instituto de Investigación Sanitaria de Navarra (IdISNA) and CCUN, 31008 Pamplona, Spain
9 Facultad de Ingeniería, Universidad ORT Uruguay, 11100 Montevideo, Uruguay; lvanrell@unav.es
10 Nanogrow Biotech, Montevideo 11500, Uruguay
* Correspondence: lav.imas12@h12o.es

check for updates

Citation: Rubio-Pérez, L.; Frago, S.; Compte, M.; Navarro, R.; Harwood, S.L.; Lázaro-Gorines, R.; Gómez-Rosel, M.; Hangiu, O.; Silva-Pilipich, N.; Vanrell, L.; et al. Characterization of a Trispecific PD-L1 Blocking Antibody That Exhibits EGFR-Conditional 4-1BB Agonist Activity. *Antibodies* **2024**, *13*, 34. https://doi.org/10.3390/antib13020034

Academic Editors: Christian Klein and Arne Skerra

Received: 12 January 2024
Revised: 22 April 2024
Accepted: 22 April 2024
Published: 24 April 2024

Abstract: Immune checkpoint blockade has changed the treatment paradigm for advanced solid tumors, but the overall response rates are still limited. The combination of checkpoint blockade with anti-4-1BB antibodies to stimulate tumor-infiltrating T cells has shown anti-tumor activity in human trials. However, the further clinical development of these antibodies has been hampered by significant off-tumor toxicities. Here, we generated an anti-4-1BB/EGFR/PD-L1 trispecific antibody consisting of a triple-targeting tandem trimerbody (TT) fused to an engineered silent Fc region. This antibody (IgTT-4E1-S) was designed to combine the blockade of the PD-L1/PD-1 axis with conditional 4-1BB costimulation specifically confined to the tumor microenvironment (TME). The antibody demonstrated simultaneous binding to purified EGFR, PD-L1, and 4-1BB in solution, effective blockade of the PD-L1/PD1 interaction, and potent 4-1BB-mediated costimulation, but only in the presence of EGFR-expressing cells. These results demonstrate the feasibility of IgTT-4E1-S specifically blocking the PD-L1/PD-1 axis and inducing EGFR-conditional 4-1BB agonist activity.

Keywords: cancer immunotherapy; trispecific antibody; epithelial growth factor receptor; immune checkpoint blockade; 4-1BB costimulation

1. Introduction

One of the most promising strategies for enhancing anti-tumor immune responses is the blockade of inhibitory immune checkpoints, such as cytotoxic T lymphocyte antigen 4 (CTLA-4), programmed cell death protein 1 (PD-1), or PD-1 ligand (PD-L1) [1]. Immune checkpoint blockers have transformed cancer treatment for a wide range of tumor types, but the overall response rates are still limited, as many patients have no response or only a transient response [2,3]. As of January 2024, seven PD-L1 blockers and eight PD-1 blockers have

been approved for clinical use in the United States and Europe, with atezolizumab being the first anti-PD-L1 monoclonal antibody (mAb) on the market (2017) [4]. Another strategy involves targeting costimulatory pathways, such as 4-1BB, also known as CD137, a member of the TNF receptor (TNFR) superfamily (TNFRSF9), which is an activation-induced surface receptor that provides antigen-primed T cells with augmented survival, proliferation and effector functions, as well as metabolic advantages [5]. Anti-4-1BB agonistic mAbs have shown considerable potential in promoting tumor rejection in preclinical cancer models [6]. However, the clinical development of full-length anti-4-1BB antibodies has been hampered by off-tumor toxicity, which is mainly due to Fc-FcγR interactions [6–8]. Therefore, to fully exploit their therapeutic potential, novel approaches are being developed that generally aim to confine 4-1BB costimulation to the TME and draining lymph nodes by adding tumor-specific moieties to generate bispecific 4-1BB agonistic antibodies [8–10]. Tumor-associated antigens (TAAs), such as epidermal growth factor receptor (EGFR), fibroblast activation protein (FAP), CD19, B7-H3 (CD276), carcinoembryonic antigen (CEA), and EGFR 2 (HER2) have been targeted to develop 4-1BB bispecifics [8–15]. Recently, a range of bispecific constructs targeting 4-1BB-mediated T cell costimulation to PD-L1-overexpressing tumor cells and simultaneously blocking the PD-1/PD-L1 axis have been generated [16–22] and are being clinically evaluated.

Here, we generated and characterized a multispecific antibody by fusing a trispecific 4-1BB/EGFR/PD-L1 tandem trimerbody (TT) [23] with the human IgG_1 hinge and Fc regions based on a previously described IgTT platform [24]. We used an engineered silenced Fc region to inhibit the binding of FcγR but retain the binding of FcRn for IgG-like pharmacokinetics [25]. The trispecific and hexavalent antibody was designed to simultaneously modulate two key pathways to enhance anti-tumor immune responses: PD-L1 blockade and tumor-specific 4-1BB costimulation. Our choice of TAA was the EGFR, a well-characterized tyrosine kinase receptor whose dysregulation promotes cancer cell proliferation, inhibits apoptosis, and promotes invasion [26].

2. Materials and Methods

2.1. Cell Lines and Culture Conditions

Dulbecco's modified Eagle's medium (DMEM) (Life Technologies, Carlsbad, CA, US; cat# 10313021) supplemented with antibiotics (100 units/mL of penicillin, 100 µg/mL of streptomycin; both from Life Technologies), 10% (*v*/*v*) heat-inactivated fetal bovine serum (FBS) (Merck Life Science, Darmstadt, Germany; cat# F7524-500 ML), and 2 mmol/L L-glutamine was used to culture HEK-293 (CRL-1573), NIH/3T3 (CRL-1658), CHO-K1 (CCL-61), and MDA-MB-231 (HTB-26) cells at 37 °C in 5% CO_2. All these cell lines were obtained from the American Type Culture Collection. NIH/3T3 cells expressing human EGFR ($3T3^{EGFR}$) were kindly provided by Dr. A. Villalobo (Instituto de Investigaciones Biomédicas "Alberto Sols", IIBm CSIC-UAM, Madrid, Spain). Expi293F cells (from Gibco, Thermo Fisher Scientific, Waltham, MA, USA) were cultured in Expi293 expression medium in a humidified, 8% CO_2 incubator rotating at 95 rpm at 37 °C. Jurkat T cells (TIB-152) were cultured in RPMI-1640 (Lonza Bioscience, Basel, Switzerland; cat# 12-702Q) supplemented with 10% (*v*/*v*) heat-inactivated FBS, 2 mmol/L of L-glutamine, and antibiotics. Jurkat T cells stably expressing human PD-1 and NFAT-induced luciferase ($Jurkat^{NFAT\text{-}PD\text{-}1}$) and CHO-K1 cells stably expressing human PD-L1 (PD-L1 aAPC/CHO-K1) were obtained from Promega (Madison, WI, USA; cat# J1250). Jurkat T cells stably expressing human 4-1BB and NFAT-induced luciferase ($Jurkat^{NFAT\text{-}4\text{-}1BB}$) were obtained from Promega (cat# JA2351). CHO-K1 cells stably expressing human PD-L1 ($CHO^{PD\text{-}L1}$) were obtained from Genlantis (xCELLerateTM PD-L1 Stable Cell Line, XCL-PDL1), and CHO-K1 cells stably expressing human EGFR (CHO^{EGFR}) were generated using human EGFR-encoding lentiviral particles (G&P Biosciences, Santa Clara, CA, US; cat# LTV0169). Jurkat T cells expressing GFP-tagged 4-1BB ($Jurkat^{4\text{-}1BB}$) were generated by lentiviral transduction using commercial lentiviral particles (Origene, Rockville, MD, USA; cat# RC200664L4V). The ORF present in the lentivirus contains 4-1BB sequence followed by mGFP sequence in the C-terminus, a

P2A cleavage site, and a puromycin resistance gene, all in frame. Briefly, 1×10^4 cells were incubated with the lentiviral particles (titer of 5.5×10^7 TU/mL) at a MOI (multiplicity of infection) of 20 for 8 h in retronectin-coated 24-well plates (20 μg/cm^2). The cells were allowed to recover for 48 h and subsequently selected in 2 μg/mL of puromycin. The cells were maintained in culture in the presence of 1 μg/mL of puromycin. All cell lines were routinely screened for mycoplasma contamination by PCR using the Mycoplasma Plus TM Primer Set (Biotools B&M Labs, Madrid, Spain; cat# 90022).

2.2. Construction of the Expression Vectors

To generate the 4-1BB/EGFR/PD-L1 trispecific IgTT Fc^{wt} (IgTT-4E1) expression vector, the plasmid pCR3.1-FLAG/Strep-α4-1BB-αEGFR-αPD-L1-hFc^{wt}-Myc-His was generated by cloning the insert OncoM-FLAG/Strep-α4-1BB scFv SAP3.28 [13] flanked by *Hind*III-*Not*I sites (GeneArt AG, Thermo Fischer, Waltham, MA, USA) and the insert αPD-L1 V_{HH} (Nb6p generated in llama immunized with human PD-L1 ectodomain [27]) flanked by *Afe*I-*Sac*II sites (GeneArt AG, Thermo Fischer) into the plasmid from pCR3.1-FLAG/Strep-αPD-L1-αEGFR-hFc^{wt}-Myc-His encoding the bispefic IgTT-1E [24]. Then, to generate the 4-1BB/EGFR/PD-L1 trispecific IgTT Fc^{silent} (IgTT-4E1-S), the insert hFc^{silent}-Myc-His flanked by *Sac*II-*Xba*I sites (GeneArt AG, Thermo Fischer) was subcloned into the plasmid pCR3.1-FLAG/Strep-α41BB-αEGFR-αPD-L1-hFc^{wt}-Myc-His. Finally, to generate the 4-1BB/PD-L1/EGFR trispecific IgTT Fc^{silent} (IgTT-41E-S), the insert αPD-L1 V_{HH}/αEGFR V_{HH} flanked by *Xho*I-*Sac*II sites (GeneArt AG, Thermo Fischer) was cloned into the plasmid pCR3.1-FLAG/Strep-α41BB-αEGFR-αPD-L1-hFc^{silent}-Myc-His. All the sequences were verified using the FwCMV and RvBGH oligonucleotide primers (Table S1).

2.3. Expression and Purification of the Recombinant Antibodies

HEK-293 cells (4×10^5 cells/well) were transfected with different vectors (2.5 μg of DNA/well) using a Lipofectamine 3000 kit (Fisher Scientific, Waltham, MA, USA; cat# 15292465) and cultured at 37 °C. The cells were then selected in complete DMEM supplemented with 500 μg/mL of G418 to generate stable cell lines. To produce large amounts of protein, 5.8×10^8 Expi293F cells were transfected with 180 μg of DNA using the Expifectamine 293 transfection reagent (Life Technologies) in 180 mL of medium and cultured at 37 °C for four days. The conditioned media were collected and processed using the Strep-Tactin purification system (IBA Lifesciences, Göttingen, Germany) in an ÄKTA Prime plus system (Life Technologies). The purified antibodies were then dialyzed at 4 °C with PBS pH 7.4 supplemented with 150 mM NaCl, analyzed by sodium dodecyl sulphate (SDS)–polyacrylamide gel electrophoresis (PAGE) under reducing conditions, and assayed for endotoxin levels using a limulus amebocyte lysate (LAL) endotoxin quantitation kit according to the manufacturer's specifications (Thermo Fisher Scientific, Waltham, MA, USA; cat# A39552S). The endotoxin levels were <0.25 EU/mL.

2.4. Enzyme-Linked Immunosorbent Assay

To determine the binding activity of the purified or secreted protein, human EGFR-Fc (hEGFR-Fc, R&D Systems, Minneapolis, MN, USA; cat# 344-ER), human PD-L1-Fc (hPD-L1-Fc, R&D Systems, cat# 156-B7-100), or human 4-1BB-Fc (h4-1BB-Fc, R&D Systems, cat# 838-4B-100) chimeras were immobilized (2.5 μg/mL in PBS) on Maxisorp 96-well plates (NUNC Brand Products, Thermo Fisher Scientific; cat# 44240) overnight at 4 °C. After washing and blocking with PBS–5% BSA, the conditioned medium or the purified protein solution (1 μg/mL) was added, and the plates were incubated for 1 h at room temperature. After washing, proteins were detected with HRP-conjugated anti-FLAG mAb (M2 clone, Sigma-Aldrich, Burlington, MA, USA; cat# A8592) (1 μg/mL) for 45 min at room temperature. The plates were then developed with 100 μL of 3,3′,5,5′-tetramethylbenzidine (TMB) (Sigma-Aldrich, cat# T0440), and the reaction was stopped with 100 μL of 1 N H_2SO_4. Absorbance was read at 450–620 nm using a Multiskan FC photometer (Thermo Scientific, Waltham, MA, USA).

2.5. Western Blotting

Conditioned medium samples containing 0.1% (*v*/*v*) FBS were analyzed by 10–20% tris-glycine SDS-PAGE under reducing conditions and transferred onto nitrocellulose membranes (Thermo Fisher Scientific, cat# IB23002). They were incubated with mouse anti-FLAG mAb (clone M2, Sigma-Aldrich, cat# F3165) (1 µg/mL) and probed with HRP-conjugated goat anti-mouse polyclonal antibody (GAM-HRP) (Sigma-Aldrich, Burlington, MA, USA; cat# A2554) (1:10,000 dilution). The visualization of protein bands was performed with Pierce ECL Plus Western Blotting Substrate (Thermo Scientific, cat# 32132) using the ChemiDoc MP Imaging System and Image Lab software (version 6.0.1, both from BioRad, Hercules, CA, USA).

2.6. Size-Exclusion Chromatography

Size-exclusion chromatography (SEC) was performed on a Superdex 200 Increase 10/300 GL column (Cytiva) on an ÄKTA go chromatography system (Cytiva). The column was equilibrated in 0.22 µm filtered PBS. Analytical runs of the antibody were performed at room temperature at a flow rate of 0.75 mL/min, injecting 20 µg of protein. The column was calibrated using the Gel Filtration HMW Calibration Kit from Cytiva (cat# 28403842). Data acquisition and analysis were performed using ASTRA software (version 7.6, Wyatt Technology, Santa Barbara, CA, USA). The reported molar mass corresponds to the center of the chromatography peaks.

2.7. Molecular Modeling

The three-dimensional representation of IgTT-4E1 was built by comparative homology modeling using MODELLER [28]. The model was created by using different templates for the different domains. The V_{HH} monospecific TT model was generated utilizing as a template the monospecific anti-CEA TT from a prior study [23]. The Fc region was modeled based on the human IgG_1 B12 structure (pdb:1HZH.H) [29], obtained from the Protein Data Bank [30] (99% sequence identity, e-value of 1×10^{-169} as calculated by BLAST (version 2.2.24) [31]). The 1HZH structure also guided the dimer modeling. The scFv domain was modeled using the interleukin 18 receptor antagonist scFv (pdb:6NK9.D) [32] as a template (83% sequence identity, e-value of 2×10^{-138} as calculated by BLAST). Ultimately, the final representation was generated by merging the models.

2.8. Biolayer Interferometry

The simultaneous binding of all three cognate antigens by IgTT-4E1 was investigated using biolayer interferometry (BLI) on an Octet RED96 system (Fortebio, Fremont, CA, USA). We immobilized 5 g/L of hEGFR-Fc onto AR2G biosensors (Fortebio) at pH 5.0 using amine-reactive coupling. Then, IgTT-4E1 in HEPES-buffered saline (HBS; 20 mM HEPES, 150 mM NaCl, pH 7.4) at 20 nM was allowed to associate with the hEGFR-Fc-coated biosensors for 20 min, after which the dissociation of the antibody from the biosensors was measured for 5 min in HBS buffer only. The biosensors were then moved into HBS containing 50 nM hPD-L1-Fc for 20 min and subsequently into HBS containing 50 nM h4-1BB-Fc for 20 min, followed by 5 min of dissociation in HBS.

2.9. Flow Cytometry

The purified antibody IgTT-4E1 or control monospecific mAbs (6.67 nM) were incubated with CHO, CHO^{EGFR}, $CHO^{PD\text{-}L1}$, 3T3, $3T3^{EGFR}$, Jurkat, or $Jurkat^{4\text{-}1BB}$ T cells (1×10^5 cells/well) for 30 min on ice. After washing, PE-conjugated $F(ab')_2$ goat anti-human (GAH) polyclonal antibody (Jackson ImmunoResearch, West Grove, PA, USA; cat# 109-116-170) was added and incubated for 30 min. Rituximab (Fritz Hoffmann-La Roche, Basel, Switzerland), urelumab (MedChemExpress, Monmouth Junction, NJ, USA; cat# HY-p99055), atezolizumab (Fritz Hoffmann-La Roche), and cetuximab (Merck KGaA, Darmstadt, Germany) (6.67 nM) were used as monospecific controls. To immunophenotype MDA-MB-231 cells and peripheral blood mononuclear cells (PBMC), the following mAbs

were used: PE-conjugated anti-EGFR (Becton Dickinson, Franklin Lakes, NJ, USA; cat# 555997), APC-conjugated anti-PD-L1 (BD, cat# 563741), FITC-conjugated anti-PD-1 (BD, cat# 557860), PE-conjugated anti-CD137 (BD, cat# 555956), PE-conjugated isotype IgG_1 (BD, cat# 554680), APC-conjugated isotype IgG_1 (BD, cat# 554681), and FITC-conjugated isotype IgG_1 (ImmunoTools; Friesoythe, Germany; cat# 21275513) and incubated for 30 min. Finally, after washing, DAPI (Sigma Aldrich, cat# D9542) was added, and the samples were analyzed with a FACSCanto II flow cytometer (Becton Dickinson).

2.10. ADCC Reporter Bioassay

The ADCC reporter bioassay (Promega, cat# G7010) was performed according to the manufacturer's instructions. Briefly, 3T3 or $3T3^{EGFR}$ cells (1.2×10^4/well) were seeded in 96-well white plates in DMEM-10% FBS and incubated overnight at 37 °C. Then, the medium was removed, and different amounts of rituximab, IgTT-4E1, or IgTT-4E1-S (final concentrations 66.7; 6.67; 0.667 nM) were added in 40 µL of RPMI-1% FBS/well. Then, $Jurkat^{NFAT\text{-}CD16}$ effector cells (7.5×10^4/well) were added to RPMI-1% FBS (40 µL/well) and incubated for 6 h at 37 °C. Finally, 80 µL/well of BioGlo Reagent (Promega) was added, and bioluminescence was measured in a Tecan Infinite F200 Fluorescence Microplate Reader (Life Sciences, St. Petersburg, FL, USA; Tecan).

2.11. PD-1/PD-L1 Blockade Bioassay

The PD-1/PD-L1 Bioassay (Promega, cat# J1250) was used following the manufacturer's instructions. Briefly, PD-L1 aAPC/CHO-K1 cells (2.5×10^4/well) were seeded in 96-well white plates in DMEM-10% FBS and incubated overnight at 37 °C. Then, the medium was removed, and different amounts of atezolizumab, cetuximab, or IgTT-4E1-S (final concentrations 66.7; 6.67; 0.667 nM) were added in RPMI-1% FBS (40 µL well). Then, $Jurkat^{NFAT\text{-}PD\text{-}1}$ cells (1.25×10^5/well) were added to RPMI-1% FBS (40 µL/well) and incubated for 6 h at 37 °C. Finally, 80 µL/well of BioGlo Reagent was added, and bioluminescence was measured in a Tecan Infinite F200 Fluorescence Microplate Reader.

2.12. Antigen-Dependent Jurkat 4-1BB Activation Assay

The 4-1BB Bioassay (Promega, cat#. J2332) was used, following the manufacturer´s instructions. Briefly, CHO, CHO^{EGFR}, or $CHO^{PD\text{-}L1}$ cells (3×10^4/well) were seeded in 96-well white plates in DMEM-10% FBS and incubated overnight at 37 °C. Then, the medium was removed, and different amounts of urelumab, rituximab, purified IgTT-4E1-S (final concentrations 66.7; 6.67; 0.667 and 0.0667 nM), or conditioned media containing IgTT-1E, IgTT-4E1-S, and IgTT-41E-S were added. Then, $Jurkat^{NFkB\text{-}4\text{-}1BB}$ cells (1.25×10^5/well) were added to RPMI-1% FBS (40 µL/well) and incubated for 6 h at 37 °C. Finally, 80 µL/well of BioGlo Reagent was added, and bioluminescence was measured in a Tecan Infinite F200 Fluorescence Microplate Reader.

2.13. IFNγ Secretion Analysis

Human peripheral blood mononuclear cells (PBMCs) were isolated from healthy donors by density gradient centrifugation (Lymphoprep, Axis–Shield, Dundee, UK; cat# AXS-1114544). All donors provided a written informed consent in accordance with the Declaration of Helsinki. PBMCs were activated overnight with 0.3 µg/mL of anti-CD3 mAb (OKT3; BD, cat#. 566685) and co-cultured with MDA-MB-231 cells (5×10^4/well) at an effector/target (E/T) ratio of 1:1 (5×10^4 cells/well) and 2:1 (1×10^5 cells/well) in the presence of 6.67 nM control polyclonal human IgG (Griffols, Barcelona, Spain), urelumab, atezolizumab, or IgTT-4E1-S for 48 h. The supernatants were collected, and IFNγ levels were analyzed by ELISA (Bionova, Fremont, CA, USA; cat# 851.560.010) following the manufacturer's instructions. The experiment was performed in triplicate.

2.14. Statistical Analysis

All graphs and statistical analyses were performed using GraphPad Prism 9.0. Most in vitro experiments were performed in triplicate, and the values are presented as mean ± SD. Significant differences (p value) were identified using one-way analysis of variance (ANOVA), adjusted by Dunnett's test for multiple comparisons, as indicated. p values are shown in the corresponding figures. Two-way ANOVA was used to analyze experiments that evaluated the interaction of two variables, such as cell type and therapy, following multiple comparison testing using either Dunnett's or Tukey's test, as appropriate.

3. Results

3.1. Generation of IgTT-4E1 and IgTT-4E1-S

In this study, we generated a trispecific 4-1BBxEGFRxPD-L1 IgTT by replacing the N-terminal scFv from IgTT-1E [24] with an anti-4-1BB agonistic scFv [13], and the C-terminal anti-EGFR V_{HH} with an anti-PD-L1 blocking V_{HH} [27] (IgTT-4E1, Figure 1a). This antibody was further modified by replacing the parental wild-type IgG_1 Fc region with an engineered Fc region containing P329G L234A/L235A (PGLALA) mutations attenuating FcγR binding [33] (IgTT-4E1-S, Figure S1a). As shown in Figure 1b,c, the middle V_{HH} (green) and the C-terminal V_{HH} (blue) were each connected to the trimerization domains by two linkers, whereas the N-terminal scFv (magenta) had a single linker, providing the binding domains with variable distances and broad areas of action around the central Fc region. Both IgTT-4E1 and IgTT-4E1-S antibodies were purified from the conditioned medium of transfected Expi293 cells by Strep-Tactin affinity chromatography and eluted as a single and an symmetrical peak with protein yields of approximately 13 mg/L. The analysis of the purified IgTT-4E1-S by SEC showed a major symmetric peak with an elution volume corresponding to an experimental molecular mass of 305 kDa, in accordance with the calculated value for the dimeric species in solution (240 kDa) (Figure S1b). A major band corresponding to the IgTT-4E1-S monomer was identified by visual inspection of the reducing SDS-PAGE analysis after SEC (Figure S1c). Both IgTT-4E1 and IgTT-4E1-S specifically recognized human 4-1BB-Fc (4-1BB), human EGFR-Fc (EGFR), and human PD-L1 Fc (PD-L1) (Figure S1d).

BLI experiments were used to investigate whether IgTT-4E1 could simultaneously bind to all three antigens. First, IgTT-4E1 was found to interact with EGFR immobilized onto biosensors. Then, the IgTT-4E1-loaded biosensors were incubated with PD-L1 and subsequently with 4-1BB, which resulted in cumulative increases in the signal (Figure 1d). The signal increases were not observed when the antigens were incubated with EGFR-coated biosensors not loaded with IgTT-4E1, demonstrating that they in fact represented complex formation with IgTT-4E1 and not non-specific interactions with EGFR or the biosensor surface. Complex formation between IgTT-4E1 and all three antigens showed that IgTT-4E1 is functionally trispecific, demonstrating a lack of steric hindrance between its three cognate interactions in this experimental context.

The ability to specifically detect antigens in a cellular context was studied by flow cytometry, using urelumab, cetuximab, and atezolizumab as binding controls, and rituximab as a negative control (Figure 1e). With Jurkat$^{4\text{-}1BB}$ cells, a specific displacement in fluorescence intensity was observed with IgTT-4E1 and urelumab compared to untransfected Jurkat cells. A specific increase in fluorescence intensity was observed upon the addition of both IgTT-4E1 and cetuximab to EGFR-positive cells (3T3^{EGFR} and CHO^{EGFR}) when compared to EGFR-negative cells (3T3 and CHO). For CHO$^{PD\text{-}L1}$ cells, a shift is shown with IgTT-4E1 and atezolizumab, with respect to CHO cells. Moreover, with IgTT-4E1 and atezolizumab, a shift was observed in both Jurkat and Jurkat$^{4\text{-}1BB}$ cells with respect to the control, due to PD-L1 expression in Jurkat cells.

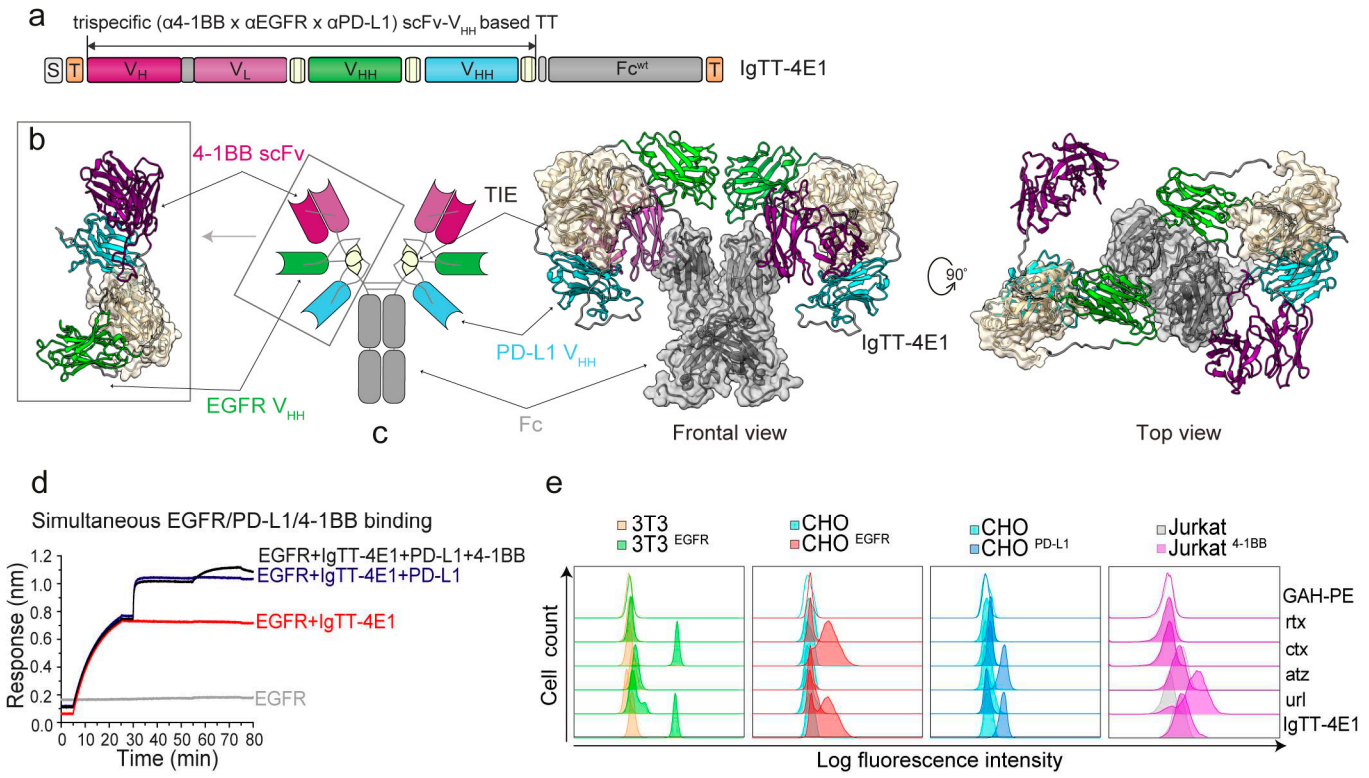

Figure 1. Gene construct, molecular model, and binding characteristics of the IgTT-4E1 antibody. (**a**) Gene layout of the IgTT-4E1 antibody bearing a signal peptide from oncostatin M (white box), one anti-4-1BB scFv (magenta boxes), one anti-EGFR V_{HH} (green box), one anti-PD-L1 V_{HH} (blue box), three collagen-derived trimerization (TIE) domains (yellow boxes) flanked by peptide linkers, and the Fc-encoding element (gray box). N-terminal FLAG-Strep and C-terminal Myc-His tags (orange boxes) were appended for purification and immunodetection purposes. (**b**) Schematic diagram showing the three-dimensional model of the anti-4-1BB/EGFR/PD-L1 tandem trimerbody (TT). (**c**) Molecular diagram of the IgTT-4E1 antibody and its three-dimensional modelizations, in front and top views. (**d**) Human EGFR-Fc (EGFR) was immobilized onto four different biosensors; three biosensors were incubated in 20 nM IgTT-4E1 for 20 min (red trace), while the fourth was kept in HBS as a negative control (gray trace). Then, 50 nM human PD-L1-Fc (PD-L1) was added to two of the IgTT-4E1-loaded biosensors (blue trace) and the control biosensor for 20 min. Also, 50 nM human 4-1BB-hFc (4-1BB) was then added to one PD-L1- and IgTT-4E1-treated biosensor (black trace) and the control biosensor. The cumulative signal increases on the biosensor receiving IgTT-4E1, PD-L1, and 4-1BB demonstrate that all three antigens can be bound by the IgTT-4E1 antibody simultaneously. (**e**) The binding to human EGFR, PD-L1, and 4-1BB on the cell surface of 3T3, $3T3^{EGFR}$, CHO, CHO^{EGFR}, $CHO^{PD\text{-}L1}$, Jurkat, and $Jurkat^{4\text{-}1BB}$ cells by rituximab (rtx), cetuximab (ctx), atezolizumab (atz), urelumab (url), and IgTT-4E1 at 6.67 nM was measured by FACS. Cells incubated with PE-conjugated GAH antibody (GAH-PE) are shown as non-filled histogram. The *y*-axis shows the relative cell number, and the *x*-axis represents the intensity of fluorescence expressed on a logarithmic scale.

3.2. Determination of Fc-Mediated Effector Functions

To measure differences in ADCC activity, Jurkat cells constitutively expressing human FcγRIIIa (CD16) on the cell surface ($Jurkat^{NFAT\text{-}CD16}$) and a luciferase reporter driven by an NFAT response element were co-cultured with $3T3^{EGFR}$ cells or with 3T3 cells as a negative control. IgTT-4E1 induced the activation of $Jurkat^{NFAT\text{-}CD16}$ cells in co-cultures with $3T3^{EGFR}$ cells, as evidenced by a significant increase in luciferase activity ($p < 0.0001$; Figure 2a), while the IgTT-4E1-S protein and rituximab (negative control) did not show an increase in luciferase activity. In the absence of EGFR-mediated interactions (co-cultures

with 3T3 cells), rituximab and both IgTT-4E1 and IgTT-4E1-S showed no induction on Jurkat^{CD16} cells.

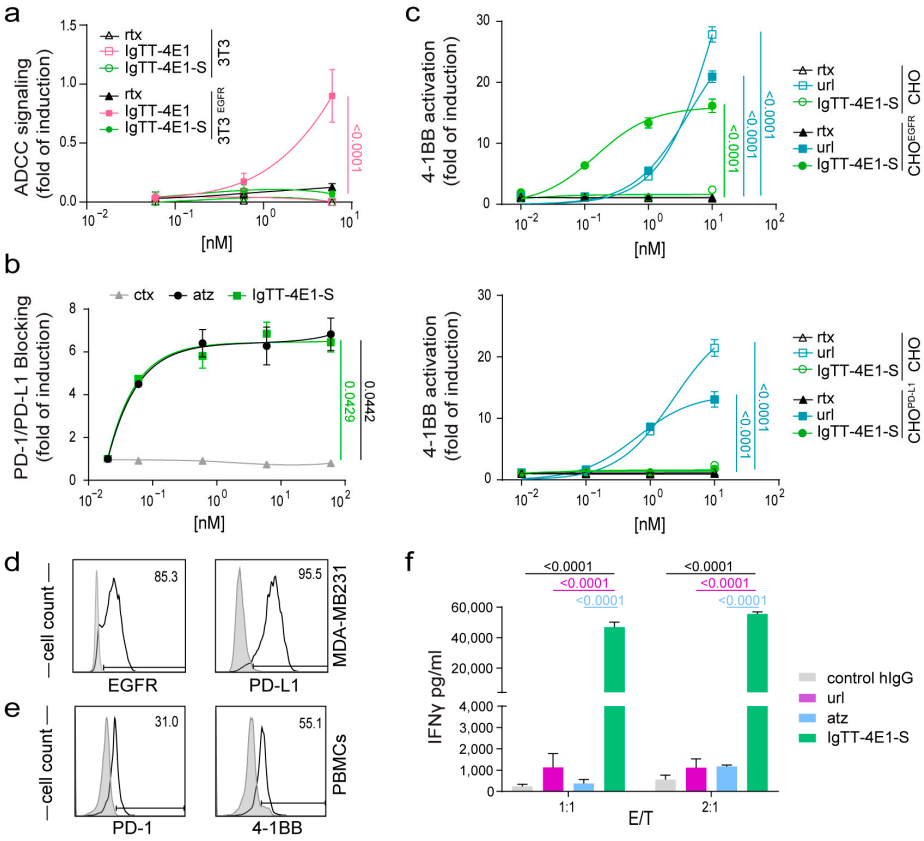

Figure 2. Effect of IgTT-4E1-S on PD-L1/PD-1 blockade, 4-1BB costimulation, and IFNγ secretion. (**a**) ADCC reporter bioassay response to rituximab (rtx), IgTT-4E1, and IgTT-4E1-S, using ADCC bioassay effector Jurkat$^{NFAT-CD16}$ cells co-cultured with 3T3 or 3T3^{EGFR} target cells at a 6:1 E/T ratio for 6 h at 37 °C. After incubation, Bio-Glo™ Luciferase Assay Reagent was added for luminescence determination. Data shown represent the mean ± standard deviation of triplicates. Data are presented as the mean ± SD (n = 3). Significance was determined by two-way ANOVA with Tukey's multiple comparison test. (**b**) PD-L1/PD-1 blockade bioassay assesses the inhibitory activities of IgTT-4E1-S. *Y*-axis represents reporter gene fold induction. Cetuximab (ctx) was used as a negative control, and atezolizumab (atz) as a positive control. Fold induction relative to negative control (ctx)-incubated cells. Results are expressed as mean ± SD (n = 3). Significance was measured by one-way ANOVA with Dunnett's multiple comparison test. (**c**) Costimulation of Jurkat$^{NFkB-4-1BB}$ cells co-cultured with CHO cells, CHO^{EGFR}, or CHO^{PD-L1} cells in the presence of 10-fold increasing concentrations of IgTT-4E1-S, urelumab (url), and rituximab (rtx) antibodies for 6 h at 37 °C. After incubation, luminescence was determined. Data are presented as fold induction relative to the values obtained from unstimulated Jurkat$^{NFkB-4-1BB}$ cells. Representative dose–concentration curves are presented and expressed as mean ± SD (n = 3). Significance was determined by two-way ANOVA with Tukey's multiple comparison test. (**d**) Flow cytometry analysis of EGFR and PD-L1 expression in MDA-MB-231 cancer cells. Cells incubated with PE-conjugated and APC-conjugated isotypes are shown as gray-filled histogram. (**e**) Flow cytometry analysis of PD-1 and 4-1BB expression in PBMCs preactivated with anti-CD3 mAb for 24 h. PBMCs incubated with FITC-conjugated and PE-conjugated isotypes are shown as gray-filled histogram. (**f**) Anti-CD3 preactivated PBMCs were co-cultured with MDA-MB231 target cells at effector/target (E/T) ratios of 1:1 and 2:1. Control human polyclonal IgG (control hIgG), urelumab (url), atezolizumab (atz), and IgTT-4E1-S were added at 6.67 nM. The IFNγ concentrations in supernatant after 48 h were analyzed and expressed as mean ± SD (n = 3). Significance was determined by two-way ANOVA with Tukey's multiple comparison test.

3.3. Effect of IgTT-4E1-S on PD-1/PD-L1 Blockade

To demonstrate the ability of IgTT-4E1-S to block PD-1/PD-L1 interactions, Jurkat cells expressing human PD-1 and a luciferase reporter driven by an NFAT response element (Jurkat$^{NFAT\text{-}PD\text{-}1}$) were co-cultured with APC/CHO-K1 cells, which express human PD-L1, and an engineered cell surface protein designed to activate cognate TCRs in an antigen-independent manner. As shown in Figure 2b, IgTT-4E1-S efficiently blocked PD-1/PD-L1 interactions, leading to a significant induction of luciferase activity in Jurkat$^{NFAT\text{-}PD\text{-}1}$ cells (p = 0.0429), similar to that observed with the PD-L1 blocking antibody atezolizumab (p = 0.0442). In contrast, no PD-1/PD-L1 blocking activity was observed in the presence of cetuximab.

3.4. Costimulatory Activity of IgTT-4E1-S

The agonist activities of IgTT-4E1-S and urelumab were assessed using Jurkat cells stably transfected with NFκB-inducible luciferase and 4-1BB (Jurkat$^{NFkB\text{-}4\text{-}1BB}$), co-cultured with target cells expressing either EGFR (CHO^{EGFR}) or PD-L1 (CHO$^{PD\text{-}L1}$), and untransfected CHO cells as a negative control. In the absence of EGFR- or PD-L1-mediated cross-linking at the target cell surface (CHO cells), IgTT-4E1-S showed no induction in untreated Jurkat$^{NFkB\text{-}4\text{-}1BB}$ cells at all tested concentrations, whereas urelumab showed an approximately 25-fold induction (EC_{50} = 0.3115 nM, Figure 2c). In the presence of EGFR-mediated cross-linking (i.e., using CHO^{EGFR} as target cells), IgTT-4E1-S induced an NFκB dose-dependent activation with a 15-fold induction ($p < 0.0001$). Effective costimulation was achieved at concentrations that were an order of magnitude lower than those of urelumab (EC_{50} = 0.02635 nM) (Figure 2c). In contrast, in co-cultures with PD-L1-positive cells (CHO$^{PD\text{-}L1}$), IgTT-4E1-S showed no induction of luciferase at any concentration tested (Figure 2d). The negative control rituximab showed no activation (Figure 2c,d).

Thus, IgTT-4E1-S demonstrated potent and conditional costimulation that was dependent on EGFR but not on PD-L1 expression. To further investigate this issue, we generated an additional IgTT silent molecule with the order of the V_{HH} domains reversed (Figure S1a). This construct (IgTT-41E-S) was also efficiently secreted, and Western blot analysis under reducing conditions showed a migration pattern consistent with the molecular weight calculated from their amino acid sequence (Figure S2a). ELISA analysis demonstrated that IgTT-41E-S specifically recognized 4-1BB, EGFR, and PD-L1 (Figure S2b). In the presence of PD-L1-expressing cells, IgTT-41E-S also showed no induction of luciferase in Jurkat$^{NFkB\text{-}4\text{-}1BB}$ cells. However, in the presence of EGFR cells, IgTT-41E-S showed a fold induction similar to that observed with IgTT-4E1-S (Figure S2c). These results show that EGFR but not PD-L1 enabled cross-linking-mediated 4-1BB signaling with two different configurations of the PD-L1- and EGFR-binding V_{HHs}, indicating that the issue did not arise from steric hindrance of the PD-L1-binding domain.

3.5. IgTT-4E1-S Enhances the Activation of Primary Human T Cells

The triple-negative breast cancer MDA-MB-231 cells expressing both EGFR and PD-L1 (Figure 2d) were co-cultured for 48 h at two different effector/target ratios (1:1 and 2:1) with anti-CD3-prestimulated PBMCs expressing PD-1 and 4-1BB (Figure 2e). The agonistic anti-4-1BB mAb (urelumab) and anti-PD-L1 blocking mAb (atezolizumab) had a modest effect on IFNγ production (Figure 2f). In contrast, the IgTT-4E1-S antibody strongly enhanced IFNγ secretion levels, which were significantly higher ($p < 0.0001$) than those observed in the single-treated co-cultures (Figure 2f).

4. Discussion

The design of multi-specific antibodies against a combination of immunomodulatory targets is a promising approach to enhance the clinical benefit of conventional checkpoint blockers. Here, we generated a trispecific IgG-like antibody by fusing an anti-4-1BB x anti-EGFR x anti-PD-L1 TT with an engineered Fc silent region to abrogate FcγR binding. This molecule was based on the previously described IgTT platform, which is a fusion of a

mono- or multispecific TT with an Fc region to generate a hexavalent IgG-like antibody capable of bivalently recognizing up to three different antigens [24]. The binding domains of IgTT-4E1 are positioned around the human collagen homodimerization domain, and BLI studies showed that IgTT-4E1 could bind all three antigens simultaneously in solution. Furthermore, IgTT-4E1 was able to recognize the antigens in a cellular context. These results suggest that the binding domains are predominantly sterically unhindered and available for antigen binding.

Anti-4-1BB agonistic mAbs can be classified as either strong or weak agonists. Here, we confirmed in a 4-1BB-reporting cell line that urelumab, a strong agonist, could induce signaling activation without FcγR-mediated cross-linking. The anti-4-1BB antibody used to generate IgTT-4E1-S is a weak agonist [13], and therefore 4-1BB signaling was only induced with additional cross-linking. IgTT-4E1-S exhibited conditional 4-1BB agonist activity dependent on the cross-linking with EGFR but not with PD-L1. This finding was independent of the position of the anti-EGFR and anti-PD-L1 V_{HH} domains in the TT, suggesting that the agonist activity was not influenced by steric hindrance issues. These results are not consistent with those published for other anti-4-1BB × anti-PD-L1 antibodies [19–22,34,35], where conditional 4-1BB agonist activity dependent on PD-L1 cross-linking was reported. These differences in the ability of IgTT to induce 4-1BB-mediated costimulation may be related to structural determinants or to the epitopes recognized by the binding domains. The anti-4-1BB antibody binds to the N-terminal CRD1 domain [36]; anti-EGFR V_{HH} binds in the cleft formed between domains II and III [37], while the epitope recognized by anti-PD-L1 V_{HH} has not been characterized. In the IgTT molecule, each TT is trispecific, and the three binding domains are very close and spatially restricted, which may limit the potential for the simultaneous recognition of distally located epitopes and epitopes more proximal to the membrane [38], as might occur with 4-1BB (86 kDa) and PD-L1 (30 kDa) interactions. This would probably not be a limitation with conventional bispecific antibodies, where each arm recognizes a different antigen, and the area of influence is significantly greater. In the context of simultaneous interactions between 4-1BB and EGFR (134 kDa) mediated by IgTT-4E1-S, available structural data suggest that the epitopes may be in closer proximity to each other. The ability to block the PD-L1/PD-1 interaction in a CHO cell system was similar to that obtained with atezolizumab. This was also previously observed with a dimeric version of the same anti-PD-L1 V_{HH} by using an ELISA-type blocking assay [27]. Simultaneous targeting of PD-L1 and EGFR by bispecific antibodies promotes PD-L1 blockade selectively in the TME due to EGFR overexpression in malignant cells, while reducing potential off-tumor binding to normal PD-L1-expressing cells [35]. In addition, EGFR overexpression and activation enhances PD-L1 expression by tumor cells [39]. IgTT-4E1-S enhanced the activation and effector functions of human primary T cells co-cultured with $EGFR^+/PD\text{-}L1^+$ cancer cells. However, to determine the ability of IgTT-4E1-S to restrict 4-1BB costimulation to EGFR-expressing tumors while minimizing off-target costimulation, further studies are required in cancer cell lines expressing different levels of EGFR and PD-L1, as well as in humanized mouse models carrying patient-derived xenografts. In addition, IgTT-4E1-S carries a silenced Fc domain to avoid or minimize anti-4–1BB-induced hepatic damage, which is partly explained by Fc-FcγRs interactions [6–8], but studies in non-human primates are warranted to further explore its toxicity profile.

In summary, here we described the generation of IgTT-4E1-S, the first IgG-like trispecific antibody designed to provide EGFR-conditional 4-1BB stimulation to antigen-experienced T cells while constitutively blocking the PD-1/PD-L1 inhibitory axis. This apparent asymmetry between conditional 4-1BB agonism and PD-L1 blockade may be relevant when comparing our antibody to other bispecific antibodies already on the market [17,20,22,35], but further studies are needed to determine the efficacy and safety of the IgTT-4E1-S antibody.

Supplementary Materials: The following supporting information can be downloaded at: https://www.mdpi.com/article/10.3390/antib13020034/s1, Figure S1: Gene constructs and structural characterization of the IgTT-4E1-S antibody; Figure S2: Characterization of the IgTT-41E-S antibody; Table S1: Oligonucleotides used in this study.

Author Contributions: Conception and design of the study: L.Á.-V.; sample acquisition of the data: L.R.-P., S.F., R.N., S.L.H., M.G.-R., O.H., N.S.-P., L.V. and C.S.; analysis and interpretation of the data: L.R.-P., S.F., R.N., S.L.H. and M.C.; investigation: L.R.-P., S.F., R.N. and S.L.H.; writing—original draft preparation, L.R.-P. and R.L.-G.; writing—review and editing: all authors; visualization: L.Á.-V.; supervision: L.Á.-V.; project administration: L.Á.-V.; funding acquisition: C.S. and L.Á.-V. All authors have read and agreed to the published version of the manuscript.

Funding: L.Á.-V. was supported by grants from the MCIN/AEI/10.13039/501100011033 (PID2020-117323RB-100 and PDC2021-121711-100), the Instituto de Salud Carlos III (DTS20/00089), the Comunidad de Madrid (S2022/BMD-7225 Next Generation CART MAD), the CRIS Cancer Foundation (FCRIS-2021-0090), the Spanish Association Against Cancer (PROYE19084ALVA and PRYGN234844ALVA), the Fundación "La Caixa" (HR21-00761 project IL7R_LungCan), and the Fundación de Investigación Biomédica 12 de Octubre Programa Investiga (2022-0082). L.R.-P. was supported by a predoctoral fellowship from the Immunology Chair, Universidad Francisco de Vitoria/Merck. O.H. was supported by an industrial PhD fellowship from the Comunidad de Madrid (IND2020/BMD-17668). C.S. was supported by the Instituto de Salud Carlos III (PI20/00415) and the Gobierno de Navarra, Departamento de Salud, GN21-2022.

Institutional Review Board Statement: Not applicable.

Informed Consent Statement: Informed consent was obtained from all subjects involved in the study.

Data Availability Statement: The datasets used and/or analyzed during the current study are available from the corresponding author [L.Á.-V.] on reasonable request.

Conflicts of Interest: M.C., R.N., S.F., and O.H. are all employees of Leadartis. L.Á.-V. is a co-founder of Leadartis. The authors declare no conflicts of interest.

References

1. Sharma, P.; Goswami, S.; Raychaudhuri, D.; Siddiqui, B.A.; Singh, P.; Nagarajan, A.; Liu, J.; Subudhi, S.K.; Poon, C.; Gant, K.L.; et al. Immune checkpoint therapy-current perspectives and future directions. *Cell* **2023**, *186*, 1652–1669. [CrossRef]
2. Wei, S.C.; Duffy, C.R.; Allison, J.P. Fundamental Mechanisms of Immune Checkpoint Blockade Therapy. *Cancer Discov.* **2018**, *8*, 1069–1086. [CrossRef]
3. Sharpe, A.H.; Pauken, K.E. The diverse functions of the PD1 inhibitory pathway. *Nat. Rev. Immunol.* **2018**, *18*, 153–167. [CrossRef] [PubMed]
4. Antibody Therapeutics Approved or in Regulatory Review in the EU or US. The Antibody Society. Available online: https://www.antibodysociety.org/resources/approved-antibodies/ (accessed on 10 January 2024).
5. Chester, C.; Sanmamed, M.F.; Wang, J.; Melero, I. Immunotherapy targeting 4-1BB: Mechanistic rationale, clinical results, and future strategies. *Blood* **2018**, *131*, 49–57. [CrossRef]
6. Melero, I.; Shuford, W.W.; Newby, S.A.; Aruffo, A.; Ledbetter, J.A.; Hellström, K.E.; Mittler, R.S.; Chen, L. Monoclonal antibodies against the 4-1BB T-cell activation molecule eradicate established tumors. *Nat. Med.* **1997**, *3*, 682–685. [CrossRef] [PubMed]
7. Li, F.; Ravetch, J.V. Antitumor activities of agonistic anti-TNFR antibodies require differential FcγRIIB coengagement in vivo. *Proc. Natl. Acad. Sci. USA* **2013**, *110*, 19501–19506. [CrossRef]
8. Compte, M.; Harwood, S.L.; Muñoz, I.G.; Navarro, R.; Zonca, M.; Perez-Chacon, G.; Erce-Llamazares, A.; Merino, N.; Tapia-Galisteo, A.; Cuesta, A.M.; et al. A tumor-targeted trimeric 4-1BB-agonistic antibody induces potent anti-tumor immunity without systemic toxicity. *Nat. Commun.* **2018**, *9*, 4809. [CrossRef] [PubMed]
9. Claus, C.; Ferrara, C.; Xu, W.; Sam, J.; Lang, S.; Uhlenbrock, F.; Albrecht, R.; Herter, S.; Schlenker, R.; Hüsser, T.; et al. Tumor-targeted 4-1BB agonists for combination with T cell bispecific antibodies as off-the-shelf therapy. *Sci. Transl. Med.* **2019**, *11*, eaav5989. [CrossRef]
10. Hinner, M.J.; Aiba, R.S.B.; Jaquin, T.J.; Berger, S.; Dürr, M.C.; Schlosser, C.; Allersdorfer, A.; Wiedenmann, A.; Matschiner, G.; Schüler, J.; et al. Tumor-Localized Costimulatory T-Cell Engagement by the 4-1BB/HER2 Bispecific Antibody-Anticalin Fusion PRS-343. *Clin. Cancer Res.* **2019**, *25*, 5878–5889. [CrossRef]
11. Compte, M.; Harwood, S.L.; Martínez-Torrecuadrada, J.; Perez-Chacon, G.; González-García, P.; Tapia-Galisteo, A.; Van Bergen En Henegouwen, P.M.P.; Sánchez, A.; Fabregat, I.; Sanz, L.; et al. Case Report: An EGFR-Targeted 4-1BB-agonistic Trimerbody Does Not Induce Hepatotoxicity in Transgenic Mice With Liver Expression of Human EGFR. *Front. Immunol.* **2020**, *11*, 614363. [CrossRef]
12. Hangiu, O.; Compte, M.; Dinesen, A.; Navarro, R.; Tapia-Galisteo, A.; Mandrup, O.A.; Erce-Llamazares, A.; Lázaro-Gorines, R.; Nehme-Álvarez, D.; Domínguez-Alonso, C.; et al. Tumor targeted 4-1BB agonist antibody-albumin fusions with high affinity to FcRn induce anti-tumor immunity without toxicity. *iScience* **2022**, *25*, 104958. [CrossRef]

13. Compte, M.; Harwood, S.L.; Erce-Llamazares, A.; Tapia-Galisteo, A.; Romero, E.; Ferrer, I.; Garrido-Martin, E.M.; Enguita, A.B.; Ochoa, M.C.; Blanco, B.; et al. An Fc-free EGFR-specific 4-1BB-agonistic Trimerbody Displays Broad Antitumor Activity in Humanized Murine Cancer Models without Toxicity. *Clin. Cancer Res.* **2021**, *27*, 3167–3177. [CrossRef]
14. Mikkelsen, K.; Harwood, S.L.; Compte, M.; Merino, N.; Mølgaard, K.; Lykkemark, S.; Alvarez-Mendez, A.; Blanco, F.J.; Álvarez-Vallina, L. Carcinoembryonic Antigen (CEA)-Specific 4-1BB-Costimulation Induced by CEA-Targeted 4-1BB-Agonistic Trimerbodies. *Front. Immunol.* **2019**, *10*, 1791. [CrossRef]
15. Shen, A.; Liu, W.; Wang, H.; Zeng, X.; Wang, M.; Zhang, D.; Zhao, Q.; Fang, Q.; Wang, F.; Cheng, L.; et al. A novel 4-1BB/HER2 bispecific antibody shows potent antitumor activities by increasing and activating tumor-infiltrating T cells. *Am. J. Cancer Res.* **2023**, *13*, 3246–3256.
16. Tapia-Galisteo, A.; Compte, M.; Álvarez-Vallina, L.; Sanz, L. When three is not a crowd: Trispecific antibodies for enhanced cancer immunotherapy. *Theranostics* **2023**, *13*, 1028–1041. [CrossRef]
17. Geuijen, C.; Tacken, P.; Wang, L.-C.; Klooster, R.; van Loo, P.F.; Zhou, J.; Mondal, A.; Liu, Y.; Kramer, A.; Condamine, T.; et al. A human CD137×PD-L1 bispecific antibody promotes anti-tumor immunity via context-dependent T cell costimulation and checkpoint blockade. *Nat. Commun.* **2021**, *12*, 4445. [CrossRef]
18. Cheng, L.-S.; Zhu, M.; Gao, Y.; Liu, W.-T.; Yin, W.; Zhou, P.; Zhu, Z.; Niu, L.; Zeng, X.; Zhang, D.; et al. An Fc-muted bispecific antibody targeting PD-L1 and 4-1BB induces antitumor immune activity in colorectal cancer without systemic toxicity. *Cell Mol. Biol. Lett.* **2023**, *28*, 47. [CrossRef]
19. Jeong, S.; Park, E.; Kim, H.-D.; Sung, E.; Kim, H.; Jeon, J.; Kim, Y.; Jung, U.; Son, Y.-G.; Hong, Y.; et al. Novel anti-4-1BB×PD-L1 bispecific antibody augments anti-tumor immunity through tumor-directed T-cell activation and checkpoint blockade. *J. Immunother. Cancer* **2021**, *9*, e002428. [CrossRef]
20. Peper-Gabriel, J.K.; Pavlidou, M.; Pattarini, L.; Morales-Kastresana, A.; Jaquin, T.J.; Gallou, C.; Hansbauer, E.-M.; Richter, M.; Lelievre, H.; Scholer-Dahirel, A.; et al. The PD-L1/4-1BB Bispecific Antibody-Anticalin Fusion Protein PRS-344/S095012 Elicits Strong T-Cell Stimulation in a Tumor-Localized Manner. *Clin. Cancer Res.* **2022**, *28*, 3387–3399. [CrossRef] [PubMed]
21. Muik, A.; Altintas, I.; Gieseke, F.; Schoedel, K.B.; Burm, S.M.; Toker, A.; Salcedo, T.W.; Verzijl, D.; Eisel, D.; Grunwitz, C.; et al. An Fc-inert PD-L1×4-1BB bispecific antibody mediates potent anti-tumor immunity in mice by combining checkpoint inhibition and conditional 4-1BB co-stimulation. *Oncoimmunology* **2022**, *11*, 2030135. [CrossRef] [PubMed]
22. Muik, A.; Garralda, E.; Altintas, I.; Gieseke, F.; Geva, R.; Ben-Ami, E.; Maurice-Dror, C.; Calvo, E.; LoRusso, P.M.; Alonso, G.; et al. Preclinical Characterization and Phase I Trial Results of a Bispecific Antibody Targeting PD-L1 and 4-1BB (GEN1046) in Patients with Advanced Refractory Solid Tumors. *Cancer Discov.* **2022**, *12*, 1248–1265. [CrossRef]
23. Alvarez-Cienfuegos, A.; Nuñez-Prado, N.; Compte, M.; Cuesta, A.M.; Blanco-Toribio, A.; Harwood, S.L.; Villate, M.; Merino, N.; Bonet, J.; Navarro, R.; et al. Intramolecular trimerization, a novel strategy for making multispecific antibodies with controlled orientation of the antigen binding domains. *Sci. Rep.* **2016**, *6*, 28643. [CrossRef]
24. Rubio-Pérez, L.; Lázaro-Gorines, R.; Harwood, S.L.; Compte, M.; Navarro, R.; Tapia-Galisteo, A.; Bonet, J.; Blanco, B.; Lykkemark, S.; Ramírez-Fernández, Á.; et al. A PD-L1/EGFR bispecific antibody combines immune checkpoint blockade and direct anti-cancer action for an enhanced anti-tumor response. *Oncoimmunology* **2023**, *12*, 2205336. [CrossRef]
25. Delidakis, G.; Kim, J.E.; George, K.; Georgiou, G. Improving Antibody Therapeutics by Manipulating the Fc Domain: Immunological and Structural Considerations. *Annu. Rev. Biomed. Eng.* **2022**, *24*, 249–274. [CrossRef]
26. Roskoski, R. The ErbB/HER family of protein-tyrosine kinases and cancer. *Pharmacol. Res.* **2014**, *79*, 34–74. [CrossRef]
27. Silva-Pilipich, N.; Blanco, E.; Lozano, T.; Martisova, E.; Igea, A.; Herrador-Cañete, G.; Ballesteros-Briones, M.C.; Gorraiz, M.; Sarrión, P.; González-Sapienza, G.; et al. Local delivery of optimized nanobodies targeting the PD-1/PD-L1 axis with a self-amplifying RNA viral vector induces potent antitumor responses. *Cancer Lett.* **2023**, *561*, 216139. [CrossRef]
28. Šali, A.; Blundell, T.L. Comparative protein modelling by satisfaction of spatial restraints. *J. Mol. Biol.* **1993**, *234*, 779–815. [CrossRef]
29. Saphire, E.O.; Parren, P.W.; Pantophlet, R.; Zwick, M.B.; Morris, G.M.; Rudd, P.M.; Dwek, R.A.; Stanfield, R.L.; Burton, D.R.; Wilson, I.A. Crystal structure of a neutralizing human IGG against HIV-1: A template for vaccine design. *Science* **2001**, *293*, 1155–1159. [CrossRef]
30. Berman, H.M.; Westbrook, J.; Feng, Z.; Gilliland, G.; Bhat, T.N.; Weissig, H.; Shindyalov, I.N.; Bourne, P.E. The Protein Data Bank. *Nucleic Acids Res.* **2000**, *28*, 235–242. [CrossRef]
31. Altschul, S.F.; Gish, W.; Miller, W.; Myers, E.W.; Lipman, D.J. Basic local alignment search tool. *J. Mol. Biol.* **1990**, *215*, 403–410. [CrossRef]
32. Liu, S.; Miersch, S.; Li, P.; Bai, B.; Liu, C.; Qin, W.; Su, J.; Huang, H.; Pan, J.; Sidhu, S.S.; et al. A Synthetic Human Antibody Antagonizes IL-18Rβ Signaling Through an Allosteric Mechanism. *J. Mol. Biol.* **2020**, *432*, 1169–1182. [CrossRef] [PubMed]
33. Lo, M.; Kim, H.S.; Tong, R.K.; Bainbridge, T.W.; Vernes, J.-M.; Zhang, Y.; Lin, Y.L.; Chung, S.; Dennis, M.S.; Zuchero, Y.J.Y.; et al. Effector-attenuating Substitutions That Maintain Antibody Stability and Reduce Toxicity in Mice. *J. Biol. Chem.* **2017**, *292*, 3900–3908. [CrossRef] [PubMed]
34. Zhai, T.; Wang, C.; Xu, Y.; Huang, W.; Yuan, Z.; Wang, T.; Dai, S.; Peng, S.; Pang, T.; Jiang, W.; et al. Generation of a safe and efficacious llama single-domain antibody fragment (vHH) targeting the membrane-proximal region of 4-1BB for engineering therapeutic bispecific antibodies for cancer. *J. Immunother. Cancer* **2021**, *9*, e002131. [CrossRef] [PubMed]

35. Warmuth, S.; Gunde, T.; Snell, D.; Brock, M.; Weinert, C.; Simonin, A.; Hess, C.; Tietz, J.; Johansson, M.; Spiga, F.M.; et al. Engineering of a trispecific tumor-targeted immunotherapy incorporating 4-1BB co-stimulation and PD-L1 blockade. *Oncoimmunology* **2021**, *10*, 2004661. [CrossRef]
36. Bitra, A.; Doukov, T.; Croft, M.; Zajonc, D.M. Crystal structures of the human 4-1BB receptor bound to its ligand 4-1BBL reveal covalent receptor dimerization as a potential signaling amplifier. *J. Biol. Chem.* **2018**, *293*, 9958–9969. [CrossRef] [PubMed]
37. Schmitz, K.R.; Bagchi, A.; Roovers, R.C.; van Bergen en Henegouwen, P.M.P.; Ferguson, K.M. Structural evaluation of EGFR inhibition mechanisms for nanobodies/VHH domains. *Structure* **2013**, *21*, 1214–1224. [CrossRef] [PubMed]
38. Bluemel, C.; Hausmann, S.; Fluhr, P.; Sriskandarajah, M.; Stallcup, W.B.; Baeuerle, P.A.; Kufer, P. Epitope distance to the target cell membrane and antigen size determine the potency of T cell-mediated lysis by BiTE antibodies specific for a large melanoma surface antigen. *Cancer Immunol. Immunother.* **2010**, *59*, 1197–1209. [CrossRef]
39. Zhang, W.; Pang, Q.; Yan, C.; Wang, Q.; Yang, J.; Yu, S.; Liu, X.; Yuan, Z.; Wang, P.; Xiao, Z. Induction of PD-L1 expression by epidermal growth factor receptor-mediated signaling in esophageal squamous cell carcinoma. *Onco. Targets Ther.* **2017**, *10*, 763–771. [CrossRef]

Supplementary materials

Characterization of a Trispecific PD-L1 Blocking Antibody That Exhibits EGFR-Conditional 4-1BB Agonist Activity

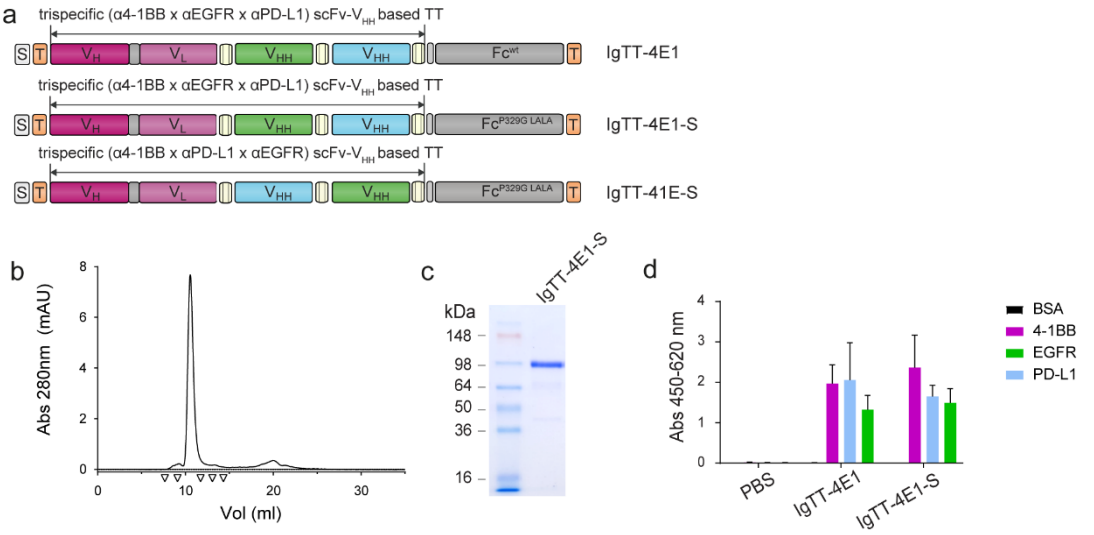

Figure S1. Gene constructs and structural characterization of IgTT-4E1-S antibody. (a) Gene layout of the IgTT-4E1, IgTT-4E1-S and IgTT-41E-S bearing a signal peptide from oncostatin M (white box), one anti-4-1BB scFv (magenta boxes), one anti-EGFR VHH (green box), one anti-PD-L1 VHH (blue box), three collagen-derived trimerization (TIE) domains (yellow boxes) flanked by peptide linkers and the Fc encoding element (gray boxes). N-terminal FLAG-Strep and C-terminal Myc-His tags (orange boxes) were appended for purification and immunodetection purposes. **(b)** SEC analysis of IgTT-4E1-S molecules in Superdex 200 Increase 10/300 GL column. Experiments were performed once after calibrating the column using a Gel Filtration HMW Calibration Kit from Cytiva. ▽ Corresponds to the elution volumes of the well-defined protein standards used for calibrating, from left to right: thyroglobulin (8.73ml), ferritin (9.89 ml), aldolase (12.11 ml), conalbumin (13.59 ml) and ovalbumin (14.60 ml). **(c)** Reducing SDS-PAGE analysis of the central fraction of the major peak from SEC experiment. **(d)** ELISA analysis where both purified protein IgTT-4E1 and IgTT-4E1-S specifically recognized human 4-1BB-Fc (4-1BB), human EGFR-Fc (EGFR) and human PD-L1- Fc (PD-L1) followed by anti-FLAG-HRP detection.

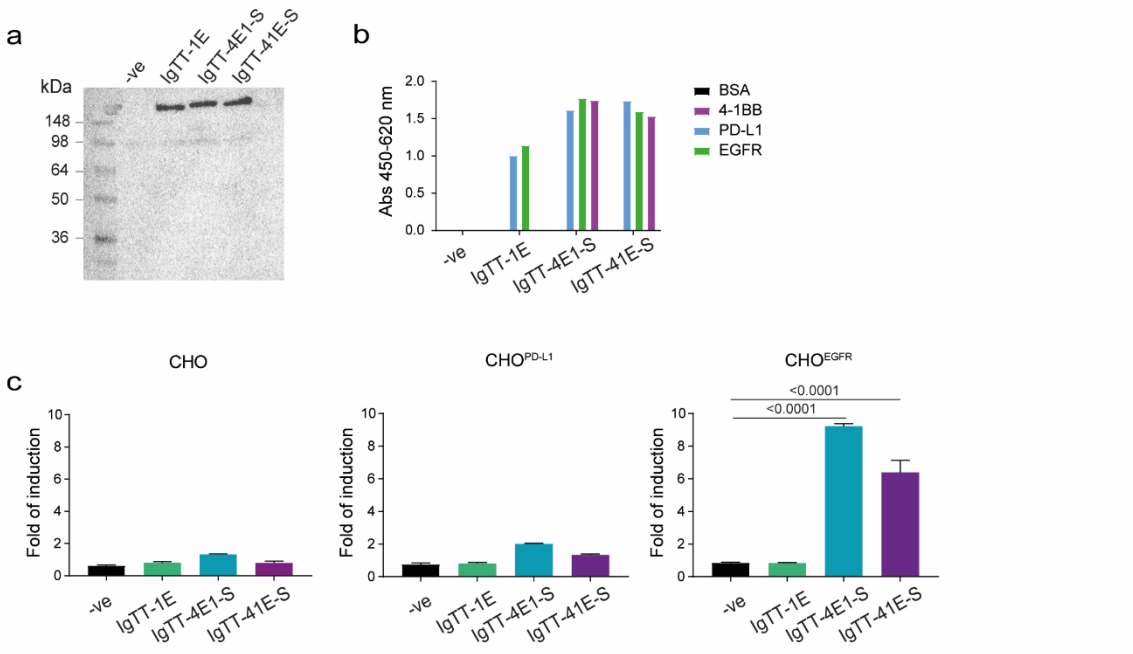

Figure S2. Characterization of IgTT-41E-S antibody. (a) Conditioned media (0.1% FBS) from negative control (vehicle), IgTT-1E, IgTT-4E1-S and IgTT-41E-S were analyzed by Western blot and probed with mouse anti-FLAG IgG1, followed by incubation with GAM-HRP. Three proteins were efficiently secreted by Expi293 cells and exhibited a migration pattern consistent with the molecular weight calculated from the amino acid sequences. **(b)** ELISA analysis where three purified proteins specifically recognized ELISA analysis where both purified protein IgTT-4E1 and IgTT-4E1-S specifically recognized human 4-1BB-Fc (4-1BB), human EGFR-Fc (EGFR) and human PD-L1- Fc (PD-L1) followed by anti-FLAG-HRP detection. **(c)** T cell co-stimulation of Jurkat$^{NFkB\text{-}4\text{-}1BB}$ cells co-cultured with CHO cells, CHO^{EGFR} or CHO$^{PD\text{-}L1}$ cells in the presence of conditioned media of negative control (vehicle), IgTT-1E, IgTT-4E1-S and IgTT-41E-S, and after 6 hours at 37 °C luminescence determined. Data were presented as fold induction relative to the values obtained from unstimulated Jurkat$^{NFkB\text{-}4\text{-}1BB}$ cells. Results are expressed as mean ± SD (n = 3). Significance was measured by one-way ANOVA with Dunnett's multiple comparison test.

Table S1. Oligonucleotides used in this study

Name	**Sequence (5′-3′)**
FwCMV	CGCAAATGGGCGGTAGGCGTG
RvBGH	TAGAAGGCACAGTCGAGG

Oligonucleotides were synthesized by Thermo Scientific.

ARTÍCULO III: ***Dendritic cell-mediated cross-priming by a bispecific neutralizing antibody boosts cytotoxic T cell responses and protects mice against SARS-CoV-2.***

Rodrigo Lázaro-Gorines, Patricia Pérez, Ignacio Heras-Murillo, Irene Adán-Barrientos, Guillermo Alberici o, David Astorgano, Sara Flores, Joanna Luczkowiak, Nuria Labiod, Seandean L. Harwood, Alejandro Segura-Tudela, Laura Rubio-Pérez, Yudhi Nugraha, Xiaoran Shang, Yuxing Li, Carlos Alfonso, Kaylin A. Adipietro, Dinendra L. Abeyawardhane, Rocío Navarro, Marta Compte, Wenbo Yu, Alexander D. MacKerell Jr, Laura Sanz, David J. Weber, Francisco J. Blanco, Mariano Esteban, Edwin Pozharski, Raquel Godoy-Ruiz, Inés G. Muñoz, Rafael Delgado, David Sancho, Juan García-Arriaza, and Luis Álvarez-Vallina

Adv. Sci., 2023, 10, 2304818

DOI: 10.1002/advs.202304818

Introducción:

Numerosas estrategias basadas en los anticuerpos neutralizantes han demostrado eficacia para proporcionar protección inmediata contra el virus SARS-CoV-2. Sin embargo, la aparición de múltiples variantes del virus provoca evasión inmune y exige el desarrollo de terapias más efectivas, ya que las mutaciones en la región RBD evitan el reconocimiento y la neutralización mediada por anticuerpos. En este trabajo se ha desarrollado una estrategia dual que combina la neutralización del virus y el *cross-priming* de células dendríticas para inducir estimulación inmune y potenciar respuestas específicas de células T citotóxicas.

Objetivos:

1. Diseño y generación de vectores de expresión que codifican para los *trimerbodies* TN^T y TN^TDNGR1.
2. Expresión de los anticuerpos recombinantes en células de mamífero, purificación y caracterización estructural y funcional.
3. Evaluación *in vitro* de la capacidad del anticuerpo TN^TDNGR1 de dirigir al virus hacia las células dendríticas y promover su internalización.
4. Evaluación *in vivo* de la capacidad del anticuerpo TN^TDNGR1 para proteger contra la infección letal del SARS-CoV-2 en ratones transgénicos K18-hACE2.

Conclusiones:

1. Los anticuerpos recombinantes TN^T y TN^TDNGR1 se secretaron eficientemente por células humanas y se purificaron mediante cromatografía de afinidad. Las fracciones presentaban un alto grado de pureza y el tamaño esperado mediante electroforesis en geles SDS-PAGE en condiciones reductoras.
2. Ambos anticuerpos purificados son funcionales, ya que se unen específicamente a su antígeno diana y bloquean la interacción con hACE2, interaccionando simultáneamente con tres dominios RBDs de la proteína S gracias a su estructura trimérica. Esto permite mejorar la neutralización del SARS-CoV-2.
3. El anticuerpo TN^TDNGR1 moviliza el virus hacia las células dendríticas y promueve su internalización.
4. El anticuerpo TN^TDNGR1 demostró una potente actividad *in vivo* en ratones transgénicos K18-hACE2 sometidos a una infección letal por el SARS-CoV-2, potenciando respuestas específicas tanto humorales como de células T $CD8^+$.

Publicación:

ADVANCED SCIENCE Open Access
www.advancedscience.com

Dendritic Cell-Mediated Cross-Priming by a Bispecific Neutralizing Antibody Boosts Cytotoxic T Cell Responses and Protects Mice against SARS-CoV-2

*Rodrigo Lázaro-Gorines, Patricia Pérez, Ignacio Heras-Murillo, Irene Adán-Barrientos, Guillermo Albericio, David Astorgano, Sara Flores, Joanna Luczkowiak, Nuria Labiod, Seandean L. Harwood, Alejandro Segura-Tudela, Laura Rubio-Pérez, Yudhi Nugraha, Xiaoran Shang, Yuxing Li, Carlos Alfonso, Kaylin A. Adipietro, Dinendra L. Abeyawardhane, Rocío Navarro, Marta Compte, Wenbo Yu, Alexander D. MacKerell Jr, Laura Sanz, David J. Weber, Francisco J. Blanco, Mariano Esteban, Edwin Pozharski, Raquel Godoy-Ruiz, Inés G. Muñoz, Rafael Delgado, David Sancho, Juan García-Arriaza, and Luis Álvarez-Vallina**

Administration of neutralizing antibodies (nAbs) has proved to be effective by providing immediate protection against SARS-CoV-2. However, dual strategies combining virus neutralization and immune response stimulation to enhance specific cytotoxic T cell responses, such as dendritic cell (DC) cross-priming, represent a promising field but have not yet been explored. Here, a broadly nAb, TN^{T}, are first generated by grafting an anti-RBD biparatopic tandem nanobody onto a trimerbody scaffold. Cryo-EM data show that the TN^{T} structure allows simultaneous binding to all six RBD epitopes, demonstrating a high-avidity neutralizing interaction. Then, by C-terminal fusion of an anti-DNGR-1 scFv to TN^{T}, the bispecific trimerbody TN^{T}DNGR-1 is generated to target neutralized virions to type 1 conventional DCs (cDC1s) and promote T cell cross-priming. Therapeutic administration of TN^{T}DNGR-1, but not TN^{T}, protects K18-hACE2 mice from a lethal SARS-CoV-2 infection, boosting virus-specific humoral responses and CD8^{+} T cell responses. These results further strengthen the central role of interactions with immune cells in the virus-neutralizing antibody activity and demonstrate the therapeutic potential of the Fc-free strategy that can be used advantageously to provide both immediate and long-term protection against SARS-CoV-2 and other viral infections.

1. Introduction

Coronavirus disease 2019 (COVID-19), caused by severe acute respiratory syndrome coronavirus 2 (SARS-CoV-2), has given rise to one of the worst pandemics in recent history. As July 2023, the virus has infected more than 767 million individuals, causing over 6.9 million deaths (https://covid19.who.int/). Although multiple effective vaccines preventing COVID-19 are being widely administered worldwide,[1–3] the emergence of multiple SARS-CoV-2 variants causing increased viral dispersion and immune evasion requires the continual development of effective therapeutics against COVID-19.[4–6] In this context, monoclonal antibodies (mAb) have shown efficacy in animal models of SARS-CoV-2 infection[7–9] and several mAb-based therapeutics received Emergency Use Authorization.[10–12]

SARS-CoV-2 infection requires the spike (S) protein receptor-binding domain

The ORCID identification number(s) for the author(s) of this article can be found under https://doi.org/10.1002/advs.202304818

DOI: 10.1002/advs.202304818

R. Lázaro-Gorines, A. Segura-Tudela, L. Rubio-Pérez, L. Álvarez-Vallina
Cancer Immunotherapy Unit (UNICA)
Department of Immunology
Hospital Universitario 12 de Octubre
Madrid 28041, Spain
E-mail: lav.imas12@h12o.es

R. Lázaro-Gorines, A. Segura-Tudela, L. Rubio-Pérez, L. Álvarez-Vallina
Immuno-Oncology and Immunotherapy Group
Instituto de Investigación Sanitaria 12 de Octubre (imas12)
Madrid 28041, Spain

(RBD) docking to the cell surface receptor angiotensin-converting enzyme 2 (ACE2) for viral entry into host cells,[13–15] so most SARS-CoV-2-neutralizing antibodies (nAb) block this interaction by direct binding to the RBD.[16,17] Accordingly, viral strains with mutations altering the RBD surface can avoid antibody recognition and neutralization. A particularly negative effect has been attributed to the K417N/T, L452R, T478K, and E484K/Q mutations, as seen in the B.1.351 (beta), P.1 (gamma), B.1.617.2 (delta), or B.1.1.529 (omicron) variants of concern (VOCs). The spread of these VOCs has reduced the efficacy of vaccines and mAb-based therapeutics,[4,18,19] making it mandatory to update them against present and future SARS-CoV-2 variants.

Camelid-derived single-domain antibodies, also known as V_{HH}s or nanobodies, combine antigen-binding affinities that are comparable to conventional antibodies with a smaller size (15 kDa), high stability, and engineering simplicity.[20,21] Their potential for use against SARS-CoV-2 infection has been widely reported both in vitro[22–25] and in vivo.[26–28] Many multimerization strategies have been used to increase their potency, such as bispecific and biparatopic fusions,[23,29,30] V_{HH}-Fc constructs[22,24] and N-terminal V_{HH}-based trimerbodies.[31] Some of these multimerized V_{HH}s completely neutralize the infectivity of SARS-CoV-2 and even suppress the emergence of escape mutants.[23,29,31]

Dendritic cells (DCs) are professional antigen-presenting cells that play a central role in the induction of antigen-specific adaptive immune responses during infection.[32] C-type lectin receptors (CLR), such as DEC-205, DCIR-2 and DC-SIGN, have been increasingly used in preclinical models for in vivo targeting of antigens to DCs.[33–36] Dendritic cell natural killer lectin group receptor-1 (DNGR-1), encoded by the gene *Clec9a*, is a CLR selectively expressed at high levels by mouse CD8α^+[37] and CD103$^+$ DCs,[38] and by their human equivalents.[39] In this DC subset, defined as conventional type 1 DCs (cDC1s), DNGR-1 promotes cross-priming of cytotoxic CD8$^+$ T cell (CTL) responses by diverting of necrotic cell cargo into a recycling endosomal compartment, preferentially resulting in major histocompatibility complex class I cross-presentation to CTLs.[40,41] Therefore, DNGR-1 may be used as a target to enhance anti-viral CTL responses by specific-priming of cDC1s with viral components, such as antigens or whole virions.[42]

Here, we report the development of TN^T, a SARS-CoV-2-nAb comprising an anti-RBD biparatopic tandem-nanobody (TN) integrated in a trimerbody scaffold.[43] It neutralized Wuhan-Hu-1/B.1 lineage S protein-pseudotyped vesicular stomatitis virus

R. Lázaro-Gorines, A. Segura-Tudela, L. Rubio-Pérez, L. Álvarez-Vallina
H12O-CNIO Cancer Immunotherapy Clinical Research Unit
Centro Nacional de Investigaciones Oncológicas (CNIO)
Madrid 28029, Spain

P. Pérez, G. Albericio, D. Astorgano, S. Flores, M. Esteban, J. García-Arriaza
Department of Molecular and Cellular Biology
Centro Nacional de Biotecnología (CNB)
Consejo Superior de Investigaciones Científicas (CSIC)
Madrid 28049, Spain

P. Pérez, J. García-Arriaza
Centro de Investigación Biomédica en Red de Enfermedades Infecciosas (CIBERINFEC)
Madrid 28029, Spain

I. Heras-Murillo, I. Adán-Barrientos, D. Sancho
Immunobiology lab
Centro Nacional de Investigaciones Cardiovasculares (CNIC)
Madrid 28029, Spain

J. Luczkowiak, N. Labiod, R. Delgado
Virology and HIV/AIDS Group
Instituto de Investigación Sanitaria 12 de Octubre (imas12)
Madrid 28041, Spain

S. L. Harwood
Department of Molecular Biology and Genetics – Protein Science
Aarhus University
Aarhus 80000, Denmark

L. Rubio-Pérez, L. Álvarez-Vallina
Chair for Immunology UFV/Merck
Universidad Francisco de Vitoria (UFV)
Pozuelo de Alarcón, Madrid 28223, Spain

Y. Nugraha, I. G. Muñoz
Protein Crystallography Unit
Structural Biology Programme
Centro Nacional de Investigaciones Oncológicas (CNIO)
Madrid 28029, Spain

X. Shang, Y. Li, D. L. Abeyawardhane, W. Yu, A. D. MacKerell Jr, D. J. Weber, E. Pozharski, R. Godoy-Ruiz
Institute for Bioscience and Biotechnology Research
University of Maryland
Rockville, MD 20850, USA

X. Shang, Y. Li
Department of Microbiology and Immunology
University of Maryland School of Medicine
Baltimore, MD 21201, USA

Y. Li, K. A. Adipietro, D. L. Abeyawardhane, D. J. Weber, E. Pozharski, R. Godoy-Ruiz
The Center for Biomolecular Therapeutics
Rockville, MD 20850, USA

C. Alfonso, F. J. Blanco
Centro de Investigaciones Biológicas Margarita Salas (CIB)
Consejo Superior de Investigaciones Científicas (CSIC)
Madrid 28040, Spain

K. A. Adipietro, D. L. Abeyawardhane
Biochemistry and Molecular Biology
University of Maryland School of Medicine
Baltimore MD 21201, USA

R. Navarro, M. Compte
Department of Antibody Engineering
Leadartis SL
Tres Cantos, Madrid 28002, Spain

A. D. MacKerell Jr
Computer Aided Drug Design Center
Department of Pharmaceutical Sciences
University of Maryland School of Pharmacy
Baltimore, MD 21201, USA

A. D. MacKerell Jr
Center for Biomolecular Therapeutics (CBT)
University of Maryland School of Medicine
Baltimore MD 21201, USA

L. Sanz
Molecular Immunology Unit
Hospital Universitario Puerta de Hierro Majadahonda
Majadahonda, Madrid 28220, Spain

R. Delgado
Department of Microbiology
Hospital Universitario 12 de Octubre
Madrid 28041, Spain

R. Delgado
Department of Medicine
Universidad Complutense de Madrid
Madrid 28040, Spain

(VSV) and live SARS-CoV-2 viruses 10- and 20-fold more effectively, respectively, than the monomeric TN and demonstrated potent neutralization of the K417N/T, E484K, N501Y, and L452R antibody-escape mutations found in the beta, gamma, and delta VOCs. In a second engineering step, the DNGR-1-specific 7H11 single-chain variable fragment (scFv) was C-terminally fused to TN^T to target SARS-CoV-2 neutralized virions to DCs and induce virus-specific CTL responses. This bispecific TN^TDNGR-1 antibody selectively targeted viral antigens to DCs expressing DNGR-1, promoting their receptor-mediated internalization. In a prime-boost regime coadministration in mice of TN^TDNGR-1 and S protein significantly improved antiviral S-specific responses, enhancing the generation of SARS-CoV-2 S-specific $CD8^+$ T cells and the polarization of the humoral responses towards the pro-Th1 response IgG2c subclass. Remarkably, intraperitoneal administration of TN^TDNGR-1, but not of TN^T, in SARS-CoV-2 infected K18-hACE2 mice protected all mice from lethal SARS-CoV-2 challenge. TN^TDNGR-1 reduced viral load in the lungs, increased IgG and IgM antibody titers against S protein and other viral antigens in serum samples and mediated effective SARS-CoV-2 neutralizing activity. Particularly, TN^TDNGR-1 treatment boosted the generation of S-specific $CD8^+$ T cells in the lungs, indicating an enhancement of T cell-mediated antiviral responses.

2. Results

2.1. Design of a Broadly Neutralizing Biparatopic Trimeric Antibody Targeting the SARS-CoV-2 S Protein RBD

For the generation of the biparatopic V_{HH}-tandem neutralizing antibody (TN), we used two well-characterized neutralizing V_{HH}s (E and V) that recognize two non-overlapping epitopes on the SARS-CoV-2 Wuhan-Hu-1/B.1 RBD as building blocks,[23] fusing them with a 15-amino acid-long $(G_4S)_3$ linker. To improve TN's binding to RBD through multivalency (i.e., the avidity effect) and to increase RBD occupancy within the S protein trimer, TN was integrated into a trimerbody scaffold by fusing it to a human collagen XVIII-derived homo-trimerization (TIE) domain[44] generating a biparatopic V_{HH}-based trimerbody (TN^T) (**Figure 1**A). TN and TN^T were purified from HEK-293 conditioned media, showing migration patterns in SDS-PAGE under reducing conditions consistent with their theoretical molecular weights (29.6 and 38 kDa, respectively) (Figure S1A, Supporting Information). In a size exclusion chromatography-multiangle light scattering (SEC-MALS) analysis TN eluted as a major peak with a molar mass of 31 kDa and TN^T as a single peak with 118 kDa (calculated masses are 29.6 and 114 kDa, respectively) (Figure S1B, Supporting Information). Circular dichroism (CD) spectra (Figure S1C, Supporting Information) display minima at 217 nm, characteristic of β-sheet secondary structure. The cooperative thermal denaturation curves, with mid-point temperatures >60 °C (Figure S1D, Supporting Information), indicate stable three-dimensional structures in both antibodies.

2.2. TN-Based Antibodies Bind SARS-CoV-2 S Protein RBD with High Affinity and Efficiently Block the RBD-ACE2 Interaction

Biolayer interferometry (BLI) analysis confirmed the ability of TN and TN^T to bind B.1 RBD and block its interaction with human ACE2 (hACE2). Treating the biosensor-immobilized B.1 RBD with any of the two antibodies prevented nearly all (>95%) subsequent binding of hACE2 (Figure 1B). Moreover, TN and TN^T exhibited similar reactivity against B.1.351 (beta), P.1 (gamma), B.1.617.1 (kappa), and B.1.617.2 (delta) RBDs compared to the B.1 RBD, as measured by enzyme-linked immunosorbent assay (ELISA) (Figure S1E, Supporting Information). BLI analysis confirmed that TN and TN^T bind with high affinity to immobilized B.1 RBD (Figure S1F, Supporting Information) and demonstrated negligible dissociation over one hour of measurement. This precluded a precise determination of their dissociation rate but was indicative of high-affinity sub-nanomolar dissociation constants (K_D). As expected from their respective monomeric and trimeric natures, TN^T association rate constant was approximately threefold greater than for TN (k_a values of ≈16 and $\approx 6 \times 10^4$ M^{-1} s^{-1}, respectively). A similar study was performed where both TN and TN^T bound the beta variant RBD essentially identically to the B.1 RBD (Figure S1G, Supporting Information).

2.3. Biparatopic TN^T Binds Simultaneously to all Three S Protein RBDs

The stoichiometry of the interaction between S protein and TN^T was studied by microfluidic diffusional sizing (MDS) analysis. The hydrodynamic radius (R_h) of TN^T (5.06 nm) is consistent with its trimeric form, increasing to 16.6 nm when mixed with equimolar amount of HexaPro S protein. This indicates that TN^T binds to trimeric S protein at a 1:1 stoichiometry (Figure S2A,B, Supporting Information). Cryo-electron microscopy (cryo-EM) was used to determine the structure of the HexaPro S protein/TN^T complex (Figure S2C–H; see Experimental Section in the Supporting Information for details). An electron density map with 3.8 Å resolution was used to build a consistent model of the S protein ectodomain (yellow, blue and green, Figure 1C). While the isolated S protein exists predominantly in a closed RBD conformation,[14] the TN^T-bound S protein is mainly in the prefusion state with all three RBDs in the open conformation (Figure 1C; Figure S3A,B, Supporting Information). The TIE domain and the linkers of TN^T were not observed (likely due to their flexibility and lack of direct binding to the S protein), but there were densities in the map that made it possible to model the six TN^T V_{HH}s bound to their RBD epitopes (Figure 1C,D; Figure S3A,B, Supporting Information). As the length of the 15-amino acid linker connecting the C-terminus of E V_{HH} and the N-terminus of V V_{HH} (53 Å in an extended conformation) is compatible with this distance between the E and V V_{HH}s binding to the same RBD (43 Å), but not compatible with those bound to different RBDs (>90 Å), each tandem V_{HH} must interact with a single RBD. In concert, the three tandem V_{HH}s of TN^T completely block all of the S protein's sites of interaction with the hACE2 receptor. The RBD binding by the E and V V_{HH}s within the TN^T is very similar to that of the monomeric tandem V_{HH}s, which was previously described (PDB: 7B18),[23] although in the S protein/TN^T model there is a major shift in the position of one of the RBDs relative to the other two in the complex (Figure S3C, Supporting Information).

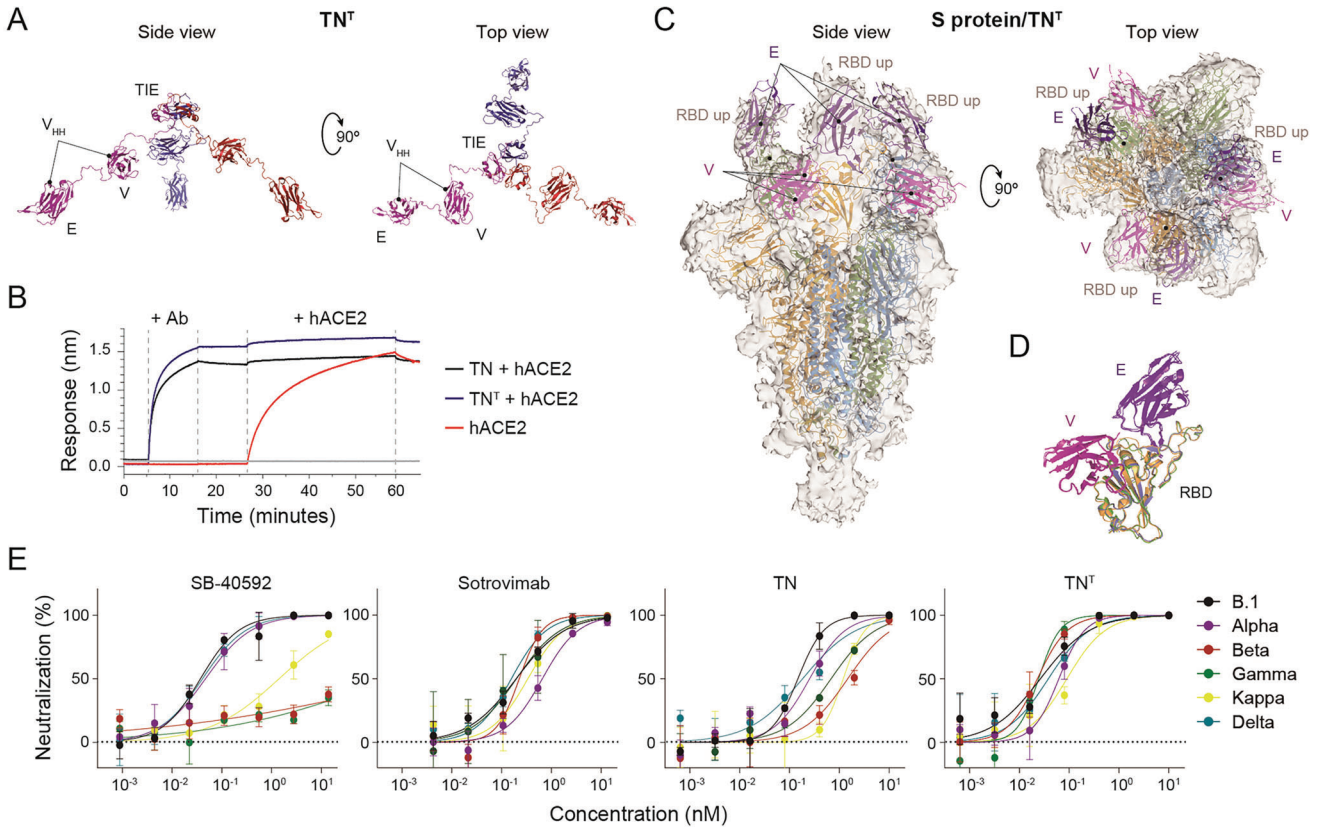

Figure 1. The TN^T trimerbody efficiently blocks RBD-hACE2 interaction by simultaneous binding to the three RBDs of the SARS-CoV-2 S protein causing broad effective neutralization activity. A) Hypothetical model of the TN^T trimerbody displayed in lateral and top views showing V_{HH}s and TIE trimerization domain disposition. Each monomer was colored differently (blue, red and purple). B) The ability of TN and TN^T antibodies to block the interaction of ACE2 with RBD was investigated using BLI. TN (black) or TN^T (blue) were associated with immobilized B.1 RBD, after which ACE2 was added. Unblocked control is also shown (red). C) Side and top views of sharpened cryo-EM map corresponding to the trimeric S protein ectodomain after incubation with TN^T. The map is shown in pale grey and the S protein/TN^T modelization is included in the map as cartoon representation. Each protomer of the S protein (3-up RBD) is colored differently (yellow, blue, and green) and the docked domains, E and V V_{HH}s forming the three-arms of the TN^T, bound simultaneously to the three RBDs are shown in purple and magenta, respectively. D) The alignment of the three RBDs bound to E and V V_{HH}s from our model illustrates the similar way of interaction between the three arms of TN^T and each RBD. E) Neutralization of SARS-CoV-2 S-pseudotyped rVSV-luc. Twofold serial dilutions of control nAb (SB-40592 or sotrovimab), TN or TN^T were incubated with pseudoviruses expressing S protein from different variants prior to Vero E6 cells infection. Normalized values from three independent experiments ± SEM are plotted. Overall, there was an excellent correlation between the three neutralization assays ($R^2 = 0.92$).

2.4. Trimerization Enhances SARS-CoV-2 Neutralization by the TN Antibody and Prevents Escape Caused by Mutations Found in Most VOCs

The neutralizing activity of TN and TN^T was assessed using replication-deficient G-luciferase VSV pseudotyped with the SARS-CoV-2 S protein. SB-40592 and sotrovimab biosimilar were used as control mAbs. SB-40592 neutralized S protein-pseudotyped particles with half-maximal effective concentration (EC_{50}) of 37×10^{-12} M for B.1, 47×10^{-12} M for VOC B.1.1.7 (alpha) and 41×10^{-12} M for VOC delta, but was ineffective against beta, gamma, and kappa strains (Figure 1E). Sotrovimab EC_{50} values were between 156 and 335×10^{-12} M for all assayed strains (Figure 1E). TN neutralized infection strongly in a dose-dependent manner, with EC_{50} values of 147 and 182×10^{-12} M for the B.1 and delta pseudoviruses, respectively; however, its efficacy was significantly decreased against beta (approximately tenfold), kappa (approximately eightfold), and gamma (approximately fivefold) variants (Figure 1E). The trimerization-conveyed avidity of TN^T reduced the EC_{50} concentration against B.1 pseudovirus to 26×10^{-12} M (approximately sixfold) and it retained this efficacy against all the variants studied. Specifically, TN^T was nearly 70- and 30-fold more effective than TN against beta and gamma VOCs (EC_{50} of 23 and 24×10^{-12} M, respectively) (Figure 1E).

2.5. Design of a SARS-CoV-2-Neutralizing Trimerbody Targeting Dendritic Cells

To allow TN^T to prime adaptive immune responses in addition to its short-term virus-neutralizing capacity, we aimed to deliver the TN^T-bound virus to cDC1s, which excel at priming anti-viral responses. With this purpose, we generated a bispecific trimerbody (TN^{T}DNGR-1) by fusing the anti-DNGR-1 7H11 scFv[37] to the C-terminus of TN^T through a flexible 15-amino acid linker (**Figure 2**A). SDS-PAGE analysis of purified TN^{T}DNGR-

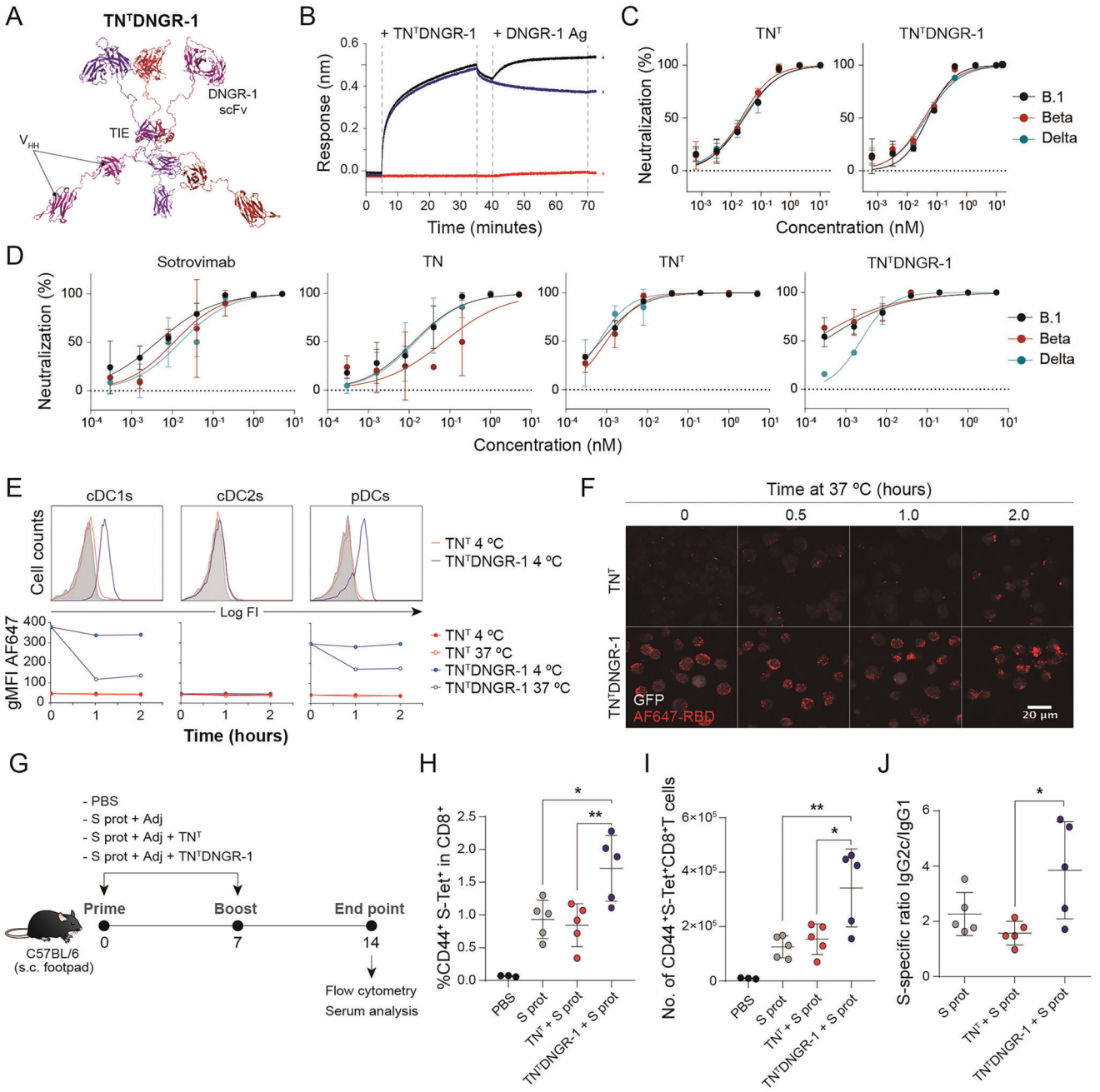

Figure 2. The bispecific TN^{T}DNGR-1 trimerbody combines potent and broad SARS-CoV-2 neutralization with specific targeting of viral antigens to DNGR-1-expressing DCs for boosting systemic S-specific effector CD8$^+$ T cell responses. A) TN^{T}DNGR-1 hypothetic model showing V_{HH}-tandem, TIE trimerization domain and anti-DNGR-1 7H11 scFv antibody. Each polypeptide chain is represented in one different color (blue, red and purple). B) Bispecificity of TN^{T}DNGR-1 was investigated using BLI by incubating RBD-coated biosensors first with antibody, and then with DNGR-1. Control RBD-coated biosensors with TN^{T}DNGR-1 but without DNGR-1 and just with DNGR-1 were also included. C) Neutralization of SARS-CoV-2 S-pseudotyped rVSV-luc. Twofold serial dilutions of each trimerbody were incubated with SARS-CoV-2 S-pseudotyped rVSV-luc expressing S protein from beta and delta variants prior to infecting Vero E6 cells. D) B.1, beta and delta SARS-CoV-2 virus neutralization of infection. Five-fold serial dilutions of sotrovimab, TN, TN^T or TN^{T}DNGR-1 were incubated with live viruses prior to infecting Vero E6/TMPRSS2 cells. E) Flow cytometry analysis of Flt3-L BMDCs after incubation at 4 or 37 °C with TN^{T}DNGR-1 or control TN^T and subsequent stained with AF647-RBD staining and antibodies to discriminate DC subsets. Upper histograms represent actual staining for the different cell subsets at 1 h and 4 °C. Lower data represent geometric mean fluorescence intensity (gMFI) for the cDC1, cDC2, and pDC subsets at the different conditions. F) Representative pictures of MuTu-DC cells incubated with TN^{T}DNGR-1 or control TN^T and AF647-RBD at 4 °C and then for different times at 37 °C before fixation and visualization using confocal microscopy. G) Immunization of C57BL/6 mice using a prime-boost scheme with either: (1) PBS; (2) S protein + adjuvants (poly I:C + CpG); (3) S protein + TN^T + adjuvants; or (4) S protein + TN^{T}DNGR-1 + adjuvants. One representative from two independent experiments (n = 3–5 mice/group /experiment) is shown. Spleens were harvested on day 14 and stained for S-specific CD8$^+$ T cells using specific S protein tetramer, H-2Kb (539-VNFNFNGL-546) (S-Tet). H) Frequency of

1 revealed a single band consistent with its estimated molecular weight (64.7 kDa) (Figure S4A, Supporting Information) and SEC-MALS analysis showed one major symmetric peak with a molar mass of 175 kDa (Figure S4B, Supporting Information), close to its theoretical trimeric mass of 194 kDa. BLI studies proved that TN^{T}DNGR-1 bound to immobilized B.1 RBD with high affinity (Figure 2B) and could bind soluble DNGR-1 while remaining bound to the immobilized RBD, demonstrating its ability to bind both antigens simultaneously (Figure 2B). TN^{T}DNGR-1 bound B.1 RBD in ELISA assays and HEK-293 cells expressing B.1 S protein as efficiently as TN^{T} (Figure S4C,D, Supporting Information). Furthermore, in accordance with its high-affinity binding to immobilized RBD protein, TN^{T}DNGR-1 neutralized pseudovirus infection as efficiently as TN^{T}, with EC_{50} values of 49.2, 36.9, and 42.6 × 10^{-12} M for B.1, beta and delta variants, respectively (Figure 2C). Moreover, TN inhibited SARS-CoV-2 infection of Vero E6/TMPRSS2 cells in a similar way to sotrovimab for B.1 and delta strains, but its EC_{50} was 5-fold increased against beta VOC. Comparatively, TN^{T}DNGR-1 and TN^{T} promoted a higher neutralization effect than monomeric TN and sotrovimab for all assayed variants (Figure 2D). Both trimerbodies avoid viral escape with EC_{50} of 0.3 and 0.7 × 10^{-12} M for B.1 strain, 0.15 and 1 × 10^{-12} M for VOC beta, and 2.3 and 0.64 × 10^{-12} M for VOC delta, respectively (Figure 2D). Comparatively sotrovimab EC_{50} values for these strains were 21, 11, and 16 × 10^{-9} M, respectively (Figure 2D).

2.6. TN^{T}DNGR-1 Trimerbody Targets RBD to DNGR-1-Expressing Dendritic Cells Promoting its Internalization

To test the specificity of TN^{T}DNGR-1 we stained B3Z and B3Z^{DNGR-1} cells with AF647-conjugated B.1 RBD (AF647-RBD) preincubated with TN^{T} or TN^{T}DNGR-1 and found that B3Z^{DNGR-1} cells were labeled by AF647-RBD only in the presence of TN^{T}DNGR-1 but not the TN^{T} control (Figure S4E, Supporting Information). To address whether TN^{T}DNGR-1 (as well as neutralized RBD or virions) is internalized by DCs, we incubated Flt3L bone marrow-derived dendritic cells (BMDCs) with TN^{T} or TN^{T}DNGR-1 for up to two hours at 4 or 37 °C and then added AF647-RBD for detecting cell surface-bound trimerbodies. DNGR1-expressing DCs, mainly cDC1s but also plasmacytoid (pDCs), were stained with AF647-RBD when DCs were preincubated with TN^{T}DNGR-1, but not with TN^{T}, at 4 °C (Figure 2E; Figure S4F, Supporting Information). Notably, after 1- or 2-h incubation with TN^{T}DNGR-1 at 37 °C, the AF647-RBD signal was reduced 4-fold in these subpopulations, suggesting its internalization (Figure 2E, lower graphs). The ability of TN^{T}DNGR-1 to promote cell internalization of soluble RBD was confirmed in MuTu-DCs (a mouse DC cell line expressing DNGR-1) by confocal microscopy. Only cell preparations treated with TN^{T}DNGR-1, but not with TN^{T}, followed by immediate AF647-RBD incubation showed specific staining and internalization of the TN^{T}DNGR-1/AF647-RBD complex after 2 h of incubation at 4 or 37 °C (Figure 2F).

2.7. TN^{T}DNGR-1 Trimerbody Increases S Protein-Specific CD8^{+} T Cells in Immunocompetent Mice

We investigated whether TN^{T}DNGR-1 could increase the generation of adaptive immunity by specific targeting of captured SARS-CoV-2 S protein towards cDC1s. We treated immunocompetent C57BL/6 mice in a prime-boost scheme with the following stimuli: 1) PBS; 2) S protein + adjuvants (poly I:C + CpG); 3) S protein + TN^{T} + adjuvants; or 4) S protein + TN^{T}DNGR-1 + adjuvants (Figure 2G). Immunization with S protein, like S protein + TN^{T}, led to a significant increase in the generation of systemic S protein-specific effector CD8^{+} T cells quantified by S protein-specific tetramer (S-Tet) staining, compared to PBS-treated control mice (Figure 2H,I; Figure S4G, Supporting Information). Notably, immunization with S protein in the presence of TN^{T}DNGR-1 resulted in a further increase of the frequency and number of S protein-specific effector CD8^{+} T cells (Figure 2H,I; Figure S4G, Supporting Information). Moreover, ELISA analysis in serum samples reveals that all the S protein treated mice groups induced potent S protein-specific IgM and total IgG antibody responses compared to PBS-treated mice (Figure S4H, Supporting Information). By contrast, RBD-specific IgM and total IgG antibody responses were only induced in mice immunized with S protein and with S protein + TN^{T}DNGR-1, but not in animals immunized with S protein + TN^{T} or PBS-treated mice (Figure S4I, Supporting Information). Interestingly, the measurement of S protein-specific IgG1 and IgG2c responses (Figure S4H, Supporting Information) showed that S protein + TN^{T}DNGR-1 administration induced lower levels of S protein-specific IgG1, increasing the ratio of IgG2c to IgG1, suggesting a fostered Th1-polarized antibody profile response (Figure 2J). RBD-specific IgG1 and IgG2c responses were only enhanced compared PBS by the immunization with S protein, but no significant differences were found for TN^{T} and TN^{T}DNGR-1 coadministration groups (Figure S4I, Supporting Information).

2.8. TN^{T}DNGR-1 Trimerbody Protects Against a Lethal SARS-CoV-2 Challenge

To evaluate the capacity of the TN^{T}DNGR-1 trimerbody to protect against SARS-CoV-2 infection, we performed an in vivo protection study in K18-hACE2 transgenic mice, which express the human ACE2, and are therefore susceptible to SARS-CoV-2 infection (**Figure 3**).[45] K18-hACE2 mice (n = 8/group) were challenged intranasally (i.n.) with a lethal dose (1 × 10^{5} plaque-forming units (PFUs)/mouse) of SARS-CoV-2 (isolate MAD6, a prototypic B.1 strain) and 17 h later were treated by intraperitoneal (i.p.) injection of TN^{T}, TN^{T}DNGR-1, sotrovimab or PBS

CD44^{+} S-Tet^{+} cells within the T CD8 gate and I) total number of CD44^{+} S-Tet^{+} CD8^{+} T cells are shown. *$p < 0.05$; **$p < 0.01$ by one-way ANOVA followed by Tukey's multiple comparison test. CD44^{+} S-Tet^{+} representative dot plots gated on CD8^{+} T cells for the different treatment groups are presented in Figure S4F in the Supporting Information, G,J) The S-specific IgG2c/IgG1 ratio by mean of serum S-specific subclass IgG determination by ELISA at a 1/250 dilution in serum samples obtained on day 14. Raw data for IgG1 and IgG2c, in serum samples diluted 1/250 are presented in Figure S4H in the Supporting Information. *$p < 0.05$ by one-way ANOVA followed by Tukey's multiple comparison test.

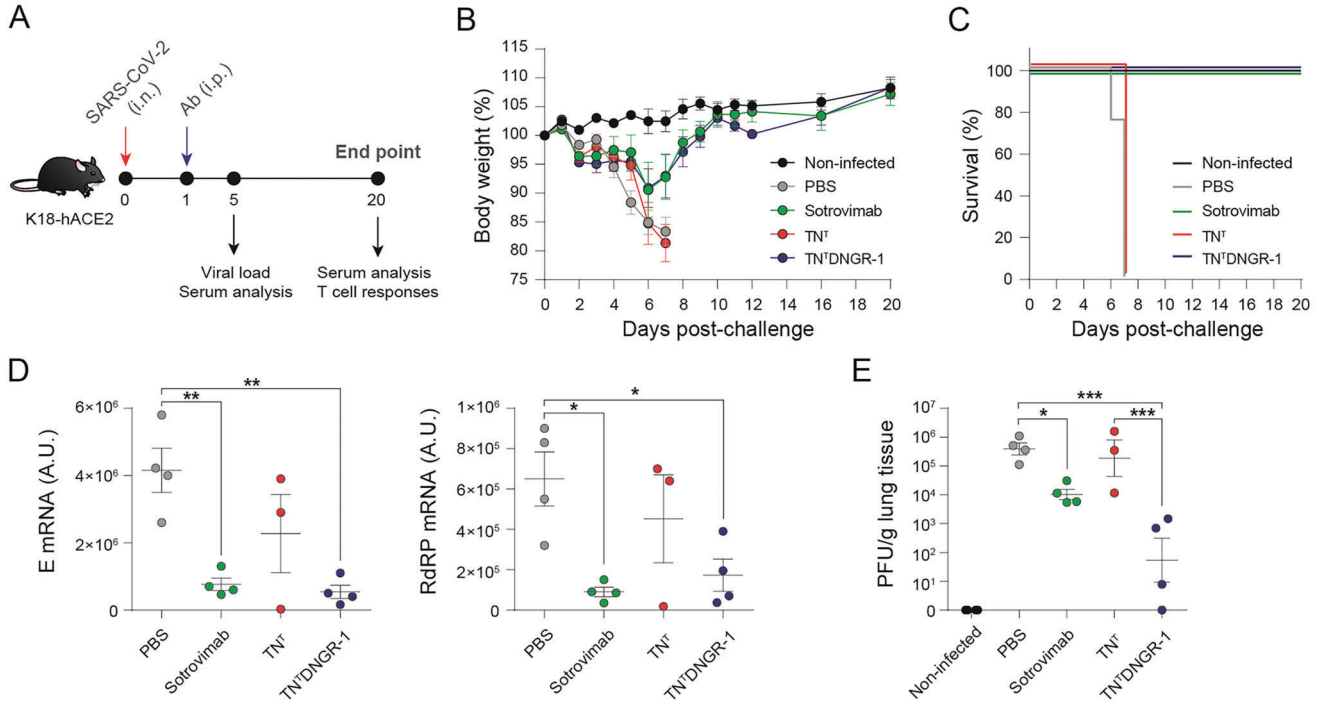

Figure 3. Therapeutic application of TN^{T}DNGR-1, but not TN^T, protects mice of SARS-CoV-2 lethal infection by reducing viral load in the lungs. A) Efficacy experiment in K18-hACE2 mice was done using a single antibody (Ab) intraperitoneal (i.p.) administration 17 h after intranasal (i.n.) viral challenge (10^5 PFUs/mouse). Experimental groups ($n = 8$ mice/group, 1 experiment) included: uninfected control group (black) and infected groups treated with PBS (grey), sotrovimab biosimilar (green), TN^T (red), and TN^{T}DNGR-1(blue). On day 5 p.c. 4 mice per group were euthanized to obtained serum samples and lungs ($n = 3$ in the case of the TN^T group). Serum was collected on day 5 and 20 post-challenge (p.c.) for humoral immune response analysis. Lungs were harvested on day 5 p.c. for viral load determination and on day 20 p.c. for the analysis of S-specific T cell responses. B) Weight change after B.1 (isolate MAD6) SARS-CoV-2 challenge followed by antibody administration (mean ± SEM) expressed as percentage of initial body weight. C) Kaplan-Meyer survival representation of the efficacy experiment. D) Viral mRNA levels at day 5 p.c. in the right lung measured for E (envelope) and RNA-dependent RNA polymerase (RdRP) genes. E) Infective virus in the lungs at day 5 p.c. represented as PFUs/g of lung tissue. All graphs represent individual values plus mean ± SEM for a single experiment. *$p < 0.05$; **$p < 0.01$; ***$p < 0.001$ by one-way ANOVA followed by Tukey's multiple comparison test.

(as a nontreated infected control). In addition, noninfected and nontreated mice were used as a control group of healthy animals (Figure 3A). Mice were monitored for 20 d to determine body weight loss and survival (Figure 3B,C). All treated animals lost approximately 5% to 8% of their initial body weight during the first days postchallenge (p.c.), 10% to 13% in the case of the control PBS-treated group, but by day 6 p.c. mice treated with TN^{T}DNGR-1 or sotrovimab began to recover body weight reaching the baseline body weight by day 9 p.c. (Figure 3B) and all survived (Figure 3C). However, PBS- and TN^T-treated mice continue to lose body weight (Figure 3B) and succumbed or were euthanized on day 7 p.c. (Figure 3C). Next, to assess the impact of TN^{T}DNGR-1 treatment on the replication of SARS-CoV-2, four mice per group were sacrificed on day 5 p.c., the lungs were harvested and processed, and the presence of SARS-CoV-2 subgenomic E and genomic RdRp RNA (Figure 3D), and infectious virus (Figure 3E) analyzed. Treatment with TN^{T}DNGR-1 and sotrovimab significantly reduced the subgenomic and genomic SARS-CoV-2 RNA levels in the lungs compared to PBS- or TN^T-treated mice (Figure 3D). Live infectious virus determination showed that TN^{T}DNGR-1 induced a more potent reduction than sotrovimab in virus titers in the lungs, whereas PBS- and TN^T-treated mice show similar titers (Figure 3E).

2.9. TN^{T}DNGR-1 Trimerbody Induces SARS-CoV-2-Specific Humoral and Cellular Immune Responses

Next, to study whether TN^{T}DNGR-1 could promote SARS-CoV-2-specific adaptive immunity, we analyzed the humoral and cellular immune responses induced in K18-hACE2 mice. On day 5 p.c., mice treated with TN^{T}DNGR-1 and sotrovimab induced significantly higher titers of S-specific IgM (**Figure 4**A; Figure S5A, Supporting Information) and S-, RBD-, and N-specific IgG antibodies than nontreated or TN^T-treated mice (Figure 4B; Figure S5B–D, Supporting Information). Furthermore, on day 20 p.c., mice treated with TN^{T}DNGR-1 or sotrovimab both elicited similar high titers of S-, RBD-, and N-specific IgG antibodies (Figure 4C; Figure S5E–G, Supporting Information), which were highly increased when compared to the levels induced on day 5 p.c. Treatment with TN^{T}DNGR-1 and sotrovimab led to higher titers of serum nAb against live SARS-CoV-2 on day 5 p.c, than PBS- or TN^T-treated mice. (Figure 4D; Figure S6A, Supporting Information). Consistently and similar to IgG antibody titers at day 20 p.c., neutralizing antibody titers increased highly in TN^{T}DNGR-1- and sotrovimab-treated mice compared to day 5 p.c. levels (Figure 4E; Figure S6B, Supporting Information). To assess the contribution of the administrated antibodies to this neutralizing

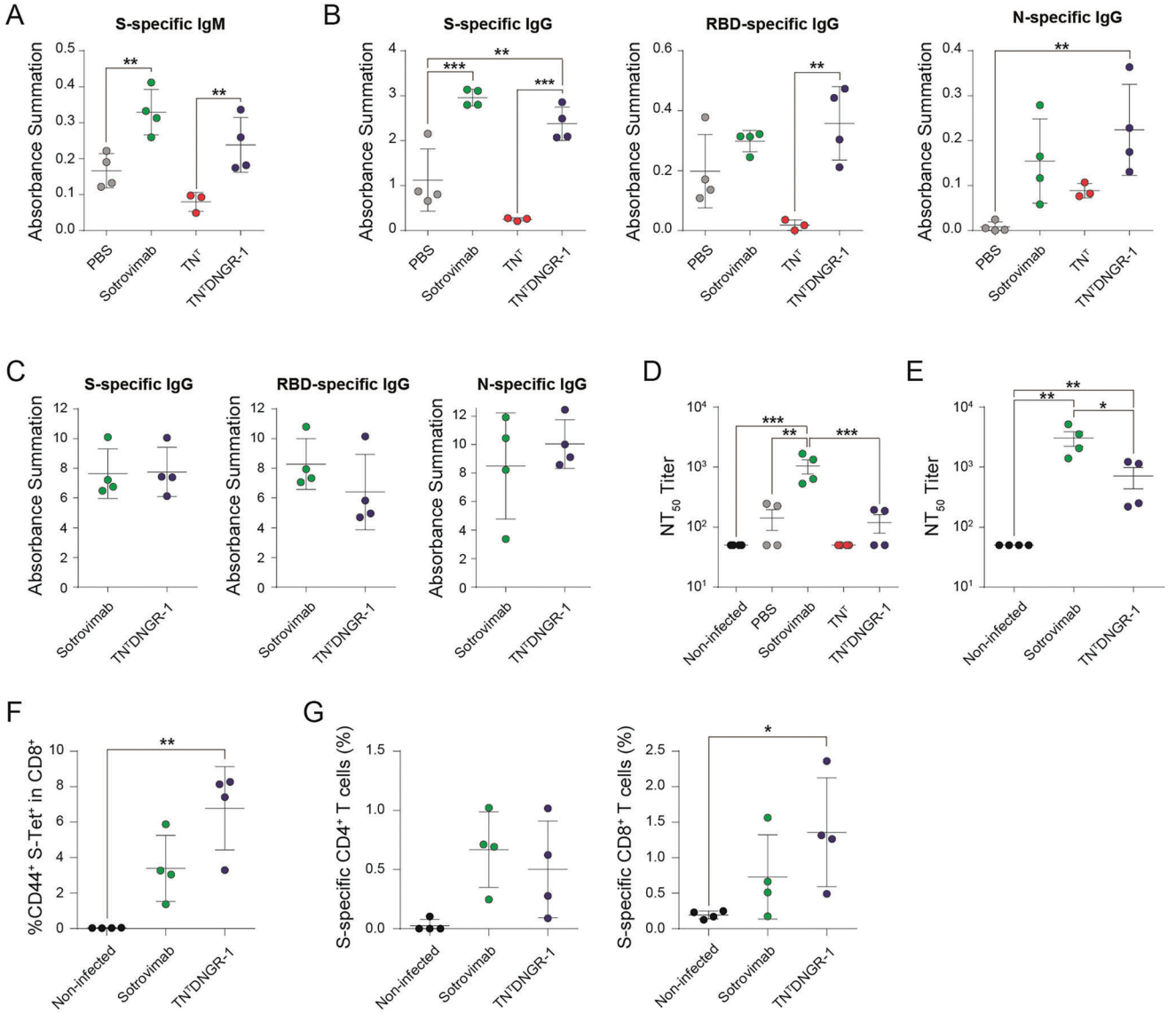

Figure 4. TN^{T}NDGR-1 mediates an effective humoral and cellular immune response against SARS-CoV-2, specifically by providing enhanced S-specific cytotoxic T CD8$^+$ cell responses in the lungs. A) Anti-S IgM levels in serum 5 d p.c. expressed as absorbance summation. B) Quantification of S-, RBD-, and N-specific total IgG levels at 5 d p.c. expressed as absorbance summation. C) Quantification of S-, RBD-, and N-specific total IgG levels at 20 d p.c. expressed as absorbance summation. D,E) SARS-CoV-2 neutralization. Serum neutralization of live SARS-CoV-2 (B.1 strain), expressed as NT_{50}, at day 5 (D) and 20 (E) p.c. Lungs were harvested on day 20 p.c. and stained for S-specific CD8$^+$ T cells using specific S protein tetramer H-2Kb (539-VNFNFNGL-546) (S-Tet). F) Frequency of CD44$^+$ S-Tet$^+$ cells within the T CD8 gate. G) Frequency of S-specific T CD4$^+$ (left panel) and T CD8$^+$ cells (right panel) in the lungs at 20 d p.c. and evaluated by an intracellular cytokine staining assay measuring expression of CD107a, and secretion of IFN-γ, TNF-α, and IL-2. All graphs represent individual values plus mean ± SEM (n = 4 mice/group; n = 3 mice in the case of TN^T at day 5 p.c.) for a single experiment. *$p < 0.05$; **$p < 0.01$; ***$p < 0.001$ by one-way ANOVA followed by Tukey's multiple comparison test. *$p < 0.05$ for S-specific CD8$^+$ T cells analysis (G) was done by Dunn's multiple comparisons test following Friedman test.

activity, we determined the concentration of TN^T, TN^{T}DNGR-1 and sotrovimab in mice serum at day 5 and 20 p.c., obtaining significant higher levels for sotrovimab (8.26 µg mL^{-1} and 12.72 ng mL^{-1}, respectively) than for TN^{T}DNGR-1 (38.73 and 0.11 ng mL^{-1}, respectively) and TN^T (0.32 ng mL^{-1} and undetermined, respectively) (Figure S6C, Supporting Information).

The study of T cell responses by S-Tet staining in the lungs obtained on day 20 p.c. showed that TN^{T}DNGR-1 treatment selectively induced a significant local increase of S protein-specific effector CD8$^+$ T cells compared to non-infected mice (Figure 4F). Notably, the magnitude of this effect was superior to that promoted by sotrovimab in the same non-infected mice (Figure 4F). In addition, the presence of S-specific CD4$^+$ and CD8$^+$ T cell immune responses was further assessed by an intracellular cytokine staining (ICS) assay in lungs cells obtained on day 20 p.c. and restimulated in vitro with SARS-CoV-2 S peptide pools. Treatment with TN^{T}DNGR-1 and sotrovimab induced S-specific CD4$^+$ and CD8$^+$ T cells expressing the cytotoxic marker CD107a

and/or secreting IFNγ, TNFα, and/or IL-2 cytokines (Figure 4G). While TN^{T}DNGR-1 and sotrovimab elicited similar levels of S-specific CD4$^+$ T cells, TN^{T}DNGR-1-treatment specifically triggered a significantly increased number of S-specific CD8$^+$ T cells compared to non-treated group (Figure 4G). In detail, TN^{T}DNGR-1 triggered a trend towards a higher amount of S-specific CD8$^+$ T cells individually secreting IFNγ, TNFα, or expressing CD107a compared to sotrovimab, but did not show any differences in the CD4$^+$ T cell subset (Figure S7E, Supporting Information). Together, these results suggest that the addition of DNGR-1 specificity to the TN^T moiety redirects the virus to cDC1s and favors cross-priming and a boosted adaptive response against the S protein of SARS-CoV-2.

3. Discussion

To date, most mAb-based therapeutic strategies against SARS-CoV-2 have focused on virus neutralization and clearance, either with conventional mAbs or by implementing multispecificity through Fc fusion or other multimerization strategies.[10,29,46–48] Furthermore, it has been widely demonstrated in SARS-CoV-2 infection in vivo models that virus-neutralizing antibody activity depends on Fc-FcγR interactions.[49–51] Different approaches of nAbs with Fc-optimized binding to FcγIIa and FcγIIIa receptors have been described with superior potency to prevent or treat COVID-19 disease.[10,52] Nonetheless, the lately emergence of SARS-CoV-2 strains, showing reduced sensitivity to both vaccine-elicited and clinically administrated nAbs, or the upcoming emergence of other viruses with pandemic potential demands the development of innovative approaches for the effective treatment of viral infections.

In this study, we evaluated the potential of an Fc-free bispecific antibody, TN^{T}DNGR-1, incorporating an anti-RBD V_{HH}-tandem (TN) and an anti-DNGR-1 scFv into a trimerbody scaffold, for priming virus-specific CD8$^+$ T cell responses and protect transgenic K18-hACE2 mice against SARS-CoV-2 infection. Although vaccine-like approaches targeting specific tumor or viral antigens to DCs by fusing them to mAbs have been previously described,[37,53] a strategy that combines immediate virus neutralization with specific cDC1s targeting, aiming to accelerate and boost adaptive immune responses during infection, has never been explored.

RBD-targeted V_{HH}s have shown effective in neutralizing SARS-CoV-2 infection in vitro and in protecting animals from SARS-CoV-2 challenge,[23,25,27,28,54] making them a valuable alternative for the development of multivalent and multiparatopic agents (targeting multiple viral epitopes) with improved neutralization efficiency and decreased vulnerability to escape mutations.[29,55,56] Here, we used the high-affinity biparatopic V_{HH}-tandem, TN, previously described to potently neutralize SARS-CoV-2 strain Wuhan-Hu-1 and prevent the emergence of escape mutants.[23] To maximize its neutralizing efficacy instead of generating a conventional Ig-like Fc-fusion,[24,26,56] we generated an anti-RBD hexavalent nAb, TN^T, made by fusing TN to the human collagen XVIII homo-trimerization domain, an effective scaffold for the generation of trimeric antibodies for clinical use.[44]

TN^T demonstrated a complete, potent blocking of the RBD-hACE2- interaction and a strong similar binding to beta, gamma, kappa, and delta variants RBDs. Furthermore, compared to TN, TN^T revealed a significant improvement in neutralization efficacy against all tested VOCs (six- and fivefold for B.1 and delta, respectively), but especially for those containing E484K/Q mutation, as beta and gamma (70- and 30-fold superior, respectively). Compared to sotrovimab,[10,57] the only formerly clinically used nAb active against all VOCs, TN^T shows three- to tenfold induction in neutralization potency against all studied VSV-pseudotyped strains and TN^{T}DNGR-1 efficacy was almost identical to the parental TN^T antibody (B.1, 49 vs 26 $\times$ 10^{-12} M; beta, 36 vs 22 $\times$ 10^{-12} M, and delta, 42 vs 38 $\times$ 10^{-12} M, respectively). Similar results were obtained in live-virus neutralization, where TN^{T}DNGR-1 and TN^T trimerbodies exhibited a more potent neutralization activity than TN and sotrovimab against B.1, beta and delta VOCs, with 10- to 100-fold and 6- to 50-fold reductions in EC_{50} values. Together with the structural data for the S protein:TN^T complex, showing an equimolar (1:1) interaction mechanism between TN^T and the trimeric S protein, where both V_{HH}s of each TN arm bind simultaneously to the 3-RBDs, our functional results demonstrate that TN^T scaffold represent an optimal design for the neutralization of viruses presenting trimeric proteins for receptor attachment, such as SARS-CoV-2, influenza, respiratory syncytial virus and human immunodeficiency 1 virus.[58–60] Thereby, although TN^T, and subsequently TN^{T}DNGR-1, are not active against the latest emerged VOC (omicron and subsequent emerging linages) because of its V_{HH}s binding limitations, TN^T scaffold provides efficient epitope accessibility for biparatopic V_{HH}-tandem assuring a broad and efficient neutralization of mutational variants, superior to other previously described trimeric or multimeric designs.[31,61]

TN^{T}DNGR-1 shows specific binding to mouse BMDC cDC1s and pDCs, but not to the DNGR-1-negative cDC2 subset in vitro, mediating RBD delivery and internalization into cDC1 DNGR-1-positive cells. Remarkably, TN^{T}DNGR-1 contributes to the activation of adaptive immunity in vivo by the specific targeting of captured SARS-CoV-2 S protein towards cDC1s. In a prime-boost immunization experiment in immunocompetent C57BL/6 mice, the coadministration of S protein and TN^{T}DNGR-1 resulted in a significant increase in the frequency and number of S-specific effector CD8$^+$ T cells and suggest a more Th1-polarized antibody profile response, compared to the administration of protein S alone or coadministered with TN^T. Furthermore, our results emphasize that the neutralizing capacity of an antibody is not sufficient for effective protection when applied therapeutically, with interactions with immune system receptors, such as FcγRs or DNGR-1 on DCs or other antigen-presenting cells, being essential for the development of effective immunity and disease control.[51,52] In this sense, even with exceptional neutralizing activity in vitro, the absence of effective interactions with immune receptors would explain why TN^T did not prevent viral spread in the lungs, elicit virus-specific adaptative immune responses or prevent the death of mice. The protective effect against lethal SARS-CoV-2 challenge is rescued for TN^{T}DNGR-1 by targeting neutralized virions to cDC1, triggering their clearance and promoting adaptive immune responses, specifically CTL activity.

Accordingly, TN^{T}DNGR-1 also reduced virus load in the lungs, indicating that DNGR-1-targeting provides an effective control of the infection spread as conventional Fc-containing nAbs.[50–52,62] TN^{T}DNGR-1 induced an early and efficient S-specific IgM and

S-, RBD-, and N-specific IgG antibody response, while TN^T treatment did not increase endogenous antibody induction over non-treated animal levels. The superior serum neutralizing activity at day 5 p.c. for the sotrovimab group, relates with its higher serum concentration compared to TN^TDNGR-1 and TN^T (8.26 µg mL^{-1}, 12.72 and 0.32 ng mL^{-1}, respectively), because of the longer half-life of IgG,[44] and does not indicate a higher level of induction of endogenous nAbs. By day 20 p.c. the induction of endogenous nAbs shows a potent effect for both TN^TDNGR-1 and sotrovimab treatment groups.

Finally, TN^TDNGR-1 and sotrovimab induced a significant increase in S protein-specific $CD4^+$ and $CD8^+$ T cells in the lungs at day 20 p.c. But, while both treatments elicited similar levels of S-specific $CD4^+$ T cells, TN^TDNGR-1-treatment specifically triggered a higher magnitude of S-specific $CD8^+$ T cells, characterized by secretion of IFNγ, TNFα, and IL-2 or CD107a expression. The TN^TDNGR-1 protective effect, via cDC1s targeting through DNGR-1 receptor, appears superior to that observed with a conventional neutralizing IgG, previously described to be mediated by $CCR2^+$ monocytes, as well as cytotoxic $CD8^+$ T cells infiltrating the lung.[51] Taken together, in the context of a respiratory viral infection, TN^TDNGR-1 elicits efficient humoral responses and suggest an improved effect on local expansion of virus-specific $CD8^+$ T cells due to its alternative mechanism of action. In summary, we have generated a bispecific trimeric antibody that, in addition to its potent and broad SARS-CoV-2 neutralization activity, delivers virus antigens or whole virions to cDC1s in an Fc-independent manner, priming systemic virus-specific humoral and local $CD4^+$ and $CD8^+$ T cell responses in vivo. The therapeutical administration of TN^TDNGR-1 antibody in SARS-CoV-2-infected K18-hACE2 mice provided full protection against SARS-CoV-2 morbidity and mortality, causing reduced viral load in the lungs and increased S-specific humoral and $CD4^+$ and $CD8^+$ T cell immune responses. Therefore, the strategy provides a bridge between passive immunotherapy with nAbs and a DC vaccination-like action for the induction of enhanced adaptive immunity without the involvement of FcγRs. Our results indicate that TN^TDNGR-1is a promising candidate for the development of improved viral treatments, and readily adaptable to other SARS-CoV-2 VOCs or other viruses, given the modular nature of the molecule.

4. Conclusions

In summary, our study addresses a novel strategy based on a broadly neutralizing bispecific anti-SARS-CoV2 antibody that targets virions to type 1 conventional DCs (cDC1s) for promoting in vivo T cell cross-priming. The strategy was shown to be therapeutically effective in protecting K18-hACE2 mice from a lethal viral challenge while enhancing protein S-specific $CD8^+$ T cell responses.

5. Experimental Section

Cell Lines: HEK-293 (# ACC-305, DSMZ) and 293T (# CRL-3216, ATCC) cells were obtained from the ATCC and cultured in Dulbecco's Modified Eagle Medium (DMEM) (Lonza) supplemented with 2 mmol L^{-1} L-glutamine (Gibco), 10% v/v heat-inactivated fetal bovine serum (FBS) (Merck Life Science), and antibiotics (100 units mL^{-1} penicillin, 100 mg mL^{-1} streptomycin; Life Technologies) referred as to DMEM complete medium (DCM) As previously described, the parental B3Z cell line[63] and its derived mouse cell line expressing CLEC9A/DNGR-1 (B3Z^{DNGR-1}) were cultured in Roswell Park Memorial Institute (RPMI) medium (Gibco) supplemented with 2 mmol L^{-1} L-glutamine, 10% v/v heat-inactivated FBS, antibiotics (100 units mL^{-1} penicillin, 100 mg mL^{-1} streptomycin), herein referred as RCM, and 1 mmol L^{-1} sodium pyruvate (Gibco), 0.1 mmol L^{-1} MEM nonessential amino acids (NEAA) (Gibco), 55 pmol L^{-1} β-mercaptoethanol (Gibco), and. Generation and characterization of the B3Z^{DNGR-1} cell line was previously described.[40,64] BHK-21/WI-2 (# EH1011, Kerafast) cells, used for recombinant VSV generation, were grown in DCM. Vero E6 (# 60 476, BCRC) cells used in the S-pseudotyped neutralization experiments were grown in DCM supplemented with 0.1 mmol L^{-1} NEAA and 12.5 units mL^{-1} Nystatin (penicillin-streptomycin-nystatin) (Biological Industries). Vero E6 cells expressing the transmembrane serine protease TMPRSS2 (VeroE6/TMPRSS2) used in the live SARS-CoV-2 neutralization experiments were maintained in DCM, supplemented with 10 mM HEPES (Gibco), 100 mg mL^{-1} geneticin (G 418 disulfate salt, Sigma-Aldrich) and 0.1 mmol L^{-1} NEAA. Mouse BMDCs were obtained by using Flt3-Ligand (Flt3-L BMDCs) as previously described[37] with slight modifications. Briefly, femur and tibia from C57BL/6J mice were collected, bone marrow was flushed, red blood cells were lysed and cells were cultured in RCM 1000 units mL^{-1} penicillin, 100 µg mL^{-1} streptomycin (both from Sigma-Aldrich), 0.1 mmol L^{-1} NEAA, 1 mmol L^{-1} sodium pyruvate, 2 mmol L^{-1} L-glutamine, 10 mmol L^{-1} HEPES (all from HyClone), and 50 µmol L^{-1} β-mercaptoethanol (Merck), herein called R10, plus 200 ng mL^{-1} human Flt3-L (Miltenyi). Media was refreshed on day 7 and cells were harvested on day 9. Mutu-DC cells (kindly provided by Hans Acha-Orbea, Laussane, Switzerland)[65] were cultured in R10 and passaged when confluent using 5 mmol L^{-1} EDTA. All adherent cell lines were cultured at 37 °C in 5% v/v CO_2 at 95% air in a humidified atmosphere. FreeStyle 293F and Expi293F (both from Gibco;) cells were respectively cultured in FreeStyle 293 and Expi293 Expression Medium at 37 °C in a humidified 8% CO_2 incubator rotating at 95 rpm. All cell lines were used within three months of thawing and checked for Mycoplasma by PCR every month using the Mycoplasma Gel Detection Kit (Biotools B&M Labs).

SARS-CoV-2 Viruses: Several SARS-CoV-2 viruses were used in the live SARS-CoV-2 neutralization assays. SARS-CoV-2 MAD6 isolate, a prototypic strain B.1 containing the D614G mutation in the S protein, is a virus collected from a nasopharyngeal swab from a 69-year-old male COVID-19 patient from Hospital 12 de Octubre in Madrid, Spain.[66] The VOCs B.1.351 (beta; hCoV-19/France/PDL-IPP01065/2021, clade 10H/501Y.V2) and B.1.617 (delta; SARS-CoV-2, Human, 2021, Germany ex India, 20A/452R) were supplied through the European Virus Archive Global (EVAg) platform, by the National Reference Centre for Respiratory Viruses hosted by Institut Pasteur (Paris, France) and the Robert Koch Institute (German Federal Institute for Infectious and Non-Communicable Diseases, Berlin, Germany), respectively. All SARS-CoV-2 virus stocks were grown on Vero E6 cells and virus infectivity titers were determined by standard plaque or median tissue culture infectious dose ($TCID_{50}$) assays as previously described.[67]

Mouse Strains: C57BL/6 mice (Charles River Laboratories) were bred at CNIC under specific pathogen-free conditions. Age-matched female 6- to 8-week-old mice were used and randomized before treatment. Immunogenicity experiments in C57BL/6 mice were approved by the animal ethics committee at CNIC and by the Division of Animal Protection of the Comunidad de Madrid (PROEX 240/16). Transgenic K18-hACE2 mice (The Jackson Laboratory), expressing hACE2 under control of the cytokeratin 18 promoter on the C57BL/6 background, were used in the protective efficacy studies. 9-week-old female K18-hACE2 mice were used and randomized between treatment groups after SARS-CoV-2 challenge. Protective efficacy experiments with K18-hACE2 mice were performed in the biosafety level 3 (BSL-3) facilities at the Centro de Investigación en Sanidad Animal (CISA)-Instituto Nacional de Investigaciones Agrarias (INIA)-CSIC (Valdeolmos, Madrid, Spain). Efficacy experiments were approved by the animal ethics committee at INIA and by the Division of Animal Protection of the Comunidad de Madrid (PROEX 161.5/20). All animal procedures were

conformed to Spanish law under the Royal Decree (RD 53/2013) and in accordance with EU Directive 2010/63EU and Recommendation 2007/526/EC.

Production and Purification of the SARS-CoV-2 S and RBD Proteins: The SARS-CoV-2 HexaPro S protein cDNA,[68] corresponding to Wuhan-Hu-1 strain, was codon-optimized and synthesized (GenScript). The gene was cloned into mammalian expression vector pcDNA3.1(−) carrying a C-terminal Twin-Strep tag. Four days following the transfection in FreeStyle 293F cells with 293fectin transfection reagent (Life Technologies), the culture supernatants were collected and purified with Strep-Tactin affinity chromatography resin (IBA LifeSciences) followed by SEC using a Superose 6 Increase 10/300 GL column (Cytiva). Concentrated purified fractions were analyzed by 0.1% w/v sodium dodecyl sulfate (SDS)−4–20% w/v polyacrylamide gel electrophoresis (PAGE). Proper protein folding and conformation was certified by antibody recognition in ELISA using anti-RBD (# A2286, Biovision), anti-N-terminal domain (NTD) (# A2269, Biovision) and anti-S2 (# 40590-D001, SinoBiological) mAbs.

The SARS-CoV-2 Wuhan-Hu-1/B.1 strain S protein RBD, defined as amino acids R328-L533, was expressed in pcDNA3.1(+) with an N-terminal mu-phosphatase signal peptide and a C-terminal octa-histidine tag (BEI Resources NR-52422).[14] The RBD was produced using Expi293F transfection, supernatant was harvested after 3 d, and protein was purified using a 10 mL bed volume of Talon Superflow Metal Affinity Cobalt Resin (Takara Bio). Purified protein was filtered and concentrated into buffer containing 20×10^{-3} M Tris, 300×10^{-3} M NaCl, and 200×10^{-3} M imidazole, pH 8.0. SDS-PAGE was run to check purity and a modified competition ELISA as control for binding to hACE2 (Acro BioSystems).

Generation of Antibody Expression Vectors: DNA fragments encoding for E, V, and TN (EV-tandem) nanobodies were synthesized by GeneArt (Thermo Fisher Scientific) including them within the following vectors: pcDNA3.1(+)-E V_{HH}-Myc-His, pcDNA3.1(+)-V V_{HH}-Flag-His and pcDNA3.1(+)-TN-StrepTagII (Key Resources Table). All constructs included an in frame fused wild type N-terminal interleukin-2 (IL-2) signal peptide for effective protein secretion to the medium. The expression vector for the TN^T trimerbody was generated by subcloning L23-TIE cDNA fragment from vector pCR3.1 (+)-MFE23scFv-L23-TIE-Myc-His (previously described[43]) into pCR3.1-TN-StrepTagII by mean of *Not*I/*BamH*I restriction enzymes. To generate the TN^TDNGR-1 construct, the cDNA for L15-7H11scFv-StrepTagII fragment (GeneArt) was subcloned using *Bgl*II/*Xba*I cloning sites into the TN^T trimerbody parental vector resulting in pcDNA3.1(+)-TN-L23-TIE-L15-7H11-StrepTagII. All the sequences were verified using primers FwCMV and RvBGH (Key Resources Table).

Production and Purification of Recombinant Engineered Antibodies: The generation of HEK-293 stable transfectants was done in DCM by selection with 500 mg mL^{-1} G418 (Life Technologies) after Lipofectamine 3000 (Invitrogen) transfection. Large-scale protein production was done by collecting periodically the media of stable transfectants. TN, TN^T, and TN^TDNGR-1 were purified from conditioned culture media by Strep-Tactin affinity chromatography in an AKTA Prime Plus FPLC System (Amersham Biosciences). Finally, the elution fractions corresponding to purified antibodies were dialyzed against PBS. Protein concentration calculation was carried out by UV-absorbance measurements on an Uvikon 930 spectrophotometer (Kontron Instruments). Purified antibodies were analyzed by 0.1% w/v SDS-15% w/v PAGE in reducing conditions followed by Coomassie brilliant blue R-250 (BioRad Laboratories) staining, for optimal band visualization. Gel image acquisition was performed with a ChemiDoc MP Imaging System (BioRad Laboratories).

ELISA Assays: The ability of TN based constructs to bind purified SARS-CoV-2 RBD was analyzed by ELISA. Briefly, Nunc MaxiSorp flat-bottom 96-well plates (Thermo Fischer Scientific) were coated (0.2 µg/well) with recombinant B.1 RBD. After washing and blocking with 300 µL PBS-BSA, 100 µL of conditioned media from transfected HEK-293 cells were added to the wells and incubated for 1 h at room temperature. After three washes, 100 µL of the corresponding anti-Strep mAb (# 2-1507-001, IBA Lifesciences) were added for 1 h at room temperature. Finally, HRP-conjugated GAM IgG (# 115-035-003, Jackson ImmunoResearch Labs) was added, after which the plate was washed again and developed. Purified TN and TN^T (50, 10, and 1×10^{-9} M) ability to bind different strain RBDs was performed in the same way. RBD interaction with biotinylated hACE2 (# Q9BYF1-1, AcroBiosystems) was used as control by adding 100 µL at 0.1 µg mL^{-1} for 1 h, followed by HRP-conjugated streptavidin (# 554 066, BD Biosciences) in the same conditions. All optical density measurements were done using a Multiskan FC apparatus (Thermo Scientific Scientific).

Biolayer Interferometry: The binding of TN and TN^T to immobilized B.1 or B.1.351 (beta) RBDs was measured using biolayer interferometry (BLI) on an Octet RED96 system (Fortebio). The RBD was immobilized onto AR2G biosensors (Fortebio) at pH 5.0 using a standard amine reactive coupling protocol (activation with EDC/s-NHS and quenching with ethanolamine). The antibodies in HEPES-buffered saline (HBS; 20×10^{-3} M HEPES, 150×10^{-3} M NaCl, pH 7.4) at 50 and 10×10^{-9} M were associated with the RBD for 30 min, after which the dissociation of antibody from the biosensor was measured for 1 h, to determine their binding kinetics. The experimental data was then fitted to a 1:1 binding model using the Octet Data Analysis software (Fortebio). To determine the blocking of ACE2's RBD binding, 150×10^{-9} M of TN monomer or 50×10^{-9} M of TN^T were associated with immobilized B.1 RBD for 10 min, after which 100×10^{-9} M of soluble hACE2 (Acro Biosystems) was added and associated with RBD for 30 min. To investigate bispecific interactions between the TN^TDNGR-1, immobilized RBD and DNGR-1 in solution, RBD-coated biosensors were first prepared as described above. Then, 50×10^{-9} M of the TN^TDNGR-1 in HBS was then incubated with the biosensors for 30 min, followed by 5 min of dissociation in HBS. The biosensors were then moved into 50×10^{-9} M of mouse DNGR-1 Fc chimera in HBS and incubated for 30 min, followed by 5 min of dissociation.

SEC-MALS Experiments: Static light scattering experiments were performed on a Superdex 200 Increase 10/300 GL column (Cytiva) attached in-line to a DAWN EOS light scattering photometer and an Optilab rEX differential refractive index detector (both from Wyatt Technology). The chromatography was run at room temperature and the scattering detector was thermostated at 23 °C. The column was equilibrated with running buffer (PBS pH 7.4 plus 150×10^{-3} M NaCl, 0.1 µm filtered) and the SEC-MALS system was calibrated with a sample of BSA at 2 mg mL^{-1} in the same buffer. ≈150 µL of the solutions at 0.5 mg mL^{-1} were injected into the column at a flow rate of 0.5 mL min^{-1}. Data acquisition and analysis were performed using ASTRA software (Wyatt Technology). The reported molar masses correspond to the center of the chromatography peaks. Based on numerous measurements on BSA samples under similar conditions it was estimated that the experimental error in the molar mass is around 5%.

Circular Dichroism: Circular dichroism (CD) measurements were performed with a Jasco J-715 spectropolarimeter (JASCO). The spectra were recorded on protein samples at 0.02 mg mL^{-1} in PBS pH 7.4 plus 150×10^{-3} M NaCl using a 0.2 cm path length quartz cuvette at 25 °C. Thermal denaturation curves from 10 to 95 °C were recorded on the same protein samples and cuvette by increasing temperature at a rate of 1 °C min^{-1} and measuring the change in ellipticity at 218 nm.

Microfluidic Diffusional Sizing: The change in hydrodynamic radius (R_h) of TN^T trimerbody and its subsequent complex with SARS-CoV-2 S protein was measured by microfluidic diffusional sizing (MDS).[69] Then, R_h values of fluorescently labeled species in their native state in solution are included into a plot of the hydrodynamic radii of a range of native and denatured standard proteins obtained using dynamic light scattering and pulsed field gradient nuclear magnetic resonance.[70] TNT (1×10^{-6} M) was labelled with Fluidiphore rapid amine 503 through amine coupling. The sample was incubated at 4 °C overnight and the size of the conjugated protein was determined through measuring the hydrodynamic radius, R_h, using the Fluidity One-W platform. To determine the R_h upon complex formation, the unlabeled HexaPro S protein (1×10^{-6} M) was incubated 1:1 with labeled TN^T for 5 min. The change in R_h was monitored by Fluidity One-W instrument.

Cryo-EM: A sample of 0.5 mg mL^{-1} HexaPro S protein was prepared in the protein production core (C1) of the Center for Biomolecular Therapeutics (Rockville, Maryland, USA), as previously described.[71] It was mixed in 1:1 molar ratio with TN^T trimerbody and vitrified on cryo-EM grids using standard protocols with an FEI Vitrobot Mark IV. Images were collected on an FEI 200 kV Glacios electron microscope equipped with a

Gatan K3 direct electron detector and processed in cryoSPARC (data collection statistics are shown in Figure S5F in the Supporting Information). Particles were selected using blob picking and these were used to produce an ab initio model that was quickly refined and used to generate particle templates for repicking and 2D classification/ filtering. Multiple cycles of 3D refinement in cryoSPARC[72] resulted in electron density maps at 3.80 Å resolution as determined from gold-standard Fourier shell correlation (GSFSC) curves. This model was in excellent agreement with overall structure of the S protein; however, density regions corresponding to bound TN^T elements were difficult to resolve likely due to heterogeneity and dynamic nature of the protein complex. To improve the quality and interpretability of the electron density, particle stacks were exported into Relion[73] and subjected to 3D refinement with imposed C3 symmetry followed by 3D classification without any symmetry to allow determination of subconformations not compliant with C3 symmetry. This produced 3 distinct subconformations that were subjected to a single final round of non-uniform refinement in cryoSPARC and local map sharpening in PHENIX.[73]

Cryo-EM Model Building and Refinement: Model building on the map resulting after the incubation of TN^T with the HexaPro S protein was done in Coot 0.9.6.[74] The coordinates corresponding to PDB 7B18[23] were used as a starting model, placed into it after performing a molecular replacement step and posterior refinement in PHENIX,[75] that included rigid body, simulated annealing and morphing. The model was manually fitted into the density sharpened map and several runs of refinement done in PHENIX until a final reliable model were obtained. Figures were generated using ChimeraX.[76]

Flow Cytometry Studies: The ability of both TN-based trimerbodies to bind SARS-CoV-2 B.1 S protein on cell surface was studied by flow cytometry. HEK-293 or HEK-293^S cells were incubated with supernatants or purified trimerbodies (1 µg mL^{-1}) followed by anti-Strep mAb and PE-GAM IgG antibody (# 115-116-071, Jackson ImmunoResearch Labs) for 30 min at 4 °C, each of them. Between incubations and after the final one, the cells were sedimented by centrifugation (1200 g, 4 °C, 5 min) and washed with PBS supplemented with 0.05% v/v FBS (PBS-FBS) for three times. As a control, both cell types were incubated with rabbit anti-SARS-CoV-2 IgG SB-40592 (# 40592-R001, Sino Biological) followed by AF488-conjugated donkey anti-rabbit IgG (# 711-545-152, Jackson ImmunoResearch Labs). The binding of TN^TDNGR-1 to cell surface mouse CLEC9A/DNGR-1 was assayed using parental B3Z and transfected $B3Z^{DNGR-1}$ cell lines following the same protocol and staining as explained above for S protein labelling. The PE-conjugated rat anti-human Clec9A (CD370) antibody (clone 3A4/Clec9A) (# 563 488, BD Biosciences) was used as control. Furthermore, the capacity of TN^TDNGR-1 for targeting soluble RBD specifically to $B3Z^{DNGR-1}$ cells was analyzed by preincubating AF647-conjugated RBD (1 µg mL^{-1}) with TN^TDNGR-1 or TN^T (1 µg mL^{-1}) for 30 min at room temperature. Then, the mixtures were added to the cells and followed by incubation of 30 min at 4 °C. All the samples were processed on a FACScan apparatus (BD Biosciences) while data analysis was done using the FlowJo Software (BD Biosciences). For labeling and endocytosis studies in BMDCs, cells were incubated with culture media containing TN^T or TN^TDNGR-1 (1× supernatant and 10×, respectively) for 30 min at 4 °C. Cells were then washed and kept for different times at 37 °C or 4 °C before being incubated with AF647-conjugated RBD (1 µg mL^{-1}) for 1 h at 4 °C and further stained with antibodies to distinguish the main DC subpopulations: type 1 DCs (cDC1s, $CD11c^+B220^-XCR1^+$), type 2 DCs (cDC2s, $CD11c^+B220^-SIRPa^+$), and pDCs ($CD11c^+B220^+$). Stained cells were analyzed on BD FACSCanto flow cytometer (BD Biosciences).

Confocal Microscopy: MuTuDC cells were incubated with culture media containing TN^T or TN^TDNGR-1 (1× supernatant and 10×, respectively) for 30 min at 4 °C, washed and stained with AF647-conjugated RBD (1 µg mL^{-1}) for 1 h at 4 °C. Cells were then thoroughly washed and incubated in complete media for different times at 4 or 37 °C. Then, stained cells were resuspended in PBS, plated in Cell-Tak (Corning) coated coverslips, fixed using 4% paraformaldehyde (PFA) and mounted for visualization in a Zeiss LSM 700 confocal microscope.

Production of SARS-CoV-2 S-Pseudotyped VSV Particles: Vesicular stomatitis virus-G (VSV-G) pseudotyped rVSV-luc recombinant viruses were produced according to previously published protocol by cotransfection of BHK-21 cells (BHK-21/WI-2, Kerafast) with expression vector coding for VSV-G and rVSVΔG-luciferase vector (G*ΔG-luciferase; Kerafast) that contains firefly luciferase instead of the VSV-G open reading frame.[77] Briefly, BHK-21 cells were transfected using Lipofectamine 3000 protocol to express the SARS-CoV-2 S protein and after 24 hours, the transfected cells were inoculated with a replication-deficient VSV-G-rVSV-luc pseudotype (multiplicity of infection (MOI) of 3). Following 1 h incubation at 37 °C, the inoculum was removed, cells were washed extensively with PBS and fresh DCM was added. SARS-CoV-2 S-pseudotyped rVSV-luc particles were harvested 20 h postinoculation, clarified from cellular debris by centrifugation and stored at −80 °C. Infectious titers were estimated as $TCID_{50}$ mL^{-1} by limiting dilution of the SARS-CoV-2 S rVSV-luc-containing supernatants on Vero E6 cells. Luciferase activity was determined by Steady-Glo Luciferase Assay System in a Glo-Max Navigator Microplate Luminometer (both from Promega). The SARS-CoV-2-pseudotyped rVSV-luc variants used were SARS-CoV-2 S protein B.1, alpha, beta, gamma, delta, and kappa. The SARS-CoV-2 S protein mutant D614G (B.1) was generated by site-directed mutagenesis using as an input DNA the expression vector encoding SARS-CoV-2 S 614D by Q5 Site Directed Mutagenesis Kit (New England Biolabs) following the manufacturer's instructions. SARS-CoV-2 alpha (B.1.1.7; GISAID: EPI_ISL_608 430), beta (B.1.351; GISAID: EPI_ISL_712 096), gamma (P.1; GISAID: EPI_ISL_833 140), delta (B.1.617.2; GISAID: EPI_ISL_1 970 335), and kappa (B.1.617.1; GISAID: EPI_ISL_1 970 331) were optimized, synthesized and cloned into pcDNA3.1 (GeneArt).

SARS-CoV-2 S Protein-Pseudotyped VSV Neutralization Assay: TN and TN^T neutralization activity were examined in triplicates at concentrations in the range 0.64×10^{-12} M – 10×10^{-9} M using a SARS-CoV-2-pseudotyped rVSV-luc system. As controls, the SB-40592 anti-RBD neutralizing mAb and sotrovimab biosimilar (anti-S glycoprotein mAb) were used in the range 0.88×10^{-12} M – 13.86×10^{-9} M. For neutralization experiments, viruses-containing transfection supernatants were normalized for infectivity to a MOI of 0.5-1 and incubated with the antibodies at 37 °C for 1 hour in 96-well plates. After the incubation time, 2×10^4 Vero E6 cells were seeded onto the virus-antibody mixture and incubated at 37 °C for 24 h. Cells were then lysed and assayed for luciferase expression. Half maximal effective concentration (EC_{50}) and 95% confidence intervals (95% CI) were calculated using a nonlinear regression model fit with settings for log agonist versus normalized response curve using GraphPad Prism v8 Software.

Live SARS-CoV-2 Neutralization Assay: The neutralization activity of TN-based trimerbodies was also measured by a microneutralization test assay by using live SARS-CoV-2 virus, as previously described.[67] Serially five-fold diluted antibodies (in the range 0.3×10^{-12} M – 5×10^{-9} m) in DMEM-2% v/v FBS medium were incubated at a 1:1 ratio with 200 $TCID_{50}$ of live SARS-CoV-2 B.1 (MAD6 isolate, containing the D614G mutation), B.1.351 (beta) and B.1.617.2 (delta) VOCs in U-bottom 96-well tissue culture plates for 1 h at 37 °C. Then, mixtures of antibodies and live SARS-CoV-2 virus were added in triplicates to Vero E6/TMPRSS2 cell monolayers seeded in 96-well plates at 2×10^4 cells/well, and plates were incubated at 37 °C, in a 5% CO_2 incubator for 3 d. Then, cells were fixed with 10% formaldehyde for 1 h and stained with crystal violet. When plates were dried, crystal violet was diluted in H_2O-10% w/v SDS and optical density was measured in a luminometer at 570 nm. Fifty percent neutralization titer (NT_{50}) and 95% CI were calculated using a nonlinear regression model fit with settings for log agonist versus normalized response curve using GraphPad Prism v8 Software.

Immunization of Immunocompetent C57BL/6 Mice: Trimerbodies in combination with SARS-CoV-2 S protein super stable trimer (Acro Biosystems) were injected subcutaneously (s.c.) into both hind paws of C57BL/6 mice. The immunization followed a prime-boost scheme 7 days apart. Mice (n = 5/group, but PBS n = 3/group) were primed either with (1) PBS as control; (2) 2 µg of S protein alone; (3) 3 µg of TN^T + 2 µg of S protein; or (4) 3 µg of TN^TDNGR-1 + 2 µg of S protein. For the boost, mice were injected s.c. respectively with (1) PBS as control; (2) 1 µg of S protein alone; (3) 1.5 µg of TN^T + 1 µg of S protein; or (4) 1.5 µg of TN^TDNGR-1 + 1 µg of S protein. These amounts were divided equally between the two hind paws. All conditions except PBS included 5 µg CpG ODN 1826 and

5 µg Poly (I:C) LMW (both from InvivoGen) per mouse as adjuvants. The injection volume was 25 µL per paw. Mice were euthanized on day 14 (7 d post-boost) and spleens and popliteal lymph nodes (pLNs) were harvested to assess cellular responses by flow cytometry analysis, and serum samples were collected to evaluate humoral responses.

Cellular Response Analysis of Immunized C57BL/6 Mice: Spleens and pLNs were smashed through a 70 µm filter in R10 medium. In spleen suspensions, erythrocytes were lysed using 1 mL of red blood cell lysing buffer Hybri-Max (Sigma-Aldrich). Cells were stained with fluorochrome labelled antibodies directed against B220-FITC (# MABF608, Invitrogen), CD11c-BV421 (# 566 877, BD Biosciences), CD11c-APC/Fire (# 117 351, BioLegend), CD19-BV421(# 302 233, BioLegend), CD8-APC/Fire (# 100 765, BioLegend), CD4-APC (# 553 051, BD Biosciences), CD44-FITC (#11-0441-82, Invitrogen), Sirpa-PE/Cy7 (# 25-1721-82, Invitrogen), and XCR1-PE (# 148 203, Biolegend), CD16/CD32 Fc Shield (# 70-0161, Tonbo Biosciences) was used to reduce nonspecific binding. All antibodies were used at a 1:200 dilution. Tetramer specific for SARS-CoV-2 S protein, H-2Kb (^{539}VNFNFNGL^{546}), was provided by the NIH Tetramer Facility at Emory University (1:100 dilution). Samples were stained in cold PBS supplemented with 2.5% v/v FBS and 2 mM EDTA. Tetramer staining was performed at room temperature for 15 min, followed by sequential surface staining with the appropriate antibody cocktail at 4 °C for 15 min. Dead cells were excluded using DAPI. Data was acquired on a LSRFortessa Cell Analyzer (BD Biosciences), using FACSDiva software, and analyzed using FlowJo v10.8 Software (BD Biosciences).

Humoral Response Analysis of Immunized C57BL/6 Mice: Serum samples were prepared by incubating blood samples in collection tubes without anticoagulant for 15 min at room temperature to allow clotting to occur. Then samples were centrifuged at 15,000 rpm for 15 min, and serum was moved to a fresh collection tube. S- and RBD-specific immunoglobulin (Ig) levels were determined by ELISA. Briefly, SARS-CoV-2 S protein or RBD were plated in Nunc MaxiSorp flat-bottom 96-well plates (Thermo Fischer Scientific) in carbonate buffer or PBS, respectively, at 1 µg mL^{-1} overnight at 4 °C. Then, the plates were washed three times with PBS and blocked with BSA-PBS at least 1 h at 37 °C. After washing again, serum was plated by duplicate at 1/50, 1/250, 1/1250, and 1/6250 serial dilutions in PBS containing 1% w/v BSA to visualize dose-response signals. Samples were incubated 2 h at room temperature and washed three times with PBS-0.05% v/v Tween-20. Plates containing serum samples were incubated with biotinylated anti-mouse IgM, total IgG, IgG1, and IgG2c (all from BD) at 2 µg mL^{-1} for 1 h at room temperature followed by three washes with PBS-0.05% (v/v) Tween-20 and incubation with HRP-conjugated streptavidin at 1 µg mL^{-1} for 30 min at room temperature. All plates were then washed again and developed in the presence of 3,3′,5,5′-Tetramethylbenzidine (TMB) substrate (Sigma-Aldrich) and stopped by 1 M H_2SO_4 solution. Absorbance was read at 450 nm subtracting background at 620 nm.

Protective Therapeutic Efficacy Study in Transgenic K18-hACE2 Mice: Female K18-hACE2 mice (9-weeks-old) were used to evaluate the capacity of TN^T and TN^{T}DNGR-1 antibodies to protect against SARS-CoV-2 infection in a therapeutic administration schedule. After a lethal dose challenge (1×10^5 PFUs/mouse) with SARS-CoV-2 (MAD6 strain) by intranasal route in 50 µL of PBS, mice were divided randomly in four groups ($n = 8$/group) and 17 h later were inoculated i.p. with 100 µg of TN^{T}DNGR-1, 65 µg of TN^T (equimolar to TN^{T}DNGR-1), 100 µg of sotrovimab or PBS (as a control of infection) in a total volume of 200 µL. In addition, noninfected and nontreated mice ($n = 8$) were used as a control group of healthy animals.

Mice were monitored for body weight change and mortality for 20 d p.c. Animals with more than 25% of body weight loss were euthanized. At days 5 and 20 p.c., four mice per group were euthanized, and lungs and serum samples were collected. Right lung lobes were divided longitudinally in two, with one part placed in RNALater stabilization reagent (Sigma-Aldrich) and stored at −80 °C for RNA extraction, and the other part stored also at −80 °C for the analysis of infective virus yields. At day 20 p.c. left lung was freshly processed for cellular immune response analysis. At both end point times blood was collected by submandibular bleeding, maintained at 37 °C for 1 h, kept at 4 °C overnight, and centrifuged at 3600 rpm for 20 min at 4 °C to obtain the serum samples, which was then inactivated at 56 °C for 30 min and kept at −20 °C until use.

Analysis of SARS-CoV-2 RNA by RT-qPCR: Lungs from K18-hACE2 mice were harvested at day 5 p.c. and stored in RNALater (Sigma-Aldrich) at −80 °C until homogenized with a gentleMACS dissociator (Miltenyi Biotec) in 2 mL of RLT buffer (Qiagen) plus β-mercaptoethanol (Sigma-Aldrich) and aliquoted. Then, 600 µL of homogenized lung tissue was used to isolate total RNA using the RNeasy minikit (Qiagen), according to the manufacturer's specifications. First strand cDNA synthesis and subsequent real-time PCR were performed in one step using NZYSpeedy One-step RT-qPCR Master Mix (NZYTech), according to the manufacturer's specifications using ROX as reference dye. SARS-CoV-2 viral RNA content was determined using previously validated set of primers and probes specific for the SARS-CoV-2 subgenomic RNA for the protein E and the genomic virus RNA dependent RNA polymerase (RdRp) gene.[78] Data were acquired with a 7500 real-time PCR system (Applied Biosystems) and analyzed with 7500 software v2.0.6. Relative RNA arbitrary units (A.U.) were quantified relative to a negative group (noninfected mice) and were performed using the $2^{-\Delta\Delta Ct}$ method. All samples were tested in duplicate.

Analysis of SARS-CoV-2 Virus Yields by Plaque Assay: Lungs from K18-hACE2 mice were harvested at day 5 p.c., weighted, and stored directly at −80 °C until homogenized with a gentleMACS dissociator (Miltenyi Biotec) in 2 mL of PBS and aliquoted. Then, undiluted and serial tenfold dilutions of homogenized lung tissue were added in triplicate to Vero E6/TMPRSS2 cell monolayers seeded in 12-well plates at 5×10^5 cells/well. After 1 h of adsorption the inoculums were removed and plates were incubated at 37 °C, 5% v/v CO_2 in 2:1 DMEM 2× containing 4% FBS and Avicel RC-591 (DuPont Nutrition Biosciences ApS). After 4 d, cells were fixed for 1 h with 10% formaldehyde (Sigma-Aldrich), then the supernatant was removed, and plaques were visualized by adding 0.5% w/v crystal violet solution (Sigma-Aldrich). SARS-CoV-2 titers were determined in PFUs per gram of lung tissue.

Humoral Response Analysis in the Protective Therapeutic Efficacy Experiment in Transgenic K18-hACE2 Mice: S-specific IgM measurements in individual sera samples from SARS-CoV-2 infected and treated K18-hACE2 mice were done by ELISA as described above in prime-boost immunization assays. S-, RBD-, and N-specific IgG antibody levels were determined by ELISA, as previously described.[67,78,79] Briefly, 96-well Nunc MaxiSorp plates were coated with 50 µL of purified recombinant SARS-CoV-2 S or RBD proteins (2 µg mL^{-1}) in PBS overnight at 4 °C. The SARS-CoV-2 S and RBD proteins used to coat the plates derived from the Wuhan strain (GenBank accession number MN908947.3) and were previously described.[67,78,79] Plates were washed with PBS-0.05% v/v Tween-20 and blocked with 5% milk in PBS for 2 h at room temperature. Individual serum samples were diluted in duplicate in PBS-0.05% Tween-1% milk, added to plates, and incubated for 1.5 h at room temperature. Plates were then washed, and secondary HRP-conjugated GAM IgG mAb (Southern Biotech) diluted 1:1000 in PBS-0.05% Tween-1% milk was added and incubated for 1 hour at room temperature. Plates were washed, the TMB substrate (Sigma-Aldrich) was added, and the reaction was stopped by adding 1 M H_2SO_4. Absorbance was read at 450 nm. Antigen-specific IgG and IgM serum levels were evaluated by absorbance summation method, which sums the observed absorbance values from all dilutions employed to obtain one data point for each sample to be used for comparison.[80]

Determination of Administrated Antibody Concentration in Serum: The concentration of TN^T, TN^{T}DNGR-1 or sotrovimab in serum samples at day 5 and 20 p.c. was determined by ELISA using 1:5 serial dilutions of the corresponding purified antibodies for standard. Briefly, Nunc MaxiSorp flat-bottom 96-well plates (Thermo Fischer Scientific) were coated with recombinant B.1 RBD (0.2 µg/well). After washing and blocking with 300 µL PBS-BSA, 50 µL of individual sera, 1/20 and 1/100 times diluted, were incubated for 1 h at room temperature. For TN^T and TN^{T}DNGR-1 or sotrovimab, after three washes, 100 µL of the corresponding HRP-conjugated rabbit anti-camelid V_{HH} cocktail (# A02016, Genescript) or HRP-conjugated goat anti-human IgG mAb (# A0170, Sigma-Aldrich) were added, respectively, and incubated 1 h at room temperature. Finally, the plate was washed again and developed. All samples were analyzed by duplicate per each dilution factor.

Cellular Response Analysis in the Protective Therapeutic Efficacy Experiment in Transgenic K18-hACE2 Mice: Lung cellular suspensions were obtained from the left lung of K18-hACE2 mice harvested at day 20 p.c., homogenized with a gentleMACS dissociator (Miltenyi Biotec) in R10 medium and then erythrocytes were lysed by using ACK lysis buffer (Gibco). S-specific H-2Kb tetramer staining was performed, acquired and analyzed as previously described for the C57BL/6 prime-boost immunization assay. The magnitude, breadth and polyfunctionality of SARS-CoV-2 S-specific $CD4^+$ and $CD8^+$ T cells expressing CD107a, and/or secreting IFNγ, and/or TNFα, and/or IL-2 were analyzed by ICS as previously described[78,79] in lung cell samples stimulated with a SARS-CoV-2 S peptide pool (1 µg mL^{-1}) (JPT Peptide Technologies), spanning the S1 and S2 regions of the S protein from the Wuhan strain, and containing 158 (S1) and 157 peptides (S2) as consecutive 15-mers overlapping by 11 amino acids. After left lung processing, 4×10^6 fresh isolated cells were seeded on M96 plates and stimulated overnight in complete RPMI 1640 medium supplemented with 10% FBS containing 1 µL mL^{-1} Golgiplug (BD Biosciences) to inhibit cytokine secretion, 1× monensin (eBioscience, Thermo Fisher Scientific), and anti-CD107a–FITC (BD Biosciences). Cells were then washed, stained for surface markers, fixed, permeabilized (Cytofix/Cytoperm kit; BD Biosciences), and stained intracellularly with the appropriate antibodies. Dead cells were excluded using the violet LIVE/DEAD stain kit (Invitrogen). The fluorochrome-conjugated antibodies used for functional analyses were CD3-PE-CF594, CD4-APC-Cy7, CD8-V500, IFN-γ–PE-Cy7, TNF-α–PE, and IL-2–APC. All antibodies were from BD Biosciences. Cells were acquired with a Gallios flow cytometer (Beckman Coulter), and data analyzed with the FlowJo software version 10.4.2 (Tree Star), as previously described.[78,79] Gating strategy and example is shown in Figure S7C,D in the Supporting Information.

Equipment and Settings: Gels and Western blot membrane images from Figures S2, S3, and S7 (Supporting Information) were acquired and analyzed using the ChemiDoc MP Imaging System and Image Lab analysis software (both from BioRad Laboratories). If brightness or contrast processing of gel and blot images has been performed, it was applied to the entire image, including controls. No high-contrast gels or blots have been displayed. When necessary, cropped gels and juxtaposing images were displayed to improve the clarity and conciseness of the presentation, being shown in the figure. All optical density measurements were done using a Multiskan FC apparatus (Thermo Fischer Scientific).

Statistical Analysis: Statistical analysis was performed using GraphPad Prism Software version 8.0. In general, the in vitro experiments were done in triplicates and values are presented as mean ± standard error of the mean (SEM) from one of at least two independent experiments. In the immunogenicity experiments in C57BL/6 mice, significant differences (*P* value) were discriminated by applying one-way ANOVA followed by Tukey's multiple comparison test. The multiparametric read out analysis of protective efficacy experiment in K18-hACE2 mice, in general was done by applying one-way ANOVA followed by Tukey's multiple comparison test for significant differences discrimination.

Supporting Information

Supporting Information is available from the Wiley Online Library or from the author.

Acknowledgements

SARS-CoV-2 B.1.351 and B.1.167.2 viruses used in this study were obtained through the European Virus Archive Global (EVA-GLOBAL) project that has received funding from the European Union's Horizon 2020 research and innovation programme under grant agreement No 653316. SARS-CoV-2 B.1 (MAD6 isolate) was kindly provided by José M. Honrubia and Luis Enjuanes (CNB-CSIC, Madrid, Spain). The authors thank Centro de Investigación en Sanidad Animal (CISA)-Instituto Nacional de Investigaciones Agrarias (INIA-CSIC) (Valdeolmos, Madrid, Spain) for the BSL-3 facilities. Research in LA-V laboratory was funded by the BBVA Foundation (Ayudas Fundación BBVA a Equipos de Investigación Científica SARS-CoV-2 y COVID-19); the MCIN/AEI/10.13039/501100011033 (PID2020-117323RB-I00 and PDC2021-121711-I00), partially supported by the European Regional Development Fund (ERDF); the Carlos III Health Institute (ISCIII) (DTS20/00089), partially supported by the ERDF, the Spanish Association Against Cancer (AECC 19084); the CRIS Cancer Foundation (FCRIS-IFI-2018 and FCRIS-2021-0090), the Fundación Caixa-Health Research (HR21-00761 project IL7R_LungCan), and the Comunidad de Madrid (P2022/BMD-7225 NEXT_GEN_CART_MAD-CM). Work in the DS laboratory was funded by the CNIC; the European Union's Horizon 2020 research and innovation program under grant agreement ERC-2016-Consolidator Grant 725091; MCIN/AEI/10.13039/501100011033 (PID2019-108157RB); Comunidad de Madrid (B2017/BMD-3733 Immunothercan-CM); Atresmedia (Constantes y Vitales prize); Fondo Solidario Juntos (Banco Santander); and "La Caixa" Foundation (LCF/PR/HR20/00075). The CNIC was supported by the ISCIII, the MCIN and the Pro CNIC Foundation and is a Severo Ochoa Center of Excellence (CEX2020-001041-S funded by MCIN/AEI/10.13039/501100011033). Research in RD laboratory was supported by the ISCIII (PI2100989) and CIBERINFEC; the European Commission Horizon 2020 Framework Programme (grant numbers 731868 project VIRUSCAN FETPROACT-2016, and 101046084 project EPIC-CROWN-2); and the Fundación Caixa-Health Research (grant number HR18-00469 project StopEbola). Research in CNB-CSIC laboratory was funded by Fondo Supera COVID-19 (Crue Universidades-Banco Santander) grant, CIBERINFEC, and Spanish Research Council (CSIC) grant 202120E079 (to J.G.-A.), CSIC grant 2020E84 (to M.E.), MCIN/AEI/10.13039/501100011033 (PID2020-114481RB-I00 to J.G-A. and M.E.), and by the European Commission-NextGenerationEU, through CSIC's Global Health Platform (PTI Salud Global) to J.G.-A. and M.E. Work in the CIB-CSIC laboratory was supported by MCIN/AEI/10.13039/501100011033 (PID2019-104544GB-I00 and 2023AEP105 to CA, and PID2020-113225GB-I00 to F.J.B.). Cryo-EM data were collected at the Maryland Center for Advanced Molecular Analyses which was supported by MPOWER (The University of Maryland Strategic Partnership). I.H.-M. receives the support of a fellowship from la Caixa Foundation (ID 100010434, fellowship code: LCF/BQ/IN17/11620074) and from the European Union's Horizon 2020 research and innovation programme under the Marie Skłodowska-Curie grant agreement no. 71367. L.R.-P. was supported by a predoctoral fellowship from the Immunology Chair, Universidad Francisco de Vitoria/Merck.

Conflict of Interest

L.A.-V. and L.S. are co-founders of Leadartis S.L., M.C., and R.N. are current employees of Leadartis S.L.

Author Contributions

R.L.-G., P.P., I.H.-M., I.A.-B., G.A., D.A., S.F., J.L., N.L., S.L.H., A.S.-T., L.R.-P., C.A., R.N., M.C., E.P., R.G.-R., E.G.-R. designed and performed the experiments and analyzed the data. R.L.-G., P.P., I.H.-M. and prepared the figures. X.S., Y.L., K.A.A., D.A., W.Y., A.D.M. helped with the antibody complex visualization and modeling. R.L.-G., P.P., I.H.-M., wrote the original draft. R.L.-G. and L.A.-V. prepared the manuscript. R.L.-G., P.P., I.H.-M., R.G.-R., D.S., J.G.-A., L.A.-V. contributed to the experimental and conceptual design and edited the manuscript. L.A.-V., J.G.-A., D.S., M.E., R.D., I.G.M., L.S., D.J.W., F.J.B., E.P. supervised the project.

Data Availability Statement

The data that support the findings of this study are available on request from the corresponding author. The data are not publicly available due to privacy or ethical restrictions.

Keywords

bispecific trimerbody, cross-priming, CTL responses, dendritic cells, neutralizing antibody, SARS-CoV-2

Received: July 16, 2023
Revised: September 24, 2023
Published online: October 20, 2023

[1] L. R. Baden, H. M. El Sahly, B. Essink, K. Kotloff, S. Frey, R. Novak, D. Diemert, S. A. Spector, N. Rouphael, C. B Creech, J. Mcgettigan, S. Khetan, N. Segall, J. Solis, A. Brosz, C. Fierro, H. Schwartz, K. Neuzil, L. Corey, P. Gilbert, H. Janes, D. Follmann, M. Marovich, J. Mascola, L. Polakowski, J. Ledgerwood, B. S. Graham, H. Bennett, R. Pajon, C. Knightly, et al., *N. Engl. J. Med.* **2021**, *384*, 403.

[2] F. P. Polack, S. J. Thomas, N. Kitchin, J. Absalon, A. Gurtman, S. Lockhart, J. L. Perez, G. Pérez Marc, E. D. Moreira, C. Zerbini, R. Bailey, K. A. Swanson, S. Roychoudhury, K. Koury, P. Li, W. V. Kalina, D. Cooper, R. W. Frenck, L. L. Hammitt, Ö. Türeci, H. Nell, A. Schaefer, S. Ünal, D. B. Tresnan, S. Mather, P. R. Dormitzer, U. Sahin, K. U. Jansen, W. C. Gruber, *N. Engl. J. Med.* **2020**, *383*, 2603.

[3] M. Voysey, S. A. C. Clemens, S. A. Madhi, L. Y. Weckx, P. M. Folegatti, P. K. Aley, B. Angus, V. L. Baillie, S. L. Barnabas, Q. E. Bhorat, S. Bibi, C. Briner, P. Cicconi, A. M. Collins, R. Colin-Jones, C. L. Cutland, T. C. Darton, K. Dheda, C. J. A. Duncan, K. R. W. Emary, K. J. Ewer, L. Fairlie, S. N. Faust, S. Feng, D. M. Ferreira, A. Finn, A. L. Goodman, C. M. Green, C. A. Green, P. T. Heath, et al., *South Africa, and the UK* **2021**, *397*, 99.

[4] R. E. Chen, X. Zhang, J. B. Case, E. S. Winkler, Y. Liu, L. A. Vanblargan, J. Liu, J. M. Errico, X. Xie, N. Suryadevara, P. Gilchuk, S. J. Zost, S. Tahan, L. Droit, J. S. Turner, W. Kim, A. J. Schmitz, M. Thapa, D. Wang, A. C. M. Boon, R. M. Presti, J. A. O'halloran, A. H. J. Kim, P. Deepak, D. Pinto, D. H. Fremont, J. E. Crowe, D. Corti, H. W. Virgin, A. H. Ellebedy, et al., *Nat. Med.* **2021**, *27*, 717.

[5] D. Planas, N. Saunders, P. Maes, F. Guivel-Benhassine, C. Planchais, J. Buchrieser, W.-H. Bolland, F. Porrot, I. Staropoli, F. Lemoine, H. Péré, D. Veyer, J. Puech, J. Rodary, G. Baele, S. Dellicour, J. Raymenants, S. Gorissen, C. Geenen, B. Vanmechelen, T. Wawina-Bokalanga, J. Martí-Carreras, L. Cuypers, A. Sève, L. Hocqueloux, T. Prazuck, F. A. Rey, E. Simon-Loriere, T. Bruel, H. Mouquet, et al., *Nature* **2022**, *602*, 671.

[6] P. Wang, M. S. Nair, L. Liu, S. Iketani, Y. Luo, Y. Guo, M. Wang, J. Yu, B. Zhang, P. D. Kwong, B. S. Graham, J. R. Mascola, J. Y. Chang, M. T. Yin, M. Sobieszczyk, C. A. Kyratsous, L. Shapiro, Z. Sheng, Y. Huang, D. D. Ho, *Nature* **2021**, *593*, 130.

[7] J. Hansen, A. Baum, K. E. Pascal, V. Russo, S. Giordano, E. Wloga, B. O. Fulton, Y. Yan, K. Koon, K. Patel, K. M. Chung, A. Hermann, E. Ullman, J. Cruz, A. Rafique, T. Huang, J. Fairhurst, C. Libertiny, M. Malbec, W.-Y. Lee, R. Welsh, G. Farr, S. Pennington, D. Deshpande, J. Cheng, A. Watty, P. Bouffard, R. Babb, N. Levenkova, C. Chen, et al., *Science* **2020**, *369*, 1010.

[8] A. O. Hassan, J. B. Case, E. S. Winkler, L. B. Thackray, N. M. Kafai, A. L. Bailey, B. T. Mccune, J. M. Fox, R. E. Chen, W. B. Alsoussi, J. S. Turner, A. J. Schmitz, T. Lei, S. Shrihari, S. P. Keeler, D. H. Fremont, S. Greco, P. B. Mccray, S. Perlman, M. J. Holtzman, A. H. Ellebedy, M. S. Diamond, *Cell* **2020**, *182*, 744.

[9] T. F. Rogers, F. Zhao, D. Huang, N. Beutler, A. Burns, W.-T. He, O. Limbo, C. Smith, G. Song, J. Woehl, L. Yang, R. K. Abbott, S. Callaghan, E. Garcia, J. Hurtado, M. Parren, L. Peng, S. Ramirez, J. Ricketts, M. J. Ricciardi, S. A. Rawlings, N. C. Wu, M. Yuan, D. M. Smith, D. Nemazee, J. R. Teijaro, J. E. Voss, I. A. Wilson, R. Andrabi, B. Briney, et al., *Science* **2020**, *369*, 956.

[10] A. L. Cathcart, C. Havenar-Daughton, F. A. Lempp, D. Ma, M. Schmid, M. L. Agostini, B. Guarino, J. Di iulio, L. Rosen, H. Tucker, J. Dillen, S. Subramanian, B. Sloan, S. Bianchi, J. Wojcechowskyj, J. Zhou, H. Kaiser, A. Chase, M. Montiel-Ruiz, E. Dellota Jr, A. Park, R. Spreafico, A. Sahakyan, E. J. Lauron, N. Czudnochowski, E. Cameroni, S. Ledoux, Y. Kawaoka, A. Werts, et al., *bioRxiv* **2021**, https://doi.org/10.1101/2021.03.09.434607.

[11] D. M. Weinreich, S. Sivapalasingam, T. Norton, S. Ali, H. Gao, R. Bhore, B. J. Musser, Y. Soo, D. Rofail, J. Im, C. Perry, C. Pan, R. Hosain, A. Mahmood, J. D. Davis, K. C. Turner, A. T. Hooper, J. D. Hamilton, A. Baum, C. A. Kyratsous, Y. Kim, A. Cook, W. Kampman, A. Kohli, Y. Sachdeva, X. Graber, B. Kowal, T. Dicioccio, N. Stahl, L. Lipsich, et al., *N. Engl. J. Med.* **2021**, *384*, 238.

[12] K. Westendorf, S. Žentelis, L. Wang, D. Foster, P. Vaillancourt, M. Wiggin, E. Lovett, R. van der Lee, J. Hendle, A. Pustilnik, J. M. Sauder, L. Kraft, Y. Hwang, R. W. Siegel, J. Chen, B. A. Heinz, R. E. Higgs, N. L. Kallewaard, K. Jepson, R. Goya, M. A. Smith, D. W. Collins, D. Pellacani, P. Xiang, V. de Puyraimond, M. Ricicova, L. Devorkin, C. Pritchard, A. O'Neill, K. Dalal, et al., *Cell Rep.* **2022**, *39*, 110812.

[13] J. Lan, J. Ge, J. Yu, S. Shan, H. Zhou, S. Fan, Q. Zhang, X. Shi, Q. Wang, L. Zhang, X. Wang, *Nature* **2020**, *581*, 215.

[14] A. C. Walls, Y.-J. Park, M. A. Tortorici, A. Wall, A. T. Mcguire, D. Veesler, *Cell* **2020**, *183*, 1735.

[15] R. Yan, Y. Zhang, Y. Li, Lu Xia, Y. Guo, Q. Zhou, *Science* **2020**, *367*, 1444.

[16] C. O. Barnes, C. A. Jette, M. E. Abernathy, K.-M. A. Dam, S. R. Esswein, H. B. Gristick, A. G. Malyutin, N. G. Sharaf, K. E. Huey-Tubman, Y. E. Lee, D. F. Robbiani, M. C. Nussenzweig, A. P. West, P. J. Bjorkman, *Nature* **2020**, *588*, 682.

[17] M. A. Tortorici, M. Beltramello, F. A. Lempp, D. Pinto, Ha. V. Dang, L. E. Rosen, M. Mccallum, J. Bowen, A. Minola, S. Jaconi, F. Zatta, A. De Marco, B. Guarino, S. Bianchi, E. J. Lauron, H. Tucker, J. Zhou, A. Peter, C. Havenar-Daughton, J. A. Wojcechowskyj, J. B. Case, R. E. Chen, H. Kaiser, M. Montiel-Ruiz, M. Meury, N. Czudnochowski, R. Spreafico, J. Dillen, C. Ng, N. Sprugasci, et al., *Science* **2020**, *370*, 950.

[18] C. Liu, H. M. Ginn, W. Dejnirattisai, P. Supasa, B. Wang, A. Tuekprakhon, R. Nutalai, D. Zhou, A. J. Mentzer, Y. Zhao, H. M. E. Duyvesteyn, C. López-Camacho, J. Slon-Campos, T. S. Walter, D. Skelly, S. A. Johnson, T. G. Ritter, C. Mason, S. A. Costa Clemens, F. Gomes Naveca, V. Nascimento, F. Nascimento, C. Fernandes Da Costa, P. C. Resende, A. Pauvolid-Correa, M. M. Siqueira, C. Dold, N. Temperton, T. Dong, A. J. Pollard, et al., *Cell* **2021**, *184*, 4220.

[19] P. Supasa, D. Zhou, W. Dejnirattisai, C. Liu, A. J. Mentzer, H. M. Ginn, Y. Zhao, H. M. E. Duyvesteyn, R. Nutalai, A. Tuekprakhon, B. Wang, G. C. Paesen, J. Slon-Campos, C. López-Camacho, B. Hallis, N. Coombes, K. R. Bewley, S. Charlton, T. S. Walter, E. Barnes, S. J. Dunachie, D. Skelly, S. F. Lumley, N. Baker, I. Shaik, H. E. Humphries, K. Godwin, N. Gent, A. Sienkiewicz, C. Dold, et al., *Cell* **2021**, *184*, 2201.

[20] S. Muyldermans, *Annu. Rev. Biochem.* **2013**, *82*, 775.

[21] M. Scully, S. R. Cataland, F. Peyvandi, P. Coppo, P. Knöbl, J. A. Kremer Hovinga, A. Metjian, J. De La Rubia, K. Pavenski, F. Callewaert, D. Biswas, H. De Winter, R. K. Zeldin, *N. Engl. J. Med.* **2019**, *380*, 335.

[22] J. Huo, A. Le Bas, R. R. Ruza, H. M. E. Duyvesteyn, H. Mikolajek, T. Malinauskas, T. K. Tan, P. Rijal, M. Dumoux, P. N. Ward, J. Ren, D. Zhou, P. J. Harrison, M. Weckener, D. K. Clare, V. K. Vogirala, J. Radecke, L. Moynié, Y. Zhao, J. Gilbert-Jaramillo, M. L. Knight, J. A. Tree, K. R. Buttigieg, N. Coombes, M. J. Elmore, M. W. Carroll, L. Carrique, P. N. M. Shah, W. James, A. R. Townsend, et al., *Nat. Struct. Mol. Biol.* **2020**, *27*, 846.

[23] P.-A. Koenig, H. Das, H. Liu, B. M. Kümmerer, F. N. Gohr, L.-M. Jenster, L. D. J. Schiffelers, Y. M. Tesfamariam, M. Uchima, J. D. Wuerth, K. Gatterdam, N. Ruetalo, M. H. Christensen, C. I. Fandrey, S. Normann, J. M. P. Tödtmann, S. Pritzl, L. Hanke, J. Boos, M. Yuan,

X. Zhu, J. L. Schmid-Burgk, H. Kato, M. Schindler, I. A. Wilson, M. Geyer, K. U. Ludwig, B. M Hällberg, N. C. Wu, F. I. Schmidt, *Science* **2021**, *371*, eabe6230.

[24] D. Wrapp, D. De Vlieger, K. S. Corbett, G. M. Torres, N. Wang, W. Van Breedam, K. Roose, L. Van Schie, M. Hoffmann, S. Pöhlmann, B. S. Graham, N. Callewaert, B. Schepens, X. Saelens, J. S. Mclellan, *Cell* **2020**, *181*, 1004.

[25] J. Xu, K. Xu, S. Jung, A. Conte, J. Lieberman, F. Muecksch, J. C. C. Lorenzi, S. Park, F. Schmidt, Z. Wang, Y. Huang, Y. Luo, M. S. Nair, P. Wang, J. E. Schulz, L. Tessarollo, T. Bylund, G-Yu Chuang, A. S. Olia, T. Stephens, I.-T. Teng, Y. Tsybovsky, T. Zhou, V. Munster, D. D. Ho, T. Hatziioannou, P. D. Bieniasz, M. C. Nussenzweig, P. D. Kwong, R. Casellas, *Nature* **2021**, *595*, 278.

[26] J. Huo, H. Mikolajek, A. Le Bas, J. J. Clark, P. Sharma, A. Kipar, J. Dormon, C. Norman, M. Weckener, D. K. Clare, P. J. Harrison, J. A. Tree, K. R. Buttigieg, F. J. Salguero, R. Watson, D. Knott, O. Carnell, D. Ngabo, M. J. Elmore, S. Fotheringham, A. Harding, L. Moynie, P. N. Ward, M. Dumoux, T. Prince, Y. Hall, J. A. Hiscox, A. Owen, W. James, M. W. Carroll, et al., *Nat. Commun.* **2021**, *12*, 5469.

[27] S. Nambulli, Y. Xiang, N. L. Tilston-Lunel, L. J. Rennick, Z. Sang, W. B. Klimstra, D. S. Reed, N. A. Crossland, Y. Shi, W. P. Duprex, *Sci. Adv.* **2021**, *7*, eabh0319.

[28] P. Pymm, A. Adair, L.-J. Chan, J. P. Cooney, F. L. Mordant, C. C. Allison, E. Lopez, E. R. Haycroft, M. T. O'neill, Li. L Tan, M. H. Dietrich, D. Drew, M. Doerflinger, M. A. Dengler, N. E. Scott, A. K. Wheatley, N. A. Gherardin, H. Venugopal, D. Cromer, M. P. Davenport, R. Pickering, D. I. Godfrey, D. F. J. Purcell, S. J. Kent, A. W. Chung, K. Subbarao, M. Pellegrini, A. Glukhova, W.-H. Tham, *Proc. Natl. Acad. Sci. USA* **2021**, *118*, 12.

[29] J. D. Walter, M. Scherer, C. A. J. Hutter, A. A. Garaeva, I. Zimmermann, M. Wyss, J. Rheinberger, Y. Ruedin, J. C. Earp, P. Egloff, M. Sorgenfrei, L. M. Hürlimann, I. Gonda, G. Meier, S. Remm, S. Thavarasah, G. Van Geest, R. Bruggmann, G. Zimmer, D. J. Slotboom, C. Paulino, P. Plattet, M. A. Seeger, *EMBO Rep.* **2022**, *23*, e54199.

[30] Y. Xiang, S. Nambulli, Z. Xiao, H. Liu, Z. Sang, W. P Duprex, D. Schneidman-Duhovny, C. Zhang, Y. Shi, *Science* **2020**, *370*, 1479.

[31] T. Güttler, M. Aksu, A. Dickmanns, K. M. Stegmann, K. Gregor, R. Rees, W. Taxer, O. Rymarenko, J. Schünemann, C. Dienemann, P. Gunkel, B. Mussil, J. Krull, U. Teichmann, U. Groß, V. C. Cordes, M. Dobbelstein, D. Görlich, *EMBO J.* **2021**, *40*, 107985.

[32] E. Segura, J. A. Villadangos, *Curr. Opin. Immunol.* **2009**, *21*, 105.

[33] I. Caminschi, M. H. Lahoud, K. Shortman, *Eur. J. Immunol.* **2009**, *39*, 931.

[34] Y. Do, H. Koh, C. G. Park, D. Dudziak, P. Seo, S. Mehandru, J.-H. Choi, C. Cheong, S. Park, D. S. Perlin, B. S. Powell, R. M. Steinman, *Eur. J. Immunol.* **2010**, *40*, 2791.

[35] C. Napoletano, A. Rughetti, M. P. Agervig Tarp, J. Coleman, E. P. Bennett, G. Picco, P. Sale, K. Denda-Nagai, T. Irimura, U. Mandel, H. Clausen, L. Frati, J. Taylor-Papadimitriou, J. Burchell, M. Nuti, *Cancer Res.* **2007**, *67*, 8358.

[36] B. Wang, N. Zaidi, Li-Z He, Li Zhang, J. My Kuroiwa, T. Keler, R. M. Steinman, *Breast Cancer Res.* **2012**, *14*, R39.

[37] D. Sancho, D. Mourão-Sá, O. P. Joffre, O. Schulz, N. C. Rogers, D. J. Pennington, J. R. Carlyle, C. Reis E Sousa, *J. Clin. Invest.* **2008**, *118*, 2098.

[38] L. F. Poulin, M. Salio, E. Griessinger, F. Anjos-Afonso, L. Craciun, Ji-Li Chen, A. M. Keller, O. Joffre, S. Zelenay, E. Nye, A. Le Moine, F. Faure, V. Donckier, D. Sancho, V. Cerundolo, D. Bonnet, C. Reis E Sousa, *J. Exp. Med.* **2010**, *207*, 1261.

[39] C. Huysamen, J. A. Willment, K. M. Dennehy, G. D. Brown, *J. Biol. Chem.* **2008**, *283*, 16693.

[40] D. Sancho, O. P. Joffre, A. M. Keller, N. C. Rogers, D. Martínez, P. Hernanz-Falcón, I. Rosewell, C. R. E. Sousa, *Nature* **2009**, *458*, 899.

[41] S. Zelenay, A. M. Keller, P. G. Whitney, B. U. Schraml, S. Deddouche, N. C. Rogers, O. Schulz, D. Sancho, C. Reis E Sousa, *J. Clin. Invest.* **2012**, *122*, 1615.

[42] S. Iborra, M. Martínez-López, S. C. Khouili, M. Enamorado, F. J. Cueto, R. Conde-Garrosa, C. Del Fresno, D. Sancho, *Immunity* **2016**, *45*, 847.

[43] A. Blanco-Toribio, N. Sainz-Pastor, A. Álvarez-Cienfuegos, N. Merino, Á. M. Cuesta, D. Sánchez-Martín, J. Bonet, P. Santos-Valle, L. Sanz, B. Oliva, F. J. Blanco, L. Álvarez-Vallina, *mAbs* **2013**, *5*, 70.

[44] M. Compte, S. L. Harwood, A. Erce-Llamazares, A. Tapia-Galisteo, E. Romero, I. Ferrer, E. M. Garrido-Martin, A. B. Enguita, M. C. Ochoa, B. Blanco, M. Oteo, N. Merino, D. Nehme-Álvarez, O. Hangiu, C. Domínguez-Alonso, M. Zonca, A. Ramírez-Fernández, F. J. Blanco, M. A. Morcillo, I. G. Muñoz, I. Melero, J. L. Rodriguez-Peralto, L. Paz-Ares, L. Sanz, L. Alvarez-Vallina, *Clin. Cancer Res.* **2021**, *27*, 3167.

[45] G. B. Moreau, S. L. Burgess, J. M. Sturek, A. N. Donlan, W. A. Petri, B. J. Mann, *Am. J. Trop. Med. Hyg.* **2020**, *103*, 1215.

[46] W. Du, P. Jiang, Q. Li, H. Wen, M. Zheng, J. Zhang, Y. Guo, J. Yang, W. Feng, S. Ye, S. Kamara, P. Jiang, J. Chen, W. Li, S. Zhu, L. Zhang, *Microbiol. Spectr.* **2023**, *11*, e0356222.

[47] D. Li, G. D. Sempowski, K. O. Saunders, P. Acharya, B. F. Haynes, *Annu. Rev. Med.* **2022**, *73*, 1.

[48] E. M. Obeng, C. K. O. Dzuvor, M. K. Danquah, *Nano Today* **2022**, *42*, 101350.

[49] N. Suryadevara, S. Shrihari, P. Gilchuk, L. A. Vanblargan, E. Binshtein, S. J. Zost, R. S. Nargi, R. E. Sutton, E. S. Winkler, E. C. Chen, M. E. Fouch, E. Davidson, B. J. Doranz, R. E. Chen, P.-Y. Shi, R. H. Carnahan, L. B. Thackray, M. S. Diamond, J. E. Crowe, *Cell* **2021**, *184*, 2316.

[50] I. Ullah, J. Prévost, M. S. Ladinsky, H. Stone, M. Lu, S. P. Anand, G. Beaudoin-Bussières, K. Symmes, M. Benlarbi, S. Ding, R. Gasser, C. Fink, Y. Chen, A. Tauzin, G. Goyette, C. Bourassa, H. Medjahed, M. Mack, K. Chung, C. B. Wilen, G. A. Dekaban, J. D. Dikeakos, E. A. Bruce, D. E. Kaufmann, L. Stamatatos, A. T. McGuire, J. Richard, M. Pazgier, P. J. Bjorkman, W. Mothes, et al., *bioRxiv* **2021**, https://doi.org/10.1101/2021.03.22.436337.

[51] E. S. Winkler, P. Gilchuk, J. Yu, A. L. Bailey, R. E. Chen, Z. Chong, S. J. Zost, H. Jang, Y. Huang, J. D. Allen, J. B. Case, R. E. Sutton, R. H. Carnahan, T. L. Darling, A. C. M. Boon, M. Mack, R. D. Head, T. M. Ross, J. E. Crowe, M. S. Diamond, *Cell* **2021**, *184*, 1804.

[52] R. Yamin, A. T. Jones, H.-H. Hoffmann, A. Schäfer, K. S. Kao, R. L. Francis, T. P. Sheahan, R. S. Baric, C. M. Rice, J. V. Ravetch, S. Bournazos, *Nature* **2021**, *599*, 465.

[53] Y. Wang, Y. Xiang, V. W. Xin, X.-W. Wang, X.-C. Peng, X.-Q. Liu, D. Wang, N. Li, J.-T. Cheng, Y.-N. Lyv, S.-Z. Cui, Z. Ma, Q. Zhang, H.-W. Xin, *J. Hematol. Oncol.* **2020**, *13*, 107.

[54] S. He, J. Wang, H. Chen, Z. Qian, K. Hu, B. Shi, J. Wang, *Vaccines* **2023**, *11*, 371.

[55] C. Li, W. Zhan, Z. Yang, C. Tu, G. Hu, X. Zhang, W. Song, S. Du, Y. Zhu, K. Huang, Yu Kong, M. Zhang, Q. Mao, X. Gu, Yi Zhang, Y. Xie, Q. Deng, Y. Song, Z. Chen, L. Lu, S. Jiang, Y. Wu, L. Sun, T. Ying, *Cell* **2022**, *185*, 1389.

[56] M. A. Rossotti, H. Van Faassen, A. T. Tran, J. Sheff, J. K. Sandhu, D. Duque, M. Hewitt, X. Wen, J. Bavananthasivam, S. Beitari, K. Matte, G. Laroche, P. M. Giguère, C. Gervais, M. Stuible, J. Guimond, S. Perret, G. Hussack, M.-A. Langlois, Y. Durocher, J. Tanha, *Commun. Biol.* **2022**, *5*, 933.

[57] A. Gupta, Y. Gonzalez-Rojas, E. Juarez, M. Crespo Casal, J. Moya, D. R. Falci, E. Sarkis, J. Solis, H. Zheng, N. Scott, A. L. Cathcart, C. M. Hebner, J. Sager, E. Mogalian, C. Tipple, A. Peppercorn, E. Alexander, P. S. Pang, A. Free, C. Brinson, M. Aldinger, A. E. Shapiro, *N. Engl. J. Med.* **2021**, *385*, 1941.

[58] J. J. Guthmiller, J. Han, H. A. Utset, L. Li, L. Y.-L Lan, C. Henry, C. T. Stamper, M. McMahon, G. O'dell, M. L. Fernández-Quintero, A. W.

Freyn, F. Amanat, O. Stovicek, L. Gentles, S. T. Richey, A. T. De La Peña, V. Rosado, H. L. Dugan, N.-Y. Zheng, M. E. Tepora, D. J. Bitar, S. Changrob, S. Strohmeier, M. Huang, A. García-Sastre, K. R. Liedl, J. D. Bloom, R. Nachbagauer, P. Palese, F. Krammer, et al., *Nature* **2022**, *602*, 314.
[59] D. Sok, D. R. Burton, *Nat. Immunol.* **2018**, *19*, 1179.
[60] A. Tang, Z. Chen, K. S. Cox, H.-P. Su, C. Callahan, A. Fridman, L. Zhang, S. B. Patel, P. J. Cejas, R. Swoyer, S. Touch, M. P. Citron, D. Govindarajan, B. Luo, M. Eddins, J. C. Reid, S. M. Soisson, J. Galli, D. Wang, Z. Wen, G. J. Heidecker, D. R. Casimiro, D. J. Distefano, K. A. Vora, *Nat. Commun.* **2019**, *10*, 4153.
[61] A. R. Mäkelä, H. Ugurlu, L. Hannula, R. Kant, P. Salminen, R. Fagerlund, S. Mäki, A. Haveri, T. Strandin, L. Kareinen, J. Hepojoki, S. Kuivanen, L. Levanov, A. Pasternack, R. A. Naves, O. Ritvos, P. Österlund, T. Sironen, O. Vapalahti, A. Kipar, J. T. Huiskonen, I. Rissanen, K. Saksela, *Nat. Commun.* **2023**, *14*, 1637.
[62] G. Beaudoin-Bussières, Y. Chen, I. Ullah, J. Prévost, W. D. Tolbert, K. Symmes, S. Ding, M. Benlarbi, S. Yu Gong, A. Tauzin, R. Gasser, D. Chatterjee, D. Vézina, G. Goyette, J. Richard, F. Zhou, L. Stamatatos, A. T. Mcguire, H. Charest, M. Roger, E. Pozharski, P. Kumar, W. Mothes, P. D. Uchil, M. Pazgier, A. Finzi, *Cell Rep.* **2022**, *38*, 110368.
[63] C. Kurts, W. R. Heath, F. R. Carbone, J. Allison, J. F. Miller, H. Kosaka, *J. Exp. Med.* **1996**, *184*, 923.
[64] L. F. Poulin, Y. Reyal, H. Uronen-Hansson, B. U. Schraml, D. Sancho, K. M. Murphy, U. K. Håkansson, L. Ferreira Moita, W. W. Agace, D. Bonnet, C. Reis E Sousa, *Blood* **2012**, *119*, 6052.
[65] S. A. Fuertes Marraco, F. Grosjean, A. Duval, M. Rosa, C. Lavanchy, D. Ashok, S. Haller, L. A. Otten, Q.-G. Steiner, P. Descombes, C. A. Luber, F. Meissner, M. Mann, L. Szeles, W. Reith, H. Acha-Orbea, *Front. Immunol.* **2012**, *3*, 331.
[66] J. M. Díez, C. Romero, J. Vergara-Alert, M. Belló-Perez, J. Rodon, J. M. Honrubia, J. Segalés, I. Sola, L. Enjuanes, R. Gajardo, *Immunotherapy* **2020**, *12*, 1247.
[67] P. Pérez, A. Lázaro-Frías, C. Zamora, P. J. Sánchez-Cordón, D. Astorgano, J. Luczkowiak, R. Delgado, J. M. Casasnovas, M. Esteban, J. García-Arriaza, *Front. Immunol.* **2022**, *12*, 824728.
[68] C. Hsieh, J. A. Goldsmith, J. M. Schaub, A. M. Divenere, H. Kuo, K. Javanmardi, K. C. Le, D. Wrapp, A. G. Lee, Y. Liu, C. Chou, P. O. Byrne, C. K. Hjorth, N. V Johnson, J. Ludes-meyers, A. W. Nguyen, J. Park, N. Wang, D. Amengor, J. J. Lavinder, G. C. Ippolito, J. A. Maynard, I. J. Finkelstein, J. S. Mclellan, *Science* **2020**, *369*, 1501.
[69] Y. Zhang, E. V. Yates, L. Hong, K. L. Saar, G. Meisl, C. M. Dobson, T. P. J. Knowles, *Chem. Sci.* **2018**, *9*, 3503.
[70] D. K. Wilkins, S. B. Grimshaw, V. Receveur, C. M. Dobson, J. A. Jones, L. J. Smith, *Biochemistry* **1999**, *38*, 16424.
[71] J. M. Schaub, C.-W. Chou, H.-C. Kuo, K. Javanmardi, C.-L. Hsieh, J. Goldsmith, A. M. Divenere, K. C. Le, D. Wrapp, P. O. Byrne, C. K. Hjorth, N. V. Johnson, J. Ludes-Meyers, A. W. Nguyen, N. Wang, J. J. Lavinder, G. C. Ippolito, J. A. Maynard, J. S. Mclellan, I. J. Finkelstein, *Nat. Protoc.* **2021**, *16*, 5339.
[72] A. Punjani, J. L. Rubinstein, D. J. Fleet, M. A. Brubaker, *Nat. Methods* **2017**, *14*, 290.
[73] P. V. Afonine, B. K. Poon, R. J. Read, O. V. Sobolev, T. C. Terwilliger, A. Urzhumtsev, P. D. Adams, *Acta Crystallogr., Sect. D: Struct. Biol.* **2018**, *74*, 531.
[74] P. Emsley, K. Cowtan, *Acta Crystallogr. D: Biol. Crystallogr.* **2004**, *60*, 2126.
[75] E. F. Pettersen, T. D. Goddard, C. C. Huang, E. C. Meng, G. S. Couch, T. I. Croll, J. H. Morris, T. E. Ferrin, *Protein Sci.* **2021**, *30*, 70.
[76] P. D. Adams, P. V. Afonine, G. Bunkóczi, V. B. Chen, I. W. Davis, N. Echols, J. J. Headd, Li-W Hung, G. J. Kapral, R. W. Grosse-Kunstleve, A. J. Mccoy, N. W. Moriarty, R. Oeffner, R. J. Read, D. C. Richardson, J. S. Richardson, T. C. Terwilliger, P. H. Zwart, *Acta Crystallogr. D: Biol. Crystallogr.* **2010**, *66*, 213.
[77] M. A. Whitt, *J. Virol. Methods* **2010**, *169*, 365.
[78] A. Lázaro-Frías, P. Pérez, C. Zamora, P. J. Sánchez-Cordón, M. Guzmán, J. Luczkowiak, R. Delgado, J. M. Casasnovas, M. Esteban, J. García-Arriaza, *NPJ Vaccines* **2022**, *7*, 17.
[79] J. García-Arriaza, U. Garaigorta, P. Pérez, A. Lázaro-Frías, C. Zamora, P. Gastaminza, C. Del Fresno, J. M. Casasnovas, C. Ó. S. Sorzano, D. Sancho, M. Esteban, *J. Virol.* **2021**, *95*, e02260.
[80] H. Hartman, Y. Wang, H. W. Schroeder, X. Cui, *PLoS One* **2018**, *13*, e0198528.

ADVANCED SCIENCE
Open Access

Supporting Information

for *Adv. Sci.*, DOI 10.1002/advs.202304818

Dendritic Cell-Mediated Cross-Priming by a Bispecific Neutralizing Antibody Boosts Cytotoxic T Cell Responses and Protects Mice against SARS-CoV-2

*Rodrigo Lázaro-Gorines, Patricia Pérez, Ignacio Heras-Murillo, Irene Adán-Barrientos, Guillermo Albericio, David Astorgano, Sara Flores, Joanna Luczkowiak, Nuria Labiod, Seandean L. Harwood, Alejandro Segura-Tudela, Laura Rubio-Pérez, Yudhi Nugraha, Xiaoran Shang, Yuxing Li, Carlos Alfonso, Kaylin A. Adipietro, Dinendra L. Abeyawardhane, Rocío Navarro, Marta Compte, Wenbo Yu, Alexander D. MacKerell Jr, Laura Sanz, David J. Weber, Francisco J. Blanco, Mariano Esteban, Edwin Pozharski, Raquel Godoy-Ruiz, Inés G. Muñoz, Rafael Delgado, David Sancho, Juan García-Arriaza and Luis Álvarez-Vallina**

Supporting Information

Title

Dendritic cell-mediated cross-priming by a bispecific neutralizing antibody boosts cytotoxic T cell responses and protects mice against SARS-CoV-2

Rodrigo Lázaro-Gorines, Patricia Pérez, Ignacio Heras-Murillo, Irene Adán-Barrientos, Guillermo Albericio, David Astorgano, Sara Flores, Joanna Luczkowiak, Nuria Labiod, Seandean L. Harwood, Alejandro Segura-Tudela, Laura Rubio-Pérez, Yudhi Nugraha, Xiaoran Shang, Yuxing Li, Carlos Alfonso, Kaylin A. Adipietro, Dinendra L. Abeyawardhane, Rocío Navarro, Marta Compte, Wenbo Yu, Alexander D. MacKerell Jr, Laura Sanz, David J. Weber, Francisco J. Blanco, Mariano Esteban, Edwin Pozharski, Raquel Godoy-Ruiz, Inés G. Muñoz, Rafael Delgado, David Sancho, Juan García-Arriaza, Luis Álvarez-Vallina[*]

*** Correspondence: lalvarezv@ext.cnio.es (L. A-V)**

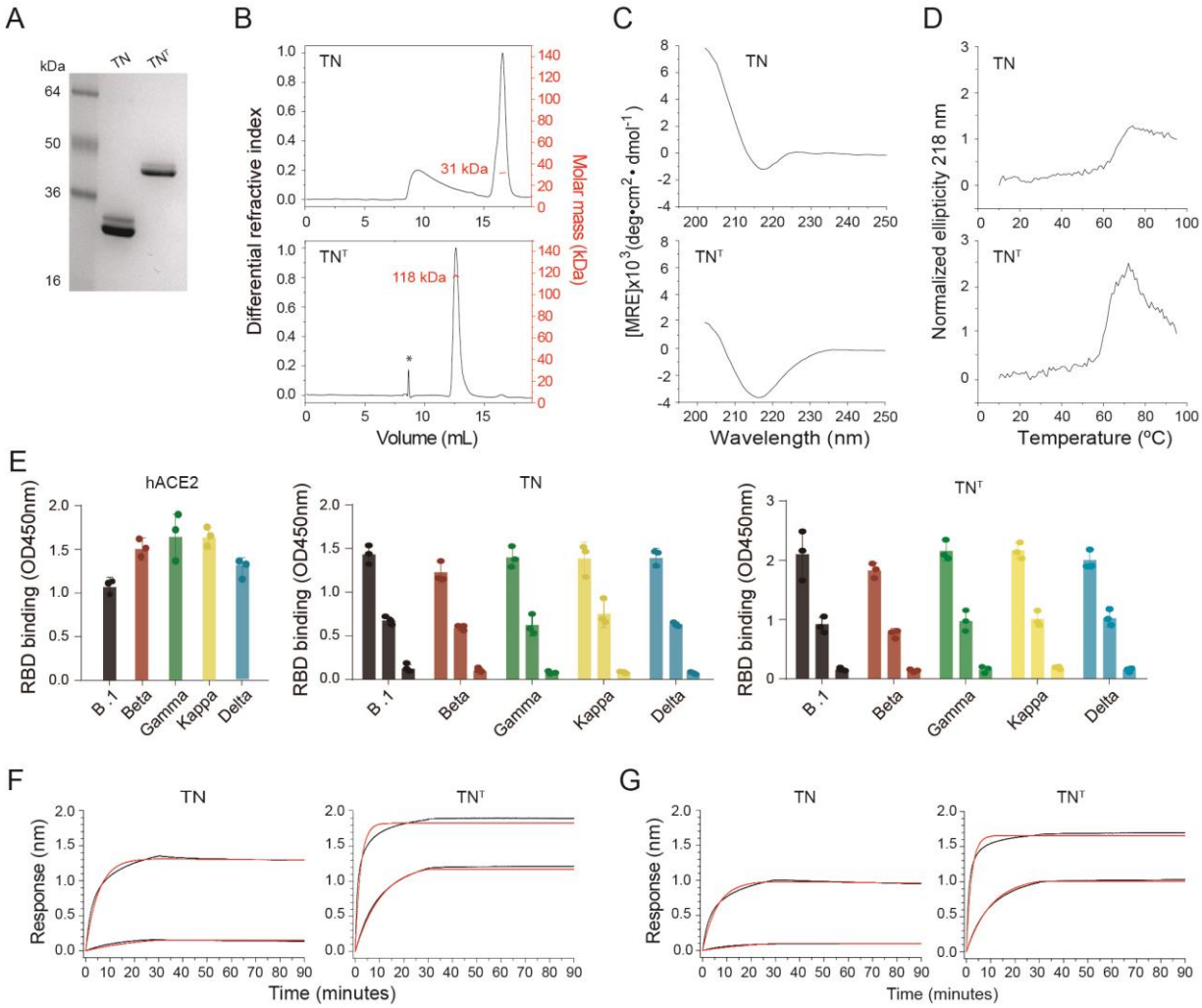

Figure S1. Purified TN tandem and TN^T trimerbody recognize efficiently and similarly SARS-CoV-2 S protein RBD from different viral strains. A) SDS-PAGE analysis in reducing conditions of purified TN and TN^T. Both antibodies were purified from HEK-293 conditioned medium. B) SEC-MALS data proving monomeric (TN, top) and trimeric (TN^T, bottom) states of each antibody. The black lines correspond to the differential refractive index (left axis) and the red line to the measured molar mass (right axis). Asterisk (*) in TN^T chromatogram indicates an experimental artifact spike cause by a chromatography pause. C) TN (top) and TN^T (bottom) far-UV CD spectra. D) TN (top) and TN^T (bottom) thermal denaturation profiles. E) TN (50, 10, 1 nM) and TN^T (10, 1, 0.1 nM) binding activity against immobilized B.1, beta, gamma, kappa and delta RBD proteins. ACE2 (0.1 µg/mL) interaction with different RBD strains was included as an inner control (left panel). All assays were performed by triplicate. Independent and mean values ± SEM are plotted. The binding kinetics of the TN and TN^T to B.1 (F) and B.1.351(beta) (G) RBD were measured, using the antibodies at 50 and 10 nM, with 0.5

hours of association and 1 hour of dissociation. Experimental sensorgrams (black) and fitted data (red) are shown.

A

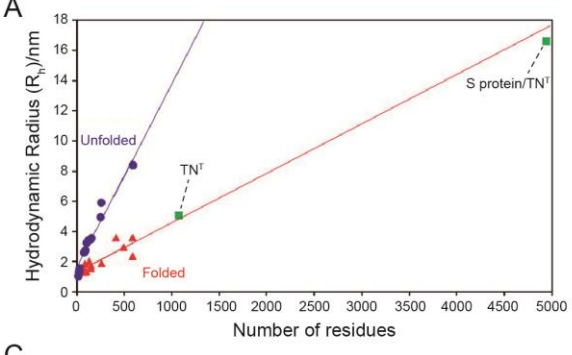

B

Unfolded proteins

Protein	No.of residues	R_h/nm
Hen lysozyme (49-64)	16	1.04
D3 fibronectin binding protein (17-37)	22	1.33
D3 fibronectin binding protein (2-38)	32	1.55
Bovine ubiquitin	76	2.63
SH3 domain of PI3K	90	2.75
Horse ferricytochrome c	104	3.24
Hen lysozyme	129	3.46
Staphylococcal nuclease	149	3.5
Horse myoglobin	153	3.6
Yeast triosephosphate isomerase	247	4.97
Bovine carbonic anhydrase B	259	5.9
BSA	589	8.4

Folded proteins

Protein	No. of residues	R_h/nm
Bovine pancreatic trypsin inhibitor	58	1.58
Bovine ubiquitin	76	1.32
SH3 domain of PI3K	90	1.86
R_h/nm-Horse ferricytochrome c	104	1.35
Hen lysozyme	129	2.05
Staphylococcal nuclease	149	1.6
Horse myoglobin	153	1.75
Bovine carbonic anhydrase B	259	1.9
S. equismilis streptokinase	414	3.6
Yeast triosephosphate isomerase	494	2.97
Yeast triosephosphate isomerase	589	2.35
BSA	589	3.6

TN^T and S protein/TN^T

Protein	No. of residues	R_h/nm
TN^T	1077 (359 x 3)	5.06
S protein+TN^T(1:1)	4941 (3864+1077)	16.6

C

D

E

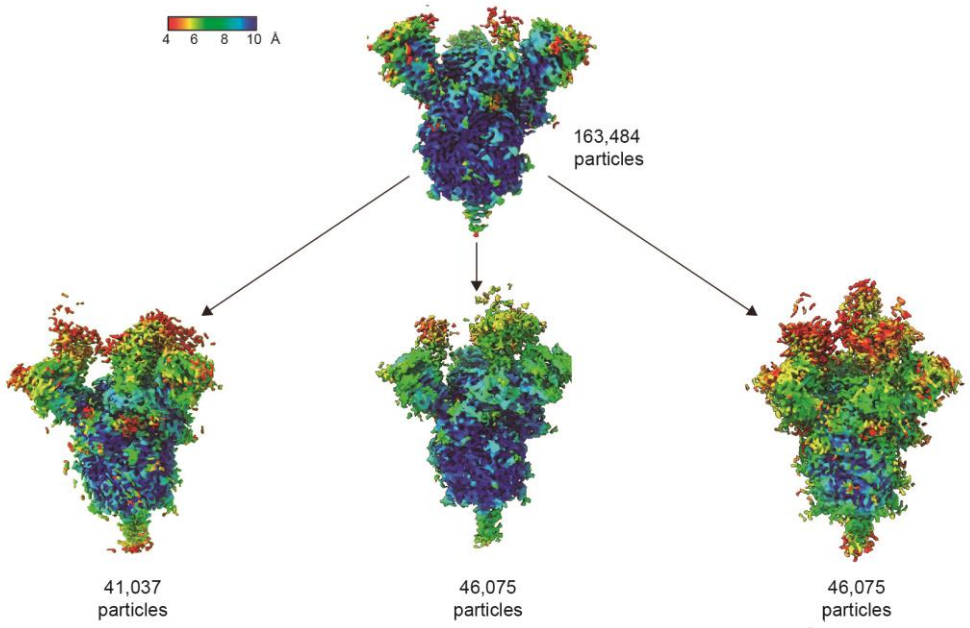

F

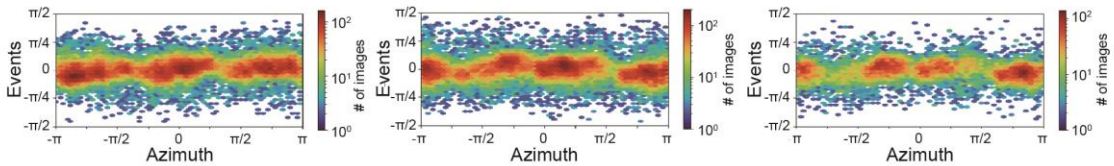

G

H

Details of cryo-EM data collection

Microscope	FEI Glacios
Voltage (kV)	200
Camera	Gatan K3
Defocus range used (μm)	0.5 – 2.7
Exposure time	3.0
Dose rate (e/pixel/s)	16.3
Total dose (e/Å^{-2})	61.9
Pixel size (Å)	0.889
Number of micrographs (total/used)	2184/1980
Frames	46
Total Particles Picked	163,484
Particles used per 3D class	22,422/46,075/41,037
Resolution in 3D classes(Å)	3.80/3.74/4.03

Figure S2. Microfluidic diffusional sizing (MDS) analysis and cryo-EM data processing and reconstruction of HexaPro S protein/TN^T complex. MDS was used to measure the change in hydrodynamic radius (R_h) of TN^T trimerbody and its subsequent complex with SARS-CoV-2 S protein. A) Plot of the R_h versus the number of residues in the polypeptide chain. The values of the hydrodynamic radii displayed in this graph correspond to the R_h values reported in the literature for a range of native folded proteins (red) and highly denatured polypeptide chains (blue) obtained using dynamic light scattering and pulsed field gradient nuclear magnetic resonance. TN^T and S protein/TN^T complex R_hs (green) correlate with the expected for folded proteins with their nominal number of amino acids. B) Charts indicating the number of residues and R_h of folded (red) and unfolded (blue) polypeptides and proteins used in this correlation according to literature. Number of residues of TN^T, 1077, and S protein/TN^T complex, 4941, trimeric conformations in solution (green). C-H, cryo-EM data processing and reconstruction of HexaPro S protein/TN^T complex**.** C) Regarding Cryo-EM analyses top panel shows an example of motion corrected micrograph. D) Subset of 7 2D classes obtained from the 2D classification job run after particle picking. E) Electron density maps representative of final 3D complex reconstruction at 3.8Å and local map resolution. Three volume subclasses were identified as the majoritarian ones. F) Viewing Direction Distribution map illustrating how many images have a viewing direction at each (elevation, azimuth) bin. G) Validation and resolution estimation results. Fourier Shell correlation (FSC) curves are measured between half-sets of particles that are used to compute two half-map reconstructions. FSC curves using a mask (green, red, purple) improved the resolution estimate of 3.8Å versus 4.5Å for conventional refinement. Notably, a local focused refinement using the same mask is unable to improve resolution beyond the conventional refinement result due to the flexibility of the region. H) Cryo-EM data collecting and analysis table.

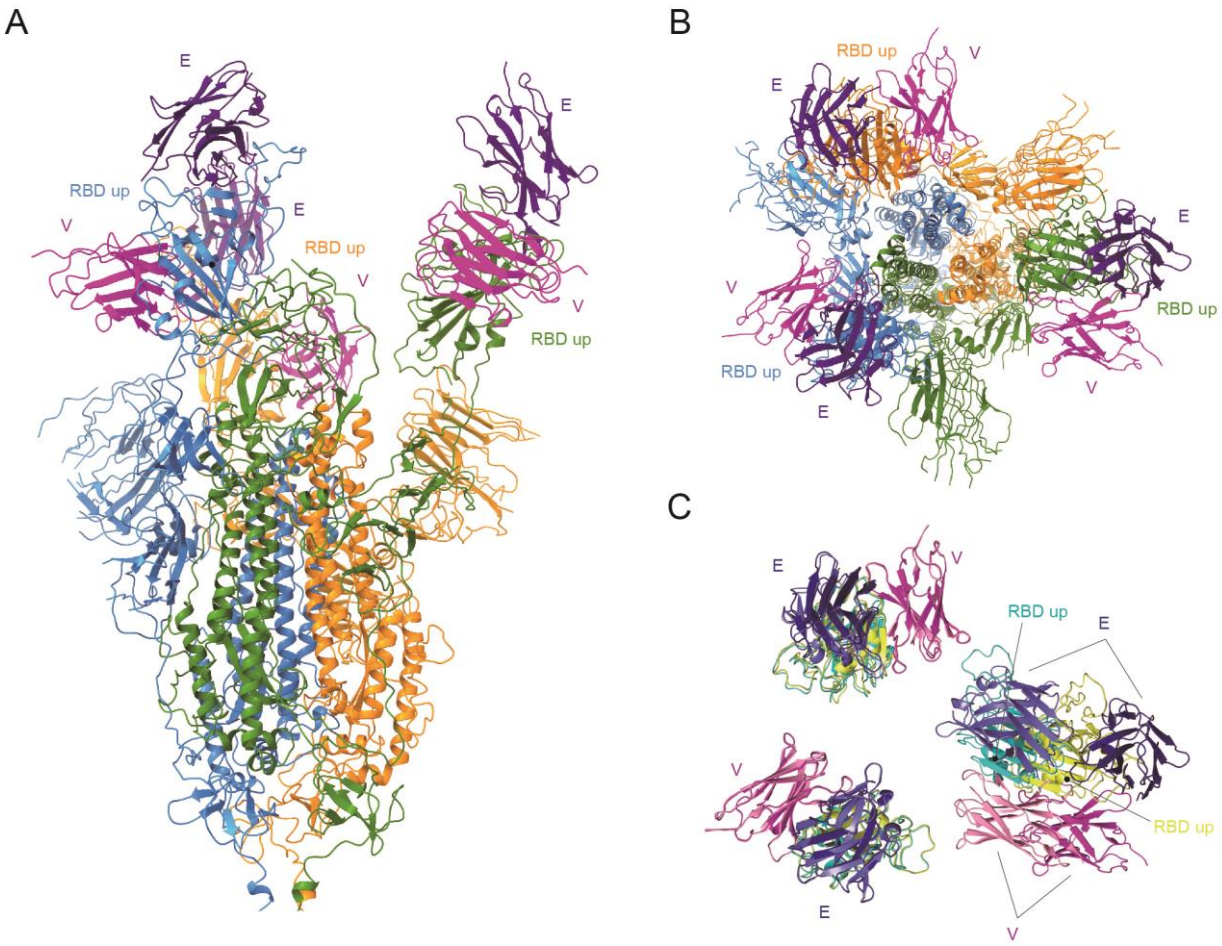

Figure S3. S protein/TN^{T} complex model shows TN^{T} hexavalent binding to S protein causing the 3-up RBD conformation with one-RBD position distortion. Side (A) and top views (B) of the HexaPro S protein/TN^{T} complex model showing TN^{T} embracing the S protein in the 3-up RBD prefusion conformation. As shown, TN^{T} binds simultaneously and in a biparatopic manner, both E V_{HH} and V V_{HH}, to the three S protein RBDs. S protein subunits are colored in yellow, steel blue and olive green, while E V_{HH} and V V_{HH} are in purple and magenta, respectively. C) Top view of the alignment of the HexaPro S protein/TN^{T} model (S protein in pale yellow, E V_{HH} in dark blue and V V_{HH} in magenta) and 7B18 PDB model (S protein in aquamarine, E V_{HH} in steel blue and V V_{HH} light pink) showing how the binding of the V_{HH}s to their respective RBDs occurs in both structures. While in two of them the positions are conserved, TN^{T} presence causes a shift in the third RBD location respect to the 7B18 model, even though the manner that both V_{HH}s recognize this RBD domain is preserved. For easy viewing just the three-RBDs from the S trimer are showed.

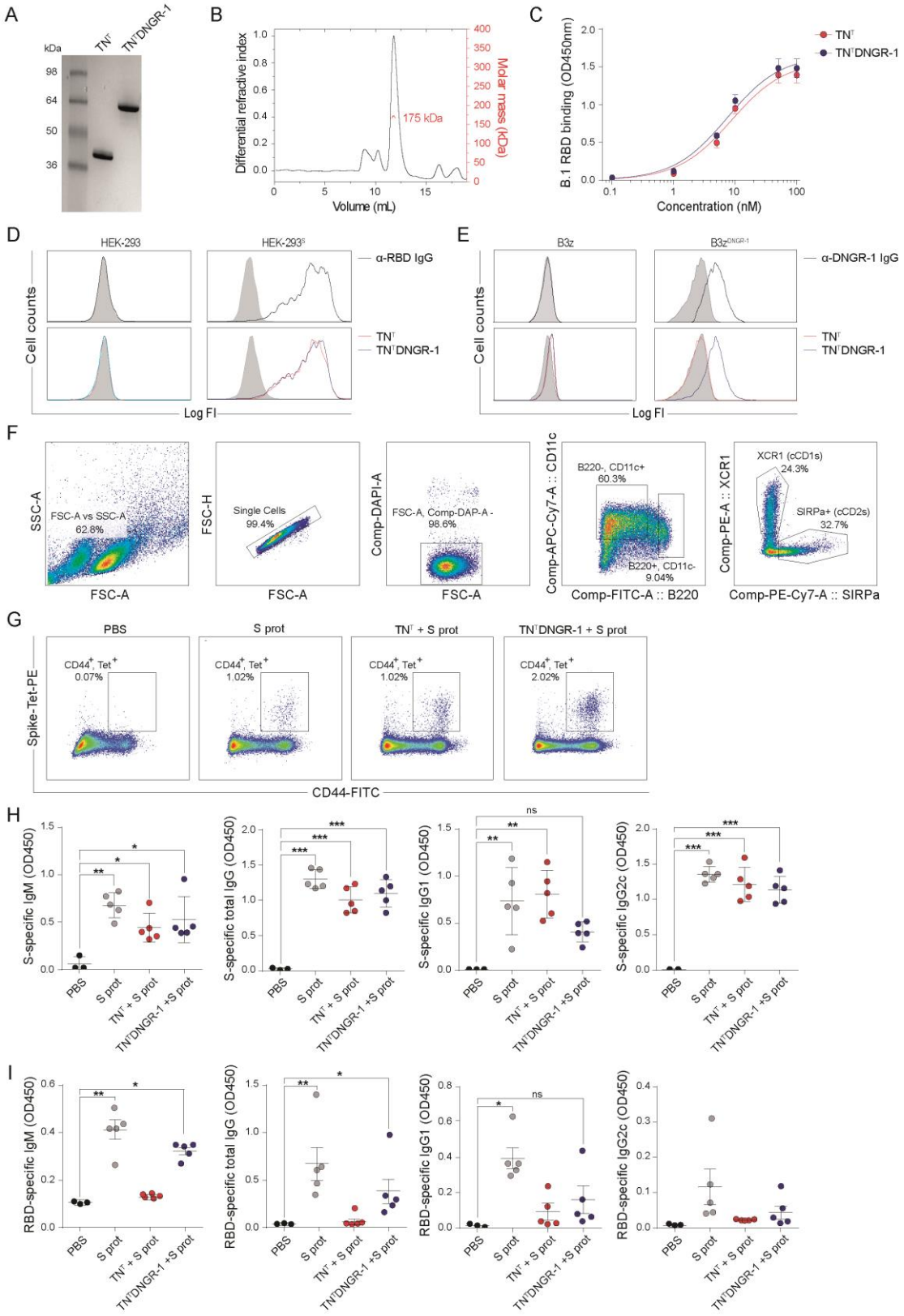

Figure S4. Purified TN^{T}DNGR-1 performs as globular bispecific trimerbody in solution targeting viral antigens to DNGR-1-expressing DCs *in vitro* and boosting systemic S-specific responses *in vivo*. A) Coomassie blue staining after SDS-PAGE analysis in reducing conditions comparing purified samples of both TN^{T} and TN^{T}DNR-

1. Each lane contains 1µg of purified protein. B) SEC-MALS analysis of TN^{T}DNR-1 showing its predominant trimeric state. The black lines correspond to the differential refractive index (left axis) and the red line to the measured molar mass (right axis). C) Comparative binding of B.1 RBD by TN^{T}DNGR-1 and parental TN^{T} by mean of ELISA assay. D) TN^{T} (red line) or TN^{T}DNGR-1 (blue line) purified proteins were incubated, 1µg/mL, with SARS-CoV-2 S $protein^{+/-}$ HEK-293 before StrepTagII detection. Histograms include anti-RBD stained (thin black line) and non-stained cells as a control (grey). E) AlexaFluor647 conjugated RBD (AF647-RBD) was added to B3z DNGR-$1^{+/-}$ cells after incubating them with TN^{T} (red line) or TN^{T}DNGR-1 (blue line). Histograms also show cells just treated with AF647-RBD (grey) and (thin black line). F) Representative gating of mouse cDC1s, cD2s and pDCs from Flt3-L BMDCs according to their surface markers staining for the analysis of TN^{T}DNGR-1 labelling assays (see Fig. 2E). Mononuclear cells isolated from mouse bone marrow were induced for differentiation *in vitro* and characterized phenotypically as follows: cDC1s ($B220^{+}$, $CD11c^{-}$, $XCR1^{+}$, $SIRPa^{-}$), cDC2s ($B220^{+}$, $CD11c^{-}$, $XCR1^{-}$, $SIRPa^{+}$) and pDCs ($B220^{+}$, $CD11c^{-}$). G) $CD44^{+}$ S-Tet^{+} dot plot representation on gated $CD8^{+}$ T cells corresponding to the different treatment groups (PBS, S protein + adjuvants, S protein + TN^{T} + adjuvants, S protein + TN^{T}DNGR-1 + adjuvants) of the prime-boost immunization experiment (see Fig. 2H, I). H, I) Analysis of the same prime-boost immunization experiment for S- (H) and RBD-specific (I) serum antibodies. Mice serum was collected on day 14 of the prime-boost scheme (7 days after the boost) (see Fig. 2G) and analyzed for antigen IgM, total IgG, IgG1 and IgG2c levels. Represented values correspond to samples obtained from the same experiment as the cellular immune response evaluation (n=3-5 mice/group/experiment; see Fig. 2G) using 1/50 dilution for IgM and 1/250 for total IgG, IgG1 and IgG2c.

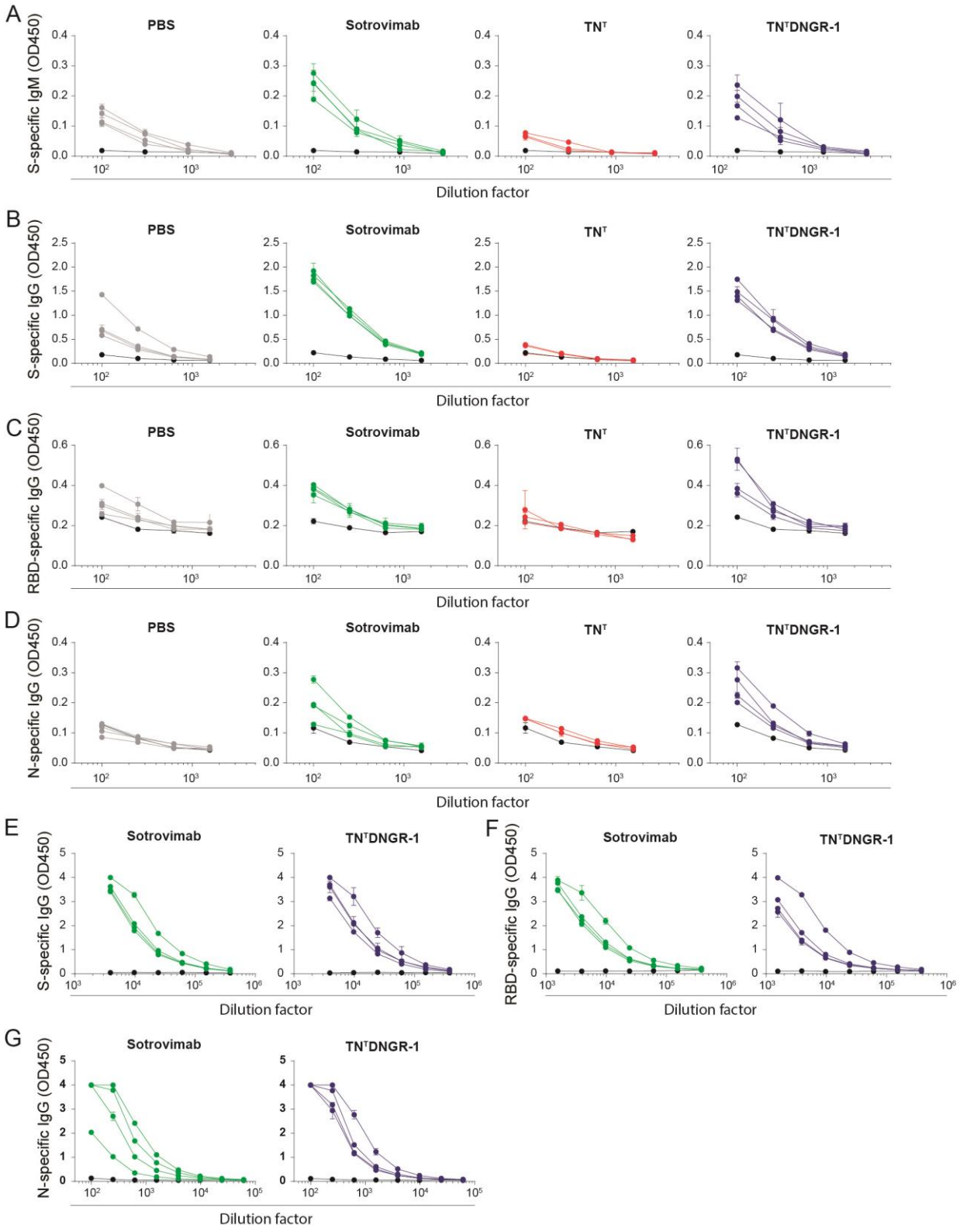

Figure S5. Absorbance measurements for serum antibodies binding to SARS-CoV-2 antigens. Data showing S-specific IgM (A), and S- (B), RBD- (C) and N-specific (D) total IgG quantification on day 5 p.c. Measurements for S- (E), RBD- (F) and N-specific (G) total IgG quantification on day 20 p.c. All graphs represent mean ± SEM (n=4

mice/group) for a single experiment. All measurements were done by ELISA by duplicate.

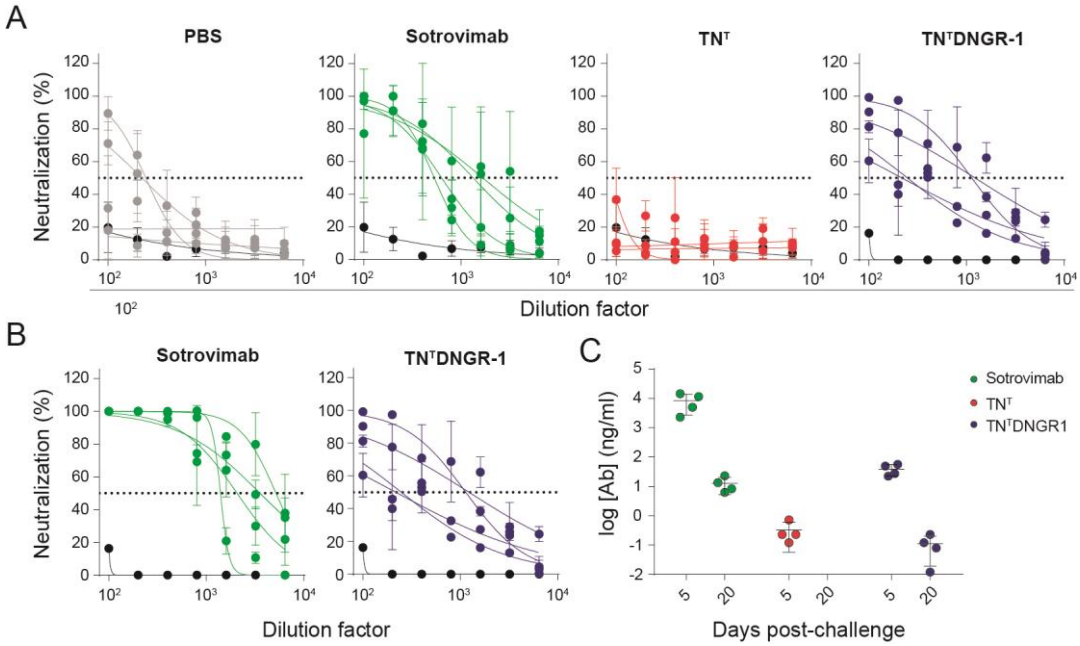

Figure S6. Efficacy experiment mice serum analysis for SARS-CoV-2 neutralization. Neutralization experiments for live SARS-CoV-2 (B.1 strain) virus using pooled mice sera from each group (n=4 mice/group) and obtained on 5 (A) and 20 (B) days p.c. NT_{50} is represented as a dotted line. C) Calculation of administrated antibodies (sotrovimab, TN^T and TN^TDNGR-1) concentration present in serum at 5- and 20-days p.c. All graphs represent mean ± SEM for a single experiment. All measurements were done by duplicate.

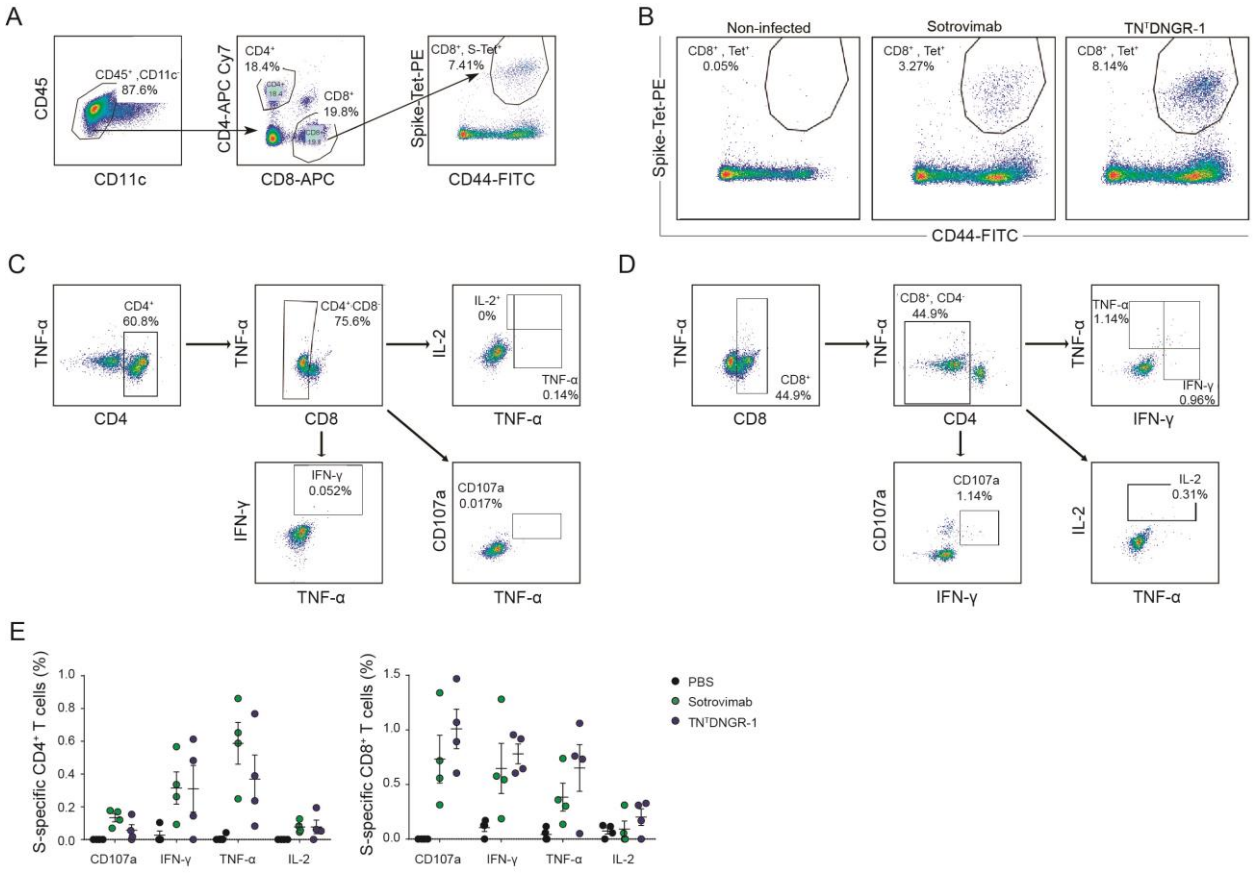

Figure S7. Flow cytometry analysis showing TN^{T}DNGR-1 treatment of SARS-CoV-2 infection induced S-specific CD8$^+$ T cell responses in the lungs. A) Representative gating for S-Tet staining of CD8$^+$ T cells obtained from processed K18-hACE2 mice lungs at day 20 p.c. Single and live CD8$^+$ T cells were gated from lymphocyte morphology cloud as CD45$^+$, CD11c-, CD8$^+$, CD4$^-$. B) CD44$^+$ S-Tet$^+$ dot plot representation from processed lung CD8$^+$ T cells at day 20 p.c. showing exemplary mice from the different treatment groups (PBS, sotrovimab and TN^{T}DNGR-1). For ICS data analysis CD4$^+$ (C) and CD8$^+$ (D) T cells were gated from single and live lymphocyte morphology cloud as CD3$^+$ and CD4$^+$ or CD8$^+$. Herein an exemplary ICS gating for CD107a, IFN-γ, TNF-α and IL-2 is represented as paired dot plot. E) ICS for CD107a, IFN-γ, TNF-α or IL-2, represented as frequency of CD4$^+$ (left panel) and CD8$^+$ (right panel) responding cells in the lungs at 20 days p.c. for each individual marker. All graphs represent individual dots and mean ± SEM (n=4 mice/group) for a single experiment.

DISCUSIÓN

Artículo 1: ***A PD-L1/EGFR bispecific antibody combines immune checkpoint blockade and direct anti-cancer action for an enhanced anti-tumor response*****.**

Los tumores se caracterizan por su heterogeneidad clonal, lo que facilita el desarrollo de mecanismos de evasión a los tratamientos convencionales debido a la selección de subpoblaciones de células resistentes y la capacidad de adaptación del microambiente tumoral. Además, la plasticidad tumoral representa un desafío significativo para el desarrollo de terapias efectivas, ya que las células tumorales pueden escapar a la destrucción inmune mediante la modificación de sus características fenotípicas o el desarrollo de mecanismos inhibidores. En los últimos años se han desarrollado anticuerpos multiespecíficos que reconocen múltiples AATs con el objetivo de superar esta heterogeneidad tumoral. Estos anticuerpos han demostrado la capacidad de inducir respuestas inmunes en modelos preclínicos con propiedades mejoradas respecto a los mAbs convencionales[2,47,149].

En la actualidad existen 9 anticuerpos biespecíficos aprobados en EE.UU. y en UE para el tratamiento del cáncer. En el año 2014 se aprobó el anticuerpo blinatumomab (CD19 x CD3ε) para la leucemia linfoblástica aguda de células B. Posteriormente, en el año 2021, se aprobó amivantamab (EGFR x cMet) para el NSCLC. En el año 2022 se aprobaron los anticuerpos mosunetuzumab (CD20 x CD3ε) para el tratamiento del linfoma folicular, tebentafusp (gp100 x CD3ε) para el melanoma uveal y el teclistamab (BCMA x CD3ε) para el mieloma múltiple. Por último, en el año 2023, se aprobaron los anticuerpos biespecíficos elranatamab (BCMA x CD3ε) para el mieloma múltiple, el epcoritamab (CD20 x CD3ε) y el glofitamab (CD20 x CD3ε) para el tratamiento de linfoma difuso de células B y el anticuerpo talquetamab (GPCR5D x CD3ε) para el mieloma múltiple[56].

A pesar de los avances en la ingeniería de anticuerpos, la generación de anticuerpos biespecíficos de tipo IgG sigue siendo un reto cuando los sitios de unión al antígeno son de tipo Fab con las regiones V_H y V_L, ya que esto dificulta la obtención de anticuerpos biespecíficos funcionales a partir del ensamblaje aleatorio de diez posibles combinaciones H_2L_2 (esto se conoce comúnmente como el problema de la asociación de cadenas)[150–153]. Para superar esta y otras limitaciones, en los últimos años se han desarrollado una amplia variedad de estrategias de ingeniería de anticuerpos[2,31]. Los anticuerpos biespecíficos simétricos se generan mediante el ensamblaje de anticuerpos con regiones constantes de cadena pesada no modificadas[31,32].

La mayoría de los anticuerpos biespecíficos simétricos en desarrollo clínico son moléculas voluminosas con diseños tetravalentes (2 + 2) en los que fragmentos de anticuerpo adicionales se fusionan a moléculas homodiméricas[154,155]. Por otra parte, la generación de anticuerpos biespecíficos asimétricos de tipo IgG sigue siendo un reto, ya que es necesario abordar simultáneamente dos cuestiones críticas: la heterodimerización de dos cadenas C_H diferentes y la discriminación entre las dos interacciones de las cadenas ligera y pesada[29,31,156]. La heterodimerización correcta de los C_H se facilita mediante estrategias de ingeniería como las tecnologías KiH y crossMAb[24,30–32]. Sin embargo, la mayoría de estas estrategias emplean múltiples mutaciones dentro de los dominios C_H, las cuales pueden afectar negativamente a las propiedades favorables de las regiones Fc nativas, como su alta estabilidad y solubilidad, así como aumentar su inmunogenicidad[157].

En este trabajo hemos generado un anticuerpo biespecífico (PD-L1 x EGFR) de tipo IgG que resuelve algunos de los problemas asociados a la generación de anticuerpos heterodiméricos biespecíficos, como el problema de la asociación de cadenas[150–153]. El formato IgTT se basa en la fusión de un TT[46] mono o multiespecífico con las regiones bisagra y Fc de la IgG_1 humana, generando un anticuerpo tipo IgG hexavalente capaz de reconocer bivalentemente hasta tres antígenos diferentes. Inicialmente se generó una molécula IgTT monoespecífica anti-EGFR, un AAT bien caracterizado que es una de las proteínas oncogénicas de membrana más sobreexpresadas en los cánceres epiteliales[158].

Además, hemos demostrado la idoneidad del formato IgTT para estrategias de doble diana que combinan el reconocimiento de un AAT con un ICI, en una única molécula denominada IgTT-1E. Ambas moléculas IgTT se unen específicamente a sus antígenos diana, y la IgTT-1E demostró interacción simultánea a ambos antígenos. La interacción de V_{HH} EgA1 con el EGFR está muy bien caracterizada a nivel estructural e inhibe la fosforilación de EGFR y la proliferación celular[62,63]. Además, la IgTT-1E bispecífica bloqueó eficazmente la interacción PD-1/PD-L1 y promovió una ADCC eficaz mediada por EGFR. Se ha demostrado que la combinación de PD-L1 y EGFR mediante anticuerpos biespecíficos mejora el bloqueo de PD-L1 selectivamente en el microambiente tumoral, debido a la sobreexpresión de EGFR en las células cancerosas, y reduce la posible unión fuera del tumor a células normales que expresan PD-L1[79].

Debido a sus propiedades, que incluyen la unión tetravalente al EGFR, la unión bivalente a PD-L1 y una masa molecular similar a la IgG, es esperable que la IgTT-1E demuestre una mejor localización tumoral en comparación con los anticuerpos biespecíficos previamente generados.

Además, la sobreexpresión y activación del EGFR promueve la expresión de PD-L1 en las células tumorales[159]. Por lo tanto, el EGFR es un AAT idóneo para el desarrollo de una nueva generación de ICI biespecíficos. En comparación con otros anticuerpos biespecíficos de tipo IgG dirigidos simultáneamente contra EGFR y PD-L1[33,34], la IgTT-1E se basa en una región Fc IgG_1 de tipo salvaje que conserva la actividad ADCC[33]. De hecho, la IgTT-1E podría inducir actividad ADCC a nivel intratumoral reduciendo la masa tumoral y estimulando las respuestas inmunes, como se ha demostrado con cetuximab[160]. La presencia concomitante de dominios bloqueantes de PD-L1 en la misma localización espacial sería esencial para superar los mecanismos inmunosupresores en el microambiente tumoral e inducir o reactivar respuestas inmunes adaptativas e innatas frente a las células tumorales. Además, se ha demostrado que la presencia de una región Fc funcional, como en el caso del cetuximab, induce la interacción entre CD y células NK, promoviendo la maduración de las CD y la estimulación de las células T $CD8^{+}$[161]. En conclusión, la IgTT 1E puede determinar una actividad T $CD8^{+}$ sostenida al inducir el "*crosstalk*" celular NK:DC y bloquear la interacción PD-1/PD-L1, lo que podría originar funciones efectoras más potentes de los linfocitos T infiltrantes del tumor.

Artículo 2: *Characterization of a trispecific PD-L1 blocking antibody that exhibits EGFR-conditional 4-1BB agonist activity.*

El diseño de anticuerpos multiespecíficos que combinan inmunomodulación e ICI es un enfoque prometedor para mejorar el efecto de los ICI convencionales. En este trabajo hemos generado un anticuerpo triespecífico de tipo IgG, denominado IgTT-4E1, mediante la fusión de un TT triespecífico 4-1BB x EGFR x PD-L1 con una región Fc silenciada, en la que se han introducido mutaciones para anular o reducir la interacción con FcγR. Esta molécula se basa en la plataforma IgTT, previamente descrita y caracterizada, que consiste en una fusión de un TT mono o multiespecífico con una región Fc[162]. Los dominios de unión de IgTT-4E1 se sitúan alrededor del dominio de homodimerización del colágeno humano, y los estudios cinéticos mediante interferometría de biocapa demostraron que IgTT-4E1 podía unirse a los tres antígenos simultáneamente. Además, la IgTT-4E1 era capaz de reconocer los antígenos específicamente en un contexto celular. Estos resultados sugieren que los dominios de unión están libres de obstáculos estéricos y accesible para las interacciones antigénicas.

Los mAbs agonistas anti-4-1BB pueden clasificarse como agonistas fuertes o débiles. En este trabajo confirmamos, en una línea celular 4-1BB, que urelumab, un agonista fuerte, puede inducir coestimulación sin unión concomitante a FcγR. El anticuerpo anti-4-1BB utilizado para la

generación de la IgTT-4E1-S es un agonista débil[129] y, por tanto, el coestímulo mediado por 4-1BB sólo se indujo en presencia de *cross-linking* adicional. La IgTT-4E1-S muestra una actividad agonista 4-1BB condicional dependiente de la unión a EGFR, pero no a PD-L1. Este hallazgo fue independiente de la posición de los dominios V_{HH} anti-EGFR y anti-PD-L1 en el TT, lo que sugiere que no está influenciado por problemas de impedimento estérico. Estos resultados no son concordantes con los obtenidos con otros anticuerpos anti-4-1BB x anti-PD-L1 [124–127,163,164], en los que se ha descrito una actividad agonista condicional del 4-1BB dependiente de la unión simultánea a PD-L1.

Estas diferencias en la capacidad de los IgTT para inducir la coestimulación mediada por 4-1BB pueden estar relacionadas con determinantes estructurales o con los epítopos reconocidos por los dominios de unión. El scFv anti-4-1BB reconoce el dominio CRD1 (del inglés, *Cysteine-Rich pseudo repeats Domain*) N-terminal del 4-1BB[165]; el V_{HH} anti-EGFR se une a la hendidura formada entre los dominios II y III del EGFR[62], mientras que el epítopo reconocido por el V_{HH} anti-PD-L1 no se ha caracterizado. En la molécula IgTT, cada TT es triespecífico y los tres dominios de unión están muy próximos y restringidos espacialmente, lo que puede limitar el potencial de reconocimiento simultáneo de epítopos localizados distalmente y epítopos más proximales a la membrana[166], como podría ocurrir con las interacciones con 4-1BB, una molécula relativamente grande (86 kDa), y PD-L1, un receptor más compacto (30 kDa). Esto podría no ser una limitación con anticuerpos biespecíficos convencionales, en los que cada brazo reconoce un antígeno diferente, y el área de influencia es significativamente mayor. En el contexto de las interacciones simultáneas entre 4-1BB y EGFR (134 kDa) mediadas por el IgTT-4E1-S, los datos estructurales disponibles sugieren que los epítopos pueden estar más próximos entre sí.

La capacidad de bloquear la interacción PD-L1/PD-1 fue similar a la obtenida con el anticuerpo anti-PD-L1 atezolizumab. Esta capacidad de bloqueo se ha documentado previamente con una versión dimérica del mismo V_{HH} anti-PD-L1 mediante ensayos de tipo ELISA[167]. La unión simultánea a PD-L1 y EGFR mediante anticuerpos biespecíficos promueve un bloqueo de PD-L1 más selectivo en el microambiente tumoral debido a la sobreexpresión de EGFR en las células tumorales, al tiempo que reduce las potenciales uniones a las células normales que expresan PD-L1[164]. Además, la sobreexpresión y activación del EGFR aumenta la expresión de PD-L1 en las células tumorales[168]. La IgTT-4E1-S mejoró la activación y las funciones efectoras de células T primarias humanas co-cultivadas con células tumorales que expresaban EGFR y PD-L1. Sin embargo, para determinar con precisión la capacidad de la IgTT-4E1-S de restringir la coestimulación 4-1BB a tumores $EGFR^+$, minimizando la coestimulación 4-1BB *off-target*, se

requieren más estudios con líneas celulares tumorales que expresen diferentes niveles de EGFR y PD-L1, así como estudios *in vivo* en modelos de ratón humanizados portadores de xenoinjertos derivados de pacientes. El anticuerpo IgTT-4E1-S incorpora un dominio Fc silenciado para evitar o minimizar la toxicidad hepática inducida por los anticuerpos anti-4-1BB, que se atribuye en gran medida a las interacciones Fc-FcγRs[43,169,170], pero son necesarios estudios adicionales en primates no humanos para comprobar con mayor precisión su perfil de toxicidad.

En conclusión, en este trabajo describimos la generación de la IgTT-4E1-S, el primer anticuerpo triespecífico similar a IgG diseñado para proporcionar estimulación 4-1BB condicionada por EGFR a células T activadas a través del TCR, a la vez que bloquea constitutivamente el eje inhibidor PD-1/PD-L1. Esta aparente asimetría entre el agonismo 4-1BB condicional y el bloqueo PD-L1 puede ser relevante en comparación con otros anticuerpos biespecíficos previamente descritos[122,125,127,164], pero se necesitan más estudios para determinar la eficacia y seguridad del anticuerpo IgTT-4E1-S.

Artículo 3: *Dendritic Cell-Mediated Cross-Priming by a Bispecific Neutralizing Antibody Boosts Cytotoxic T Cell Responses and Protects Mice against SARS-CoV-2.*

La mayoría de las estrategias terapéuticas frente al SARSCoV-2 basadas en anticuerpos se han centrado en la neutralización y eliminación del virus, ya sea con mAb convencionales o implementando la multiespecificidad mediante la fusión a regiones Fc u otras estrategias de multimerización[171–175]. Además, se ha documentado en modelos de infección por SARS-CoV-2 *in vivo* que la actividad neutralizante de los anticuerpos depende de las interacciones Fc-Fc*γ*R[176–178]. Se han descrito diferentes estrategias basadas en anticuerpos neutralizantes con interacciones optimizadas de la región Fc a los receptores Fc*γ*IIa y Fc*γ*IIIa con una potencia superior para la prevención o tratamiento del COVID-19[148,171]. No obstante, la aparición de cepas de SARS-CoV-2, que muestran una sensibilidad reducida a los anticuerpos neutralizantes obtenidos mediante inmunización activa (vacunas) o administrados pasivamente, o la aparición de otros virus con potencial pandémico exigen el desarrollo de enfoques innovadores para el tratamiento eficaz de las infecciones víricas.

En este estudio, evaluamos el potencial de un anticuerpo biespecífico sin región Fc, denominado TN^{T}DNGR-1, que incorpora un V_{HH} anti-RBD en tándem (TN) y un scFv anti-DNGR-1 en formato *trimerbody*, para estimular las respuestas de células T CD8^{+} específicas del virus y proteger a ratones transgénicos K18-hACE2 frente a la infección por SARS-CoV-2. Aunque ya se han descrito

enfoques similares para dirigir antígenos tumorales o víricos específicamente a las CDs mediante su fusión con mAbs[179,180], nunca se había explorado una estrategia que combine la neutralización inmediata del virus con la interacción específica a las cCD1, con el objetivo de acelerar y potenciar respuestas inmunes adaptativas.

En este trabajo utilizamos un V_{HH} en tándem biparatópico de alta afinidad, denominado TN, previamente descrito para neutralizar la cepa Wuhan-Hu-1 del SARS-CoV-2 y evitar la aparición de mutaciones de escape[181]. Para maximizar su acción neutralizante, en lugar de generar una fusión Fc tipo Ig convencional[182–184], diseñamos un anticuerpo neutralizante hexavalente anti-RBD en formato *trimerbody*, denominado TN^T, mediante la fusión del TN con el dominio de homotrimerización del colágeno humano XVIII, un formato que ha demostrado eficacia para la generación de anticuerpos con potencial terapéutico[129].

El *trimerbody* N-terminal TN^T demostró un bloqueo completo de la interacción RBD: hACE2 y una potencia similar frente a las variantes RBD beta, gamma, kappa y delta. Además, en comparación con sotrovimab[171,185], el único mAb neutralizante aprobado para uso clínico y activo frente a todos las variantes de interés, el TN^T mostró una mejora de tres a diez veces en la potencia de neutralización frente a todas las cepas VSV-pseudotipadas estudiadas; y la actividad neutralizante de TN^TDNGR-1 fue similar a la del *trimerbody* TN^T parental.

Los datos estructurales del complejo proteína S:TN^T muestran un mecanismo de interacción equimolar (1:1) entre TN^T y la proteína S trimérica, en el que ambos V_{HH} de cada brazo TN se unen simultáneamente a los 3 RBD. Los resultados funcionales demuestran que la plataforma TN^T representa un diseño óptimo para la neutralización de virus que presentan proteínas triméricas para la unión al receptor, como el SARS-CoV2, el virus de la gripe, el virus respiratorio sincitial y el VIH-1[186–188]. De este modo, el formato TN^T proporciona una accesibilidad epitópica óptima para los V_{HH} biparatópicos en tándem, asegurando una neutralización de variantes mutacionales superior a otros diseños triméricos o multiméricos previamente descritos[189,190].

El *trimerbody* biespecífico TN^TDNGR-1 origina la activación de la inmunidad adaptativa *in vivo* mediante la redirección específica de la proteína S neutralizada hacia las células cCD1. En un experimento de inmunización *prime-boost* en ratones inmunocompetentes, la coadministración de proteína S y TN^TDNGR-1 originó un aumento significativo en la frecuencia y número de células T $CD8^+$ efectoras específicas de la proteína S y una respuesta de anticuerpos más polarizada hacia un perfil Th1, en comparación con la administración de proteína S aislada o coadministrada con el *trimerbody* TN^T. Además, nuestros resultados demuestran que la capacidad neutralizante

de un anticuerpo requieren de las interacciones con receptores del sistema inmune, como los FcγRs o el DNGR-1 en DCs o en otras APCs, esenciales para el desarrollo de respuestas inmunes eficaces para el control de la enfermedad[148,177]. El efecto protector se observó en los ratones tratados con TN^{T}DNGR-1 al redirigir los viriones neutralizados hacia las células cCD1, originando su eliminación y promoviendo respuestas inmunes adaptativas.

Por último, aunque tanto el tratamiento con el *trimerbody* TN^{T}DNGR-1 como el tratamiento con sotrovimab provocaron niveles similares de células T CD4^{+} específicas de la proteína S, el tratamiento con TN^{T}DNGR-1 originó una respuesta de células T CD8+ S-específicas de mayor magnitud, caracterizadas por la secreción de IFN-γ, TNF-α (del inglés, *Tumor Necrosis Factor* α) y expresión de IL-2 o CD107a.

En conclusión, hemos generado y caracterizado un anticuerpo biespecífico que, además de una actividad de neutralización del SARS-CoV-2 muy potente, redirige los antígenos virales o viriones hacia las células cCD1 de forma independiente del dominio Fc, induciendo respuestas específicas sistémicas humorales y respuestas locales de células T CD4^{+} y CD8^{+}. La administración terapéutica del anticuerpo TN^{T}DNGR-1 en ratones transgénicos K18-hACE2 proporcionó una protección total frente a la morbilidad y mortalidad asociada a la infección por SARS-CoV-2, provocando una reducción de la carga viral a nivel pulmonar y un aumento de las respuestas inmunes humorales y celulares S-específicas. Por lo tanto, estos resultados indican que el trimerbody TN^{T}DNGR-1 es un candidato prometedor para el desarrollo de tratamientos anti-virales más efectivos, fácilmente adaptable frente a otras variantes del SARS-CoV-2 o frente a otros virus, dada la estructura y naturaleza modular de la molécula.

CONCLUSIONES

I. La plataforma *trimerbody* permite la generación de anticuerpos tipo IgG hexavalentes, denominados IgTT, mediante la fusión de un TT mono, bi o triespecífico con una región Fc salvaje o silenciada.

II. El anticuerpo biespecífico IgTT-1E interacciona simultáneamente con los antígenos EGFR y PD-L1, inhibe la proliferación mediada por EGF, bloquea la interacción PD-1/ PD-L1 e induce actividad ADCC.

III. El anticuerpo IgTT-1E promueve una inhibición significativa del crecimiento tumoral en modelos de ratones humanizados portadores de tumores. Este efecto se asocia a un incremento significativo del número células T $CD8^+$ intratumorales.

IV. El anticuerpo triespecífico IgTT-4E1 interacciona simultáneamente con los antígenos EGFR, PD-L1 y 4-1BB; bloquea la interacción PD-L1/PD1; induce actividad agonista 4-1BB condicional en co-cultivos con células $EGFR^+$, pero no en co-cultivos con células $PD\text{-}L1^+$, y potencia la función efectora de células T primarias co-cultivadas con células tumorales.

V. La plataforma *trimerbody* permite generar anticuerpos sin región Fc con gran capacidad de neutralización del virus SARS-CoV-2 mediante la fusión de V_{HHs} anti-RBD biparatópicos en tándem al dominio de trimerización del colágeno XVIII.

VI. La incorporación de un scFv anti-DNGR-1 adicional permite generar un *trimerbody* biespecífico, denominado $TN^TDNGR\text{-}1$, que redirige el virus neutralizado hacia las células cCD1 de forma independiente al Fc, generando respuestas inmunes humorales y celulares específicas.

VII. La administración terapéutica del anticuerpo $TN^TDNGR\text{-}1$ en ratones transgénicos K18-hACE2 proporcionó una protección total frente a una dosis letal de SARS-CoV-2.

BIBLIOGRAFÍA

1. Weiner, L. M., Surana, R. & Wang, S. Antibodies and cancer therapy: versatile platforms for cancer immunotherapy. *Nat Rev Immunol* **10**, 317–327 (2010).

2. Cuesta, A. M., Sainz-Pastor, N., Bonet, J., Oliva, B. & Alvarez-Vallina, L. Multivalent antibodies: when design surpasses evolution. *Trends Biotechnol* **28**, 355–362 (2010).

3. Kandari, D. & Bhatnagar, R. Antibody engineering and its therapeutic applications. *Int Rev Immunol* **42**, 156–183 (2023).

4. Köhler, G. & Milstein, C. Continuous cultures of fused cells secreting antibody of predefined specificity. *Nature* **256**, 495–497 (1975).

5. Adams, G. P. & Weiner, L. M. Monoclonal antibody therapy of cancer. *Nat Biotechnol* **23**, 1147–1157 (2005).

6. Riechmann, L., Clark, M., Waldmann, H. & Winter, G. Reshaping human antibodies for therapy. *Nature* **332**, 323–327 (1988).

7. Chames, P., Van Regenmortel, M., Weiss, E. & Baty, D. Therapeutic antibodies: successes, limitations and hopes for the future. *Br J Pharmacol* **157**, 220–233 (2009).

8. Brewis, N. Improvement of Key Characteristics of Antibodies. in *Introduction to Antibody Engineering* (eds. Rüker, F. & Wozniak-Knopp, G.) 303–317 (Springer International Publishing, Cham, 2021). doi:10.1007/978-3-030-54630-4_11.

9. Ma, B. & Osborn, M. Transgenic Animals for the Generation of Human Antibodies. in *Introduction to Antibody Engineering* (eds. Rüker, F. & Wozniak-Knopp, G.) 97–127 (Springer International Publishing, Cham, 2021). doi:10.1007/978-3-030-54630-4_5.

10. Sanz, L., Blanco, B. & Alvarez-Vallina, L. Antibodies and gene therapy: teaching old ‘magic bullets’ new tricks. *Trends Immunol* **25**, 85–91 (2004).

11. Orlandi, R., Güssow, D. H., Jones, P. T. & Winter, G. Cloning immunoglobulin variable domains for expression by the polymerase chain reaction. *Proc Natl Acad Sci U S A* **86**, 3833–3837 (1989).

12. Loo, L., Robinson, M. K. & Adams, G. P. Antibody engineering principles and applications. *Cancer J* **14**, 149–153 (2008).

13. Kumar, R., Parray, H. A., Shrivastava, T., Sinha, S. & Luthra, K. Phage display antibody libraries: A robust approach for generation of recombinant human monoclonal antibodies. *Int J Biol Macromol* **135**, 907–918 (2019).

14. Lu, R.-M. *et al.* Development of therapeutic antibodies for the treatment of diseases. *J Biomed Sci* **27**, 1 (2020).

15. Harmsen, M. M. & De Haard, H. J. Properties, production, and applications of camelid single-domain antibody fragments. *Appl Microbiol Biotechnol* **77**, 13–22 (2007).

16. Tapia-Galisteo, A., Compte, M., Álvarez-Vallina, L. & Sanz, L. When three is not a crowd: trispecific antibodies for enhanced cancer immunotherapy. *Theranostics* **13**, 1028–1041 (2023).

17. Wu, X. & Demarest, S. J. Building blocks for bispecific and trispecific antibodies. *Methods* **154**, 3–9 (2019).

18. Blanco, B., Domínguez-Alonso, C. & Alvarez-Vallina, L. Bispecific Immunomodulatory Antibodies for Cancer Immunotherapy. *Clin Cancer Res* **27**, 5457–5464 (2021).

19. Zhu, Z., Presta, L. G., Zapata, G. & Carter, P. Remodeling domain interfaces to enhance heterodimer formation. *Protein Sci* **6**, 781–788 (1997).

20. Johnson, S. *et al.* Effector cell recruitment with novel Fv-based dual-affinity re-targeting protein leads to potent tumor cytolysis and in vivo B-cell depletion. *J Mol Biol* **399**, 436–449 (2010).

21. Chichili, G. R. *et al.* A CD3xCD123 bispecific DART for redirecting host T cells to myelogenous leukemia: preclinical activity and safety in nonhuman primates. *Sci Transl Med* **7**, 289ra82 (2015).

22. Kipriyanov, S. M. *et al.* Bispecific tandem diabody for tumor therapy with improved antigen binding and pharmacokinetics. *J Mol Biol* **293**, 41–56 (1999).

23. Bogen, J. P. *et al.* Design of a Trispecific Checkpoint Inhibitor and Natural Killer Cell Engager Based on a 2 + 1 Common Light Chain Antibody Architecture. *Front Immunol* **12**, 669496 (2021).

24. Nuñez-Prado, N. *et al.* The coming of age of engineered multivalent antibodies. *Drug Discov Today* **20**, 588–594 (2015).

25. Silencing Fc Domains in T cell-Engaging Bispecific Antibodies Improves T-cell Trafficking and Antitumor Potency - PubMed. https://pubmed.ncbi.nlm.nih.gov/31615814/.

26. Shields, R. L. *et al.* High resolution mapping of the binding site on human IgG1 for Fc gamma RI, Fc gamma RII, Fc gamma RIII, and FcRn and design of IgG1 variants with improved binding to the Fc gamma R. *J Biol Chem* **276**, 6591–6604 (2001).

27. Ghetie, V. *et al.* Increasing the serum persistence of an IgG fragment by random mutagenesis. *Nat Biotechnol* **15**, 637–640 (1997).

28. Suresh, M. R., Cuello, A. C. & Milstein, C. Bispecific monoclonal antibodies from hybrid hybridomas. *Methods Enzymol* **121**, 210–228 (1986).

29. Marvin, J. S. & Zhu, Z. Recombinant approaches to IgG-like bispecific antibodies. *Acta Pharmacol Sin* **26**, 649–658 (2005).

30. Ridgway, J. B., Presta, L. G. & Carter, P. 'Knobs-into-holes' engineering of antibody CH3 domains for heavy chain heterodimerization. *Protein Eng* **9**, 617–621 (1996).

31. Brinkmann, U. & Kontermann, R. E. The making of bispecific antibodies. *MAbs* **9**, 182–212 (2017).

32. Merchant, A. M. *et al.* An efficient route to human bispecific IgG. *Nat Biotechnol* **16**, 677–681 (1998).

33. Li, L. *et al.* Tumor-targeting anti-EGFR x anti-PD1 bispecific antibody inhibits EGFR-overexpressing tumor growth by combining EGFR blockade and immune activation with direct tumor cell killing. *Transl Oncol* **14**, 100916 (2021).

34. Koopmans, I. *et al.* A novel bispecific antibody for EGFR-directed blockade of the PD-1/PD-L1 immune checkpoint. *Oncoimmunology* **7**, e1466016 (2018).

35. Steinmetz, A. *et al.* CODV-Ig, a universal bispecific tetravalent and multifunctional immunoglobulin format for medical applications. *MAbs* **8**, 867–878 (2016).

36. Gramer, M. J. *et al.* Production of stable bispecific IgG1 by controlled Fab-arm exchange: scalability from bench to large-scale manufacturing by application of standard approaches. *MAbs* **5**, 962–973 (2013).

37. Castoldi, R. *et al.* Molecular characterization of novel trispecific ErbB-cMet-IGF1R antibodies and their antigen-binding properties. *Protein Eng Des Sel* **25**, 551–560 (2012).

38. Lewis, S. M. *et al.* Generation of bispecific IgG antibodies by structure-based design of an orthogonal Fab interface. *Nat Biotechnol* **32**, 191–198 (2014).

39. Shoulders, M. D. & Raines, R. T. Collagen structure and stability. *Annu Rev Biochem* **78**, 929–958 (2009).

40. Cuesta, A. M. *et al.* Improved stability of multivalent antibodies containing the human collagen XV trimerization domain. *MAbs* **4**, 226–232 (2012).

41. Sánchez-Arévalo Lobo, V. J. *et al.* Enhanced antiangiogenic therapy with antibody-collagen XVIII NC1 domain fusion proteins engineered to exploit matrix remodeling events. *International Journal of Cancer* **119**, 455–462 (2006).

42. Blanco-Toribio, A. *et al.* Generation and characterization of monospecific and bispecific hexavalent trimerbodies. *MAbs* **5**, 70–79 (2013).

43. Compte, M. *et al.* A tumor-targeted trimeric 4-1BB-agonistic antibody induces potent anti-tumor immunity without systemic toxicity. *Nat Commun* **9**, 4809 (2018).

44. Mikkelsen, K. *et al.* Carcinoembryonic Antigen (CEA)-Specific 4-1BB-Costimulation Induced by CEA-Targeted 4-1BB-Agonistic Trimerbodies. *Front Immunol* **10**, 1791 (2019).

45. Lázaro-Gorines, R. *et al.* A novel Carcinoembryonic Antigen (CEA)-Targeted Trimeric Immunotoxin shows significantly enhanced Antitumor Activity in Human Colorectal Cancer Xenografts. *Sci Rep* **9**, 11680 (2019).

46. Alvarez-Cienfuegos, A. *et al.* Intramolecular trimerization, a novel strategy for making multispecific antibodies with controlled orientation of the antigen binding domains. *Sci Rep* **6**, 28643 (2016).

47. Harwood, S. L. *et al.* ATTACK, a novel bispecific T cell-recruiting antibody with trivalent EGFR binding and monovalent CD3 binding for cancer immunotherapy. *Oncoimmunology* **7**, e1377874 (2017).

48. Compte, M., Sanz, L. & Álvarez-Vallina, L. Chapter Three - Applications of trimerbodies in cancer immunotherapy. in *International Review of Cell and Molecular Biology* (eds. Aranda, F., Berraondo, P. & Galluzzi, L.) vol. 369 71–87 (Academic Press, 2022).

49. Chen, D. S. & Mellman, I. Elements of cancer immunity and the cancer-immune set point. *Nature* **541**, 321–330 (2017).

50. Mellman, I., Coukos, G. & Dranoff, G. Cancer immunotherapy comes of age. *Nature* **480**, 480–489 (2011).

51. Chen, D. S. & Mellman, I. Oncology meets immunology: the cancer-immunity cycle. *Immunity* **39**, 1–10 (2013).

52. Yaddanapudi, K., Mitchell, R. A. & Eaton, J. W. Cancer vaccines. *Oncoimmunology* **2**, e23403 (2013).

53. Farkona, S., Diamandis, E. P. & Blasutig, I. M. Cancer immunotherapy: the beginning of the end of cancer? *BMC Med* **14**, 73 (2016).

54. Morgillo, F. & Lee, H.-Y. Resistance to epidermal growth factor receptor-targeted therapy. *Drug Resistance Updates* **8**, 298–310 (2005).

55. Kontermann, R. E. Dual targeting strategies with bispecific antibodies. *MAbs* **4**, 182–197 (2012).

56. Antibody therapeutics approved or in regulatory review in the EU or US. *The Antibody Society* https://www.antibodysociety.org/resources/approved-antibodies/.

57. The EGF receptor family as targets for cancer therapy - PubMed. https://pubmed.ncbi.nlm.nih.gov/11426640/.

58. Lemmon, M. A. & Schlessinger, J. Regulation of signal transduction and signal diversity by receptor oligomerization. *Trends Biochem Sci* **19**, 459–463 (1994).

59. Alroy, I. & Yarden, Y. The ErbB signaling network in embryogenesis and oncogenesis: signal diversification through combinatorial ligand-receptor interactions. *FEBS Lett* **410**, 83–86 (1997).

60. Riese, D. J. & Stern, D. F. Specificity within the EGF family/ErbB receptor family signaling network. *Bioessays* **20**, 41–48 (1998).

61. Pozzi, C. *et al.* The EGFR-specific antibody cetuximab combined with chemotherapy triggers immunogenic cell death. *Nat Med* **22**, 624–631 (2016).

62. Schmitz, K. R., Bagchi, A., Roovers, R. C., van Bergen en Henegouwen, P. M. P. & Ferguson, K. M. Structural evaluation of EGFR inhibition mechanisms for nanobodies/VHH domains. *Structure* **21**, 1214–1224 (2013).

63. Schmiedel, J., Blaukat, A., Li, S., Knöchel, T. & Ferguson, K. M. Matuzumab binding to EGFR prevents the conformational rearrangement required for dimerization. *Cancer Cell* **13**, 365–373 (2008).

64. Pardoll, D. M. & Topalian, S. L. The role of CD4+ T cell responses in antitumor immunity. *Curr Opin Immunol* **10**, 588–594 (1998).

65. Dobosz, P. & Dzieciątkowski, T. The Intriguing History of Cancer Immunotherapy. *Front Immunol* **10**, 2965 (2019).

66. Peterson, C., Denlinger, N. & Yang, Y. Recent Advances and Challenges in Cancer Immunotherapy. *Cancers* **14**, 3972 (2022).

67. Hargadon, K. M., Johnson, C. E. & Williams, C. J. Immune checkpoint blockade therapy for cancer: An overview of FDA-approved immune checkpoint inhibitors. *Int Immunopharmacol* **62**, 29–39 (2018).

68. Naimi, A. *et al.* Tumor immunotherapies by immune checkpoint inhibitors (ICIs); the pros and cons. *Cell Commun Signal* **20**, 44 (2022).

69. Horn, L. *et al.* First-Line Atezolizumab plus Chemotherapy in Extensive-Stage Small-Cell Lung Cancer. *N Engl J Med* **379**, 2220–2229 (2018).

70. D'Angelo, S. P. *et al.* First-line avelumab in a cohort of 116 patients with metastatic Merkel cell carcinoma (JAVELIN Merkel 200): primary and biomarker analyses of a phase II study. *J Immunother Cancer* **9**, e002646 (2021).

71. Antonia, S. J. *et al.* Durvalumab after Chemoradiotherapy in Stage III Non-Small-Cell Lung Cancer. *N Engl J Med* **377**, 1919–1929 (2017).

72. Kubli, S. P., Berger, T., Araujo, D. V., Siu, L. L. & Mak, T. W. Beyond immune checkpoint blockade: emerging immunological strategies. *Nat Rev Drug Discov* **20**, 899–919 (2021).

73. Ishida, Y., Agata, Y., Shibahara, K. & Honjo, T. Induced expression of PD-1, a novel member of the immunoglobulin gene superfamily, upon programmed cell death. *EMBO J* **11**, 3887–3895 (1992).

74. Picardo, S. L., Doi, J. & Hansen, A. R. Structure and Optimization of Checkpoint Inhibitors. *Cancers (Basel)* **12**, 38 (2019).

75. Dong, H. *et al.* Tumor-associated B7-H1 promotes T-cell apoptosis: a potential mechanism of immune evasion. *Nat Med* **8**, 793–800 (2002).

76. Chen, L. & Han, X. Anti-PD-1/PD-L1 therapy of human cancer: past, present, and future. *J Clin Invest* **125**, 3384–3391 (2015).

77. Schroder, K., Hertzog, P. J., Ravasi, T. & Hume, D. A. Interferon-gamma: an overview of signals, mechanisms and functions. *J Leukoc Biol* **75**, 163–189 (2004).

78. Parsa, A. T. *et al.* Loss of tumor suppressor PTEN function increases B7-H1 expression and immunoresistance in glioma. *Nat Med* **13**, 84–88 (2007).

79. Akbay, E. A. *et al.* Activation of the PD-1 pathway contributes to immune escape in EGFR-driven lung tumors. *Cancer Discov* **3**, 1355–1363 (2013).

80. Marzec, M. *et al.* Oncogenic kinase NPM/ALK induces through STAT3 expression of immunosuppressive protein CD274 (PD-L1, B7-H1). *Proc Natl Acad Sci U S A* **105**, 20852–20857 (2008).

81. Prognostic and predictive value of PDL1 expression in breast cancer - PubMed. https://pubmed.ncbi.nlm.nih.gov/25669979/.

82. Muenst, S. *et al.* Expression of programmed death ligand 1 (PD-L1) is associated with poor prognosis in human breast cancer. *Breast Cancer Res Treat* **146**, 15–24 (2014).

83. Sznol, M. & Chen, L. Antagonist antibodies to PD-1 and B7-H1 (PD-L1) in the treatment of advanced human cancer. *Clin Cancer Res* **19**, 1021–1034 (2013).

84. Topalian, S. L., Drake, C. G. & Pardoll, D. M. Immune checkpoint blockade: a common denominator approach to cancer therapy. *Cancer Cell* **27**, 450–461 (2015).

85. Chester, C., Sanmamed, M. F., Wang, J. & Melero, I. Immunotherapy targeting 4-1BB: mechanistic rationale, clinical results, and future strategies. *Blood* **131**, 49–57 (2018).

86. Goodwin, R. G. *et al.* Molecular cloning of a ligand for the inducible T cell gene 4-1BB: a member of an emerging family of cytokines with homology to tumor necrosis factor. *Eur J Immunol* **23**, 2631–2641 (1993).

87. DeBenedette, M. A., Shahinian, A., Mak, T. W. & Watts, T. H. Costimulation of CD28- T lymphocytes by 4-1BB ligand. *J Immunol* **158**, 551–559 (1997).

88. Lee, D. Y. *et al.* 4-1BB signaling activates the t cell factor 1 effector/β-catenin pathway with delayed kinetics via ERK signaling and delayed PI3K/AKT activation to promote the proliferation of CD8+ T Cells. *PLoS One* **8**, e69677 (2013).

89. Alderson, M. R. *et al.* Molecular and biological characterization of human 4-1BB and its ligand. *Eur J Immunol* **24**, 2219–2227 (1994).

90. Sabbagh, L., Pulle, G., Liu, Y., Tsitsikov, E. N. & Watts, T. H. ERK-Dependent Bim Modulation Downstream of the 4-1BB-TRAF1 Signaling Axis Is a Critical Mediator of CD8 T Cell Survival In Vivo1. *The Journal of Immunology* **180**, 8093–8101 (2008).

91. Wilcox, R. A. *et al.* Cutting edge: Expression of functional CD137 receptor by dendritic cells. *J Immunol* **168**, 4262–4267 (2002).

92. Lee, H.-W. *et al.* 4-1BB promotes the survival of CD8+ T lymphocytes by increasing expression of Bcl-xL and Bfl-1. *J Immunol* **169**, 4882–4888 (2002).

93. Gauttier, V. *et al.* Agonistic anti-CD137 antibody treatment leads to antitumor response in mice with liver cancer. *Int J Cancer* **135**, 2857–2867 (2014).

94. Houot, R. *et al.* Therapeutic effect of CD137 immunomodulation in lymphoma and its enhancement by Treg depletion. *Blood* **114**, 3431–3438 (2009).

95. Melero, I., Grimaldi, A. M., Perez-Gracia, J. L. & Ascierto, P. A. Clinical development of immunostimulatory monoclonal antibodies and opportunities for combination. *Clin Cancer Res* **19**, 997–1008 (2013).

96. Combination CTLA-4 blockade and 4-1BB activation enhances tumor rejection by increasing T-cell infiltration, proliferation, and cytokine production - PubMed. https://pubmed.ncbi.nlm.nih.gov/21559358/.

97. An Update on Anti-CD137 Antibodies in Immunotherapies for Cancer - PubMed. https://pubmed.ncbi.nlm.nih.gov/31013788/.

98. 4-1BB agonism: adding the accelerator to cancer immunotherapy - PubMed. https://pubmed.ncbi.nlm.nih.gov/27034234/.

99. Phase I study of BMS-663513, a fully human anti-CD137 agonist monoclonal antibody, in patients (pts) with advanced cancer (CA) | Journal of Clinical Oncology. https://ascopubs.org/doi/10.1200/jco.2008.26.15_suppl.3007.

100. Segal, N. H. *et al.* Results from an Integrated Safety Analysis of Urelumab, an Agonist Anti-CD137 Monoclonal Antibody. *Clinical Cancer Research* **23**, 1929–1936 (2017).

101. Zhang, J. *et al.* S100A4 blockage alleviates agonistic anti-CD137 antibody-induced liver pathology without disruption of antitumor immunity. *Oncoimmunology* **7**, e1296996 (2018).

102. Chu, D.-T. *et al.* An Update on Anti-CD137 Antibodies in Immunotherapies for Cancer. *Int J Mol Sci* **20**, 1822 (2019).

103. Chin, S. M. *et al.* Structure of the 4-1BB/4-1BBL complex and distinct binding and functional properties of utomilumab and urelumab. *Nat Commun* **9**, 4679 (2018).

104. Goebeler, M.-E. & Bargou, R. C. T cell-engaging therapies — BiTEs and beyond. *Nat Rev Clin Oncol* **17**, 418–434 (2020).

105. Klein, C., Brinkmann, U., Reichert, J. M. & Kontermann, R. E. The present and future of bispecific antibodies for cancer therapy. *Nat Rev Drug Discov* (2024) doi:10.1038/s41573-024-00896-6.

106. Seimetz, D., Lindhofer, H. & Bokemeyer, C. Development and approval of the trifunctional antibody catumaxomab (anti-EpCAM x anti-CD3) as a targeted cancer immunotherapy. *Cancer Treat Rev* **36**, 458–467 (2010).

107. Budde, L. E. *et al.* Safety and efficacy of mosunetuzumab, a bispecific antibody, in patients with relapsed or refractory follicular lymphoma: a single-arm, multicentre, phase 2 study. *Lancet Oncol* **23**, 1055–1065 (2022).

108. Moreau, P. *et al.* Teclistamab in Relapsed or Refractory Multiple Myeloma. *N Engl J Med* **387**, 495–505 (2022).

109. Rosenberg, S. A., Restifo, N. P., Yang, J. C., Morgan, R. A. & Dudley, M. E. Adoptive cell transfer: a clinical path to effective cancer immunotherapy. *Nat Rev Cancer* **8**, 299–308 (2008).

110. Paucek, R. D., Baltimore, D. & Li, G. The Cellular Immunotherapy Revolution: Arming the Immune System for Precision Therapy. *Trends Immunol* **40**, 292–309 (2019).

111. June, C. H., O'Connor, R. S., Kawalekar, O. U., Ghassemi, S. & Milone, M. C. CAR T cell immunotherapy for human cancer. *Science* **359**, 1361–1365 (2018).

112. Gross, G., Waks, T. & Eshhar, Z. Expression of immunoglobulin-T-cell receptor chimeric molecules as functional receptors with antibody-type specificity. *Proc Natl Acad Sci U S A* **86**, 10024–10028 (1989).

113. Shah, N. N. *et al.* CD4/CD8 T-Cell Selection Affects Chimeric Antigen Receptor (CAR) T-Cell Potency and Toxicity: Updated Results From a Phase I Anti-CD22 CAR T-Cell Trial. *J Clin Oncol* **38**, 1938–1950 (2020).

114. Pre-conditioning modifies the TME to enhance solid tumor CAR T cell efficacy and endogenous protective immunity - PubMed. https://pubmed.ncbi.nlm.nih.gov/33647456/.

115. T Cell-Redirecting Strategies to 'STAb' Tumors: Beyond CARs and Bispecific Antibodies - PubMed. https://pubmed.ncbi.nlm.nih.gov/30827461/.

116. Blanco, B., Ramírez-Fernández, Á. & Alvarez-Vallina, L. Engineering Immune Cells for in vivo Secretion of Tumor-Specific T Cell-Redirecting Bispecific Antibodies. *Front Immunol* **11**, 1792 (2020).

117. Blanco, B. *et al.* Overcoming CAR-Mediated CD19 Downmodulation and Leukemia Relapse with T Lymphocytes Secreting Anti-CD19 T-cell Engagers. *Cancer Immunol Res* **10**, 498–511 (2022).

118. Díez-Alonso, L. *et al.* Engineered T cells secreting anti-BCMA T cell engagers control multiple myeloma and promote immune memory in vivo. *Sci Transl Med* **16**, eadg7962 (2024).

119. Lee, C. M. & Tannock, I. F. The distribution of the therapeutic monoclonal antibodies cetuximab and trastuzumab within solid tumors. *BMC Cancer* **10**, 255 (2010).

120. Bauman, J. E. & Grandis, J. R. Targeting secondary immune responses to cetuximab: CD137 and the outside story. *J Clin Invest* **124**, 2371–2375 (2014).

121. Srivastava, R. M. *et al.* CD137 Stimulation Enhances Cetuximab-Induced Natural Killer: Dendritic Cell Priming of Antitumor T-Cell Immunity in Patients with Head and Neck Cancer. *Clin Cancer Res* **23**, 707–716 (2017).

122. Geuijen, C. *et al.* A human CD137×PD-L1 bispecific antibody promotes anti-tumor immunity via context-dependent T cell costimulation and checkpoint blockade. *Nat Commun* **12**, 4445 (2021).

123. Cheng, L.-S. *et al.* An Fc-muted bispecific antibody targeting PD-L1 and 4-1BB induces antitumor immune activity in colorectal cancer without systemic toxicity. *Cell Mol Biol Lett* **28**, 47 (2023).

124. Jeong, S. *et al.* Novel anti-4-1BB×PD-L1 bispecific antibody augments anti-tumor immunity through tumor-directed T-cell activation and checkpoint blockade. *J Immunother Cancer* **9**, e002428 (2021).

125. Peper-Gabriel, J. K. *et al.* The PD-L1/4-1BB Bispecific Antibody-Anticalin Fusion Protein PRS-344/S095012 Elicits Strong T-Cell Stimulation in a Tumor-Localized Manner. *Clin Cancer Res* **28**, 3387–3399 (2022).

126. Muik, A. *et al.* An Fc-inert PD-L1×4-1BB bispecific antibody mediates potent anti-tumor immunity in mice by combining checkpoint inhibition and conditional 4-1BB co-stimulation. *Oncoimmunology* **11**, 2030135 (2022).

127. Muik, A. *et al.* Preclinical Characterization and Phase I Trial Results of a Bispecific Antibody Targeting PD-L1 and 4-1BB (GEN1046) in Patients with Advanced Refractory Solid Tumors. *Cancer Discov* **12**, 1248–1265 (2022).

128. Shen, A. *et al.* A novel 4-1BB/HER2 bispecific antibody shows potent antitumor activities by increasing and activating tumor-infiltrating T cells. *Am J Cancer Res* **13**, 3246–3256 (2023).

129. Compte, M. *et al.* An Fc-free EGFR-specific 4-1BB-agonistic Trimerbody Displays Broad Antitumor Activity in Humanized Murine Cancer Models without Toxicity. *Clin Cancer Res* **27**, 3167–3177 (2021).

130. Hangiu, O. *et al.* Tumor targeted 4-1BB agonist antibody-albumin fusions with high affinity to FcRn induce anti-tumor immunity without toxicity. *iScience* **25**, 104958 (2022).

131. Compte, M. *et al.* Case Report: An EGFR-Targeted 4-1BB-agonistic Trimerbody Does Not Induce Hepatotoxicity in Transgenic Mice With Liver Expression of Human EGFR. *Front Immunol* **11**, 614363 (2020).

132. Hinner, M. J. *et al.* Tumor-Localized Costimulatory T-Cell Engagement by the 4-1BB/HER2 Bispecific Antibody-Anticalin Fusion PRS-343. *Clin Cancer Res* **25**, 5878–5889 (2019).

133. Claus, C. *et al.* Tumor-targeted 4-1BB agonists for combination with T cell bispecific antibodies as off-the-shelf therapy. *Sci Transl Med* **11**, eaav5989 (2019).

134. von Behring, E. & Kitasato, S. [The mechanism of diphtheria immunity and tetanus immunity in animals. 1890]. *Mol Immunol* **28**, 1317, 1319–1320 (1991).

135. Laursen, N. S. *et al.* Universal protection against influenza infection by a multidomain antibody to influenza hemagglutinin. *Science* **362**, 598–602 (2018).

136. Dong, J. *et al.* Development of humanized tri-specific nanobodies with potent neutralization for SARS-CoV-2. *Sci Rep* **10**, 17806 (2020).

137. Ali, M. G. *et al.* Recent advances in therapeutic applications of neutralizing antibodies for virus infections: an overview. *Immunol Res* **68**, 325–339 (2020).

138. Koff, W. C. *et al.* Accelerating next-generation vaccine development for global disease prevention. *Science* **340**, 1232910 (2013).

139. Marasco, W. A. & Sui, J. The growth and potential of human antiviral monoclonal antibody therapeutics. *Nat Biotechnol* **25**, 1421–1434 (2007).

140. Caskey, M. *et al.* Viraemia suppressed in HIV-1-infected humans by broadly neutralizing antibody 3BNC117. *Nature* **522**, 487–491 (2015).

141. Ross, R. W. The Newala epidemic. III. The virus: isolation, pathogenic properties and relationship to the epidemic. *J Hyg (Lond)* **54**, 177–191 (1956).

142. Maher, M. C. *et al.* Predicting the mutational drivers of future SARS-CoV-2 variants of concern. *Sci Transl Med* eabk3445 doi:10.1126/scitranslmed.abk3445.

143. Lan, J. *et al.* Structure of the SARS-CoV-2 spike receptor-binding domain bound to the ACE2 receptor. *Nature* **581**, 215–220 (2020).

144. Shanmugaraj, B., Siriwattananon, K., Wangkanont, K. & Phoolcharoen, W. Perspectives on monoclonal antibody therapy as potential therapeutic intervention for Coronavirus disease-19 (COVID-19). *Asian Pac J Allergy Immunol* **38**, 10–18 (2020).

145. Chen, R. E. *et al.* Resistance of SARS-CoV-2 variants to neutralization by monoclonal and serum-derived polyclonal antibodies. *Nat Med* **27**, 717–726 (2021).

146. Xiang, Y. *et al.* Versatile and multivalent nanobodies efficiently neutralize SARS-CoV-2. *Science* **370**, 1479–1484 (2020).

147. Güttler, T. *et al.* Neutralization of SARS-CoV-2 by highly potent, hyperthermostable, and mutation-tolerant nanobodies. *EMBO J* **40**, e107985 (2021).

148. Yamin, R. *et al.* Fc-engineered antibody therapeutics with improved anti-SARS-CoV-2 efficacy. *Nature* **599**, 465–470 (2021).

149. Surowka, M., Schaefer, W. & Klein, C. Ten years in the making: application of CrossMab technology for the development of therapeutic bispecific antibodies and antibody fusion proteins. *MAbs* **13**, 1967714 (2021).

150. Klein, C. *et al.* Progress in overcoming the chain association issue in bispecific heterodimeric IgG antibodies. *MAbs* **4**, 653–663 (2012).

151. Clarke, S. C. *et al.* Multispecific Antibody Development Platform Based on Human Heavy Chain Antibodies. *Front Immunol* **9**, 3037 (2019).

152. Labrijn, A. F. *et al.* Efficient generation of stable bispecific IgG1 by controlled Fab-arm exchange. *Proc Natl Acad Sci U S A* **110**, 5145–5150 (2013).

153. Wu, Y., Yi, M., Zhu, S., Wang, H. & Wu, K. Recent advances and challenges of bispecific antibodies in solid tumors. *Exp Hematol Oncol* **10**, 56 (2021).

154. Labrijn, A. F., Janmaat, M. L., Reichert, J. M. & Parren, P. W. H. I. Bispecific antibodies: a mechanistic review of the pipeline. *Nat Rev Drug Discov* **18**, 585–608 (2019).

155. Spiess, C., Zhai, Q. & Carter, P. J. Alternative molecular formats and therapeutic applications for bispecific antibodies. *Mol Immunol* **67**, 95–106 (2015).

156. Ha, J.-H., Kim, J.-E. & Kim, Y.-S. Immunoglobulin Fc Heterodimer Platform Technology: From Design to Applications in Therapeutic Antibodies and Proteins. *Front Immunol* **7**, 394 (2016).

157. Rath, T. *et al.* Fc-fusion proteins and FcRn: structural insights for longer-lasting and more effective therapeutics. *Crit Rev Biotechnol* **35**, 235–254 (2015).

158. Thomas, R. & Weihua, Z. Rethink of EGFR in Cancer With Its Kinase Independent Function on Board. *Front Oncol* **9**, 800 (2019).

159. Chen, N. *et al.* Upregulation of PD-L1 by EGFR Activation Mediates the Immune Escape in EGFR-Driven NSCLC: Implication for Optional Immune Targeted Therapy for NSCLC Patients with EGFR Mutation. *J Thorac Oncol* **10**, 910–923 (2015).

160. Ferris, R. L. *et al.* Rationale for combination of therapeutic antibodies targeting tumor cells and immune checkpoint receptors: Harnessing innate and adaptive immunity through IgG1 isotype immune effector stimulation. *Cancer Treat Rev* **63**, 48–60 (2018).

161. Srivastava, R. M. *et al.* Cetuximab-activated natural killer and dendritic cells collaborate to trigger tumor antigen-specific T-cell immunity in head and neck cancer patients. *Clin Cancer Res* **19**, 1858–1872 (2013).

162. Rubio-Pérez, L. *et al.* A PD-L1/EGFR bispecific antibody combines immune checkpoint blockade and direct anti-cancer action for an enhanced anti-tumor response. *Oncoimmunology* **12**, 2205336.

163. Zhai, T. *et al.* Generation of a safe and efficacious llama single-domain antibody fragment (vHH) targeting the membrane-proximal region of 4-1BB for engineering therapeutic bispecific antibodies for cancer. *J Immunother Cancer* **9**, e002131 (2021).

164. Warmuth, S. *et al.* Engineering of a trispecific tumor-targeted immunotherapy incorporating 4-1BB co-stimulation and PD-L1 blockade. *Oncoimmunology* **10**, 2004661 (2021).

165. Bitra, A., Doukov, T., Croft, M. & Zajonc, D. M. Crystal structures of the human 4-1BB receptor bound to its ligand 4-1BBL reveal covalent receptor dimerization as a potential signaling amplifier. *J Biol Chem* **293**, 9958–9969 (2018).

166. Bluemel, C. *et al.* Epitope distance to the target cell membrane and antigen size determine the potency of T cell-mediated lysis by BiTE antibodies specific for a large melanoma surface antigen. *Cancer Immunol Immunother* **59**, 1197–1209 (2010).

167. Silva-Pilipich, N. *et al.* Local delivery of optimized nanobodies targeting the PD-1/PD-L1 axis with a self-amplifying RNA viral vector induces potent antitumor responses. *Cancer Letters* **561**, 216139 (2023).

168. Zhang, W. *et al.* Induction of PD-L1 expression by epidermal growth factor receptor–mediated signaling in esophageal squamous cell carcinoma. *Onco Targets Ther* **10**, 763–771 (2017).

169. Melero, I. *et al.* Monoclonal antibodies against the 4-1BB T-cell activation molecule eradicate established tumors. *Nat Med* **3**, 682–685 (1997).

170. Li, F. & Ravetch, J. V. Antitumor activities of agonistic anti-TNFR antibodies require differential FcγRIIB coengagement in vivo. *Proc Natl Acad Sci U S A* **110**, 19501–19506 (2013).

171. Cathcart, A. *et al.* The dual function monoclonal antibodies VIR-7831 and VIR-7832 demonstrate potent in vitro and in vivo activity against SARS-CoV-. Preprint at https://doi.org/10.1101/2021.03.09.434607 (2021).

172. Walter, J. D. *et al.* Biparatopic sybodies neutralize SARS-CoV-2 variants of concern and mitigate drug resistance. *EMBO Rep* **23**, e54199 (2022).

173. Du, W. *et al.* Novel Affibody Molecules Specifically Bind to SARS-CoV-2 Spike Protein and Efficiently Neutralize Delta and Omicron Variants. *Microbiol Spectr* **11**, e0356222 (2023).

174. Li, D., Sempowski, G. D., Saunders, K. O., Acharya, P. & Haynes, B. F. SARS-CoV-2 Neutralizing Antibodies for COVID-19 Prevention and Treatment. *Annu Rev Med* **73**, 1–16 (2022).

175. Obeng, E. M., Dzuvor, C. K. O. & Danquah, M. K. Anti-SARS-CoV-1 and -2 nanobody engineering towards avidity-inspired therapeutics. *Nano Today* **42**, 101350 (2022).

176. Suryadevara, N. *et al.* Neutralizing and protective human monoclonal antibodies recognizing the N-terminal domain of the SARS-CoV-2 spike protein. *Cell* **184**, 2316-2331.e15 (2021).

177. Winkler, E. S. *et al.* Human neutralizing antibodies against SARS-CoV-2 require intact Fc effector functions for optimal therapeutic protection. *Cell* **184**, 1804-1820.e16 (2021).

178. Ullah, I. *et al.* Live Imaging of SARS-CoV-2 Infection in Mice Reveals Neutralizing Antibodies Require Fc Function for Optimal Efficacy. *bioRxiv* 2021.03.22.436337 (2021) doi:10.1101/2021.03.22.436337.

179. Sancho, D. *et al.* Tumor therapy in mice via antigen targeting to a novel, DC-restricted C-type lectin. *J Clin Invest* **118**, 2098–2110 (2008).

180. Wang, Y. *et al.* Dendritic cell biology and its role in tumor immunotherapy. *J Hematol Oncol* **13**, 107 (2020).

181. Koenig, P.-A. *et al.* Structure-guided multivalent nanobodies block SARS-CoV-2 infection and suppress mutational escape. *Science* **371**, eabe6230 (2021).

182. Rossotti, M. A. *et al.* Arsenal of nanobodies shows broad-spectrum neutralization against SARS-CoV-2 variants of concern in vitro and in vivo in hamster models. *Commun Biol* **5**, 933 (2022).

183. Wrapp, D. *et al.* Structural Basis for Potent Neutralization of Betacoronaviruses by Single-Domain Camelid Antibodies. *Cell* **181**, 1004-1015.e15 (2020).

184. Huo, J. *et al.* A potent SARS-CoV-2 neutralising nanobody shows therapeutic efficacy in the Syrian golden hamster model of COVID-19. *Nat Commun* **12**, 5469 (2021).

185. Gupta, A. *et al.* Early Treatment for Covid-19 with SARS-CoV-2 Neutralizing Antibody Sotrovimab. *N Engl J Med* **385**, 1941–1950 (2021).

186. Guthmiller, J. J. *et al.* Broadly neutralizing antibodies target a haemagglutinin anchor epitope. *Nature* **602**, 314–320 (2022).

187. Sok, D. & Burton, D. R. Recent progress in broadly neutralizing antibodies to HIV. *Nat Immunol* **19**, 1179–1188 (2018).

188. Tang, A. *et al.* A potent broadly neutralizing human RSV antibody targets conserved site IV of the fusion glycoprotein. *Nat Commun* **10**, 4153 (2019).

189. Mäkelä, A. R. *et al.* Intranasal trimeric sherpabody inhibits SARS-CoV-2 including recent immunoevasive Omicron subvariants. *Nat Commun* **14**, 1637 (2023).

190. Güttler, T. *et al.* Neutralization of SARS-CoV-2 by highly potent, hyperthermostable, and mutation-tolerant nanobodies. *EMBO J* **40**, e107985 (2021).

ANEXOS

Tabla 3. Anticuerpos en revisión en la UE y/o US para uso terapéutico en oncología (marzo de 2024).

Nombre genérico	Nombre comercial	Diana	Fuente/Modificaciones Fc	Primeras indicaciones
Camrelizumab	AiRuiKa	PD-1	Huz/S228P	LH
Cosibelimab	(Pending)	PD-L1	Hum/No	CCE
Penpulimab	ANNIKO	PD-1	Huz/L234A L235A G237A	Carcinoma nasofaríngeo metastásico
Serplulimab	HANSIZHUANG	PD-1	Huz/S228P	Tumores sólidos con MSI-H
Sintilimab	Tyvyt	PD-1	Hum/S228P	NSCLC
Sugemalimab	Cejemly®	PD-L1	Hum/S228P	NSCLC
Trastuzumab duocarmazine	(Pending)	HER2	Huz/No	Cáncer de mama
Zolbetuximab	(Pending)	Claudin-18.2	Quim/No	Adenocarcinoma gástrico/gastroesofágico HER2 negativo
Odronextamab	(Pending)	CD20, CD3	Hum/*f)	(R/R) linfoma folicular; R/R LCBGD
Tarlatamab	(Pending)	DLL3, CD3 (scFv-scFv-scFc)	R292C, N297G, V302C	SCLC
Patritumab deruxtecan	(Pending)	HER3	Hum/No	NSCLC
Zanidatamab	(Pending)	HER2, HER2 (biparatópico; scFv-Fc x Fab-Fc)	Huz/*g)	Cáncer de vías biliares
Linvoseltamab	(Pending)	BCMA, CD3	Hum/*h)	MM
Datopotamab deruxtecan	(Pending)	TROP-2	Huz	NSCLC

Mur: murino; **Huz**: humanizado; **Hum**: humano; **Quim**: quimérico; **MM**: mieloma multiple; **NSCLC:** cáncer de pulmón de células no pequeñas (del inglés, *Non-small cell lung cáncer*); **SCLC***:* cáncer de pulmón de células pequeñas (del inglés, *small cell lung cáncer*); **LH**: linfoma Hodgkin; **CCE**: cáncer de células escamosas; **LCBGD**: linfoma de células B grandes difuso; **R/R**: Recaída/refractario; **MSI-H:** Inestabilidad de microsatélites (del inglés, *microsatellite instability-high*); ***f)** Hetero HH: WT x H435R-Y436F; emparejamiento HL: cL ; ambas cadenas: E233P, F234V, L235A, G236del, S228P; ***g)** T350V-L351Y-F405A-

Y407V x T350V-T366L-K392L-T394W; ***h)*** Hetero H, CL; Hetero HH: WT x H435R-Y436F; ambas cadenas: E233P, F234V, Huz/L235A, G236del; ***i)*** IgG4: S228P; IgG1: K147D, F170C, V173C, C220G, R255K, D399R, K409E en cadena pesada, y S131K, Q160C, S162C, C214S en cadena ligera; **rev**: en revisión.

El trabajo desarrollado durante esta Tesis Doctoral ha generado una serie de resultados que han sido recogidos en tres artículos científicos. Además, como resultado de colaboraciones con otros miembros del equipo y otros grupos de investigación, también se han publicado varios artículos no relacionados directamente con esta Tesis Doctoral.

ARTÍCULOS RELACIONADOS DIRECTAMENTE CON LA TESIS DOCTORAL

1. **Laura Rubio-Pérez**, Rodrigo Lázaro-Gorines, Seandean L. Harwood, Marta Compte, Rocío Navarro, Antonio Tapia-Galisteo, Jaume Bonet, Belén Blanco, Simon Lykkemark, Ángel Ramírez-Fernández, Mariola Ferreras-Gutiérrez, Carmen Domínguez-Alonso, Laura Díez-Alonso, Alejandro Segura-Tudela, Oana Hangiu, Ainhoa Erce-Llamazares, Francisco J. Blanco, Cruz Santos, José L. Rodríguez-Peralto, Laura Sanz and Luis Álvarez-Vallina. A PD-L1/EGFR bispecific antibody combines immune checkpoint blockade and direct anti-cancer action for an enhanced anti-tumor response. *Oncoimmunology*, 2023, VOL. 12, NO. 1, 2205336 DOI: 10.1080/2162402X.2023.2205336.
2. **Laura Rubio-Pérez**, Susana Frago, Marta Compte, Rocío Navarro, Seandean L. Harwood, Rodrigo Lázaro-Gorines, Marina Gómez-Rosel, Oana Hangiu, Noelia Silva-Pilipich, Lucía Vanrell, Cristian Smerdou, Luis Álvarez-Vallina. Characterization of a trispecific PD-L1 blocking antibody that exhibits EGFR-conditional 4-1BB agonist activity. *Antibodies*, 2024, 13(2), 34. DOI:10.3390/antib13020034.
3. Rodrigo Lázaro-Gorines, Patricia Pérez, Ignacio Heras-Murillo, Irene Adán-Barrientos, Guillermo Alberici o, David Astorgano, Sara Flores, Joanna Luczkowiak, Nuria Labiod, Seandean L. Harwood, Alejandro Segura-Tudela, **Laura Rubio-Pérez**, Yudhi Nugraha, Xiaoran Shang, Yuxing Li, Carlos Alfonso, Kaylin A. Adipietro, Dinendra L. Abeyawardhane, Rocío Navarro, Marta Compte, Wenbo Yu, Alexander D. MacKerell Jr, Laura Sanz, David J. Weber, Francisco J. Blanco, Mariano Esteban, Edwin Pozharski, Raquel Godoy-Ruiz, Inés G. Muñoz, Rafael Delgado, David Sancho, Juan García-Arriaza, and Luis Álvarez-Vallina. Dendritic cell-mediated cross-priming by a bispecific neutralizing antibody boosts cytotoxic T cell responses and protects mice against SARS-CoV-2. *Adv. Sci*., 2023, 10, 2304818. DOI: 10.1002/advs.202304818.

ARTÍCULOS NO RELACIONADOS DIRECTAMENTE CON LA TESIS DOCTORAL

1. Díez-Alonso L, Falgas A, Arroyo-Ródenas J, Romencín PA, Martínez A, Gómez-Rosel M, Blanco B, Jiménez-Reinoso A, Mayado A, Pérez-Pons A, Aguilar-Sopeña Ó, Ramírez-Fernández Á, Segura-Tudela A, Perez-Amill L, Tapia-Galisteo A, Domínguez-Alonso C,

Rubio-Pérez L, Jara M, Solé F, Hangiu O, Almagro L, Albitre Á, Penela P, Sanz L, Anguita E, Valeri A, García-Ortiz A, Río P, Juan M, Martínez-López J, Roda-Navarro P, Martín-Antonio B, Orfao A, Menéndez P, Bueno C, Álvarez-Vallina L. Engineered T cells secreting anti-BCMA T cell engagers control multiple myeloma and promote immune memory in vivo. *Sci Transl Med*. 2024 Feb 14;16(734):eadg7962. doi: 10.1126/scitranslmed.adg7962.

2. Blanco B, Ramírez-Fernández Á, Bueno C, Argemí-Muntadas L, Fuentes P, Aguilar-Sopeña Ó, Gutierrez-Agüera F, Zanetti SR, Tapia-Galisteo A, Díez-Alonso L, Segura-Tudela A, Castellà M, Marzal B, Betriu S, Harwood SL, Compte M, Lykkemark S, Erce-Llamazares A, **Rubio-Pérez L**, Jiménez-Reinoso A, Domínguez-Alonso C, Neves M, Morales P, Paz-Artal E, Guedan S, Sanz L, Toribio ML, Roda-Navarro P, Juan M, Menéndez P, Álvarez-Vallina L. Overcoming CAR-Mediated CD19 Downmodulation and Leukemia Relapse with T Lymphocytes Secreting Anti-CD19 T-cell Engagers. *Cancer Immunol Res*. 2022 Apr 1;10(4):498-511. doi: 10.1158/2326-6066.CIR-21-0853.
3. Hangiu O, Compte M, Dinesen A, Navarro R, Tapia-Galisteo A, Mandrup OA, Erce-Llamazares A, Lázaro-Gorines R, Nehme-Álvarez D, Domínguez-Alonso C, Harwood SL, Alfonso C, Blanco B, **Rubio-Pérez L**, Jiménez-Reinoso A, Díez-Alonso L, Blanco FJ, Sanz L, Howard KA, Álvarez-Vallina L. Tumor targeted 4-1BB agonist antibody-albumin fusions with high affinity to FcRn induce anti-tumor immunity without toxicity. *iScience*. 2022 Aug 17;25(9):104958. doi: 10.1016/j.isci.2022.104958.